Novel development of eco-friendly porous thermal insulation materials and the application

A thesis in fulfilment of the requirements for the degree of Doctor of Philosophy

By

Kaibao Wang

Department of Mechanical and Aerospace Engineering

University of Strathclyde

Glasgow

UK

2021

Declaration of Authenticity and Author’s rights

This thesis is the result of the author’s original research. It has been composed by the author and has not been previously submitted for examination which has led to the award of a degree.

Signed:

Date:

Acknowledgements

I would like to start by thanking my supervisor Dr Liu Yang for his invaluable advice during this research project. I appreciate the confidence he placed in me, giving me the opportunity to carry out this independent and challenging research. Without his guidance, this thesis would not have been possible.

I would also like to express my great gratitude to the Tobermory Fishing Company and the University of Strathclyde for funding this project.

I would also like to acknowledge all the present and past members of the Advanced Composites Group for their kind assistance and friendship.

I appreciate the time and expertise shared by the staffs in the Advance Materials Research Laboratory, technicians and administrative staffs in the Department of Mechanical and Aerospace Engineering. Their support made this possible.

Finally, I am especially grateful to my family. My parents-in-law and my parent for inspiration and financial support, my wife, Mrs. Wenqi Wang for encouragement and support. My sister and brother-in-law deserve my wholehearted thanks as well. I also need to thank my sweet heart, Ellie Jiayi Wang, who supply happy distractions to rest my mind outside of my research.

Publications

Several results of this thesis have been published over the course of this PhD project in the following journal articles.

Wang K, Yang L. Kucharek M. Investigation of the effect of thermal insulation materials on packaging performance. Packaging technology and science. 2020; 33:227-236

Kucharek M, Yang L, Wang K. Assessment of insulating package performance by mathematical modelling. Packaging technology and science. 2020; 1-9

Abstract

Inorganic thermal insulation materials, such as porous geopolymer and aerogel, have received unprecedented attention due to their excellent thermal insulation performance and non-burning characteristics. They are also more environmentally friendly compared to conventional synthetic insulation materials. The environmental benefit could be further enlarged when recycled glass fibre (rGF) is introduced in the geopolymer and aerogel system.

Waste glass has been investigated extensively in the geopolymer system. However, the effect of recycled glass fibre on the thermal property of geopolymer is not commonly mentioned. In this thesis, the effect of rGF content on the mechanical and thermal properties of geopolymer was examined. Results indicated that the addition of rGF in geopolymer significantly increased the compressive strength (92 to 165 kPa) without diminishing the thermal performance (51.1 to 54.6 mW/m.K). In addition, a considerable amount of recycled glass fibres (25 g for three specimens) was reused. This paves a promising way to maximise environmental benefits and shows great potential in the thermal insulation field.

Another avenue of research in this thesis was assessing the feasibility of fabricating short rGF mats and incorporating the prepared rGF mats with aerogel since these are rarely reported. In this thesis, rGF was used to fabricate the glass fibre mat via wet deposition and chemical bonding process to support the aerogel network. The mechanical and thermal performance of the rGF-aerogel composites was then characterised. The successfully prepared rGF mat provides a valuable reference for the preparation of recycled short fibre mats. The prepared rGF-aerogel had a low thermal conductivity (23.8 mW/m.K). Although the thermal conductivity of the rGF-aerogel is slightly higher than the prepared aerogel reinforced with the commercial GF mat (18.3 mW/m.K), it still paves a promising way to maximise environmental benefits and shows great potential in the thermal insulation field.

The potential application of aerogel composites in packaging was also explored since it is rarely reported. In this thesis, an optimised mathematical model was derived by incorporating two mathematical models described in the literature to improve the accuracy of the calculated results. A number of experiments were then set up to validate the optimised model. The results showed that the insulating performance of packages insulated with aerogel composites was significantly improved (2 times better than expanded polystyrene). This finding suggests that aerogel composites have a great potential to satisfy the requirement of temperature control for long-haul transportation of fresh goods. The optimised model can be utilised as a cost-effective tool for packaging design concerning passive temperature control with improved accuracy.

Contents

List of symbols

AA	Alkaline activator
AB	Aerogel blanket
AFFF	Aqueous film forming foam
Al	Alumina
Al_2O_3	Aluminium oxide
AlO_4	Aluminium-oxygen tetrahedron
APD	Ambient pressure drying
APS	Aminopropyltriethoxysilane
ATR	Attenuated total internal reflectance
BET	Brunauer-Emmett-Teller
BJH	Barrett-Joyner-Halenda
BPDA	Biohenyltetracarboxulic dianhydride
BTC	Benzenetricarbonyl trichloride
BTDA	Benzophenone tetracarboxylic dianhydride
CaO	Calcium oxide
cGF	Commercial glass fibre
CFD	Computational fluid dynamics
CNT	Carbon nanotube
CO_2	Carbon dioxide
CTAB	Cetyltrimethylammonium bromide
DCCA	Drying control chemical additive
$DI{\cdot}H_2O$	Deionised water
DMBZ	Dimethylbenzidine
DMCS	Dimethylchlorosilane
DMF	N,N-dimethylformamide
DMSO	Dimethyl sulfoxide
EIA	Energy Information Administration

EMI	Electromagnetic interference
EPS	Expanded polystyrene
EtOH	Ethanol
Fe_2O_3	Iron oxide
FE-SEM	Field Emission Scanning Electron Microscope
FTIR	Fourier transform infrared analysis
GAFs	Graphene aerogel fibres
GF	Glass fibre
GFEP	Glass fibre reinforced epoxy composites
GFRP	Glass fibre reinforced polymer
GGBS	Ground granulated blast furnace slag
GPTMS	Glycidoxypropyltrimethoxysilane
GUI	Graphical user interface
H_2O_2	Hydrogen peroxide
HCl	Hydrochloric acid
HEPA	High efficiency particulate air
HMDS	Hexamethyldisilazane
HMDSO	Hexamethyldisiloxane
HPR	Heat penetration rate
HTSCD	High-temperature supercritical drying
IEA	International Energy Agency
ILs	Ionic liquids
IR	Infrared
ISA	International symposium on aerogels
Kn	Knudsen number
KOH	Potassium hydroxide
LTSCD	Low-temperature supercritical drying
MF	Melamine-formaldehyde
MIT	Maximum insulation time

MPTMS	Methacryloxypropyltrimethoxy-silane
MTMS	Methyltrimethoxysilane
Na_2CO_3	Sodium carbonate
Na_2SiO_3	Sodium silicate
NaOH	Sodium Hydroxide
NH_4OH	Ammonia solution
NMP	N-methyl-2-pyrrolidone
OAPS	Octa(amino-phenyl)silsesquioxane
ODA	Oxydianiline
OPC	Ordinary Portland Cement
PBT	Polybutylene terephthalate
PCM	Phase change materials
PE	Polyethylene
PET	Polyethylene tetraphalate
PF	Phenolic furfural
PI	Polyimide
PIR	Polyisocyanurate
PMDA	Pyromellitic dianhydride
PP	Polypropylene
PSD	Pore size distribution
PUR	Polyurethane
PVDF	Polyvinylidene fluoride
RF	Resorcinol Formaldehyde
rGF	Recycled glass fibre
RW	Thermal resistance of a multi-layered wall
SAC	Sound absorption coefficient
SCD	Supercritical drying
SDBS	Sodium dodecylbenzene sulfonate
SDS	Sodium dodecyl sulfonate

SEM	Scanning Electron Microscope
Si	Silica
SiO_2	Silicon dioxide
SiO_4	Silicon-oxygen tetrahedron
TAB	Tris(4-amino-phenoxy) benzene
TBAF	Tetrabutyl-ammonium fluoride
TEOS	Tetraethoxysilane
TFMB	Trifluoromethyl-4,4`-diaminobiphenyl
TGA	Thermogravimetric analysis
TiO_2	Titania
TL	Transmission loss
TMCS	Trimethylchlorosilane
TMES	Trimethylethoxusilane
TMOS	Tetramethoxysilane
VIP	Vacuum insulation panel
VTES	Vinyltriethoxysilane
ZrO_2	Zirconia
ε	Surface emissivity

List of figures

List of tables

1. Introduction

1.1. Background

Global energy consumption is foreseen to be increased by 53% within the next ten years from the International Energy Agency (IEA) prediction, which is caused by the significant increase in industrial and urban activities due to the intensive country development and dramatic increase of population size [1]. Environment pollution becomes an obvious issue as a consequence of such massive energy demand [2]. Carbon dioxide (CO_2), as a pollutant substance, is contributing to the greenhouse effect significantly. The CO_2 emission ultimately leads to the rising average global temperature [3]. It was stated that a 2°C increase in the global average temperature would cause irreversible impacts on the environment, serve issues on human health, enormous damage to natural ecosystems as well as affect global agriculture sustainability [4]. Therefore, research on energy management and efficient minimisation of energy consumption has become vital more than ever in recent years [5].

Insulation in buildings or any other sector is an energy-efficient strategy leading to lower energy consumption [6]. Thermal insulation is composed of a material or several layers of materials that exhibit the characteristic of high thermal resistance, which can decrease the heat flow rate [7]. As a result, it provides the ability to maintain the heat/cool within the building and prevent heat flux with the surrounding [8]. An efficient insulation strategy can reduce the consumption rate of natural resources such as petroleum and gas reserves used for power generation. Therefore, greenhouse gas production can be lowered [9]. Furthermore, it is a cost-saving strategy too, and this is because the building has a positive net energy balance where a more considerable amount of energy is saved through the insulation application than the energy required to manufacture the insulation material itself [10]. Finally, thermal insulation provides other benefits, including fire protection (using inorganic materials), personal comfort, condensation control and sound control [6].

Conventional insulation materials such as mineral wool, expanded polystyrene (EPS), and Polyurethane (PUR) have the largest market share since they offer the best performance per unit cost [11]. In recent years, superinsulation materials such as aerogels have attracted much more attention due to their excellent thermal insulation performance. The proportion of superinsulation materials within the global insulation market in the upcoming future could increase considerably depending on the high-performance insulation, such as lower thermal conductivity and higher thermal stability, and decreasing costs [5]. Lightweight concrete and geopolymers as the load capacity components could also play an essential role in overall building insulation [12].

Table 1-1 summarises the thermophysical properties of commonly seen insulation materials, and the comparison of thermal performance is plotted in Figure 1-1. It is well indicated that vacuum insulation panel (VIP) provides the best thermal insulation performance among all listed materials, almost ten times better than conventional insulation materials such as EPS or mineral wool. Similar to foamy organic materials such as EPS or extruded polystyrene (XPS), its low thermal stability may limit its use in many applications [5]. Fibrous inorganic materials such as glass wool and rock wool exhibit greater thermal stability with excellent fire resistance grade. However, their thermal insulation performance is lower than foamy organic materials. Silica aerogels possess excellent thermal insulation and stability; however, one of the significant drawbacks is the cost, as shown in Figure 1-2. Figure 1-2 shows the material cost and insulation thickness required to achieve an R-value of 10 m^2K/W. This leads to the commercial development of low cost and sustainable silica aerogels and aerogel composites.

Table 1-1 Thermophysical properties of the commonly seen insulation material, λ: thermal conductivity at 20°C, dry material; ρ: bulk density; T_{max}: maximum service temperature; σ: compressive stress at 10% deformation except for foam concrete and foam geopolymer, reproduced from [13-18]

Insulation material	λ [mW/m.K]	ρ [kg/m^3]	T_{max} [°C]	σ [kPa]	Fire resistance grade
Vacuum Insulation Panel	4-8	65-300	90	45-120	-
Silica aerogels	4-20	3-350	750	0-5000	A
Polyurethane - Polyisocyanurate	19-30	25-100	120	100-500	B2
Extruded polystyrene	25-35	20-80	75	150-700	B2
Expanded polystyrene	29-41	10-50	80	60-260	B2
Glass wool	30-46	8-150	500	15-80	A
Rock wool	33-46	13-240	750	15-80	A
Foam glass	38-61	100-200	>400	400-1600	A
Expanded perlite	40-60	50-400	1260-1343	-	A
Foam concrete	80-250	200-700	1000	>100	A
Porous geopolymer	55-400	200-800	1300	>300	-

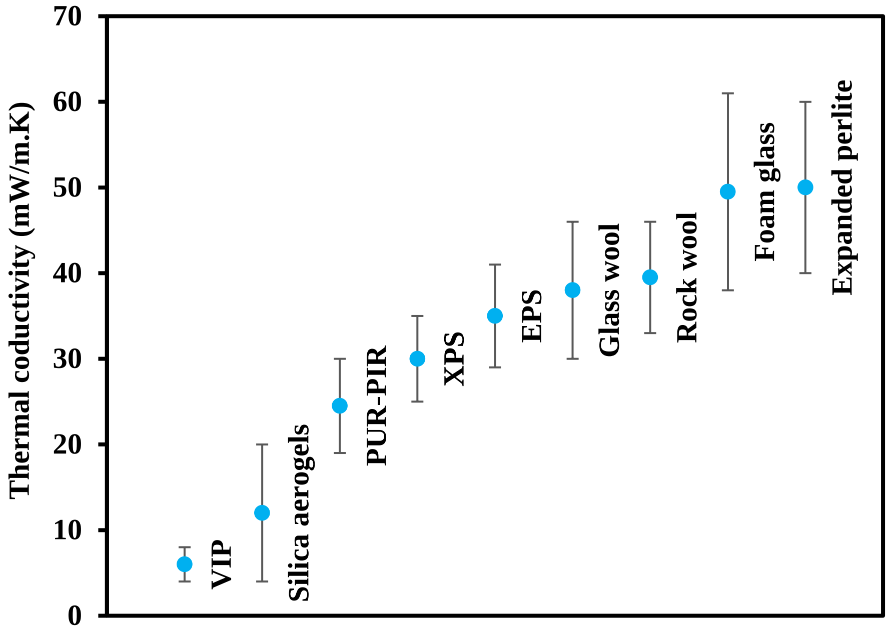

Figure 1-1 Thermal conductivity of commonly seen insulation materials (dry, at 20°C). The marks represent average values, and the bars show the range of value found in the literature, reproduced from [15]

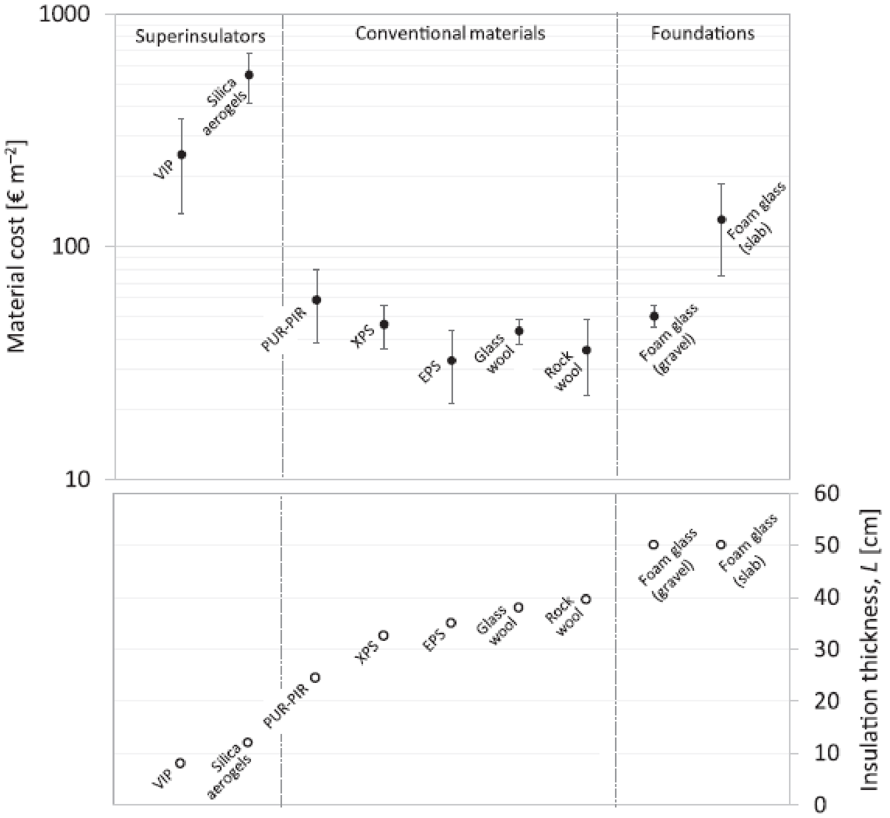

Figure 1-2 Material cost (top) and insulation thickness (bottom) required to achieve an R-value of 10 m^2K/W with various thermal insulation materials, reproduced from [15]

1.2. Current issues

Conventional inorganic materials are gradually eliminated mainly due to high energy and resource consumption during manufacturing processes [19]. Therefore, synthetic insulation materials, such as polystyrene foam and polyurethane become the predominant thermal insulation materials. Synthetic materials usually possess lower thermal conductivity (0.02 – 0.04 W/m.K), but their flammable characteristic imposes potential damages to human lives and society wealth [19]. In recent years, frequent fires on insulation materials for external walls of buildings have led to the rapid development of non-combustible inorganic insulation materials. Besides, synthetic (plastic) materials have become a significant problem to the environment nowadays as they can lead to contamination of a wide range of natural terrestrial, freshwater and marine habitats [20]. Thus, green, excellent thermal insulation and non-burning porous geopolymer and aerogel have received unprecedented attention [21]. These have stimulated the development of porous geopolymer and aerogel for thermal insulation application.

However, the major drawback of aerogel and aerogel composites is the cost, as indicated in Figure 1-2. Several strategies have been already implemented to reduce the cost of aerogels. This includes using a low-cost precursor (sodium silicate), simplifying the manufacturing process by reducing the cycle time and solvent consumption, and cost-effective ambient pressure drying. However, further research is still needed for large scale manufacturing at a lower cost [22]. The prevention of dustiness during handling also needs to be considered.

Geopolymer possesses a high potential for commercial applications since it is more economical and environmentally friendly than cement-based foamed concrete [23]. However, porous geopolymer may not exhibit high thermal insulation performance while maintaining its mechanical performance and durability. Therefore, it is required to optimise the chosen material ratio and synthesising process to solve the problems that currently exist in geopolymer production [14].

1.3. Aim and objectives

As discussed above, lower cost, more environmentally friendly, and greater thermal insulation performance are critical factors in novel insulation materials compared to conventional insulation materials. This thesis aims to investigate the potential for fabricating low-cost and more environmentally friendly insulation materials (geopolymer and aerogel) while maintaining or improving their thermal insulation and mechanical performance. The possibility of using aerogel composites in the packaging industry will also be discussed. To achieve this, five objectives are outlined:

1. **Fabrication and characterisation of inorganic porous geopolymer with excellent thermal performance**

As mentioned in the background research, insulation in buildings or any other sector is an energy-efficient strategy leading to lower energy consumption [6]. Porous geopolymer possesses a high potential for commercial insulation applications since it is more economical and environmentally friendly than cement-based foamed concrete [23]. Geopolymer can be fabricated using industrial solid waste (i.e., fly ash and furnace slag). It produces less carbon dioxide and consumes less energy during manufacturing than traditional cement [19, 24, 25]. Therefore, it is worth studying the physical, thermal, and mechanical properties of the geopolymer.

A number of researches have been carried out to investigate the properties of porous geopolymer. Foaming agents and foam stabilisers are the key factors determining the final properties of the material, and it was reported considerably. However, the foam expansion mechanism and the expansion rate at different temperature of the geopolymer slurry is rarely reported. This could be used to indicate how different pore structures are obtained by varying the foaming agent. In addition, the thermal performance of the geopolymer can be improved by varying the design parameters.

In chapter 3, the feasibility of synthesising inorganic porous geopolymer was evaluated using industry by-product fly ash as the raw material. The foaming agent was set as the variable, and the influence of the foaming agent on the properties of the geopolymer was discussed. Pore structure, bulk density, thermal conductivity, and compressive strength test were the critical parameters for characterising the prepared specimens. The effect of foaming agent amount on the foam expansion rate was also investigated, and the foam expansion mechanism was discussed.

2. **Fabrication and characterisation of inorganic silica aerogel with an improved fabrication process**

Apart from porous geopolymer, silica aerogel also shows great potential in thermal insulation application due to its highly porous structure. It gives unique properties such as high specific surface area (500-1500 m^2/g), high porosity (80-99%), low bulk density (0.03-0.35 g/cm^3) [26], extremely low thermal conductivity (12-30 mW/m.K) [22], high acoustic resistance and strong adsorption [22]. The involvement of aerogel in buildings or any other sector could be an energy-efficient strategy leading to lower energy consumption. Therefore, it is worth studying the synthesising mechanism as well as the characterisation of the materials.

Silica aerogel and its fabrication process have been investigated extensively [27]. The general fabrication process involves sol-gel, ageing, solvent exchange, surface treatment, and drying [27]. However, a few detailed descriptions of the fabrication process are not commonly mentioned, for example, the amount of solvent used for ageing and solvent exchange. It has a nonnegligible impact in terms of cost-saving, especially in the UK. The cost for one litre of Ethanol and n-Hexane is approximately £50 and £40, respectively [28, 29]. Therefore, adequate usage of these solvents could lower the manufacturing cost. In addition, the fabrication processes, including ageing temperature and drying process, could be optimised to improve the properties of the aerogel.

In chapter 4, the feasibility of synthesising silica aerogel was evaluated using a more economical sodium silicate as the precursor. The effect of ageing and solvent exchanging temperature on the pore structure of aerogel were examined. The minimum amount of solvent used to synthesise aerogel was investigated. Properties including morphology, pore structure, bulk density, BET surface area, hydrophobicity, thermal stability and thermal conductivity were examined as the critical parameters for characterising the prepared specimens.

3. Vacuum sealed fibre-reinforced silica aerogel composites with excellent thermal conductivity

The research on optimising aerogels' physical properties, such as pore structure and density, has shown extensive progress. However, the improvement of the strength, fragility and shrinkage rate of the aerogels are unsatisfactory, especially under ambient pressure drying [30]. The involvement of a secondary reinforcement seems to be an efficient way to strengthen the aerogel structure and thus widen its application [31]. Therefore, it is worth investigating the silica aerogel reinforced with fibres.

Fabrication of aerogel composites with embedded fibre is probably the most widely adopted technique in academic research and industrial manufacturing. This is because the involvement of fibre is an effective way to prevent shrinkage during the drying process, especially the ambient drying method. Thus, monolithic aerogel composites can be produced, and the mechanical properties can be improved significantly. However, the challenge is to preserve the insulation properties, minimise the increase of apparent density, and improve the dustiness due to the weak interfacial bonding between the aerogel particle and fibres [22].

In chapter 5, glass fibre mats were embedded in silica sol to form fibre reinforced aerogel composites. The fabrication process, including ageing temperature and drying process, was optimised to improve the physical, thermal and mechanical properties of the aerogel composite. The prepared aerogel composite was then vacuum sealed to prevent dustiness during handling, and its influence on thermal conductivity was investigated.

4. Eco-friendly geopolymer and aerogel composites reinforced with recycled glass fibres

The fabrication and characterisation of geopolymer and aerogel composites have been investigated in previous chapters. The mechanical performance of the prepared geopolymer could be further improved. The fibre reinforced aerogel composite could be more economical and environmentally friendly. Besides, an increasing amount of waste glass has been produced nowadays due to the widespread use of glass in different applications [32]. The glass products are non-biodegradable; thus, recycling and reusing glass are attractive, which could significantly contribute to the prevention of environmental pollution [32]. Therefore, It is worth investigating the involvement of recycled glass fibre in geopolymer and aerogel composites.

Waste glass, as a partial mineral precursor, has been investigated extensively in the fly ash-based geopolymer system [32-34]. The mechanical property of geopolymer generally improved with the addition of waste glass. However, the effect of waste glass on the thermal property of geopolymer is not commonly mentioned. In addition, the chemical structure of fibre dissolved in alkaline solution via FT-IR have not been studied comprehensively.

The fabrication of short recycled glass fibre (rGF) mats via chemical bonding and incorporating the prepared rGF mat with aerogel are scarcely reported. Needle-punching, as a more eco-friendly and lower energy consumption process, has been widely used to fabricate fibre mats compared to chemical bonding and thermal bonding [35]. However, it may be challenging to process short and low strength rGFs, as the fibres need to be long enough to sustain the repositioning force. Sizing, as a chemical bond technique, shows great potential in manufacturing rGF mat due to its ability to enhance the chemical bonding between glass fibre.

In chapter 6, recycled glass fibre (rGF) was introduced into the geopolymer and aerogel system. Within the geopolymer system, rGF was partially or fully dissolved in sodium hydroxide solution to form the alkaline activator. The effect of rGF content on the mechanical and thermal properties of geopolymer was examined. In addition, the chemical bonding state of the fibre dissolution in alkaline solution via FT-IR was investigated. Within the aerogel system, rGF was used to fabricate the glass fibre mat via wet deposition and chemical bonding process to support the aerogel network. The mechanical and thermal performance of the rGF-aerogel composites was characterised and compared with the aerogel composite reinforced with the commercial glass fibre blankets (prepared in the previous chapter).

5. The potential application of aerogel composites in thermal insulating packaging

It was stated in the background research that the aerogel composites presented an excellent thermal insulation performance [15]. In the packaging industry, conventional insulation materials may no longer satisfy the requirement of temperature control during package delivery due to increasing market demand for long-haul transportation of fresh goods (e.g. foods and medicine). Besides, Synthetic (plastic) materials have become a significant problem to the environment nowadays as they can lead to contamination of a wide range of natural terrestrial, freshwater and marine habitats [20]. Therefore, the feasibility of using aerogel composites in packaging is worth investigating to improve the thermal insulation performance of the packagings and reduce plastic pollution.

A number of researches have been focused on investigating the thermal performance of packaging, including analytical models and experimental work. However, the use of aerogel composites in this field is rarely reported. In addition, the factors influencing package insulation performance have not been studied comprehensively. Furthermore, a simplified analytical model accompanied by the ice melt test lead to significant uncertainty; therefore, both the analytical model and experimental work could be improved.

In chapter 7, the thermal insulation performance of a typical shipping container with different insulation materials, including the aerogel composite, was evaluated. An optimised mathematical model was derived and used to analyse the effect of packaging parameters on insulative performance. The novel aspect of this model was incorporating two mathematical models described in the literature to improve the accuracy of the calculated results [36, 37]. Some crucial factors, such as surface emissivity and thermal conductivity of materials, were measured experimentally instead of using literature value to improve the accuracy of the model. A number of experiments were then set up to validate the optimised model comprehensively. The effect of parameters, including surface emissivity, insulation thickness, insulation materials, amount of coolants and surrounding temperatures, on package insulative performance was investigated.

1.4. Outline of the thesis

This thesis starts with a background introduction of globally energy consumption increase and the current status of insulation materials. The current issues regarding the insulation materials are then addressed. The potential solutions to overcome these issues (described in sections 1.2 and 1.3) are then raised. Finally, the conclusion of the thesis is summarised, and future work is suggested.

Chapter 1 introduces the background of the global energy demand and insulation materials used to lower energy consumption as well as lists the current issues and objectives of this thesis.

Chapter 2 literature review of geopolymer, aerogel and composites, glass fibre recycling, and insulating packaging.

Chapter 3 evaluates the performance of fly ash-based geopolymer.

Chapter 4 investigate the performance of silica aerogel granules.

Chapter 5 assesses the performance of fibre-reinforced silica aerogel composites.

Chapter 6 evaluates the feasibility of using recycled glass fibre in geopolymer and aerogel systems.

Chapter 7 presents and discusses the potential application of aerogel composites in the packaging industry.

Chapter 8 summarises the conclusion of this thesis and gives suggestions for future work.

Appendix-A summarises the UK insulated packages market in 2018.

Appendix-B presents the Graphical User Interface (GUI) application.

2. Literature review

In this chapter, highly insulating materials, including porous geopolymer and aerogel, are reviewed comprehensively. Their reaction mechanism and fabrication process are first described. The research status and their application are then explored. Finally, the research gaps of these materials are discussed.

2.1. Research on geopolymer and applications

As mentioned in the background research, insulation in buildings or any other sector is an energy-efficient strategy leading to lower energy consumption [6]. Porous geopolymer possesses a high potential for commercial insulation applications since it is more economical and environmentally friendly than cement-based foamed concrete [23]. In this section, an introduction of geopolymer is presented, with the structure and reaction mechanism described. The influence of raw material parameters and curing conditions on mechanical and thermal performance is explored. Finally, the potential application and the knowledge gaps of geopolymer are addressed.

2.1.1. Introduction of geopolymer

In recent years, geopolymer has attracted more attention due to its excellent thermal stability, relatively high strength, and excellent fire resistance. More interestingly, geopolymer can be fabricated using industrial solid waste, and it produces less carbon dioxide as well as consumes less energy during manufacturing than traditional cement [19, 24, 25]. Joseph Daviovits initially described the term ‘Geopolymer’ as inorganic three-dimensional aluminosilicate material, which can be synthesised by the reaction of an alkaline solution with an aluminosilicate powder such as fly ash metakaolin, slag and rice husk ash [38, 39].

As the binder material used in concrete, traditional cement contributes approximately 5% of global CO_2 emissions during the production process [40]. The main reasons are the raw ingredient limestone’s calcination and the high temperature needed to heat the raw materials [24, 40, 41]. It was reported that the estimated CO_2 emissions during the production of geopolymer concrete could reduce 9-45% than traditional cement concrete [24]. Nevertheless, geopolymer is regarded as one of the optimal alternatives for traditional cement.

Apart from the environmental effect, the geopolymer’s polymerisation reaction speed is rapid, and the three-dimensional network structure can be readily formed. After being cured for 4 hours at room temperature, its compressive strength can reach 15-30 MPa. If properly cured, its strength will continue to increase with the time duration of ageing. Reinforced fibre such as carbon fibre, alkali-resistant glass fibre, mineral wool, fine powder and ultrafine powder such as zirconia, nano-alumina powder can also be added into the geological polymer to improve the overall performance of the material. The compressive strength can reach about 300 MPa [21, 42-44].

Geopolymer also possesses excellent resistance to fire and high temperature, where the melting temperature could reach 1300℃ [45]. The thermal conductivity of geopolymer is generally in the range of 0.1 to 0.38 W/m.K, which is better than lightweight fire resistance clay brick (0.3 to 0.4 W/m.K) [21]. The thermal conductivity could reduce further with porous structure [18], which could potentially be used as an insulating material with fire resistance.

Geopolymer has better volume stability than traditional cement during setting, hardening and usage. The seven-day linear shrinkage rate is only 14 to 20% of the conventional cement, and the twenty-eight-day linear shrinkage rate is around 12% of the traditional cement [21, 46].

The durability of concrete is usually improved when a certain amount of fly ash is mixed into the ordinary cement concrete [21]. Moreover, fly ash-based geopolymer can significantly reduce the leaching of toxic and harmful heavy metal ions compared to traditional Portland cement, which has attracted more attention and research [47].

2.1.2. Structure and Reaction mechanism

Geopolymer is one of the inorganic polymers with amorphous to semi-crystalline structure, and aluminosilicate is the chemical composition [48]. Among them, the silicon, aluminium, and oxygen element exists in the form of a silicon-oxygen tetrahedron (SiO_4) and aluminium-oxygen tetrahedron (AlO_4). These two basic structural units are linked by sharing all oxygen atoms, and the oxygen atom is in the middle. Such frameworks are called polysialates, where sialate stands for the silicon-oxygen-aluminate building unit. The silicon element has a stable +4 valence state, and the silicon-oxygen tetrahedron is electrically neutral. The aluminium-oxygen tetrahedron (+3 valence, 4-fold coordination) is bonded with four oxygen atoms, which appear electronegative. Metal cations Na^+, K^+, and $Ca^{2+,}$ are adsorbed around the molecular bonds and exist in the cavity of the three-dimensional structural system to balance the negative charge of Al in 4-fold coordination. The entire three-dimensional structural system appears electrically neutral. The geopolymerization process forms aluminosilicate frameworks, as shown in Figure 2-1 [48-52].

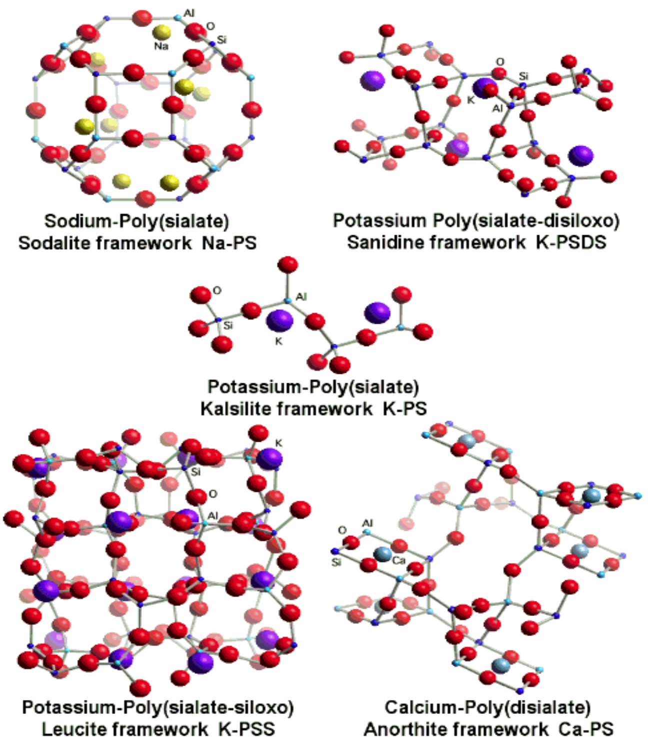

Sodium-Poly(sialate)
Sodalite framework Na-PS

Potassium Poly(sialate-disiloxo)
Sanidine framework K-PSDS

Potassium-Poly(sialate)
Kalsilite framework K-PS

Potassium-Poly(sialate-siloxo)
Leucite framework K-PSS

Calcium-Poly(disialate)
Anorthite framework Ca-PS

Figure 2-1 Polymeric structures from the polymerisation of monomers, reproduced from [52]

The geopolymerization process involves a quick reaction of silica (Si)-alumina (Al) under the alkaline condition, which subsequently creates a three-dimensional polymeric chain and ring structure consisting of Si-O-Al-O bonds [50, 53]. The following reactions occur during geopolymerization [48, 53]:

$$(Si_2O_5Al_2O_2)_n + H_2O + OH^- \rightarrow Si(OH_4) + Al(OH)^{4-} \tag{Equation 2-1}$$

$$Si(OH_4) + Al(OH)^{4-} \rightarrow (Si\text{-}O\text{-}Al\text{-}O)_n + 4H_2O \tag{Equation 2-2}$$

The polymerisation mechanism of geopolymer is very complicated, and it is different from ordinary cement. At present, geopolymer’s reaction mechanism is still unclear, especially for a relatively complicated system with a different constitution [51]. However, most proposed chemical reaction mechanism contains the following steps [50]:

(1) Dissolution of Si and Al atoms from the source material through the action of hydroxide ions.
(2) Transportation or orientation or condensation of precursor ions into monomers.
(3) Setting or polycondensation of monomers into a polymeric structure.

Although the exact reaction mechanism is still to be fully understood, the basic principle is the same. This includes fracture of the covalent bond and then recombining to form a three-dimensional network of aluminosilicate material. As research in this area is advancing, the polymerisation mechanism of geopolymer remains to be the main research direction [51].

2.1.3. Current status of geopolymer

2.1.3.1. Raw materials

The raw materials of geopolymer are mainly composed of two parts: one is solid powder rich in active aluminosilicate, and the other is the liquid activator. In addition, a foaming agent and foam stabiliser could be introduced to obtain a porous geopolymer structure.

2.1.3.1.1. Aluminosilicate solid

The choice of raw materials directly influences the ultimate performance of geopolymer. Metakaolin is mainly adopted during the initial research on geopolymer. With the development of the industry and broader study, the variety of raw materials is also increasing, such as furnace slag, steel slag, fly ash, waste glass, and construction waste [54]. The main mineral component of these industrial solid wastes is silicate or aluminosilicate, which can be used as the geopolymer's raw material like metakaolin. It also provides a route to reusing some of the industrial solid wastes. In terms of the properties, the compressive strength of geopolymers prepared from calcined materials, such as fly ash, slag and forged kaolin, is generally higher than that of geopolymers prepared from non-calcined minerals, such as kaolin, ore powder and naturally formed minerals [21, 55].

As the environmental problems increase prominently, fly ash gradually becomes the most used and suitable waste material in geopolymerization due to the enormous amount produced worldwide and its workability. It is estimated that 780 million tons of fly ash are produced annually [56]. The main composition of fly ash is amorphous silica and alumina with a favourable shape and size, improving the workability and making it suitable for geopolymer production. Fly ash is a by-product derived from the combustion of coal powders and collected by mechanical and electrostatic separators from the power plants' fuel gases [57]. The characteristics of fly ash are directly influenced by coal. The main oxide components of fly ash are SiO_2, Al_2O_3, FeO, Fe_2O_3, CaO, TiO_2, MgO, K_2O, Na_2O, SO_3, MnO_2, which exists in the form of amorphous and crystalline oxides or various minerals [14, 58]. The chemical composition of fly ash varies. The fly ash produced from different regions, different industries and even production processes has different phase compositions. For example, the silica and alumina content is relatively high when fly ash is produced by an iron blast furnace [14].

According to the British Standard EN450 [58], fly ash can be classified as Category N and Category S based on fly ash's fineness. The fineness of fly ash shall be expressed as the mass proportion in per cent of ash retained when sieved on a 0.045 mm mesh sieve. The fineness of Category N shall not exceed 40% by mass, and Category S shall not exceed 12% by mass. Unlike the American Society for Testing and Materials standard ASTM C618 [59], fly ash is not classified based on the chemical composition in EN450. However, the requirement for the contents of silicon dioxide (SiO_2), aluminium oxide (Al_2O_3) and iron oxide (Fe_2O_3) shall not be less than 70% by mass, and the content of reactive calcium oxide (CaO) shall not exceed 10% by mass. This requirement is equivalent to Class F fly ash that is classified in ASTM C618, which is identified as low calcium fly ash. Low calcium fly ash is more commonly used for geopolymer fabrication due to its relatively pure and high content of silica-aluminium [21, 60]. However, research also shows that the increase of calcium content promotes hydration within the geopolymer system, shortens the coagulation process; the early strength is, therefore, improved [39].

2.1.3.1.2. Alkaline activator

At present, the common activation methods in geopolymer preparation mainly include alkali activation and acid activation. Alkali reaction refers mostly to geopolymer preparation by the activation reaction of alkaline solutions such as sodium hydroxide and potassium hydroxide with aluminosilicate materials. This method has been studied for a considerable amount of time and is relatively mature [61]. Acid reaction mainly uses acidic solutions such as phosphoric acid as the acid activator to synthesise geopolymer materials [62].

The most commonly used alkaline activator is the mixture of sodium hydroxide or potassium hydroxide with sodium silicate or potassium silicate solution. A single alkaline activator is also adopted by some researchers. Huang et al. [17] successfully synthesised geopolymer using sodium silicate as the sole alkaline activator. It was found that the density, thermal conductivity, as well as compressive strength decreased as the amount of sodium silicate increased. However, Palomo et al. [63] suggested that the role of the alkaline activator was crucial in the polymerisation process, and the reaction speed of sodium or potassium solution containing soluble silicate was faster than that of hydroxide alone. Yahya et al. [64] proved that geopolymer activated with a combination of sodium hydroxide and sodium silicate displayed a significant strength increment compared to samples activated with sodium hydroxide only. Xu et al. [65] also demonstrated that the combination of sodium silicate and sodium hydroxide solution could promote the reaction between the raw material and the activator liquid.

Sodium silicate and sodium hydroxide, as the widely used alkaline activator, still have some shortcomings. On the one hand, sodium silicate solution is prone to self-polymerisation under alkaline conditions, increasing geopolymer viscosity and low workability. On the other hand, sodium silicate solution, as a complex solution of many kinds of polysilicates, its chemical composition is easy to change over time and difficult to predict, which brings inconvenience to the large-scale application in practice [39].

2.1.3.1.3. Foaming

The role of foaming agents in lightweight geopolymers is to create small and enclosed air bubbles by reducing the surface tension of a solution and increasing air bubbles' stability [66]. There are three main techniques used to produce foams within geopolymer: reactive emulsion templating, ice templating and direct foaming [67]. Direct foaming is perhaps the most widely adopted method. In this method, wet geopolymer foams are produced by incorporating a gas into a homogeneous slurry, which is then cured at certain temperatures (even room temperature) to obtain a porous solid structure. The generation of gas into the homogeneous liquid can be chemically or physically [17]. Chemical foaming forms gaseous products such as O_2 and H_2 as well as other by-products by thermal decomposition or chemical reactions. Physical foaming generates porosity by a phase change, e.g., a liquid is volatilised or a gas dissolved in the system under high pressure may be desorbed by decompression [18]. Either way, the slurry needs to have suitable rheology to enable gas retention for a sufficient time to ensure the wet foam to be set. Physical foaming can result in a uniform distribution of fine pores, but geopolymer's density may not always be reduced significantly [12]. Chemical foaming may be more efficient in lowering density, but large pores may be generated, which have a negative effect on the thermal and mechanical properties of geopolymer [68, 69].

Chemical foaming widely used for the fabrication of lightweight geopolymers involves metal powders, (e.g. aluminium, silicon powders) or Si-containing compounds (e.g. silica fume, hydrogen peroxide (H_2O_2), NaOCl, and $FeSO_3$). The reaction leads to a gas release in an alkaline solution [18]. Among them, hydrogen peroxide is a well-known chemical foaming agent. Hydrogen peroxide is an inorganic liquid that is miscible with water at any ratio, and it is more efficient and controlled using catalyst [70]. During the decomposition process, gas is generated at the molecular scale and produces a more homogeneous foam [71]. Hydrogen peroxide is thermodynamically unstable and can be easily decomposed into water and oxygen. The bubble of O_2 is trapped within the paste, expanding and generating void (macropores). The expansion volume of the material depends on the amount of oxygen produced by the following reaction [68, 71]:

$$H_2O_2 \rightarrow H_2O + {}^{1}/_{2}\,O_2 \qquad \text{(Equation 2-3)}$$

The usage of hydrogen peroxide is much dependent on the type of fly ash. As mentioned in section 2.1.3.1.1, the slurry of fly ash in different regions may possess different characteristics. The influence of alkaline solution on the foaming of hydrogen peroxide and slurry curing speed cannot be ignored, which cannot be adjusted by those acid-base substances [17]. This may limit the usage of hydrogen peroxide in geopolymer fabrication. Nevertheless, the appropriate hydrogen peroxide content within the slurry system significantly influences the apparent density, pore size, and homogeneity. It consequently influences the ultimate properties of the lightweight geopolymers [71].

2.1.3.1.4. Stabilizing agent

Foaming is a thermodynamically unstable process. The gas bubbles in the wet foams usually present spontaneous drainage, continuous Ostwald ripening, and coalescence to minimise the overall Gibbs free energy of the system [18]. Due to the instability of the wet foams, large pores (hundreds of microns) and a wide range of pore sizes are typically present in the porous geopolymer. Stabilizing agents such as surfactants, particles and fibre are generally added to the system to improve the microstructure of geopolymer with fine and homogeneous pores [18].

The impact of surfactant on foamed geopolymer's final properties has been investigated extensively [72-75]. The surfactant can be ionic (cationic and anionic), non-ionic or amphiphilic. Their structure and chemical formula can change the interactions between the constituents of the paste, which can modify the workability of the paste in the liquid state and the topology of the final solid material, particularly the connectivity of the macro-porous network [71, 76]. In particular, foam stabilizer as a surfactant could reduce the bubble's surface free energy and enhance the toughness of the bubble wall, therefore decreasing the burst and coalesce of bubbles [74]. It has a significant influence on the stability, optimization and development of pore in lightweight geopolymer. Moreover, pore characteristics governed by the size, volume and connectivity in geopolymer play a crucial role in determining the density, strength and thermal conductivity [74, 77, 78].

Calcium stearate is an effective foam stabilizer in the fabrication of lightweight geopolymers [79, 80]. Calcium stearate is insoluble in water, and part of the hydrophobic solid particles will be adsorbed on the gas-liquid interface (known as liquid film) of the bubbles within the system, making them coalescing stable. This can slow down the thinning rate of the liquid film and reduce the rate of gas diffusion in the foam [72, 81]. Therefore, the foam has a longer stabilization time. The effect of calcium stearate content was also investigated [72]. As the amount of calcium stearate increases, under the same amount of hydrogen peroxide, the foaming volume and foam half-life period are gradually increased. This shows that the more calcium stearate is added, the more hydrophobic particles in the system and the more stable the foam behaves. This further proves that the hydrophobic solid particles can better stabilize the solid three-phase foam [72]. However, when the foam stabilizer content continues to increase, the foam half-life period slightly decreases. This may be because the foam stabilizer is excessive, and the thickness of the foam film becomes smaller, resulting in reduced foam stability [82].

2.1.3.2. Research status of geopolymer fabrication

It is well indicated that several factors influence the mechanical and thermal performance of porous geopolymers. This includes the choice of precursor, alkaline activator, foaming agent, and foam stabilizer [17, 72, 83, 84]. The fabrication processes, including curing conditions and the mixing ratio of the chosen raw materials, are also critical.

2.1.3.2.1. Curing condition

The curing temperature of geopolymer usually is higher than that of traditional cement. Curing at 60°C to 100°C for 24 to 48 hours and then post-curing at room temperature is typically necessary [85, 86].

Huang et al. [17] explored the effect of curing temperature on the sample density, porosity, thermal conductivity and compressive strength. The curing temperature was set to 45℃, 55℃ and 65℃. The results indicated that the bulk density of samples increased, and the porosity decreased with increased curing temperature, but the change was limited. In addition, as the curing temperature increased, the thermal conductivity of samples increased slightly. This is because thermal conductivity depends on the porosity, and the effect of curing temperature on porosity is not significant. However, the curing temperature had a noticeable influence on the compressive strength. An increase of 21% in strength was gained as the curing temperature increased from 45℃ to 65℃. The compressive strength depends on the microstructure, such as porosity, the pore wall’s thickness, and pore size. The pore expansion was also affected by the solidification rate of the matrix [17]. As the curing temperature increased, the solidification rate was faster. The pore expansion was, therefore, restricted, the pore size and porosity were reduced [87]. As a result, the compressive strength was improved as the curing temperature increased [17]. Feng et al. [88] synthesised porous geopolymer at a curing temperature of 55℃ and 85℃, and a similar trend was obtained.

It was stated that overheating the specimen could result in a much lower mechanical strength [89]. Since the exothermic reaction occurred during the curing process, the internal temperature may be higher than the surrounding temperature. If the sample was cured at 90℃, the internal temperature could be above the boiling point of water. Cracks might be presented due to internal stresses. Therefore, mechanical strength would be lower [90, 91].

Apart from traditional heat curing, a few novel curing methods such as water curing [85], microwave curing [92] and solar curing [93] are also reported. The compressive strength of geopolymer by microwave curing was more remarkable than an oven-cured sample due to the different heat transfer mechanisms. However, in the microwave oven, the penetration depth is only a few centimetres depending on the wavelength. Therefore, care should be taken when curing is carried out in the microwave oven [92]. Solar curing is a green way to accelerate the geopolymerization process hence the hardening rate. Therefore, it will significantly increase the strength of the geopolymer due to a high peak temperature during an early period of drying. However, solar curing is only limited to sunny areas, and special equipment may be needed to monitor or control the temperature fluctuation [93].

2.1.3.2.2. Aluminosilicate solid and alkaline activator ratio

There are many factors (e.g., aluminosilicate solid and alkaline activator ratio, sodium silicate and sodium hydroxide ratio, and sodium hydroxide concentration) that can significantly influence the geopolymer properties. The choice of parameters depends on the application, such as thermal insulation or structural replacement.

Hadi et al. [94] examined the effect of the alkaline activator's weight ratio to fly ash content, the weight ratio of sodium silicate to sodium hydroxide, and sodium hydroxide concentration on the mechanical properties of solid geopolymer. Their results indicated that the optimum alkaline activators to fly ash weight ratio was in the range of 0.5 and 0.6, regardless of sodium silicate to sodium hydroxide ratio and sodium hydroxide concentration.

Shao et al. [16] and Hameed et al. [95] investigated the effect of NaOH concentration on geopolymer's compressive strength. The results clearly showed that the concentration of sodium hydroxide played a vital role in the compressive strength of geopolymer. Increasing sodium hydroxide concentration led to an improvement in compressive strength. The geopolymerization process needed strong alkali to activate the Si and Al in fly ash and Metakaolin. The ability to leach Si and Al was improved by increasing the sodium hydroxide concentration since the alumino-silicate gel was formed at an early stage.

Wang et al. [96] investigated the influence of alkaline activator content on foamed geopolymer's physical properties. The results indicated that as the amount of alkaline activator increased, the foam expansion rate of slurry gradually increased. This led to a decrease in dry density and thermal conductivity, as well as a drop in the compressive strength [96].

2.1.4. Geopolymer aerogel composites

The thermal performance of geopolymer may not meet the higher thermal requirements on some occasions [38]. Even though the addition of a foaming agent may reduce the thermal conductivity, as mentioned previously, the mechanical properties dropped significantly. The unique nano-porous structure of silica aerogel leads to outstanding thermal performance, whereas the low mechanical property has greatly limited its application [38]. Therefore, the combination of geopolymer and silica aerogel could favour its mechanical and thermal insulation performance [38]. Besides, aerogels' hydrophobic nature is beneficial for water resistance in building insulation applications, such as external building envelopes [97].

Huang et al. [38] prepared a lightweight, highly hydrophobic, and super thermal insulating geopolymer/aerogel composite by immersing the pre-prepared geopolymer into silica sol, followed by ambient pressure drying. The thermal conductivity of the composites was as low as 0.048 W/m.K. The hydrophobicity measurement indicated that the contact angle increased from 0° to 138° after the impregnation of silica aerogel, as demonstrated in Figure 2-2. However, the obtained composites exhibited a poor mechanical performance (maximum compressive strength of 0.79 MPa) since the foaming agent was introduced during the fabrication of geopolymer.

Figure 2-2 Aerogel/geopolymer composites during the hydrophobicity test, reproduced from [38]

Another technique used to prepare aerogel/geopolymer composite is to mix the silica aerogel powder or granules with aluminosilicate solid and alkaline activator to form a uniform slurry. The mixed slurry was then cured to form geopolymer/aerogel composites [98, 99]. Cui et al. [98] investigated the influence of aerogel content on the properties of aerogel/geopolymer composites. The results showed that as the volume per cent of aerogel increased from 0% to 6%, the composites' bulk density dropped from 1.75 to 0.95 g/cm^3, and the thermal conductivity decreased from 0.55 to 0.22 W/m.K. However, the compressive strength reduced significantly from 74 MPa to 15 MPa. The aerogel surface was further modified with epoxy resin adhesive and silane coupling agent to improve the mechanical performance while maintaining the thermal properties. As a result, the compressive strength of the modified composites reached 46 MPa, due to the enhancement of the inter-transition zone between aerogel and geopolymer matrix. This is demonstrated in Figure 2-3. The contact angle between the aerogel and alkaline activator/ water indicated that the aerogel could stably exist in the geopolymer matrix [98], whereas the hydrophobicity of aerogel/geopolymer composites was not mentioned.

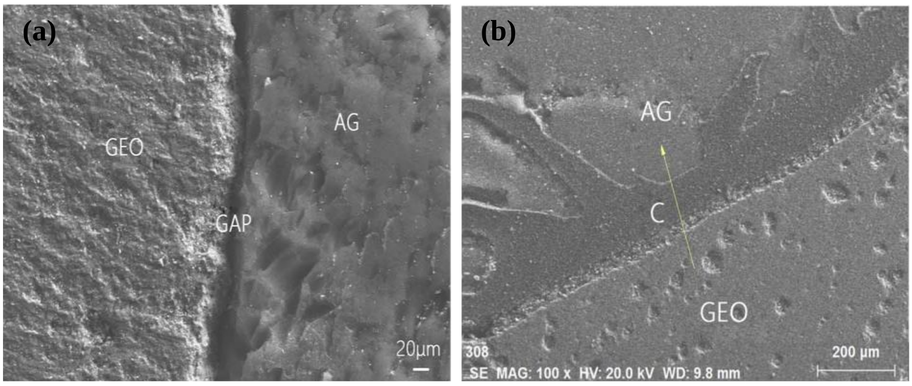

Figure 2-3 SEM image of aerogel/geopolymer composite (a) without and (b) with modification. GEO = geopolymer; AG = aerogel; and C = coating, reproduced from [56]

Similarly, Li et al. [99] established a numerical model for predicting the aerogel foam concrete's thermal conductivity based on a modified Maxwell model. An optimal ratio of the design parameters was obtained and prepared experimentally. The results showed that the thermal conductivity and density were approximately 50% lower than those of existing foam concrete. The prepared aerogel foam concrete exhibited a low density of 198 kg/m^3 and thermal conductivity of 0.049 W/m.K. The calculated results were in excellent agreement with the experimental data, with an error of less than 5% [99]. Thus, this design shows excellent potential in a green and zero-energy consumption building application.

2.1.5. Application of geopolymer

Geopolymer possesses a high potential for commercial applications due to their enhanced durability, chemical and thermal resistance properties, relatively low thermal conductivity, and excellent mechanical strength. Besides, geopolymer can be produced using the industrial by-product, which is more economical and environmentally friendly [23].

2.1.5.1. Thermal insulation

Conventional inorganic materials are gradually eliminated mainly due to high energy and resource consumption during manufacturing processes [19]. Therefore, synthetic insulation materials, such as polystyrene foam and polyurethane become the predominant thermal insulation materials. Synthetic materials usually possess lower thermal conductivity (0.02 – 0.04 W/m.K), but their flammable characteristic imposes potential damages to human lives and society wealth [19]. In recent years, frequent fires on insulation materials for external walls of buildings have led to the rapid development of non-combustible inorganic insulation materials. Green, high strength and non-burning porous geopolymer are also receiving unprecedented attention [21]. These have stimulated the development of porous geopolymer for thermal insulation application.

Kong et al. [83] analysed the strength behaviour of fly ash-based geopolymer after exposure to elevated temperature (800°C) for one hour. The results indicated that the samples did not have any cracks on the surface after the temperature exposure, and the compressive strength increased by 6%. It was suggested that the fly ash-based geopolymer had large numbers of small pores, which facilitate the escape of moisture when heated, thus causing minimal damage to the geopolymer matrix. The strength increase could also be partly attributed to the sintering reactions of un-reacted fly ash particles. It was indicated that fly ash-based geopolymer possessed high thermal and mechanical stability at a higher temperature. Therefore, geopolymer could be used in the furnace, pipe and external structural wall [83].

As mentioned in section 2.1.3.1.3, the porous structure can be introduced by adding a foaming agent to reduce thermal conductivity. Cui et al. [74] synthesised the fly ash-based geopolymer using H_2O_2 as the foaming agent. The thermal conductivity reached a bottom point at 0.095 W/m.K. Overall, this could promote the development of porous geopolymer for thermal insulation application.

2.1.5.2. Repair agent

Geopolymer exhibits the characteristics of fast hardening and high early strength, which can be used in civil engineering. Such characteristics can significantly shorten the de-moulding time, speed up the operation cycle and improve construction efficiency. It is often used to repair high-speed roads, especially in some public places such as airports and motorways. Geopolymer is often used for rapid repair of concrete and other materials, especially in historical buildings, due to their early strength and high interface bonding with aggregates [21, 43, 89].

2.1.5.3. Solid Adsorbents

Another promising application for porous geopolymer is used as absorbent components [18]. Chindaprasirt and Rattanasak [100] synthesised fly ash-based geopolymer and used it for CO_2 capture application. The results indicated that the adsorption rate was 0.12 g CO_2 per gram of porous geopolymer, and it was suggested that it could be used as a solid absorbent [100]. Research also indicated that porous geopolymer is a very effective sorbent for heavy metal ions, such as Ni, Pb, Cu, Cs, as well as ammonium and Ca cations [18].

2.1.5.4. Other applications

Besides the above-mentioned potential application, porous geopolymer has also been tested for sound absorption [101], water absorption [102] and self-cleaning concrete [89]. Thus, geopolymer could be a promising material used in many commercial applications.

2.1.6. Conclusion

In this section, a comprehensive review of geopolymer and its application is explored. A number of researches have been carried out to investigate the properties of porous geopolymer. Foaming agents and foam stabilizers are the key factors determining the final properties of the material, and it was reported considerably. However, the foam expansion mechanism and the expansion rate at different temperature of the geopolymer slurry is rarely reported. This could be used to indicate how different pore structures are obtained by varying the foaming agent. In addition, the thermal performance of the geopolymer can be improved by varying the design parameters.

2.2. Research on aerogel and applications

Apart from porous geopolymer, silica aerogel also shows great potential in thermal insulation application due to its highly porous structure. In this section, an overview of aerogel is presented, including aerogel structure and reaction mechanism. The influence of synthesizing conditions, including ageing, solvent exchange, surface treatment and drying method, on the mechanical and thermal performance of aerogel is explored. Finally, the potential application and knowledge gaps of aerogel are discussed.

2.2.1. Introduction of aerogel

Aerogel is a type of solid material with a highly porous structure, a chain or pearl string shape three-dimensional network [22]. It gives unique properties such as high specific surface area (500-1500 m^2/g), high porosity (80-99%), low bulk density (0.03-0.35 g/cm^3) [26], extremely low thermal conductivity (12-30 mW/m.K) [22], high acoustic resistance and strong adsorption [22]. Aerogel is a nanoporous amorphous solid material in which air replaces the entrapped solvent within the gel while maintaining the integrity of the network structure [26, 103].

Aerogel was first prepared in 1931 by Kistler of Stanford University through hydrolysis of waterglass using hydrochloric acid (HCl) combined with supercritical drying technology [104]. However, due to the limitation of knowledge and the preparation process, there was no follow-up interest in the field of aerogel until 1968 when Teichner from University Claude, Bernard, Lyon, France rediscovered this field [105, 106]. The procedure was substantially simplified by carrying out the sol-gel transition in a solvent, which was then dried at supercritical conditions [106]. Since then, aerogel has been more widely studied and discussed, and the first international symposium on aerogels (ISA) was organised in Wurzburg, Germany, in 1985 [103]. A variety of aerogel materials has now been invented, including inorganic aerogel such as SiO_2 aerogel, organic aerogel such as Resorcinol Formaldehyde (RF) aerogel, carbon aerogel, and metal aerogel. Aerogel can be used in many fields, such as aerospace, building and piping insulation, environmental protection, catalytic adsorption, sound insulation, and biomedicine [103].

2.2.2. Reaction process

The synthesis of silica aerogel has received significant attention, especially during the last two decades [107]. Different precursors, modification of synthesis parameters and drying techniques have been extensively explored. Silica aerogel is synthesised through sol-gel chemistry, defined by IUPAC as 'the Process through which a network is formed from a solution by a progressive change of liquid precursor(s) into a sol, to a gel, and in most cases finally to a dry network' [22, 108]. The synthesis process can be divided into three steps. Firstly, silica gel is prepared by the sol-gel process. The sol is obtained by adding a catalyst into a silica source solution, and gelation occurs. Secondly, the gel prepared in the first step is aged in its parent solution. This ageing process helps to strengthen the gel structure to ensure a minimum shrinkage during the drying process. Finally, the aged gel is dried through different conditions such as supercritical drying, ambient pressure drying, vacuum drying and freeze-drying. It is crucial to prevent the collapse of the gel structure during the drying process [107].

2.2.2.1. Hydrolysis and condensation

Sol-gel structure stems from the hydrolysis of precursors and subsequent condensation into primary particles. The primary particles then evolve through the developing solution and aggregate to form larger secondary particles, which link in a continuous network with liquid in the interstices [22], as shown in Figure 2-4 [109].

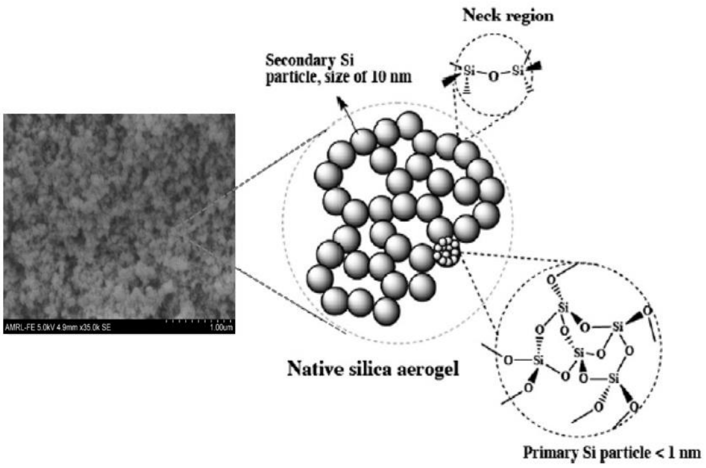

Figure 2-4 Typical SEM image of silica aerogel with a schematic representation of primary and secondary silica particles, reproduced from [109]

The chemical reaction of alkoxysilanes for hydrolysis and condensation can be summarised as [27]:

$$\equiv Si\text{-}OR + H_2O \rightleftharpoons \equiv Si\text{-}OH + R\text{-}OH \qquad \text{(hydrolysis)}$$

$$\equiv Si\text{-}OH + HO\text{-}Si\equiv \rightleftharpoons \equiv Si\text{-}O\text{-}Si\equiv + H_2O \qquad \text{(water condensation)}$$

$$\equiv Si\text{-}OR + HO\text{-}Si\equiv \rightleftharpoons \equiv Si\text{-}O\text{-}Si\equiv + R\text{-}OH \qquad \text{(alcohol condensation)}$$

Taking Tetraethoxysilane (TEOS) as an example, TEOS is hydrolysed under acidic conditions to produce a large number of silicic monomers, and a homogeneous sol system is obtained. The pH of the system is then adjusted, and the polycondensation reaction between the silicate monomers occurs. Finally, a three-dimensional molecular network is formed [103]. The formation process is shown in Figure 2-5 [103]:

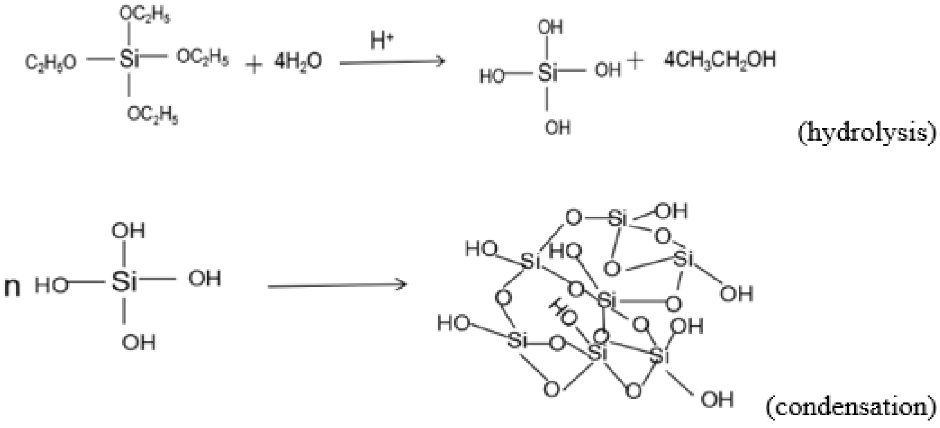

Figure 2-5 Expression of hydrolysis and condensation process, reproduced from [103]

During hydrolysis, a nucleophilic attack of oxygen lone pairs of the H_2O molecule on the silicon atoms is involved [110]. The Si atoms hold a partial positive electronic charge due to the polarized Si-O bonds, and it determines the kinetics of the nucleophilic attack and hence the overall hydrolysis reaction. In Si alkoxide, the Si atoms carry a relatively moderate partial positive charge, resulting in very slow gelation kinetics. Therefore, the hydrolysis and condensation of Si are typically catalysed either by acids (e.g., H^+) or/and by bases that carry strong negative charges (e.g., OH^-), and the reaction mechanism changes completely [27].

The hydrolysis and condensation reaction is affected by various parameters, including the metal alkoxide activity, the water/alkoxide ratio, solution pH, temperature, nature of the solvent, and additive used [105]. It is also beneficial to control the rate and extent of hydrolysis and condensation by frequently adding the catalysts [105]. The microstructures and surface chemistry of materials can be adjusted by varying these parameters. It was found that the pH value is a dominant parameter for the relative rates of hydrolysis and condensation of alkoxysilanes [22], as indicated in Figure 2-6. It is shown clearly that the condensation reaches the minimum rate around pH 1-3. This is due to silica reaching the isoelectric point at pH 2. Thus, the electrical mobility of silica particles is minimum [111, 112]. Under acidic conditions, the hydrolysis reaction is faster than the condensation reaction, favouring the simultaneous formation of smaller oligomers with reactive Si-OH groups. As a result, a weak cross-linked polymer-like gel, which is made from chains with few branches, is formed [22]. The gel can easily lose its shape and tends to crush as the chains impinge on one another due to internal movements [22]. Therefore, aerogel synthesised via acid catalyst usually has a denser structure. Hydrochloric acid (HCl) is a commonly used acidic catalyst. Under alkaline conditions, the condensation reaction occurs at a higher rate than the hydrolysis reaction [22]. This is due to the slightly positive charge of Si atoms in the presence of proton acceptors [22]. The hydrolysed species are readily consumed into denser and larger colloidal silica particles. Such structures tend to prevent network dragging and crushing caused by internal pressure, resulting in a lighter aerogel with higher pore volume being obtained [22]. Aqueous ammonia solution (NH_4OH) is the most frequently used base catalyst. Therefore, the microstructures of silica aerogels can be designed by balancing the hydrolysis and condensation rate by adjusting the initial pH according to a specific precursor [113]. At present, it is common to use a two-step catalyst process to better control the microstructure of aerogel by taking advantage of both the catalyst reaction mechanism [114].

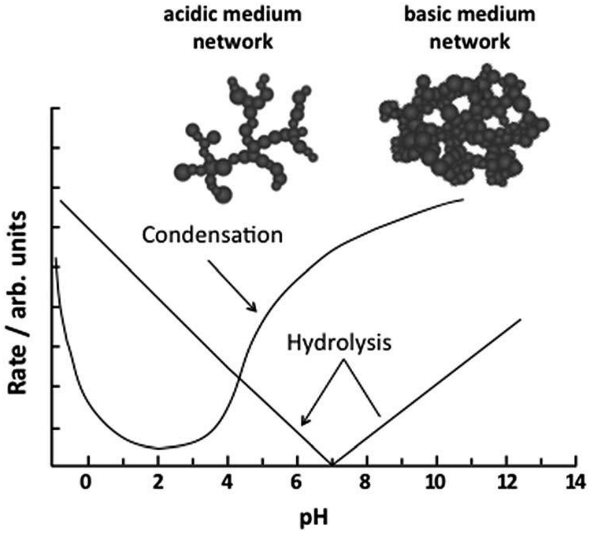

Figure 2-6 Rate of hydrolysis and condensation reactions of tetra alkoxysilanes with regard to pH dependency, reproduced from [115]

After a certain period (as less as 30 seconds), the sol no longer flows under the effect of gravity, and the gelation point is reached when a continuous network is formed [22]. In general, the gelation time is controlled by the pH of the sol, and it is longer when the pH of the sol is low [107].

2.2.2.2. Ageing

The chemical reaction of the sol-gel process still occurs after the gelation [22]. Therefore the ageing step aims to strengthen the tenuous solid skeleton generated during the sol-gel process to continue the process of cross-linking and coarsening [27]. There are two mechanisms that may operate during ageing, and it will affect the structure and properties of a gel: (1) Neck growth from reprecipitation of silica dissolved from particle surface onto necks between particles. (2) Dissolution of smaller particles with unreacted sites (OH moieties) and precipitation onto larger ones [116]. The latter occurring at the micro-level during ageing is known as Ostwald ripening [27, 117]. These two mechanisms operate simultaneously but at a different rate [116].

The morphology of materials such as the particles ‘neck’ area, the average pore size, porosity, and the apparent density of gel are influenced by ageing treatment. Therefore the mechanical properties could be improved significantly. The ageing solution, ageing time, and ageing temperature are the critical parameters that can significantly influence the ageing effect [27].

Research indicates that the liquid permeability of the solid part of the silica gel could be increased through washing in H_2O/EtOH by a dissolution reprecipitation process [118]. However, ageing in a siloxane solution improves the stiffness and the strength of the alcogel by adding new monomers to the silica network and improving the degree of siloxane cross-linking. Gels synthesised by waterglass can be strengthened by ageing in TEOS, water and ethanol solutions [107]. Smitha et al. [119] investigated the effect of ageing solution concentration and ageing time on the porosity characteristics of silica aerogel. Their results indicated that as TEOS concentration in the ageing solution increased, the bulk density and linear shrinkage decreased, whereas the surface area, pore size and pore volume increased. Ageing time also had a similar effect on bulk density, surface area and pore volume.

It was also suggested that ageing occurs at pH between 8 and 12 could better resist the capillary pressure during drying. Thus, the shrinkage of gel at the drying stage could be reduced, and the silica matrix could be strengthened [120].

2.2.2.3. Solvent exchange

Before drying, the solvent exchange and surface treatment process are necessary to minimise the capillary pressure [121]. The capillary pressure is an intrinsic property of the system which is expressed in terms of the change in free energy of the phases and interfaces due to a change in saturation [122]. The capillary pressure is equal to the difference between nonwetting and wetting phase pressures only at equilibrium [122].

As mentioned previously, to obtain aerogel successfully, the liquid should be replaced by air within the gel while maintaining the porous network structure without collapse. However, as soon as the liquid within the pores of gel begins to evaporate, concave menisci are created by the surface tension. As the evaporation of liquid continues, compressive forces build up around the pore's perimeter and try to pull the particles together [123]. The capillary pressure gets stronger due to surface tension at the liquid-vapour interface. As the surface tension is trying to minimise interfacial energy [27], it eventually causes pore collapse. The Laplace Equation applies in this case, as the smaller the capillary radius is, the higher the liquid will rise, or the higher the hydrostatic pressure will be. The liquid in a capillary is caused by the surface energy, and the interfacial pressure within a capillary can be calculated by balancing the static force as [105]:

$$2\pi r\sigma\cos\theta=\pi r^2 h\rho g \qquad \text{(Equation 2-4)}$$

$$h\rho g=P=2\sigma\cos\theta/r \qquad \text{(Equation 2-5)}$$

where P is the capillary pressure, σ is the surface tension of solvent, θ is the contact angle, r is the capillary radius, h is the height of the liquid, ρ is the density of the liquid, and g is the acceleration of gravity.

It can be seen from Equation 2-4 that the small surface tension of pore liquid and large pore radius can decrease the capillary pressure during the drying process. Table 2-1 lists the surface tension of the typical solvent used in aerogel production [121]. It is shown that the surface tension of most solvents is only a third of that in water, which means that the capillary pressure could be reduced by three times if the water is replaced by those solvents completely during drying. Another reason for the solvent exchange process is that hydrophilization agents are insoluble in water and consumed by side reactions with water and alcohol. Alcohols, as the intermediate solvent, promotes the miscibility of water and the organic phase [27].

Table 2-1 Surface tension of several solvents at 20°C (10^{-3} N m^{-1}), reproduced from [121]

Solvent	Isopropanol	n-Hexane	Acetone	Ethanol	Water
Surface tension	21.7	18.4	23.7	22.3	72.8

Rao et al. [124] investigated the effect of solvent types (n-hexane, n-heptane and toluene) on the transparency and physical properties of silica aerogel. The results showed that aerogel possessed the lowest density and best visual transparency using n-hexane or n-heptane as the solvent [124].

2.2.2.4. Surface treatment (silylation)

As mentioned in Equation 2-5, the contact angle between the pore liquid and the pore walls has to be reduced to minimise capillary pressure. This involves chemical modification of the inner surface (e.g., via silylation). As mentioned previously, the water-alcohol mixture in the pores within the gels is first exchanged for a water-free solvent. Then the silylating agent is introduced so that Si-OH groups are silylated [107]. In this process, the surface of the wet gel is chemically modified by replacing the H from the silanol group (Si-OH) with the hydrolytically stable Si-R groups through the oxygen bond, as shown in Figure 2-7. As a result, adsorption of water is prevented, and hydrophobic aerogels are obtained [105, 107]. This process can create surfaces with low energy, significantly reducing surface tension, whereas condensation reactions take place for the original surface silanol groups resulting in an irreversible shrinkage of the gel network during drying. Therefore, it is essential to modify the alcogel surface with an appropriate modifying agent so that the surface of the aerogel becomes hydrophobic [105].

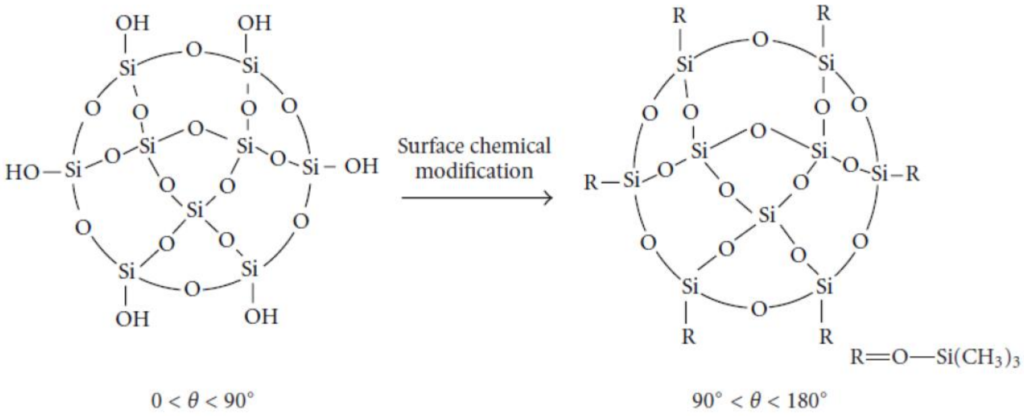

Figure 2-7 Surface chemical modification of the gel, reproduced from [105]

Hydrophobic and hydrophilic are the terms used to describe the apparent repulsion and attraction between water and surfaces [105]. When the surface energy of the material is low, it repels the water from its surface. The material is hydrophobic. Hydrophilicity or hydrophobicity can be distinguished from the value of the contact angle, small or larger than 90, as shown in Figure 2-8 [105]. The contact angle is measured by dropping a water droplet on the material surface, and the angle shown in Figure 2-8 is calculated using specialised software. The hydrophobicity of aerogel can also be confirmed by FTIR analysis. This method is a qualitative analysis that provides direct evidence for the derivatization by alkyl groups through C-H and Si-C vibrational signature [121, 125, 126].

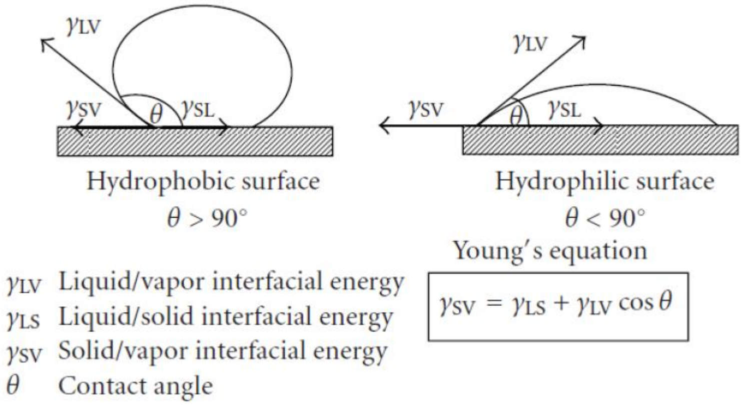

Figure 2-8 Hydrophobic and hydrophilic surfaces, reproduced from [105]

There are several surface treatment reagents that could be used to modify the surface. These include methyltrimethoxysilane (MTMS), hexamethyldisilazane (HMDS), dimethylchlorosilane (DMCS), trimethylchlorosilane (TMCS), trimethylethoxusilane (TMES), and hexamethyldisiloxane (HMDSO) [105]. TMCS and HMDS are probably the most widely used silylation agent, and this is because they yield the lowest density and highest porosity materials and also are easily accessible through commercial retail channels [126]. The chemical reaction in the modification process is shown as [121]:

$$\mathrm{(CH_3)_3SiCl{+}{\equiv}Si\text{-}OH{\rightarrow}{\equiv}Si\text{-}O\text{-}Si(CH_3)_3{+}HCl} \tag{Silylation}$$

Malfait et al. [127] demonstrated that all investigated silylating agents (HMDZ, HMDSO, TMCS) could achieve a sufficiently high degree of silylation. The final selection of the silylating agent would depend on the raw material cost and processing simplicity. The latter is determined by factors such as solvent compatibility and miscibility, corrosion of reaction vessel (e.g., reaction with TMCS produces HCl), and reaction kinetics [127]. Rao et al. [124] claimed that the HMDS does not have proper surface modification properties.

Apart from the type and amount of silylating agent, the silylation duration also plays a significant role in the surface modification process. A study was carried out to investigate the influence of the silylation duration on the bulk density of aerogel with HMDS as the silylating agent, as shown in Figure 2-9 [126]. The result showed that the density of aerogels decreased with treatment time to reach an optimum point after 30 hours. After this point, the density started to increase as the modification process continued. It means that the diffusion of HMDS into the gel’s inner pores and the surface modification reaction was slow. The reaction time for TMCS is expected to be faster than HMDS as TMCS are more reactive [126].

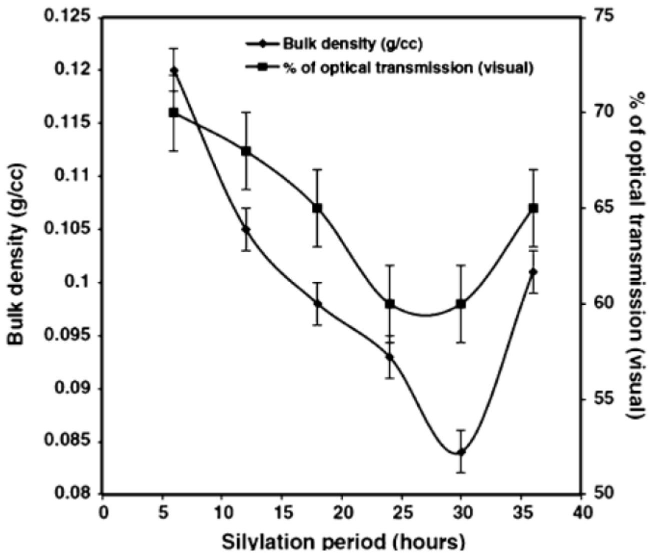

Figure 2-9 Effect of the silylation period on density and optical transmission (%) of the aerogel, reproduced from [126]

2.2.2.5. Drying

The ultimate goal of the drying process relies on solvent removal from the gel matrix by maintaining the porous network without changing the volume and shape [128]. During drying, the shape of the solid porous structure of the gel is mainly affected by two major factors. The first factor is the almost inevitable partial collapse of the network, as even the smallest shrinkage in the interior of the gel body could cause a pressure gradient that results in cracks. The other factor is that the pore dimensions are different throughout the network, which means that different degradation rates of menisci are shown for the neighbouring pores with different radii (faster on bigger pores). Therefore, varying levels of stress are applied to the walls between pores of different dimensions. As a result, a crack could occur due to unbalanced forces [129, 130]. Unmodified sol-gels under ambient conditions shrink to about 1/8 of their initial volume due to the pore collapsing, and such materials are called xerogels (dry gels) [125]. Xerogel monoliths can be produced if the drying process occurs slowly. However, to synthesise an aerogel, one must avoid crossing the vapour-liquid phase boundary [125]. At present, three general drying techniques are used to fabricate aerogel, namely supercritical drying, freeze-drying and ambient pressure drying. All the techniques are designed to minimise or even eliminate the capillary forces due to the surface tension effect to avoid pore collapsing [125].

2.2.2.5.1. Supercritical drying (SCD)

Supercritical drying is an ideal method to produce monolithic silica aerogels of rather large dimensions (the product size depends on the mould). This technique suppresses the liquid-gas interface; therefore, the solvent inside the pores is removed under a supercritical condition (a point where both liquid and vapour state can coexist) in order to eliminate the capillary pressure [22, 125].

Supercritical drying can be performed in two different procedures. The first is high-temperature supercritical drying (HTSCD), which Kistler first applied in 1931 and is still widely used for silica aerogel production [22, 104, 107]. For this method, the wet gel, together with a sufficient amount of solvent, is placed in an autoclave, and the temperature slowly rises. When the temperature and pressure in the autoclave are raised above a critical point, the solvent is transformed into a 'supercritical' fluid in which every molecule can move freely, and surface tension is mostly removed. For example, the critical temperature and pressure for methanol are 243℃ and 7.9 MPa, respectively [105], meaning that the liquid and its vapour at this point can coexist. Therefore, menisci cannot form without surface tension. The critical temperature and pressure are kept constant for a certain period (i.e., 2 hours [131]), and then the vapours are slowly released from the autoclave at a constant temperature until the atmospheric pressure is reached inside the autoclave. Finally, the vessel is cooled to room temperature. Thus, the phase boundary between liquid and gas is not crossed during the drying process. Additionally, the autoclave is flushed with dry nitrogen (~3 bar) to ensure the trapped solvent molecules is completely removed from the dried gel [105, 107]. Figure 2-10 (a) shows the pressure-temperature cycles followed during the supercritical drying of the aerogels [107]. Kirkbir et al. [118] demonstrated that the shrinkage of aerogel under the supercritical condition did not exceed 5% for several solvents used such as ethanol, butanol, pentanol and isooctane. The shrinkage was even negligible for wet gels dried in 2-pentanol at 1.8 MPa and 300℃ [118].

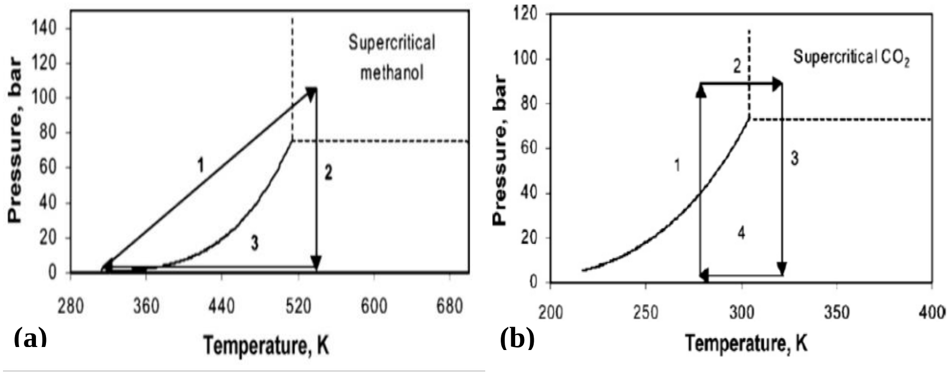

Figure 2-10 Schematic procedure of (a) high-temperature and (b) low-temperature supercritical drying, reproduced from [107]

Tewari [132] suggested an alternative method for supercritical drying in 1985, known as low-temperature supercritical drying (LTSCD). The solvent present in the gel before drying is replaced by a liquid having a crucial point closer to ambient temperature [107]. Liquid CO_2 was the most practical choice as CO_2 features a mild critical point (31.1℃ and 73.9 bar [22]), which allowed SCD to be conducted at a low temperature. Figure 2-10 (b) illustrates the LTSCD process schematically [107].

Several comparative studies regarding high-temperature and low-temperature supercritical drying techniques were conducted. Ehrburger-Dolle et al. [133] showed that the microporosity of CO_2 dried aerogel was significantly larger than that of corresponding MeOH dried aerogel. However, both techniques presented an equivalent texture in micro and mesoporous scales [133]. Dieudonne et al. [134] demonstrated that methanol dried aerogel showed a smooth surface, where tough solid particles are observed after CO_2 drying. Nevertheless, the light transmission of CO_2 dried aerogel was comparable with that of alcohol dried samples [132].

2.2.2.5.2. Freeze drying

Freeze drying is another drying method in which phase boundaries between the liquid and the gas phase does not exist. Thus, the capillary pressure can be minimised [105, 107]. This technique removes excess solvent through sublimation [125]. The wet gel is ‘frozen’, and then the solvent is allowed to sublimate at a lower pressure [107, 125]. Kalinin et al. [135] demonstrated that the ice microcrystals produced during the freeze-drying process lead to more microporous aerogels than those during supercritical drying. Unfortunately, there are many disadvantages that limit the usage of the technique. The ageing duration must be extended to stabilize the gel network, and in some cases, the network may be destroyed by the crystallisation of the solvent in the pores [105, 107].

2.2.2.5.3. Ambient pressure drying (APD)

Ambient pressure drying seems to be the most straightforward method to remove the solvent from a porous material. This method raises the temperature above the solvent's boiling point, and thus the solvent is evaporated into gas [22, 128]. Besides, traditional supercritical drying is considerably more expensive and dangerous due to the high pressure and complex equipment involved [105, 107]. Therefore, there is a great potential to lower the costs and hazard levels for aerogel production and thus represent an essential consideration for the future development of these materials for large scale commercial applications using ambient pressure drying [107].

The drawbacks, however, cannot be ignored. APD requires chemical processing with lengthy solvent exchange to either reduce the capillary forces acting on the nanostructure or increase the nanostructure's ability to withstand those forces [125]. There are three stages in which the solvent coexists within the system: the liquid filling the pores, the liquid-gas transition phase, and the gas phase. High capillary pressure (hundreds of bars within nanopores) is presented due to the receding menisci in the pores, and therefore cracks occur in the structure [128]. As a result, granular or powder aerogels are generally formed rather than monolithic shape since the capillary pressure surpass the elastic limit of the solid structure during drying [136, 137]. The term 'xerogel' is typically used to describe the materials produced by ambient pressure drying, and the volume of the xerogel is 5 to 10 times smaller than the dimensions of the gel [128].

The drying temperature in APD is also critical in determining the physical properties of aerogel. Drying at a high temperature leads to a 'spring back' effect of silylated gels [126]. It is a reversible shrinkage process as the concentration of hydrophobic moieties such as the methyl group directly attached to the silicon atom increases. This effect involves a mechanical expansion of the gel network, which recovers almost to its original volume. This phenomenon occurs during the last stage of the drying when the porous structure can endure the drying loads, and the spring back effect occurs by the repelling of hydrophobic functional groups [22, 137, 138].

As mentioned in sections 2.2.2.3 and 2.2.2.4, solvent exchange and surface modification process are critical before the ambient pressure drying process to prevent irreversible densification or partial collapse due to stresses generated by capillary pressures [22]. There are a few more strategies to minimise shrinkage during ambient pressure drying. A co-precursors method is developed where a non-hydrolysable methyl group is mixed with a hydrophobic solvent such as MTMS could prevent the collapse of gels during drying and imparts higher flexibility to the matrices [139, 140]. Besides, drying control chemical additives such as glycerol, formamide, or dimethylformamide could be introduced during the initial phase of silica gel synthesis. These additives promote the uniformity of pore size dimensions, thus minimizing stress asymmetries [128]. Finally, an effective method to strengthen silica aerogel's structure is by embedding fibre and nanofibers as the framework. This allows preserving the monolithic shape, although the fractures (both at the micro and macro levels) during the drying process cannot be avoided [22, 136].

2.2.3. Current research status

The conventional aerogel materials mainly include inorganic oxide aerogel such as SiO_2 aerogel [107], organic aerogel (RF aerogel [141]) formed by the polymerization of phenols and formaldehyde, carbon aerogel [142] (carbonized from RF aerogel), and metal oxide aerogel [143]. In particular, inorganic aerogels have been studied extensively [103]. In recent years, with the broader development of nanomaterials, other types of aerogel with new structure and performance such as graphene aerogels [144], carbon nanotube aerogels [145], and cellulose materials [146] have also been developed, which have enriched the aerogel materials.

Traditionally, silica aerogels are prepared by a more energy-intensive and expensive SCD method using alkoxide precursors such as TEOS and TMOS. However, such a combination restricts the commercialization of aerogel due to the cost and the complex process involved during SCD. Alternatively, there is a great potential for commercialization by the ambient pressure drying (APD) method employing sodium silicate (Na_2SiO_3) as the sole inorganic precursor [126].

Sodium silicate, also known as waterglass, is an inorganic compound that readily dissolves in water. The pore nature of the molecule ($Si\text{-}O^-$ and Na^+ ion pairs) could also prevent the spontaneous formation of larger silica polycondensates or gelation due to electrostatic effects [126]. Waterglass is synthesised commercially by reacting quartz sand with sodium hydroxide and sodium carbonate at elevated temperature and pressure. Waterglass is perhaps the least expensive industrial silica source due to the vast abundance and inexpensive nature of these reactants. Besides, unlike TEOS or TMOS, waterglass is easy to handle and poses no flammability hazard. It is also chemically stable in the long term under standard conditions of use and storage. However, an extra step is generally involved before gelation to remove trapped sodium ions, reducing the optical transmission and leading to low material properties.

This can be achieved by ion exchange or merely washing with water. Nevertheless, waterglass may still be the ideal precursor for cost-effective silica aerogels [126].

Sodium silicate-based silica aerogels are fabricated by a typical sol-gel process, followed by solvent exchange, surface modification and ambient pressure drying [27]. There are various factors that could influence the properties of aerogels. These include sodium silicate concentration, sol pH, type of solvent and sialylation agent used, periods of ageing, solvent exchange and silylation, and drying temperature. The effect of ageing, solvent exchange, silylation and drying on the aerogel properties are already discussed in section 2.2.2.

2.2.3.1. Effect of precursor type and concentration

Rao et al. [124] discovered the effect of precursor (TEOS, TMOS and waterglass) on the physical properties and transparency of aerogels. The results showed that waterglass-based silica aerogel possesses the highest shear modulus, permeability, and lowest density (0.15 g/cm^3) among those three precursors. The density was comparable to the aerogel prepared using supercritical drying [124]. The high shear modulus could minimise fracture during drying. The high permeability was beneficial to remove water and reaction products from the gel during the washing process prior to and after surface treatment. Thus the capillary pressure will be reduced during the drying process. In addition, waterglass-based aerogel provided the largest pore size, pore volume and porosity, as well as the highest degree of monolithic. TEO based aerogel gave the finest pore size, largest surface area; however, the density was relatively larger, accompanied by the relatively lower pore volume and porosity [124].

The concentration of sodium silicate plays a significant role in the final properties of aerogels since it determines the amount of silica per added sol volume and thus the ‘packing density’ of silica units in the gel network [126, 147]. He et al. [26, 121] discussed the effect of deionized water ($DI{\cdot}H_2O$) to Na_2SiO_3 volume ratio on the porosity and density of aerogel. The results indicated that as the volume ratio increased from 1 to 5, the porosity and specific surface area increased to an optimum point at a volume ratio of 3-4 and then decreased. The density showed an opposite trend as expected. However, the optimum point varied depending on the silica content within the sodium silicate solution [26, 121]. Furthermore, the increase in silicate concentration could also increase the gelation time. This is because as the dilution (H_2O to Na_2SiO_3) increases, the mean separation between compensating silica species becomes larger and larger, causing a less frequent effective collision. Therefore, the random three-dimensional gel structure takes a long time to form [147].

2.2.3.2. Effect of pH and gelation time

The sol-gel process involves adding acid or base catalysts to control the kinetics of condensation and network formation. The formation of gels occurs fastest at pH values greater than 6 [126].

Rao et al. [148] studied the influence of pH of the sol on the optical transmission, gelation time, porosity and density of the aerogel. The results indicated that the gelation time and optical transmission decreased as the pH of the sol increased, and the decrease was significant at higher pH (>4). The gelation time varied significantly from 32 mins to 1.2 mins as the pH of the sol increased from 3 to 8. The density decreased initially and then flattened out when the pH value reached 6, where the porosity showed an opposite trend. When the pH was less than 4, colloidal silica particles carried a positive surface charge, which caused the coulombic interparticle repulsion. Besides, the strong competing effect of H^+ shifted the equilibrium of the condensation reaction toward the side of free silanol groups. Furthermore, it became a better nucleophile due to the absence of $Si\text{-}O^-$. Therefore, the gelation time increased, and the probability of the silica particles fusing together was smaller, resulting in smaller particles that have a higher packing fraction in the gel. When the pH was greater than 6, the gelation time was extremely fast, meaning that there was not enough time for the gel to condensate into a perfect, well-distributed network structure. As a result, it was more likely to form larger pores, although the porosity was high, and the aerogel became opaque since those larger pores acted as scattering centres for light in the visible range of the spectrum [148].

The gelation time can also be controlled by introducing N,N-dimethylformamide (DMF) as a drying control chemical additive (DCCA). He et al. [26] investigated the effect of DMF on the gelation time, the density and volume shrinkage of aerogel. The results showed that an increase in Si to DMF molar ratio resulted in an increase in gelation time, where the density and volume shrinkage decreased first and then increased. This was because the polarity of DMF was relatively strong, and the hydrogen bonds would form between hydroxyls (O-H) in orthosiliconic acid and DMF molecules which would impede the polycondensation of $Si(OH)_4$. Thus, the condensation rate slowed down, and the gelation process was longer. The formed hydrogel would have a relatively uniform pore and particle size. However, the hydrogen bond would be destroyed by high energy (i.e., high temperature). When the amount of DMF was in excess, a considerable number of free hydroxyls that were not condensed during the condensation process started to condense and destroy the existing gel microstructure. As a result, the difference in pore size increased, which would increase the capillary pressure, and thus the shrinkage and density of aerogel increased [26].

2.2.3.3. Improving the fabrication process

The manufacturing of aerogel is expensive. For example, the retail price for aerogels and related products in the UK in 2018 are summarised in Table 2-2. It is also time-consuming, and it can take up to several days to fabricate aerogels. The drying step at ambient pressure requires a more or less fixed amount of time and offers less potential for speeding up the synthesis [126]. Therefore, the main focus is to optimise the ageing, solvent exchange and surface treatment process. As mentioned in section 2.2.2.3, the processing time can be reduced significantly by agitating the hydrogel mechanically before the solvent exchange due to the larger surface area. Therefore, the solvent exchange period can be shortened. Apart from this technique, some other methods could improve the fabrication process.

Table 2-2 The retail price for aerogel and related products in the UK in 2018, reproduced from [149]

Aerogel product name	**Units**	**Cost (£)**
Aerogel granules (KWARK)	1 litre	£25
Spaceloft blanket 5 mm	1 m^2	£ 30.41
Spaceloft blanket 10 mm	1 m^2	£ 39.86
Spaceloft panel 10 mm	1 m^2	£46.03

The solvent exchange and hydrophobization process can be combined to shorten the overall production period. This is achieved by immersing the hydrogel into a mixture of an alcohol/alkane (hexane or heptane)/TMCS solution [150, 151]. In some instances, the ageing is done in a water-alcohol or acetone mixture to speed up the subsequent solvent exchange and hydrophobization combination process [152, 153]. However, such a technique consumes a considerable amount of expensive hydrophobization agents such as HMDS or TMCS, making it unrealistic for large-scale industrial production. Therefore, the traditional consecutive ageing, solvent exchange and hydrophobization steps are still the main route for synthesising aerogels at an industrial scale [126].

Co-precursor methods are proved to be a faster and efficient technique to obtain silica aerogels. In this method, the organosilanes are added together with a silica precursor (waterglass) during gelation [125]. The most widely studied co-precursor materials are MTMS [154-156], methyltriethoxysilane (MTES) [157], HMDS [158] and TMES [159]. Bhagat et al. [158] fabricated the superhydrophobic silica aerogel powders using the waterglass/HMDS co-precursor method in less than 5 hours. Apart from the advantage of a faster surface modification, the co-precursor method could also improve internal hydrophobicity. Štandeker et al. [159] investigated the influence of MTMS and TMES on the hydrophobicity of silica aerogel, and the contact angle could reach as high as 180° for TMOS/TMES co-precursor method by varying the molar ratios. However, most co-precursors are prohibitively expensive, and the amount of co-precursor could significantly influence the density, transparency, and hydrophobicity. This may limit the usage of this method for large-scale industrial production [125].

More recently, Cheng et al. [156] developed a novel process to synthesise monolithic MTMS based silica aerogel using water as the only solvent under ambient pressure drying within five hours. Such a method avoids the lengthy solvent exchange and surface modification processes and reduces the production cost. During the aqueous phase, an efficient surfactant named cetyltrimethylammonium bromide (CTAB) was introduced to prevent the phase separation caused by the immiscibility between hydrophobic oligomers and water. The influence of CTAB on the properties of aerogel was discussed. The results indicated that without CTAB, the MTMS did not form a uniform gel network in polar solvent due to the high phase separation tendency. As the amount of CTAB increased, the extent of phase separation decreased, resulting in a relatively faster condensation rate, lower volume shrinkage, and lower density. However, as the content of CTAB continued to increase, the gelation process took longer with higher volume shrinkage. This may be because the excess CTAB interfered with the network formation, which resulted in lower crosslinking among the particles. As a result, the density of aerogel increased with lower BET surface area [156].

Shao et al. [157] introduced a rapid fabrication process to prepare MTES based flexible silica aerogel monoliths via ambient pressure drying. In this method, solvent exchange and surface treatment were eliminated, whereas the ageing process still occurred for 24 hours to obtain larger monolith samples. As a result, the total production time was less than two days. The prepared aerogel showed excellent formability, flexibility and compressibility (shown in Figure 2-11) while maintaining a moderate thermal conductivity (0.038 W/m.K) [157].

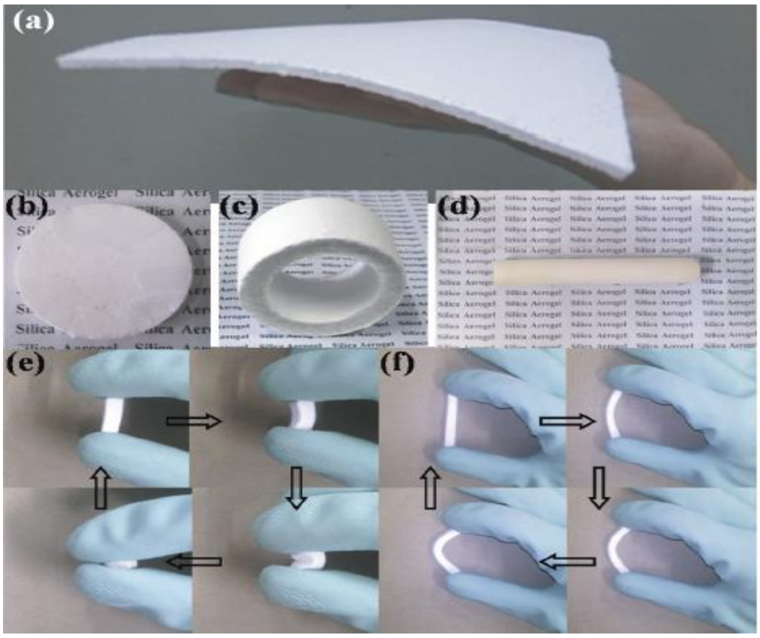

Figure 2-11 Photos of silica aerogel monoliths of (a) sheet, (b) cylinder, (c) tube and (d) rod showing (e) compressibility and (f) flexibility, reproduced from [157]

2.2.4. Physical properties and application of silica aerogel

The unique porous structure makes aerogel attractive in science and technology. Such a unique system provides a high porosity, low density, extremely low thermal conductivity, low acoustic propagation speed, very low dielectric constant, very high specific surface area and other excellent properties. Therefore, aerogel has a boarder application prospect in thermal science, optics, acoustics, microelectronics, catalysis, aerospace, energy-saving and building insulation [22, 103, 105].

2.2.4.1. Thermal and optical properties

One of the key aerogel characteristics is its low thermal conductivity (e.g. the 0.015 W/m.K for SiO_2 aerogel at the ambient condition) [27]. This is lower than the conductivity of air under the same condition (e.g., 0.025 W/m.K) [27]. Besides, silica aerogel is non-flammable, which appears to be an ideal substitute for traditional insulating materials, such as polystyrene or polyurethane foams [103]. Therefore, aerogel is an excellent heat insulation material that can be widely used in the insulation field, such as equipment insulation, pipe insulation and building external wall insulation [22, 103]. However, the fragile nature of silica aerogels limits their use without mechanically reinforced such as fibre reinforced blankets or panels [103]. Nevertheless, silica aerogel can be made optically translucent, which has great potential for opaque or translucent insulating components [27].

It is estimated that windows might be responsible for up to 60% of the building's total heat loss [160]. Thus, the application of aerogel in the glazing system will greatly improve the heat loss (could reach 50% [160]) of the window than triple glazed window while still allowing for high light transmittance [160]. Aerogel-based glazing systems may be considered as substitutes for triple-glazing or suspended film glazing systems when clear transparency is not required. The triple-glazed windows are more massive and require more extensive and robust frames to support, while the visible transmittance is generally below 0.70 [160].

Lv et al. [161] prepared eight pieces of aerogel glazed units with homemade aerogel, as shown in Figure 2-12. The aerogel granules were sieved into four different particle size groups (0.41 mm, 0.64 mm, 0.93 mm, 2.7 mm) and filled into units with a thickness of 7.5 mm and 10 mm. The effect of aerogel particle size and filling thickness on aerogel glazing units' thermal and optical properties was investigated. The results showed that the heat transfer coefficient increased as the particle size of aerogel increased. Furthermore, the direct solar transmittance increased as the particle size of aerogel increased from 0.41m to 0.93mm, while the change was limited as the particle size continued to grow. Finally, the visible light transmittance and heat transfer coefficient decreased as the filling thickness of the aerogel increased [161].

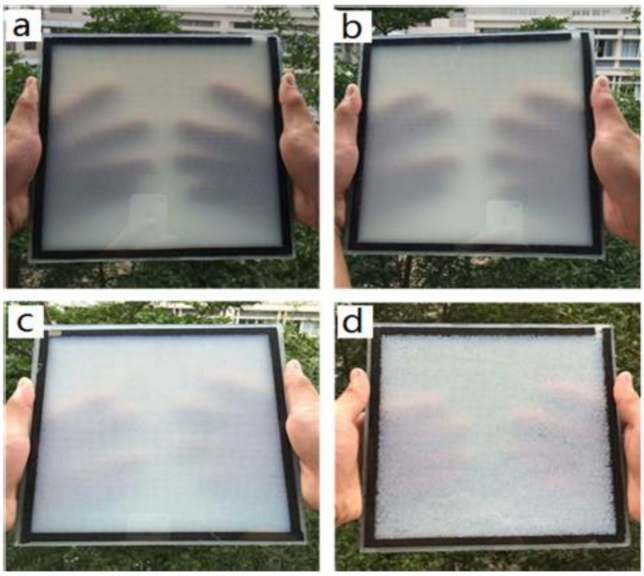

Figure 2-12 Photos of aerogel glazing units with different particle sizes (a) 0.41mm (b) 0.64mm (c) 0.93mm and (d) 2.7mm, reproduced from [161]

Apart from the glazing system, aerogel granules can be mixed with plasters to improve the thermal insulation performance of the building assemblies [160]. The rendering has the benefit of having a simple implementation regarding the uneven surface and thus creating a continuous thermal insulation layer by filling the gaps and joints [162, 163]. The aerogel enhanced plasters are water repellent due to the hydrophobic nature of aerogel, which avoids the water absorption that could change the volumetric composition and the final thermal insulation performance [164]. Berardi [160] investigated the effect of the mixing ratio of aerogel granules to hydraulic lime-based plaster on thermal conductivity. The results showed that the thermal conductivity could be reduced significantly to 0.0257 W/m.K when the volume percentage of aerogel was 95%. Over 80% reduction in thermal conductivity was achieved. However, the effect of the mixing ratio on the mechanical properties was not mentioned.

2.2.4.2. Mechanical properties

The tensile strength and elastic modulus of silica aerogels are largely dependent on the network connectivity and density [27]. It is difficult to determine these mechanical properties in terms of specimen preparation or precisely measuring the small forces applied [165]. Therefore, compression and flexural modes are usually performed to evaluate aerogel's mechanical performance [128, 166]. The compressive behaviour of aerogels shows that at a higher density, it tends to shatter after very little strain, exhibiting brittle behaviour; at smaller density, in the range of 80 to 150 kg/m^3, silica aerogels can sustain compression up to 70% strain and return back to the original volume [128]. A silica aerogel with a density of 100 kg/m^3 can withstand a maximum load of 0.02 MPa under a three-point bending flexural test [166].

As previously mentioned, in order to strengthen the silica aerogel, the ageing and hybridization process is critical [27]. Nevertheless, neat monolithic aerogel is not often used due to its fragile nature. Besides, the mechanical properties are sensitive to the gel's synthesis chemistry, the environment, and storage history [167]. For instance, the compressive strength and elastic moduli increase while the strain at fracture decrease with age [27].

2.2.4.3. Acoustic properties

The acoustic properties of silica aerogels are closely related to their thermal insulation properties [27]. The acoustic propagation depends on the interstitial gas nature, aerogel density and texture [168]. In the gel network propagation, the acoustic wave is attenuated both in amplitude and velocity due to the wave energy being progressively transferred from the gas to the aerogel's solid network, which makes aerogel suitable for acoustic insulation devices [27]. Furthermore, aerogel has a wide range of acoustic impedance (103 ~ 107 $kg/m^2.s$), which is an ideal coupling material for ultrasonic detectors [103]. Finally, aerogel can be used as underwater acoustic reflection material due to its extremely high porosity and ultra-light density. For instance, the acoustic reflection effect can be improved by introducing the aerogel on a submarine hull without increasing the overall weight [103].

2.2.4.4. Other properties and applications

Apart from the abovementioned properties and applications, aerogel has also drawn significant attention as adsorption media for removing several environmental and human health-threatening pollutants [169]. This includes CO_2 capture, volatile organic compounds removal, in water treatment including oil and toxic organic compounds and heavy metal ions removal [169].

2.2.5. Conclusion

Silica aerogel and its fabrication process have been investigated extensively [27]. The general fabrication process involves sol-gel, ageing, solvent exchange, surface treatment, and drying [27]. However, some detailed descriptions of the fabrication process are not commonly mentioned, for example, the amount of solvent used for ageing and solvent exchange. It has a nonnegligible impact in terms of cost-saving, especially in the UK. The cost for one litre of Ethanol and n-Hexane is approximately £50 and £40, respectively [28, 29]. Therefore, adequate usage of these solvents could lower the manufacturing cost. In addition, the fabrication processes, including ageing temperature and drying process, could be optimised to improve the properties of the aerogel.

2.3. Research on aerogel composites and applications

The mechanical performance of aerogel should not be ignored. However, it is rarely reported in the previous section, as it is difficult to examine this property. This is due to the fragile nature of aerogel. Fibre reinforcement could be an efficient way to enhance the material structure. In the meanwhile, the thermal insulation performance may also be improved.

In this section, an overview of aerogel composites is presented, including the techniques for preparing the composites. The influence of fibre types, fibre geometry (i.e., length, diameter and orientation) on mechanical and thermal performance is explored. Finally, the potential application and the knowledge gaps of aerogel composites are discussed.

2.3.1. Introduction of silica aerogel composites

The research on optimising aerogels' physical properties, such as pore structure and density, has shown extensive progress. However, the improvement of the strength, fragility and shrinkage rate of the aerogels are unsatisfactory, especially under ambient pressure drying [30]. This fragility could be due to the low densities and the disordered network morphology with irregular pore structure. To strengthen the aerogels, thus improving mechanical properties, researchers have mainly focused on reinforcing the silica network through Ostwald coarsening or particle ripening and growth, further condensing the silica network with molecular precursors and involvement of secondary reinforcement materials [30].

Ostwald coarsening phenomenon is generally seen in alloys, colloids, and ceramics, where the particles grow at the expense of smaller ones to reinforce the material [30, 170]. Silica gels go through Ostwald coarsening, and gels can be strengthened through extended ageing [171]. However, such a technique is time-consuming, and the prepared aerogels usually exhibit low surface area and large pore size [30].

The silica gel network can be further condensed using reactive silanes to improve aerogels' strength [30]. It is achieved by soaking the alcogel or aerogel in the solution phase silanes such as TMOS, TEOS or sodium silicate [172-174]. This allows the residual uncondensed silanols in the alcogel to further condense to form additional siloxane bonds strengthening the polymeric network. However, it is not easy to control the deposition rate, thus the physical properties such as density, porosity, and surface area [30].

The involvement of a secondary reinforcement seems to be an efficient way to strengthen the aerogel structure and thus widen its application [31]. The common reinforcement techniques involve incorporating polymer, embedment of fibres and granular reinforcement [30, 31]. These reinforcement materials are introduced into the alcogel before the gelation, and they behave as a reinforcing scaffold for the aerogel structure, creating a robust physical framework that supports the fragile aerogel network [30]. However, the involvement of the reinforcement materials increases the density of composites significantly. Meanwhile, the surface area and pore volume are decreased since the void space is replaced by the aerogel [30]. Nevertheless, the massive improvement of mechanical properties compensates for these disadvantages, and these techniques, especially for the composites embedded with fibres, has already been commercialized.

2.3.2. Fibre reinforcement

Fabrication of aerogel composites with embedded fibre is probably the most widely adopted technique in academic research and industrial manufacturing. The involvement of fibre is an effective way to prevent shrinkage during the drying process, especially the ambient drying method. Thus, monolithic aerogel composites can be produced, and the mechanical properties can be improved significantly. However, the challenge is to preserve the insulation properties, minimise the increase of apparent density, and improve the dustiness due to the weak interfacial bonding between the aerogel particle and fibres [22].

The ultimate properties of fibre reinforced aerogel composites could depend on the techniques to mix the fibres with wet gel, type of fibres chosen (organic, inorganic or nanofibre), parameters of fibres (fibre content, fibre length and diameter) and the associated drying process.

2.3.2.1. Techniques for preparing fibre-filled aerogels

There are a number of ways to reinforce silica aerogels with fibres [22]. The predominant ones are illustrated in Figure 2-13. Fibres can be dispersed in the silica sol prior to the gelation, as shown in Figure 2-13 (a). The mixture is then poured into a mould for gelation. The amount of fibres depends on the uniformity of dispersion, as aggregates or bundles could be formed due to an excess of fibres that might weaken the structure and decrease the composites' insulation performance. This procedure is usually used to fabricate strengthened and denser materials [22]. Aerogel composites can also be obtained by pouring the sol over a fibre mat previously placed within a mould, as shown in Figure 2-13 (b). A basic catalyst is usually added before pouring the sol to induce the gelation in the mould. This process is typically used to fabricate flexible aerogel composites such as aerogel blankets [22].

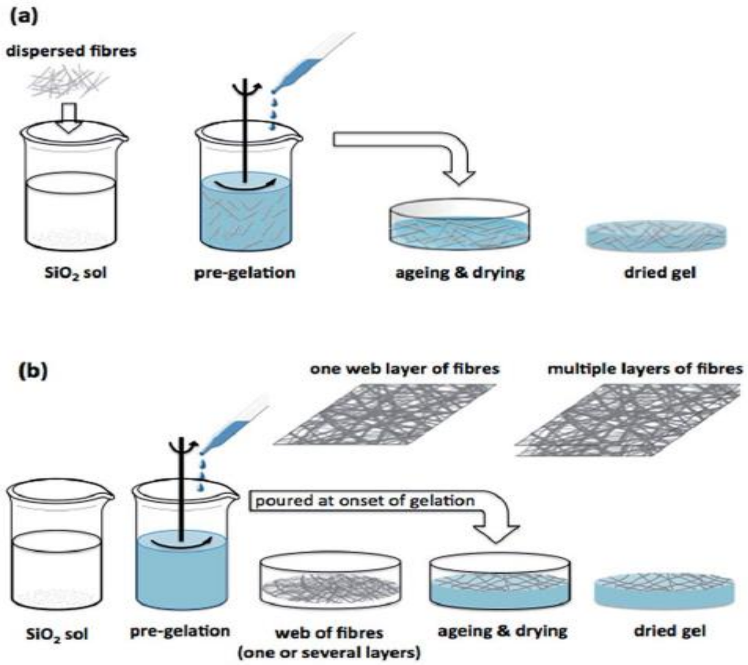

Figure 2-13 Schematic procedures of silica aerogel composite synthesis (a) the addition of dispersed fibres to the silica sol (b) silica sol poured into a mould where fibre sheet was pre-located, reproduced from [22]

There are other similar processes to synthesise silica aerogels. This includes pouring all silica sol into the mould and then immersing the fibre layer by layer and pouring the sol into a mould, and soaking a fibre mat before gelation [22]. Besides, to obtain silica aerogel composite films with extreme flexibility, the ideal technique involves the addition of electrospun nanofibres since there is an improved integration between aerogel and nanofibres [175, 176]. This is implemented by impregnating a web previously formed or electrospinning the fibres in situ [176], which fully integrates the sol under accurate control of gelation time [176, 177].

2.3.2.2. Type of fibres as reinforcement materials

It is crucial to select the correct type of fibres, mainly depending on the primary requirement of properties and the application. Fibres can be categorised into inorganic fibres and organic fibres, depending on their chemical composition, as summarised in Figure 2-14. For example, if the fibre reinforced aerogel composites are designed for use in a high-temperature environment, the chosen fibres must be thermally resistant (i.e., inorganic fibres). They should also have an extensive spectral complex refractive index throughout the infrared region [178]. Flexible fibres (i.e., organic fibre) or at least with an appropriate fraction should be considered if the flexibility of the composites is needed [22, 179].

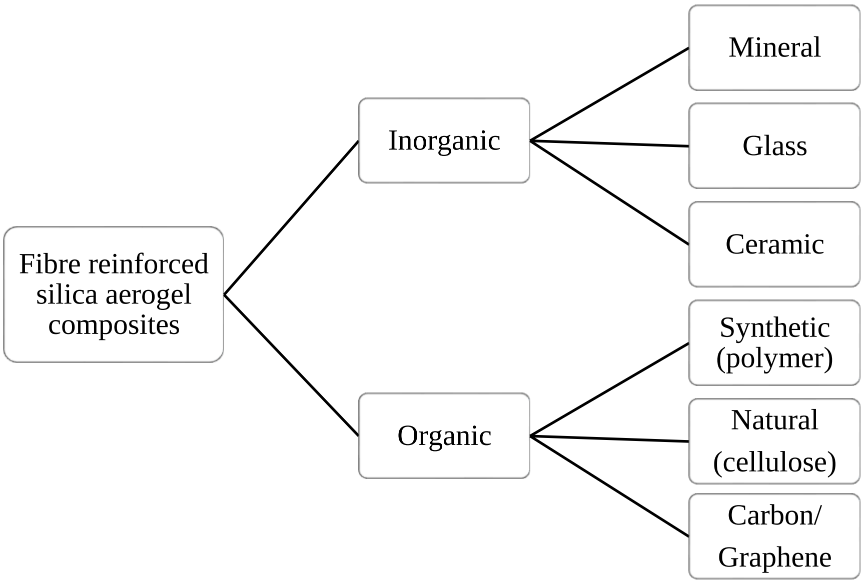

Figure 2-14 Fibre classification and typical examples

2.3.2.2.1. Organic fibre reinforcement

Organic fibres are mainly used to achieve higher flexibility and lighter weight while reducing shrinkage during drying [22]. In general, organic fibre with a high length-to-diameter ratio provides better flexibility than natural inorganic fibres, which is advantageous for manufacturing flexible aerogel composites [180]. Organic fibres can be categorized into natural and synthetic, where the former can be referred to as cellulose fibre, and the latter is known as polymer fibre.

Polymer fibres such as polypropylene, polyethene terephthalate (PET) and polyester fibres are commonly used to fabricate aerogel composites. The first organic fibre embedded in silica aerogels was a nonwoven structured polypropylene [22, 181]. The obtained silica aerogel composites exhibited a better absorption property than conventional absorbing materials, which could be used to remove hazardous chemicals from air and sewage disposal [181]. Oh et al. [182] prepared ultra-porous and flexible PET/Aerogel blankets via ambient pressure drying. The obtained sample exhibited excellent sound absorption and thermal insulating properties. Martinez et al. [183] investigated the insulation performance of polyester fibre reinforced silica aerogel composites. The obtained aerogel composites provided excellent insulation properties, where the thermal conductivity was in the range of 0.015 to 0.018 W/m.K [183].

Natural fibres are seen as a potential substitute for petroleum-based polymers due to their biocompatibility, biodegradability, and sustainability. In addition, they also reduce the carbon footprint of industrial products [22, 183]. Although natural fibre is not frequently used as silica aerogel reinforced material, it still shows a great potential to produce low-cost composites when combined with ambient pressure drying techniques [22]. For instance, silica aerogel reinforced with cotton nonwoven mat could be used as a sound absorber [184]. Aerogel reinforced with recycled cellulose fibres showed a promising potential for thermal and acoustic insulation applications [185].

2.3.2.2.2. Inorganic fibre reinforcement

Inorganic fibres such as glass, mineral and ceramics fibres are commonly considered for reinforcing aerogels, especially in thermal barrier systems due to the surpassing thermal stability, along with a low thermal expansion coefficient [22]. As inorganic fibres are thermally resistant, they are less prone to deteriorate in high-temperature environments than organic fibres [186, 187]. For very high-temperature insulation (i.e., greater than 1400℃), ceramic fibres, such as Al_2O_3, Fe_2O_3 based, or alumina-silica types, are the most suitable fibres to embed in aerogel composites as they are generally not sensitive to thermal attack [188]. For a moderate temperature range (i.e., less than 1100℃), glass fibres show a great interest in both academic and industrial fields [22]. Therefore, a border operating temperature can be achieved when aerogels are reinforced with inorganic fibres [22, 166].

As mentioned in section 2.3.2.1, fibres can be introduced into the composites mainly by dispersing the fibres into the silica sol or immersing a pre-shaped fibre mat into the sol. However, in most cases, it is not easy to get a uniform distribution of inorganic fibres in the composites since the introduced fibres usually lead to precipitating themselves to the bottom of silica sol. This may be due to the inorganic fibres typically having higher density and larger fibre diameter [189]. Therefore, it is more common to involve a pre-shaped fibre mat as the structural framework to prevent aerogel densification during ageing and ambient pressure drying. At the same time, better insulation and mechanical performance can also be achieved [22].

Among all the inorganic fibres, glass fibres are the most commonly used fibres as the aerogel reinforcement in both academic and industrial fields [190-194]. Huang et al. [190] developed a novel fabrication process to synthesise glass fibre reinforced silica aerogel composites, where the entire preparation period can be as short as 20 hours. In this work, ethanol was used as the primary solvent in the waterglass-based silica sol through ion concentration modification to eliminate the conventional solvent exchange process. The obtained aerogel composites showed an excellent flexural modulus of elasticity of 12 MPa and thermal conductivity of 0.026 W/m.K [190].

Lyu et al. [195] conducted the compression test of ceramic fibre reinforced silica aerogel composites at room temperature and elevated temperature (300℃, 600℃ and 900℃) to investigate aerogel composites' mechanical behaviour at a high-temperature environment. The results indicated that the compressive strength and modulus both increased with increasing exposure temperature, but the deformation recovery capability decreased. This may attribute to the microstructure change caused by thermal sintering. Viscous flow and matter transport caused by high temperature resulted in the fusion of aerogel particles, which led to a thicker and stronger particle skeleton; thus, the stiffness and the strength of the composites was improved. However, the formation and fracture of larger pores caused cracks, which degraded the deformation recovery capability [195].

2.3.2.2.3. Electrospinning nanofiber reinforcement

The diameter of conventional organic and inorganic fibres is usually in dozens of or several microns, which is significantly higher than the typical diameter of pores or silica secondary particles of the silica aerogels [180]. The significant difference in the sizes of the reinforced fibres and the aerogel matrix leads to a large contrast of the fibres and aerogels' strains during the drying process. This could cause larger cracks and weaker mechanical stability of the fibre reinforced aerogel composites [196]. It is essential to reduce the fibres' diameters and thus decrease the difference in sizes of the fibres and aerogel matrix. Therefore, it improves monolith integrity and the composites' mechanical stability [180].

Electrospinning is a simple and low-cost method for producing polymer and ceramic fibres with superfine diameters. This technique has been newly adopted in aerogel reinforcement [180]. The diameter of fibres produced by electrospinning is as thin as 150 nanometers [197], which is significantly smaller than the typical natural cotton fibre with an average value of 10 micrometres [198]. In the conventional nano-fibre producing process, the polymer is dissolved in a solvent to achieve the required viscosity to yield continuous nano-fibres. It is then jetted through a capillary spinneret under the influence of an electrostatic field, and finally, deposit in the form of a web in collector support or directly into the sol cast [176, 180].

Wu et al. [180] prepared flexible silica aerogel composites reinforced with electrospun polyvinylidene fluoride (PVDF) web via electrospinning and sol-gel processing. The pre-prepared PVDF webs were added into the silica sol as a framework and the fibre reinforced silica aerogel were obtained under ambient pressure. The results showed that the electrospun PVDF nanofibre could significantly improve mechanical strength (almost six-fold compared to pure aerogel) and flexibility of the silica aerogel. Meanwhile, a lower thermal conductivity

(0.028 W/m.K) could be maintained, which showed great potential for thermal insulation applications [180].

Although the obtained nano-fibres increase the adhesion between the aerogel and fibres, thus improving the mechanical stability and strength [22], a higher degree of contact could increase solid thermal conductivity, which may limit the use in the superinsulation field [180]. Therefore, continuous development is needed to improve the thermal insulation performance and scale up the manufacturing process in the various application fields.

2.3.2.2.4. Recycled fibre reinforcement

Glass fibre-reinforced polymer composites have been developed extensively due to their high specific mechanical properties, and they are increasingly used in the construction, automotive, aerospace, and energy sectors [199, 200]. However, the major issue is how to deal with material waste at the end of service life. Fibre recycling appears to be a promising option [199]. Besides, PET plastics bottles have become a significant problem to the environment nowadays as they can lead to contamination of a wide range of natural terrestrial, freshwater and marine habitats [20]. Therefore, there is an ever-increasing need to recycle PET plastic bottles and to discover new innovative ways to reuse them [20]. One of the recycling methods for PET plastic bottles is to convert them to PET fibres [20]. However, using recycled or waste fibres to strengthen silica aerogel composites is only being studied at the laboratory scale [22].

Salomo et al. [20] successfully developed recycled PET fibre reinforced silica aerogels through direct gelation of silica on PET. The PET fibres were recycled from plastic bottle waste and pre-treated with dichloromethane to dissolve partially. The obtained composites showed super-hydrophobicity with an average contact angle of 149.9°, whereas the thermal conductivity was approximately 0.037 W/m.K. Nevertheless, this work provides an alternative solution for reusing plastic wastes [20].

The use of recycled cellulose fibres as reinforcement materials also showed great potential for thermal and sound insulation [136, 201]. Feng et al. [201] successfully fabricated recycled cellulose fibre reinforced silica aerogel via freeze-drying. The resulted composites possessed excellent sound absorption properties compared to cellulose aerogels and commercial polystyrene foams [201]. Markevicius et al. [136] used recycled paper fibres as the reinforcement material to synthesise silica aerogel composites. The fibre agglomerates were first expanded to create a self-supporting three-dimensional non-woven fibre network before the gelation process. The more cost-effective ambient drying process was adopted in this work, and the obtained aerogel composites exhibited an extremely low thermal conductivity (0.016-0.023 W/m.K) [136].

It is more desirable to use inorganic fibres as reinforcement materials for thermal insulation applications, especially for the high-temperature environment due to their excellent thermal stability. Even though the use of recycled inorganic fibres such as glass is scarcely reported, and the use of recycled organic fibres is only seen at the laboratory scale. These works still pave the way towards more sustainable and cost-effective materials [22, 157, 202].

2.3.2.3. Effect of fibre on aerogel composites

During the aerogel fabrication process, gel shrinkage is the critical factor determining the bulk density and porosity [22], which consequently influences the final mechanical and thermal properties. The incorporation of fibres as the skeleton frame could minimise or prevent shrinkage during the ageing and drying process since casting volume is split into sub-volumes between two adjacent fibres [22]. Thus, the internal movement of silica chains is inhibited, while the drying stresses are limited to small units instead of one unit comprising the full body of aerogel [22]. It was reported that the linear shrinkage of the neat silica aerogels produced via supercritical drying is about 5-10%, while the shrinkage can be reduced to a negligible level if fibres are integrated [22]. The shrinkage in silica aerogel composites mainly occurs through the thickness direction, while monolithic non-reinforced aerogels shrink isotropically [120, 203].

As mentioned earlier, the ultimate properties of fibre reinforced aerogel composites could depend on various factors. The influence of fibre parameters such as fibre content, fibre length and diameter on the properties of aerogel composites have been investigated [22].

2.3.2.3.1. Effect of fibre content on aerogel composites

The effect of fibre content on properties of aerogel composites is usually investigated via the fibre dispersion method, as indicated in Figure 2-13 (a) above, where the fibres are dispersed in the silica sol before the gelation.

Li et al. [204] synthesised attapulgite fibre reinforced silica aerogel composites, and the influence of fibre content on the mechanical and thermal performance was studied. The results showed that the bulk density of the aerogel composites first decreased and then increased with increasing fibre content, while the porosity presented an opposite trend. It is worth mentioning that the trend observed for thermal conductivity was similar to that of the bulk density, where a small fraction (2%) of fibres decreased the thermal conductivity (from 0.0218 to 0.0198

W/m.K) relatively to that of the neat aerogel. The thermal conductivity then increased from 0.0198 to 0.0228 W/m.K as the fibre content increased. The slight decrease in thermal conductivity can be attributed to the rise in voids (higher porosity). However, as the fibre amount continued to increase from 5% to 20%, the thermal conductivity increased almost linearly since the fibres act as additional heat transfer passageways through the fibre structure. Hence, the total thermal conductivity of the composites was increased.

Dissimilar results were also reported. Jiang et al. [205] synthesised the ambient dried silica aerogel nanocomposites reinforced by micro-glass fibre mat (2-4 diameter), with controlled volume content of 4.5, 6.8 and 9.1%. The fibre mat was immersed in the silica sol under vacuum. The results showed that the thermal conductivity decreased from 0.0265 to 0.022 mW/m.k at a temperature of 650°C, and the bending strength increased from 1.2 to 1.45 MPa with increasing fibre volume. According to the authors, the thermal conductivity trend could be attributed to the smaller diameter of fibres. The specific surface area was higher, which resulted in lower radiative conductivity [205].

In summary, the embedment of fibres, as a structural frame, in the aerogel composites could maintain the samples' integrity due to the minimum shrinkage during the ageing and drying process. The shrinkage of silica aerogel composites generally decreases with increasing fibre content [22], and the shrinkage could be reduced further if the supercritical drying method is adopted instead of ambient pressure drying. Moreover, the composites' mechanical performance could be significantly enhanced when the fibres are introduced, and strength is generally increased with the addition of fibres content [206-208]. However, excess fibres could have a negative effect on the mechanical properties of the composites as excess fibres could lead to clusters. This causes fibres to slip off the bonding interface and crush the aerogel matrix; thus, the compressive strength could be reduced seriously [208]. Finally, the fraction of fibres reinforcing silica aerogel composites dictates their thermal conductivity [22], and it can also be influenced by the type and the size of the fibre [136, 205]. The thermal conductivity of the composites is more likely to be increased with the increase of fibre content [136, 194, 206, 208], although a small mass addition of the fibres could lower the thermal conductivity at the beginning due to the increase of total voids [204, 209].

2.3.2.3.2. Effect of fibre size and orientation on aerogel composites

The intrinsic features of fibres such as length, diameter, length-to-diameter ratio, curvature, and orientation angle also play a role in determining the ultimate performance of silica aerogel composites [22].

Jaxel et al. [206] investigated the influence of fibre length on the thermal and mechanical performance of silica aerogel composites. Short human-made cellulose fibres with a length of 2, 6, 8 and 12 mm were used as the reinforcement materials. It was stated that no noticeable influence of fibre length in cumulated shrinkage and bulk density was observed within the experimental errors. However, the thermal conductivity of samples with 6 and 8 mm fibre length (0.016 - 0.017 W/m.K) performed slightly better than that of samples with 2 and 12 mm fibre length (0.017 – 0.018 W/m.K). The authors suggested that short length fibres might not be sufficient to hold the silica phase together during the ambient drying process, resulting in a large shrinkage. Thus, more voids were obtained between the silica phases. These voids did not participate in the Knudsen effect and thus increased thermal conductivity. On the other hand, longer length fibres might increase mutual contact, which increases the solid conduction. Nevertheless, higher fibre lengths led to a significant improvement in mechanical properties. The maximum stress increased from 18.9 to 98.2 kPa as the fibre length increased from 2 to 12 mm [206].

Fibre diameter is the other major factor influencing the final properties of the aerogel composites, and there is an optimum diameter depending on the type of fibres. Zhao et al. [210] developed an analytical model to estimate the total thermal conductivity of glass fibre reinforced silica aerogel composites. The term ‘fibre extinction coefficient’ was used in the model to determine the composite’s thermal insulation ability at a higher temperature. The radiative thermal conductivity increased with increasing temperature, while it could be reduced by a larger extinction coefficient [210]. According to the results, the glass fibres with a diameter of 4, 6, and 8 µm exhibited a much higher fibre extinction coefficient at a higher temperature (>1000 K) compared to the fibre with a diameter of 1 and 10 µm. This means that the radiative thermal conductivity would be reduced when the glass fibres with a diameter of 4, 6, and 8 µm were used as the reinforcement materials. Thus, these composites displayed the best insulation performance at a higher temperature (i.e., 0.08 W/m/K at 1300 K). However, the fibre diameter was not critical at a lower operating temperature (<600 K) [210].

Apart from fibre length and diameter, fibre orientation also plays a vital role in aerogel composites’ thermal insulation performance. The fibre orientation is defined as the angle between the incident heat and the plane normal to the longitudinal axis of the fibre [211, 212]. Zhao et al. [210] investigated the influence of the incident angle of glass fibre on the thermal conductivity of silica aerogel composites using an analytical model. In this model, the total thermal conductivity was the sum of the conductive and radiative thermal conductivity. The results demonstrated that as the incident angle varied from 0° (where fibres are perpendicular relative to the heat direction) to 40°, the total thermal conductivity (heat source is perpendicular to the aerogel composite) increased from 20 to 55 mW/m.K at 250 K, as shown in Figure 2-15. As the operating temperature increased, the total thermal conductivity of aerogel composites rose from 80 to 195 mW/m.K at 1250 K, with an increasing incident angle [210]. The increase in the inclination angle resulted in an increase in the fibre extinction coefficient. As a result, the radiative thermal conductivity was decreased. However, the conductive thermal conductivity of the composite increased faster with increasing inclination angle than the decrease in radiative thermal conductivity. Thus, the total thermal conductivity of the composites increased with increasing inclination angle due to the importance of the increased conductive thermal conductivity [210].

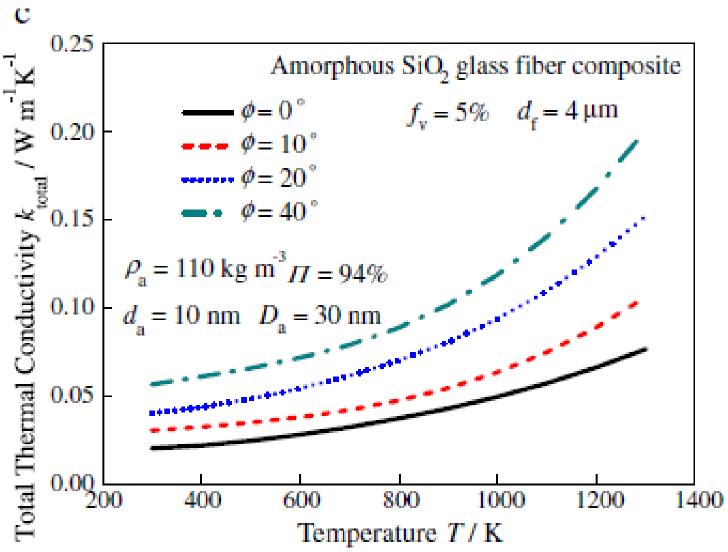

Figure 2-15 Effect of fibre orientation on the total thermal conductivity of glass fibre reinforced silica aerogel composites, reproduced from [210]

In summary, it can be concluded that the thermal and mechanical behaviours of the fibre-reinforced silica aerogel composites can be influenced significantly by the intrinsic features of fibres, such as length, diameter, and orientation angle. Therefore, the composites can be designed according to the intended applications, either to achieve optimal insulation properties or mechanical performance [22].

2.3.2.4. Modelling aerogel composites

It is often time-consuming and costly to design and fabricate fibre reinforced silica aerogel composites by varying the fibre parameter such as fibre diameter, length, and orientation through physical tests. Accurate analytical models could facilitate system thermal and mechanical analysis and guide the design of new materials for the intended applications [210].

Zhao et al. [210] developed an analytical model to estimate the total thermal conductivity of fibre reinforced silica aerogel composites. A cubic array of spherical porous secondary nanoparticles and a modified parallel-series model were proposed to model the combined solid and gaseous thermal conductivities. An anomalous diffraction theory was used to predict the fibre extinction coefficient, which is a crucial radiative property that determines the composite's thermal insulation ability at a high temperature. This model provided theoretic guidelines for material designs with optimum parameters such as fibre type, fibre incident angle, volume fraction and diameter of the fibres, as well as the aerogel nanoparticle and pore sizes. The predicted thermal conductivity agreed well with the experimental data. A similar approach was conducted by Tang [213].

Soorbaghi et al. [214] modified the classic unit cell model for nanocomposite aerogel by considering the effect of phonon scattering, secondary porosity (a type of porosity pertained to the closed-cell pores which were not measurable using BET), and clay mineral presence since the classic unit cell model could show more than 250% deviation from the experimental results. As a result, the addition of clay minerals to silica aerogel led to a 55% reduction in thermal radiation heat transfer. The modified model showed an excellent agreement with the experimental results with less than 10% deviation [214].

Webley et al. [215] discovered a simulation of fibrous thermal simulation where the thermal conductivity of glass fibre blanket can be predicted. The fibre geometry was generated using MATLAB, with the finite element analysis being carried out using ANSYS Workbench, as indicated in Figure 2-16 (a). The simulation results showed an excellent agreement with the experimental data [215].

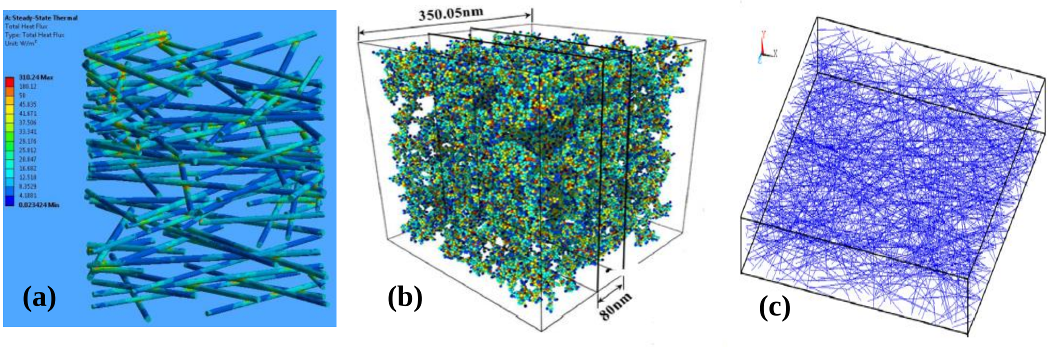

Figure 2-16 (a) the heat flux distribution in the fibrous phase, reproduced from [215], (b) the generated cluster of silica aerogel matrix and (c) fibre distribution in the representative volume element, reproduced from [216]

Lu et al. [216] proposed a new multi-scale model to investigate the relationship between the mechanical properties and microstructure of fibre reinforced silica aerogel composites, as shown in Figure 2-16 (b) and (c). A continuum damage constitutive model was established to represent the behaviour of the silica aerogel matrix in the composite by implementing the aerogel model with the discrete element method. A modified embedded element technique was then proposed to generate the finite element model of the silica aerogel composite with curve fibres. The numerical results showed that Young's modulus and the tensile strength of the composites were significantly affected by the primary particle size. Besides, the influence of fibre parameters such as volume fraction, length, and curvature on composites' mechanical properties was also predicted [216].

The use of analytical models becomes an efficient way to study the relationship between the composites design parameters (i.e., fibre length, diameter, orientation, and aerogel particle size) and mechanical/thermal performance. It provides a guide to designing appropriate materials for intended applications.

2.3.3. Aerogel composite properties and application

Fibre-reinforced aerogel composites preserve the unique properties of aerogel, such as high porosity, low density, remarkable thermal conductivity, and very high specific surface area, while the mechanical properties are improved. Therefore, aerogel composites show great potential in thermal insulation, acoustic insulation, adsorption of harmful compounds and many other applications [5, 22, 217].

2.3.3.1. Thermal properties

Linhares et al. [22] summarised a few reported thermal insulation performances of aerogel composites reinforced with different fibre types (e.g., aramid fibres, pectin nanofibers, glass fibres, and attapulgite fibres). The composites' thermal conductivity obtained via ambient pressure drying was in the range of 0.016 to 0.026 W/m.K. A better insulation performance was achieved via supercritical drying (0.014 to 0.02 W/m.K).

Aspen Aerogels, a US-based commercial aerogel developer, carried out two case studies to improve the energy efficiency of old public housing [218, 219]. The first case was to apply the Spaceloft® Insu-Cap™ on the wood frames of a nearly 300-year-old house to eliminate the thermal bridging through the frame members in the walls, as shown in Figure 2-17 (a) [218]. The Insu-Cap™ is made of a 10 mm thick strip of flexible aerogel with peel-and-stick backing for easy installation. Such modification improved the R-value of the walls by 15%. Besides, the Insul-Cap™ also reduced the noise level, which produced both more energy-efficient and quieter houses [218, 220]. The other case was to place two layers of 10 mm Spaceloft™ 9521 aerogel insulation to a building facing board, and these were then screwed directly into the internal skin of the building, as shown in Figure 2-17 (b) [219]. The installation process was 50% faster than installing conventional insulation materials, as no framing was needed. As a result, the apartment wall's U-value was reduced by 44% (from 0.63 to 0.35 W/m^{2}K), which equated to a reduction of 900 kWh/yr energy use and 400 kg/yr in carbon emission.

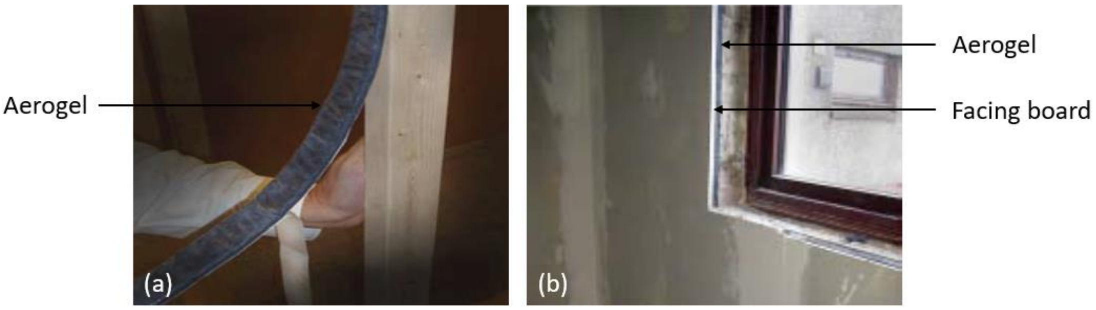

Figure 2-17 (a) Spaceloft® Insu-Cap™ flexible aerogel with peel-and-stick backing on the wood frames, (b) Spaceloft™ 9521 aerogel insulation to a building facing board, reproduced from [218, 219]

Apart from the superinsulation characteristic, silica aerogel composites reinforced with inorganic fibres can also inhibit extreme temperature heat transfer [22]. The upper limit of service temperature could be as high as 1200℃ (when reinforced with mullite fibre) [221]. Therefore, these materials can protect building steel frames during fires, which prevent structure collapse [193]. It can also be applied in the aerospace industry, where high-temperature resistance is required.

2.3.3.2. Acoustic properties

Noise pollution has become the most widespread and least controlled environmental issue [222]. It causes psychological disorders, cardiovascular disease, loss of hearing, and high blood pressure [222]. The conventional bulky nonwoven fabrics or foams may not always satisfy the technical criteria for a practical engineering solution due to either thick panels or heavy structures [222-224]. Thus, a more effective solution is needed to prevent human's health issues.

Noise mitigation is dependent on the material's thickness, interrelated with the wavelength [225]. In general, the thickness of each discrete insulation layer must be as least half of the sound wavelength to attenuate the sound wave [222]. Sound wavelength increases with a decreasing frequency, which means a low-frequency range (100-2000 Hz) requires a thicker insulation barrier [22, 225]. This could be detrimental in confined spaces [22]. The porous nature of silica aerogel inhibits heat transfer and provides an effective acoustic insulation feature [22, 27, 226]. Since aerogel's inherent fragility poses difficulties for most applications [227], fibre reinforced aerogel composites could be an ideal material for the insulation of low frequencies due to their efficiency at reduced thickness [184].

The acoustic insulation performance of aerogel could be influenced by several factors, including the bulk density, interstitial gas pressure and overall texture [22, 228]. Martin et al. [229] showed that the surface roughness and larger pores were beneficial for improving the acoustic insulation property. This was achieved by varying the concentration of water-soluble organic polymers (polyethene glycol) in the sol. The results indicated that aerogels with higher pore dimensions were produced as the concentration of polyethene glycol in the sol increased. This led to a significant reduction in acoustic velocity (from 241 to 103 m/s). However, the addition of polyethene glycol resulted in a monotonic decrease of the yield stress and Young's modulus [229].

It has been shown that the acoustic performance can be improved by combining the fibres with silica aerogels with reduced thickness compared to neat fibre blankets or polystyrene foam. It widens the applicability of aerogel composites when the space for insulation is limited [22, 230, 231].

2.3.3.3. Adsorption properties

Due to its unique three-dimensional nanoporous structure with high permeability, high specific surface area, high pore volume and porosity, aerogel has an outstanding adsorption characteristic. Therefore, it has a great potential in wastewater treatment, such as adsorbents of toluene, adsorbents of heavy metal ions, and clean-up oil spills [103, 232]. In particular, silica aerogels can be used as absorbent materials to effectively absorb oil from water, which is a promising candidate for saving the endangered environment, especially in marine oil pollution [232]. What is more, the incorporation of fibres in aerogels is another approach for such applications as the mechanical properties of the materials are improved, allowing the repeatability of adsorption and desorption processes [232]. The manufacturing cost is also lowered as ambient pressure drying could be adopted to obtain monolithic aerogel composites. Wei et al. [233] prepared silica-fibre composite aerogels via a facile one-step polymer-incorporation sol-gel process, followed by ambient pressure drying. It was concluded that the adsorption capacity for organic pollutants (benzene, toluene) was around 6 to 8 times its mass [233].

Fibre-reinforced aerogel composites present a remarkable potential in absorbing organic pollutants and oil spillage [22, 232]. The maximum absorptive ability could reach eight times the composite’s weight, and the sorption and desorption process could be repeated more than one hundred times [232]. Nevertheless, further research is still needed to improve absorption performance while lowering the manufacturing cost.

2.3.3.4. Other properties and applications

Aerogel exhibits a high energy absorption capability when cross-linking with polymers. Therefore, it opens the way to potential applications under high impact, such as in automobile collision and ballistic protection, where energy absorption at high impact speed is essential [166].

Wu et al. [234] studied the ballistic characteristics of glass fibre reinforced aerogel composites. The aerogel composite core was produced by cross-linking aerogel colloid and glass fibre via sol-gel and supercritical drying method. It was then sandwiched by two hard skins (aluminium plate, steel plate and polymethyl Methacrylate plate). The ballistic tests were conducted at both low speed (about 350 m/s) and high speed (about 750 m/s) with a 7.62 mm ballistic gun. The results showed that the anti-penetration capability of composites was improved under high-velocity impact due to the strain rate strengthening effect compared to that of low-velocity impact. The higher the strain rate is, the better the energy absorption capability will be. Despite the fact that the deformation area of the aerogel composite core was extensive, and the destructions were severe, it still shows an effective energy absorption of bullets [234].

The low refractive index of silica aerogels promotes the development of sensing devices [22]. Boday et al. [235] prepared polyaniline nanofibre reinforced silica aerogel composite with a substantial electrical conductivity. The composites could be used to prepare chemiresistor sensors to detect acidic (HCl) and basic (Ammonia) gaseous molecules in the environment. The introduction of aqueous HCl in aerogel composites resulted in a rapid colour change of the composites from dark purple to green, which is indicative of polyaniline’s highly conductive, protonated emeraldine base. In addition, as the quantities of polyaniline fibre increased, the electrical conductivity increased almost linearly, with the highest value of 1.83×10^{-5} S/cm. This value is slightly greater than the conductivity of a polyvinyl alcohol aerogel loaded with carbon nanotubes [235].

Aerogel composites could also be used in insulation clothing for protection from thermal and electric hazards, to protect workers exposed to molten substances or from flames at reduced thickness [22, 236]. Conventional insulation clothing requires higher thickness to achieve better thermal insulation performance, which could restrain the user’s movement [237]. Chakraborty et al. [236] investigated the radiant heat resistance of the aerogel blanket based fabric. The aerogel blanket was sandwiched by an outer layer of woven fabric and an inner layer of modacrylic/cotton fabric. It was found that an increase of 58% in the estimated burn injury time was achieved with the presence of an aerogel blanket, which ensured much better protection from heat and fire hazards. In addition, the effectiveness of the aerogel blanket as protective shielding was improved with the increasing amount of silylating agent (TMCS). Thus, the aerogel blankets showed great potential in the area of firefighting systems [236].

Other applications of fibre reinforced silica aerogel composites are mentioned in the literature as drug delivery [238], space [239], separation technologies (membranes) [169], catalyst and carrier materials for catalysis and electrocatalysis [240].

2.3.4. Conclusion

The fabrication of aerogel composites with embedded fibre is probably the most widely adopted technique in academic research and industrial manufacturing. This is because the involvement of fibre is an effective way to prevent shrinkage during the drying process, especially the ambient drying method. Thus, monolithic aerogel composites can be produced, and the mechanical properties can be improved significantly. However, the challenge is to preserve the insulation properties, minimise the increase of apparent density, and improve the dustiness due to the weak interfacial bonding between the aerogel particle and fibres [22].

‘Vacuumization’ could be adopted to improve the insulation performance and the service life of aerogel composites. The vacuum insulation board with aerogel composites as the core material can effectively minimise the heat transfer via air convection, which significantly reduce its thermal conductivity [241]. It was suggested that the evacuation and sealing of silica aerogels could reduce the thermal conductivity by 50% [237]. More importantly, sealing of aerogel composites can prevent dust release during handling and processing.

2.4. Research on glass fibre recycling and applications

A comprehensive review of geopolymer and aerogel composites have been explored in previous sections. The mechanical performance of the geopolymer could be further improved. The fibre reinforced aerogel composite could be more economical and environmentally friendly. Besides, an increasing amount of waste glass has been produced nowadays due to the widespread use of glass in different applications [32]. The glass products are non-biodegradable; thus, recycling and reusing glass are attractive, which could significantly contribute to the prevention of environmental pollution [32].

In this section, an introduction of recycled glass fibre (rGF) is presented, with the recycling technology described. The dissolving mechanism of glass in the alkaline environment is addressed, and the influencing parameters on the dissolution rate are explored. In addition, the reusing of glass waste in synthesizing geopolymer is reviewed, and the fabrication process of the glass fibre mat is discussed. Finally, the research gaps of rGF in geopolymer and aerogel composites are addressed.

2.4.1. Introduction of glass fibre recycling

Today, an increasing amount of waste glass has been produced due to the widespread use of glass in different applications [32]. The glass products are non-biodegradable; thus, recycling and reusing glass are attractive, which could significantly contribute to the prevention of environmental pollution [32]. Glass fibres, as one of the primary forms of glass, are extensively produced to be used in various applications. In particular, they are widely used as reinforcement materials to improve the mechanical properties of composites.

Fibre-reinforced polymer composites are increasingly used in the construction and energy sector due to their high specific mechanical properties [199]. The European Union aims to increase the renewable energy share to 27% by 2030 and reduce greenhouse gas emissions by 80-95% as of 2050. Wind power, as one of the leading renewable energy sources, will play an essential role in the future [199]. Glass fibre-reinforced polymer (GFRP) composites, as the primary constitution of wind turbine blades, will be consumed significantly. According to a market report by the German associations AVK and CCeV [242], The GFRP production volumes in Europe steadily grew by 2.5% in 2015, reaching 1.1 million tonnes. This correlates to 25% of the world's total production volumes. In particular, 34% of Europe's production (0.37 million tonnes) is associated with the construction sector, in which wind turbines are included. It was stated that the use of GFRP composites for wind turbine blades was around 50,000 tonnes in 2000 [243]. This figure increased to 150,000 – 186,000 tonnes in Europe in 2016, where a threefold increase was reached compared to the 2000 figures [243]. It is estimated that the use of GFRP composites for wind turbine blades will increase to more than 300,000 tonnes in 2030 [243]. As a result, a significant number of fibre wastes will be produced.

The standard service life of a wind turbine is approximately 20 to 25 years, and the wastes from the blades contribute to a large fraction of composite waste [243]. Table 2-3 summarises the GFRP composites waste from a life cycle perspective [243]. It is shown that the estimated waste during manufacturing contributes to the most considerable portion of the total blade weight (10-18%). This includes in-process waste such as dry fibre cut-off and cured composites cut-offs from blade edge, blade testing and defective blades. Therefore, a sustainable process for dealing with wind turbines wastes needs to be identified to ensure the maximum environmental benefits of wind power [243].

Table 2-3 Composite waste from a life cycle perspective, reproduced from [243]

Life cycle phase	Manufacture	Operation	Upgrade/Retrofit	End-of-life
Contributing causes to blade waste	-In-process waste -Blade testing -Defective blades	-Routine service -Accidental damage	Exchange of blades (due to failure or upgrade to larger rotor diameter)	Decommissioning of turbines
Estimated amount	~ 10-18% of total blade weight	~3% of total blade weight	~5% of total blade weight	~5% of total blade weight

There are usually three ways to treat GFRP waste within the wind turbine sector: landfill, incineration and recycling [243]. The landfill is not a preferred solution due to environmental regulation. The most common way is incineration. The drawback is that up to 60% of solid residuals are left behind as ash after incineration, which will either be landfilled or used in building materials. However, the use of waste as filler material might be affected by local legislation [243]. Recycling is generally achieved in three methods: mechanical, pyrolysis or chemical recycling. Mechanical recycling is mainly implemented by wire saw, jaw cutter, and crushers. The recycled GFRP composites can be reused for bridges, playgrounds, urban furniture and filler materials [243].

Research is more focused on recycling, particularly in pyrolysis and chemical treatment [243]. Pyrolysis is a thermal decomposition process where the polymer binder is incinerated under deoxidised and temperature-controlled conditions, resulting in the extraction of the fibre [243]. The recovered pyrolysis oil can potentially be used to sustain the reaction without an external energy source. However, the drawback is the degradation of mechanical properties of recovered fibre [199]. Solvolysis is a chemical process where reactive solvents are used to decompose the polymer matrix, and the full length of fibres could be recovered with minimum degradation of mechanical properties (up to 12% loss) at elevated temperature and pressure. However, an excessive amount of energy and chemicals are required, which increase the recovery cost [199]. More recently, Pender and Yang [244] from the Advanced Composites Group of the University of Strathclyde developed an in-house thermal recycling process to recycle the glass fibre from waste turbine blades. The GFRP wastes before and after the recycling process are shown in Figure 2-18.

Figure 2-18 (a) GFRP cubes before the recycling process, and (b) Recycled glass fibre after the recycling process

Despite the fact that the recycling technology of waste wind turbines has been explored extensively [199, 243-245], it will still require collaboration between the material suppliers, wind industry and end-of-life sector to mark the wind turbines as not only renewable in terms of the energy generation, but also in terms of material use [243].

2.4.2. Dissolution of rGF

Glass fibre recycling via the abovementioned technology usually suffers from a severe loss in its ultimate strength and cannot be reused in the same form of composite applications [246]. Several approaches have been developed to restore the strength of the recycled glass fibre to be reused as reinforcement again [246]. It was found that the strength of the recycled glass fibre increased after immersion in dilute hydrofluoric acid. Hydrofluoric acid is an effective chemical etchant to strengthen glass by removing surface flaws [247]. However, the toxicity of hydrofluoric acid limits its use on a commercial scale. Instead, alkaline solution, such as NaOH and KOH, is proven to be more effective in improving the strength of thermally degraded glass fibres in a similar manner to hydrofluoric acid [248]. The alkaline solution leads to modifying the damaged fibre surface and improving tensile strength [246].

The strength regeneration mechanism of thermally damaged glass fibres through alkaline treatments is based on the kinetics of the reaction between the glass and the alkaline solution [246]. The chemical reactions involved in glass corrosion have been known for a long time [249]. There are two main types of interactions between silicate glasses and aqueous solutions: leaching of alkalis and network (congruent) dissolution [250]. Leaching or ion exchange of alkali cations from glass occurs through the diffusion of H^+ or H_3O^+ from the solution into the glass to replace alkalis (e.g., Na^+), as shown in Equation 2-6 [250]:

$$\equiv Si\text{-}O\text{-}Na_{(s)} + H^+_{(aq)} \xrightarrow{leaching} \equiv Si\text{-}OH_{(s)} + Na^+_{(aq)} \qquad \text{(Equation 2-6)}$$

This reaction occurs in acid and neutral solutions, leaving the silica structure more or less intact [249]. It also increases the pH of the solution [250]. It is worth mentioning that as alkalis diffuse out of the glass surface, a Si-rich altered layer, known as the gel-layer, forms which could condense and act as a barrier against further diffusion of ions into and out of glass [250].

Network dissolution (or hydrolysis) occurs at high pH, where the polar siloxane (Si-O) bonds are broken through a nucleophilic attack of hydroxyl ions (OH-), according to Equation 2-7 [250]. The surface of silicate glass exposed to water is almost always hydrolyzed, and the Si-OH group are abundant [250]. When the glass is in contact with an alkaline solution, the hydroxyl ions attack the SiO_2 framework according to Equation 2-7 [246]. In addition, Al_2O_3

(the third-largest E-glass component) can also react with OH- from NaOH solution in a similar manner to SiO_2 [24].

$$\equiv Si\text{-}O\text{-}Si\equiv + OH^{-}H^{+} \xrightarrow{hydrolysis} \equiv Si\text{-}OH + HO\text{-}Si\equiv \qquad \text{(Equation 2-7)}$$

Due to the basic nature, CaO (the second-largest component in E-glass) and MgO may not react directly with NaOH, but instead, they are soluble in the alkaline environment, resulting in further disruption of the glass network structure [246]. The breakdown of the silicate network is thought to be an essential process of glass dissolution. The dispersion of network modifiers such as CaO into solution can also contribute to glass dissolution [246].

Similar to the leaching process, when the glass reacts with the alkaline solution, a product layer may form around the glass surface, meaning the hydroxide ions need to subsequently diffuse through this layer before reacting with the glass [246]. This product layer is likely to comprise sodium silicates, according to Equation 2-8. The product layer thickness can increase with time, meaning the hydroxide ions takes longer to diffuse through and consequently, the rate of glass dissolution will decrease [246].

$$SiO_2 + 2NaOH = Na_2SiO_3 + H_2O \qquad \text{(Equation 2-8)}$$

Several factors can significantly influence the glass dissolution rate, including solution temperature, solution concentration, glass particle size, and stirring time [246, 249, 251]. It has been shown that an increase in temperature induces an increase in dissolution rate [246, 249]. In the dissolution reaction, reactants collide not only with each other, but the collision needs to possess enough energy to overcome the activation barrier of the reaction [246]. As the solution temperature rises, the hydroxide anions gain more kinetic energy, resulting in more collisions with enough energy in the reaction [246]. Torres-Carrasco et al. [251] compared the dissolution rate of glass in the alkaline environment at room temperature (22℃) and elevated temperature (80℃). The percentage of SiO_2 solubilised could reach 60% after six hours of treatment at 80℃, while only 1% of SiO_2 was solubilised at 22℃ [251].

Solution concentration is another crucial factor affecting the glass dissolution rate. Sairah et al. [246] presented that the dissolution rate increased with solution concentration. This may be due to more hydroxyl ions being able to collide with the glass surface with enough energy for the reaction to occur [246]. This behaviour was also reported in other studies [249]. Kouassi et al. [249] and Torres-Carrasco et al. [251] investigated the influence of glass particle size on the dissolution rate. The reduction of particle size increased the dissolution rate. These results relate to a rise in surface reactivity linked to a specific surface area of glass [249].

The dissolution rate of glass is significantly influenced by the reaction temperature, solution concentration, glass composition and glass particle [250, 251]. In general, an increase in solution temperature and concentration leads to an increase in dissolution rate, and a smaller particle size favours the dissolution rate. In fact, the solubility of silica becomes significant at a pH value higher than 10 [250]. However, the dissolved silica remains in the solution and can reach high concentrations up to the solubility limit of alkali silicates [250].

2.4.3. Geopolymer with glass waste

The potential waste materials such as glass are promoted to be recycled and re-used as primary or secondary raw materials in geopolymer fabrication to lower their negative environmental impacts and preserve natural resources [33]. There are mainly two ways of introducing waste glass in the geopolymer system. One is to use as partial mineral precursors to replace the conventional aluminosilicate materials such as fly ash or metakaolin. The other is to use the glass waste as a source of silica to partially replace commercial waterglass in the alkaline activation of the geopolymer.

2.4.3.1. Waste glass as partial mineral precursors

Waste glass, as a partial mineral precursor, has been investigated extensively in the fly ash-based geopolymer system [32-34]. Tho-In et al. [34] studied the mechanical performance of geopolymer containing waste glass powder and high-calcium fly ash. The fly ash was replaced by waste glass powder at the levels of 10%, 20%, 30% and 40% by weight to produce the geopolymer pastes. The compressive strength tended to decrease as the replacement level of glass increased. The author suggested that the replacement with glass changed the silicon/aluminium ratio because of its high silicon content. High silicon/aluminium ratios induce the formation of low-crosslinked aluminosilicate materials with decreased strength [34]. In contrast, Zhang et al. [33] introduced waste glass in the fly ash/furnace slag system by replacing partial fly ash with the waste glass. The result showed that there was no apparent difference in 1-day strength as the amount of glass increased. However, the compressive strength increased significantly at 7 and 28 days with a higher amount of glass waste replacement. Up to 35% strength gain was observed when 30% of fly ash was replaced by waste glass. This increase may be attributed to the higher glass powder reactivity and availability of soluble silica provided by the reaction between glass powder and NaOH, which facilitates the geopolymerization process and leads to a higher amount of gel formation [33].

Glass fibre waste, as a reinforcement agent, was also investigated in geopolymer production [252]. The influence of glass fibre content (0.1%, 0.2%, 1%, 2% and 3%) and fibre length (6 mm and 20 mm) on the microstructure and mechanical performance of geopolymers were evaluated. The results showed that the use of short and randomly distributed fibres significantly enhanced the geopolymer's compressive strength (by up to 162%) and tensile strength (by up to 77%). It was also found that glass fibre content, rather than fibre length, was the dominant factor affecting the geopolymer's mechanical properties. Both compressive and tensile strength increased with increasing fibre content for the length of 6 mm, while the apparent density remained unchanged. For the samples with 20 mm fibre length, a further increase in the fibre content reduced the compressive strength. This might be attributed to the increase in porosity and size of the pores. Nevertheless, this research shows great potential in reducing the amount of fibre waste from landfilling and potentially lowering the production cost of geopolymer.

Novais et al. [253] introduced glass fibre fabrics waste produced during wind turbine blade manufacturing in synthesizing geopolymer composites. The influence of fabric amount (number of layers) on the sample's flexural strength and apparent density was investigated. The results showed a significant increase in flexural strength when the glass fibre fabrics were used as reinforcement materials. Increasing the number of layers further enhanced the flexural strength, with 144% improvement compared to the non-reinforced geopolymer. This study provides a sustainable solution for glass fibre off-cuts coming from wind turbine blade production, which could potentially increase the global sustainability of wind energy production [253].

2.4.3.2. Waste glass as a substitute of waterglass

The concept of using glass waste as a source of silica to replace waterglass in the alkaline activation of the geopolymer is more promising due to the expectation to provide an extra environmental advantage. It avoids the high energy consumption and CO_2 emissions associated with sodium silicate production, where temperatures around 1300°C are required to melt sodium carbonate and silica mixtures [254].

Torres-Carrasco et al. [254] explored the feasibility of using glass waste as a potential alkaline activator in geopolymers' preparation. Three alkaline activators were used, NaOH 8M, NaOH 10M + 15% waterglass, and a solution of NaOH 10M mixed with different proportions of glass powder waste (10, 15, and 25 g per 100 mL of solution). The glass waste was mixed with the NaOH 10M solution and magnetically stirred at 80°C for 6 hours. The solution was subsequently filtered, and the liquid was used as the alkaline activator. The compression results showed that samples' strength was improved when a solution of NaOH 10M was used instead of a NaOH 8M solution. In addition, the strength of samples increased further when 15% of waterglass was introduced. By replacing the commercial waterglass with waste glass powder, the 1-day and 3-day strength of specimens were slightly less. In contrast, the 7-day and 28-day strength of the specimens were higher than that of geopolymer using commercial waterglass. However, an excess of waste glass (25 g) lowered the strength to values below the findings for NaOH 8M. The author explained in terms of the solution pH, which declined considerably as the content of Si from the waste glass in the medium increased, as well as in terms of the SiO_2/Na_2O ratio [254]. Nevertheless, it still proves that waste glass can be used as an effective alkaline activator in geopolymer preparation.

More recently, Toniolo et al. [255] investigated soda-lime waste glass powder usage in the synthesis of fly ash-based geopolymer. The fly ash to glass powder ratio was varied according to the theoretical SiO_2/Al_2O_3 molar ratio in this work. The solid mixtures were directly mixed with different NaOH solution concentrations (5M, 8M and 10M) mechanically for 4 hours to obtain a homogeneous slurry of partially dissolved glass powders and activated fly ash. The results indicated that the compressive strength tended to rise as the molarity of the solution and the SiO_2/Al_2O_3 molar ratio increased. When the SiO_2/Al_2O_3 molar ratio increased, a higher replacement level of glass was introduced in the samples. Glass was partially dissolved under alkaline conditions, developing a silica-rich gel at the surface of the particles, hindering the complete dissolution of the initial waste glass [255]. The silica available in the system was enhanced with an increasing amount of glass in the formulation [255]. However, as one of the crucial reaction parameters, the higher temperature was not considered in this work.

The feasibility of reusing waste glass powder as a substitute for waterglass is well demonstrated [255]. It shows great potential in developing more economical and sustainable geopolymers. More research is still needed to explore the potential influence of using waste glass on the thermal performance of porous insulation geopolymers.

2.4.4. Fabrication of glass fibre mat

As a typical example of non-woven fabric, glass fibre mats are intended for the maintenance of thermal insulation for various branches of industry [256]. The basic concept employed in manufacturing a non-woven fabric is to convert fibre-based materials into two-dimensional sheet structures with fabric-like properties such as flexibility, porosity, and mechanical integrity [35]. The non-woven fabric manufacturing process generally consists of three stages:

web formation, web bonding, and finishing treatment. Although modern technology allows overlapping of some stages, and in some cases, all three stages can occur at the same time [257].

Web formation is a process to arrange fibres in a sheet or web, and it can be implemented via dry-laid such as carding, air-laid, wet-laid such as wet deposition and melt-blown. Since the webs formed via web formation generally have a limited initial strength; thus, the web bonding process is needed to consolidate the webs [257].

The web bonding process is classified into three types: thermal bonding (cohesive bonding), chemical bonding (adhesion bonding), and mechanical bonding. The choice of the web consolidation method strongly depends on the functional properties that are required, and the type of fibre used [257]. Thermal bonding uses the thermoplastic properties of certain synthetic fibres to form bonds under controlled heating. A low melt fibre or bicomponent fibre is generally introduced at the web formation stage to perform the binding function later in the process [257]. Chemical bonding refers to the application of a liquid-based bonding agent to the web, and it can be applied uniformly by impregnating, coating or spraying [257]. Mechanical bonding is achieved by inter-fibre friction as a result of the physical entanglement of the fibre. There are two main types of mechanical bonding: needle punching and hydroentanglement. Hydroentanglement uses high-pressure water jets to cause the fibres to interlace, and it is commonly applied to carded or wet-laid webs [257]. Needle punching uses barbed needles to reposition some of the fibres from a horizontal to a vertical orientation to be mechanically interlocked [35].

Needle punching is an inspiring and diverse trade involving technology for natural, synthetic fibres and their blends [35]. The needle-punched structures have a wide range of applications in both domestic and industrial markets, including automotive, blankets, wall coverings, and geotextiles [35]. Needle punching technology is an eco-friendly and low energy consumption process compared to chemical bonding and thermal bonding [35]. However, a considerable amount of fibres is needed for this process, and it usually requires considerable space to set up. In addition, it may be challenging to process short and low strength fibres, as the fibres need to be long enough to sustain the repositioning force. Thermally recycled glass fibre usually suffers from a severe loss in its ultimate strength [246]. The fibre length can be less than 5 mm after the recycling process [258]. Therefore, chemical bonding may be a more suitable technique for such fibres to investigate at a lab scale.

As a chemical bond technique, sizing is a thin surface coating of mainly organic materials applied to nearly all types of human-made fibres during their manufacturing process [259]. It protects the filaments during handling, processing, and subsequent compounding and composite processing [260]. On the fibre surface, size plays a vital role in determining the final composites' properties, such as improved adhesion between the fibre and the matrix, mechanical properties [260].

Thomason [259] conducted a comprehensive review on size formulation, sizing effects in fibre and composite processing, sizing and interphase adhesion, and sizing effects on composite performance. The review showed that approximately 75% of the research on sizing containing the four silanes, -aminopropyltriethoxysilane (APS), -glycidoxypropyltrimethoxysilane (GPTMS), -methacryloxypropyltrimethoxy-silane (MPTMS) and vinyltriethoxysilane (VTES) [259]. These silanes are molecules prepared from a silicon compound containing both organic and inorganic reactive groups. This allows them to function as a coupling agent [258]. Silane based coupling agents are commonly used due to the ability to join glass fibres with a range of different matrices [258].

Silane coupling agents have the general structure [X-Si(OR)$_3$], where X is a hydrolysable group, and R is a methyl or ethyl group [258, 259]. Amino-silanes, especially APS, are the most widely used silane coupling agents [258]. When silane is used to treat fibres in an aqueous sizing, hydrolysis occurs to form silanol. This unstable silanol can be condensed onto the fibres by eliminating a water molecule to produce a siloxane network. During this process, the Si-OH group on the fibre surface may also participate, resulting in the siloxane network being covalently bonded to the fibre surface [259], as indicated in Figure 2-19 [261]. Thus, the presence of coupling agents enhances the chemical bonding between glass fibre. In addition, when the treated fibre is involved in the polymer matrix, the X groups of the silane may still be available to react with the reactive functions of the polymers. This leads to a strong network bridging the fibre-polymer interphase [259]. It is suggested that sizing is probably the key component influencing the success or failure of most reinforcement products and their composites [259].

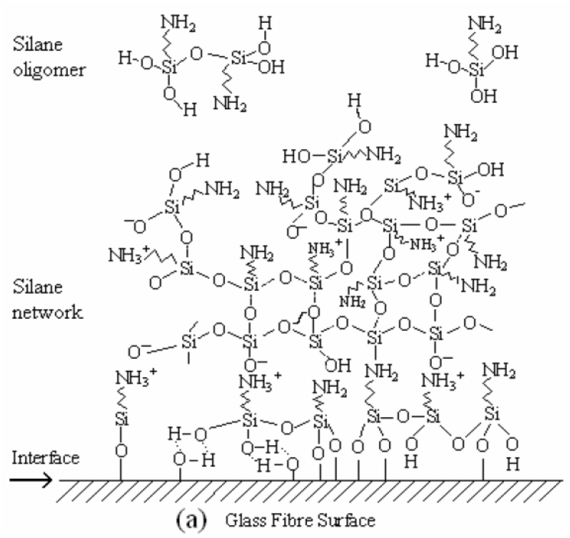

Figure 2-19 Chemical structure of hydrolysed APS on the glass fibre surface, reproduced from [261]

2.4.5. Conclusion

Glass fibre recycling has been explored extensively [243]. The recycled glass fibre (rGF) shows great potential in the fabrication of geopolymer and aerogel to lower their negative environmental impacts and preserve natural resources [33].

Waste glass, as a partial mineral precursor, has been investigated extensively in the fly ash-based geopolymer system [32-34]. The mechanical property of geopolymer generally improved with the addition of waste glass. However, the effect of waste glass on the thermal property of geopolymer is not commonly mentioned. In addition, the chemical structure of the fibre dissolved in alkaline solution via FT-IR has not been studied comprehensively.

The fabrication of short recycled glass fibre (rGF) mats and incorporating the prepared rGF mat with aerogel are rarely reported. Needle-punching, as a more eco-friendly and lower energy consumption process, has been widely used to fabricate fibre mats compared to chemical bonding and thermal bonding [35]. However, it may be challenging to process short and low strength rGFs, as the fibres need to be long enough to sustain the repositioning force. Sizing, as a chemical bond technique, shows great potential in manufacturing rGF mat due to its ability to enhance the chemical bonding between glass fibre.

2.5. Research on insulating package

It was stated in the previous research that the aerogel composites presented an excellent thermal insulation performance [15]. In the packaging industry, conventional insulation materials may no longer satisfy the requirement of temperature control during package delivery due to increasing market demand for long-haul transportation of fresh goods (e.g. foods and medicine). Besides, Synthetic (plastic) materials have become a significant problem to the environment nowadays as they can lead to contamination of a wide range of natural terrestrial, freshwater and marine habitats [20]. Therefore, the feasibility of using aerogel composites in packaging is worth investigating to improve the thermal insulation performance of the packagings and reduce plastic pollution.

In this section, an introduction of the insulating package is described, with an overview of the insulating package market. Both analytical and experimental approaches to package insulative performance are reviewed. Finally, the research gaps for both analytical and experimental approaches are addressed.

2.5.1. An introduction of insulating package

The quality of temperature-sensitive goods such as seafood products and medicines is strongly affected by the surrounding conditions [262, 263]. Insulated containers with phase change materials or refrigerated containers are usually used to deliver these products to avoid deterioration of their quality. According to the definitions of standards for special equipment for the carriage of perishable foods, the insulated container is defined as: ‘Equipment of which the body is built with rigid insulating walls, doors, floors and roofs, by which heat exchanges between the inside and outside of the body can be limited’ [264]. Such an insulated container is divided into two categories based on the overall heat transfer coefficient (U-value): a normally insulated container with a U-value equal to or less than 0.70 W/m^2K; a heavily insulated container with a U-value equal to or less than 0.4 W/m^2K [264]. Packages used to deliver temperature-sensitive products are typically insulated by polyethene (PE) or expanded polystyrene (EPS) liner, which is categorised as a heavily insulated container due to the low U-value [264].

Apart from insulative performance, it is also required by law to reduce the possibility of hazards [262]. The major hazards which might occur during transportation are physical, chemical and biological hazards. Physical hazards are common hazards that the foreign material may penetrate the container and interfere with food products [265]. However, the risk is relatively low for most insulating materials as few items are sharp or hard enough to cause physical damage. Chemical hazards are the threat posed by the usage of unsuitable packaging materials, cleaning agent's residuals (in case of a reusable container) or leaks from cooling substances [265]. Biological hazards are defined as the growth of parasites, bacteria and other biological contaminants due to inappropriate temperatures maintained through transportation [265]. These hazards need to be understood and investigated seriously to introduce new insulating materials into the packaging industry. Physical hazards are not considered in the investigation since the risk is low as mentioned earlier, and it is mainly determined by the handing during transportation, although the fragility of insulation materials could influence the insulation performance of the containers.

Regulation 450/2009/EC is adopted to provide major safety rules for all food contact material across the whole European Union to reduce the risk of chemical hazards (contamination) during the transportation of perishable goods [71]. The purpose of the law is to enhance the safety, quality and shelf-life of the packaged foods and secure a high level of protection of human health and the product. According to this regulation, all materials must not transfer their constituents to food in any quantity that could endanger human health or bring any organoleptic change or deterioration of the food [266].

As mentioned previously, biological hazards are mainly due to inappropriate temperatures maintained in transportation. The temperature control during the production and retailing process are not investigated here. Two types of food products are defined based on the post-processing temperature, namely frozen food and chilled food [267]. It is recommended to maintain the food temperature at -18°C (but must not be warmer than -12°C since few microorganisms grow below -10°C [267]) to preserve the quality and safety of the frozen food. This requires typically active cold chains such as refrigerated trucks to monitor and control the temperature. Chilled foods (generally between 0°C and +5°C, but above -1°) are more sensitive to temperature than frozen foods as the former's temperature can rise quickly [267]. Table 2-4 shows the maximum temperature limit for different types of products during transportation. At chilled temperatures, the growth and activity of microorganisms slow down only for a limited time (usually in days) [264]. Table 2-5 lists the minimum growth temperature of the most common bacterial species. Therefore, accurate temperature monitoring and control are essential to minimise contamination during any process stage to ensure chilled food quality and safety. During the transportation stage, the thermal performance of the insulation liner becomes critical to maintaining the temperature below the maximum limit [267].

Table 2-4 Maximum temperature limit for different types of products during transportation, reproduced from [264]

Product	Maximum temperature
Raw milk	+6°C
Red meat and large game	+7°C
Meat products, pasteurised milk, butter, fresh dairy products, ready-cooked foodstuffs (meat, fish, vegetables), vegetable products, concentrated fruit juice and fish products	+6°C or temperature indicated on the label
Game, poultry and rabbits	+4°C
Red offal	+3°C
Minced meat	+2°C or temperature indicated on the label
Untreated fish, molluscs and crustaceans	On melting ice or at the temperature of melting ice

Table 2-5 Minimum growth temperature of most common bacterial species, reproduced from [267]

Bacteria species	Minimum growth temperature
Salmonella	5.1°C to 8.7°C
Staphylococus aureus	9.5°C to 10.4°C
Escherichia coli	7.1°C
Listeria monocytogenes	-0.1°C to +1.2°C
Yersinia enterocolitica	-0.9°C to -1.3°C
Aeromonas hydrophilia	0.1°C to +1.2°C

2.5.2. An overview of the insulating package market

Market research shows that EPS and PE dominate the UK market share of materials used in insulating packaging production (based on the data obtained and listed in Appendix-A). This is because of its low cost and density as well as its relatively good insulation performance. These materials are also resistant to water, making them a perfect insulation material for shipping fresh seafood products. Another solution is natural materials such as natural wool and cellulose. It is more environmentally friendly, but the manufacturing cost is higher than EPS and PE with similar insulation performance. The market research data is listed in Appendix-A.

As a recent advanced insulation material, vacuum insulation panels (VIP) provide the best thermal insulative performance at a high cost. A whole vacuum panel's thermal conductivity in its initial state is approximately 4 mW/m.K, whereas typical insulation materials such as EPS or PE have a thermal conductivity of 46 to 76 mW/m.K [268]. Associated with gel packs, EPS or PE insulated boxes can only keep the product's temperature in between 2 to 8°C for less than three days, depending on the external environments. VIP can keep the temperature up to 10 days for the same cold source, or 2 to 3 times that of a classic insulation material (based on the data shown in Appendix-A). Therefore, VIP can meet the specific needs of long-haul shipping, potentially broadening the UK fishing market outside Europe for delivering chilled products. However, a few drawbacks limit their application to building or shipping medical products only [269]. Firstly, the cost is exceptionally high. Typical VIP is in a price range of £35-£175 per square meter [269], which is almost 10 to 60 times that of a standard EPS panel (£3 per square meter). Furthermore, unlike most conventional insulation materials, VIP cannot cut to size on-site, which means that the panels must be pre-designed for specific dimensions or requirements. Panels are susceptible to mechanical damage. Puncture or loss of vacuum during any stage would significantly diminish the thermal performance and service life [269].

Apart from the market share, the maximum transportation time provided by insulating container manufacture were collected and analysed, as listed in Appendix-A. For EPS or PE insulated cardboard boxes, the maximum transportation time (products stay chilled) varies between 24h to 72h, whereas the natural wool insulated container can maintain the required temperature for 24h to 62h. Maximum transportation time varies from supplier to supplier using the same materials due to a lack of testing standards for such packaging types. The difference is mainly influenced by different outside environmental conditions, the number of products, and coolants within the box.

Phase change materials (PCM) is the only cold source to maintain the products within the box to the desired temperature. Therefore, the amount of PCM, types of PCM could influence the overall packaging thermal performance. It can also be seen from Appendix-A that most package suppliers tend to use PCM to extend the thermal performance. Ice and ice-based products, especially ice pack sheets, are the most common PCM only due to their low cost. Ice pack sheets contain expandable, non-toxic beads, which could absorb 20 more time its weight in water. It is convenient to use and environmental friendly. Ice is also an entirely natural substance, meaning there is no danger of chemical hazard in case of coolant leakage. The alternative solution is to use gel packs, which typically contain water, substances to lower the freezing temperature, such as propylene glycol, a thickening agent, and non-toxic blue colouring [270]. Gel packs usually take longer to melt due to lower overall surface area but at a higher cost [271].

2.5.3. Thermal conductivity of insulation materials

Thermal insulation materials are highly porous and consist of a solid matrix full of small voids that comprise 90% or more of the total volume [272]. The material's apparent thermal conductivity is the macroscopic result of the various energy flow paths found in its complex porous structure, which includes conduction through the solid matrix, gas conduction in the voids and radiation across the internal pores [273].

The apparent thermal conductivity at the microscopic level depends on numerous factors such as cell size, diameter and arrangement of fibres or particles, transparency to thermal radiation, type and pressure of the gas and bonding materials [272]. A minimum apparent thermal conductivity of the materials could be achieved by varying these factors. At the macroscopic level, the apparent thermal conductivity largely depends on density, moisture content, temperature, and age [273]. The effect of pressure, such as compression of the material, also influences the insulation material's effective thermal conductivity [274, 275].

Domínguez-Munoz et al. [273] have summarised the density-thermal conductivity relationship with the most commonly seen insulation materials, as shown in Figure 2-20 [273]. It has been concluded that density is the crucial factor influencing the conductivity once temperature and humidity content is fixed at reference conditions [273]. At high densities, the thermal conductivity increases with the density as porosity decreases [273]. The lowest thermal conductivities are found when the density of a material is 30 to 60 kg/m^3 [273]. It is worth mentioning that the radiative portion of the thermal conductivity is a reciprocal function of density due to more solid shields being found as density increases to prevent radiant exchange [273]. However, the increase in density leads to a significant increase in solid conduction, which is predominant in the overall heat transfer. Therefore, the thermal conductivity increases at high densities.

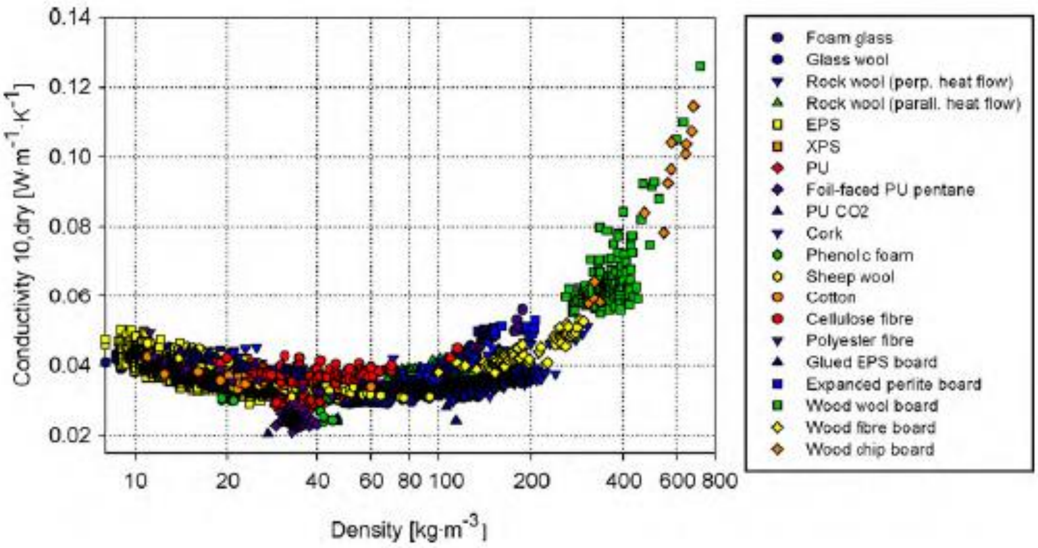

Figure 2-20 Thermal conductivity of insulating materials at 10°C and dry state, aged samples, reproduced from [273]

Kocí et al. [276] investigated the influence of moisture content on the thermal properties of porous building materials. It was found that an increase in moisture content was detrimental to the thermal properties of materials. The thermal insulation materials with similar thermal properties in a dry state may have substantially different thermal characteristics in the water-saturate state. This is because the capabilities to accept moisture are different. For example, expanded polystyrene, with its closed pore structure and hydrophobicity, was able to absorb only 3.3 vol% of moisture; thus, its thermal conductivity remained practically unaffected (increased from 0.038 to 0.05 W/m.K). The thermal conductivity of mineral wool with open pores increased significantly from 0.037 to 0.772 W/m.K as the moisture content increased to 60%. This is because the heat conduction of water is nearly twenty-five times more than air [277]. Therefore, it is necessary to use moisture-repellent insulation materials for building insulation applications.

Alvey et al. [278] studied the effects of moisture content and temperature on three commercially available aerogel blankets. It was found that the impact of moisture on thermal performance largely depended on the composition and manufacturing process of composites. Although all three aerogel blankets contained PET fibres, which is known to be hygroscopic, the combination of glass and PET fibres encompassed by the hydrophobic aerogel could minimise the uptake in moisture. However, the possibility of hygroscopy and hydrolysis is more significant when the fibres are loosely nested with the aerogel particles. The hydrolysis causes permanent damage that prevents the fibres from returning to their original state. Thus the blankets expanded significantly (shown in Figure 2-21 [278]), and thermal performance was decreased. Besides, aerogel blankets consisting of bi-component fibres could be more sensitive to change in temperature due to a difference in thermal expansion properties of the two components [278].

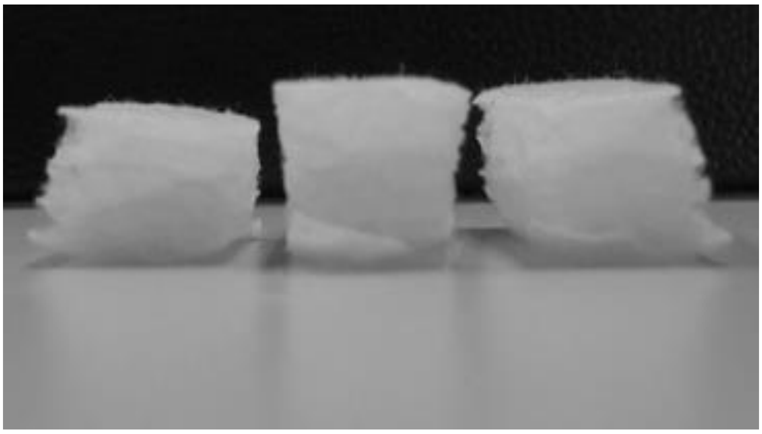

Figure 2-21 Comparison of aerogel blanket samples before exposure (left), with 1 and 5 weeks of exposure at 65.5℃ and 90% RH, reproduced from [278]

The effect of ageing is commonly seen in plastic foam materials [279]. The ageing of plastic foam can be classified into three stages. The conductivity of a foam insulation material increases at a relatively high rate early in the life cycle. It then slows down to a lower rate for most of its life until the conductivity eventually plateaus. Diffusion of the highly insulating blowing agents has a significant impact on thermal conductivity. Simultaneously, the infusion of air from the environment also influences thermal performance as it may carry moisture into the material. It is suggested that the infiltration of exterior air takes place over the first 1-2 years of the material life cycle, while the diffusion of blowing agent gasses takes place over 10-20 years [279].

The effect of mechanical loading on insulation materials' thermal performance has also been investigated [274, 275]. Kolich et al. [274] studied the influence of mechanical compression on thermophysical properties of car interior leather-foam plastic insulation. It was shown clearly that the thermal conductivity of the leather foam sample increased with increasing pressure. This behaviour may be attributed to the change in contact heat resistance between the leather and the foam. With increased compression, the cracks present either in the form of microvoids or in the leather-foam interface would highly influence the apparent thermal conductivity.

An opposite trend was found for aerogel composite materials. Sletnes et al. [275] investigated the effect of uniaxial compression on the thermal conductivity of commercially available aerogel insulation blankets by compressing the samples in a heat flow meter apparatus. The results showed that a reduction of 11.5% in apparent thermal conductivity was obtained when the load increased to 22 kPa.

Shi et al. [280] carried out a microstructure analysis on ceramic fibre reinforced aerogel composite before and after compression. It was shown clearly that the particle size was the same as that of the specimen without deformation after compression. However, as the composites were compressed, densification likely occurred as a result of a better entanglement of clusters, as illustrated in Figure 2-22 [280]. This led to a drastic decrease in the pore size located between clusters. Therefore, heat transfer in the gaseous state may be reduced, so as the apparent thermal conductivity of the materials.

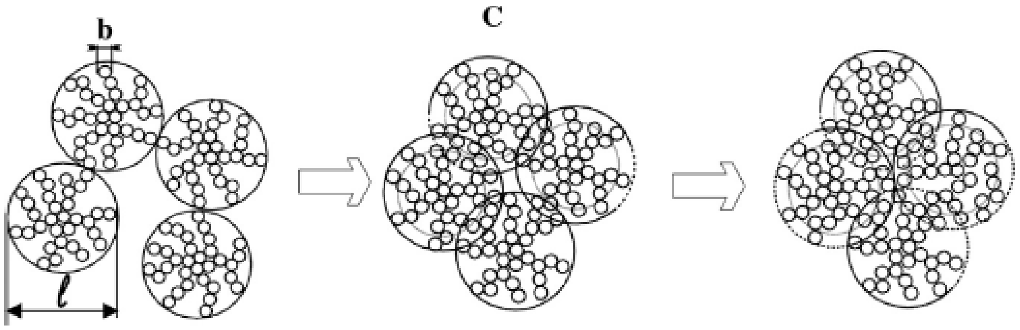

Figure 2-22 Illustration of solid transport of aerogel particles induced by compression, reproduced from [280]

It is well shown that density, moisture content, temperature, ageing, and mechanical loading significantly impact the thermal conductivity of insulation materials. However, the effect of these parameters may vary significantly between materials; thus, more research is needed to gain a deep understanding of the thermal conductivity of materials [275].

2.5.4. The analytical and experimental approaches to packaging insulative performance

It is often time-consuming and more costly to design an insulative package through physical tests [281]. Therefore, it is beneficial to develop a predictive model for packaging design under consideration of key design parameters such as insulation materials, packaging geometry, surrounding environment.

G. Burgess [282] and S. Choi [36] have developed a mathematical model that included packaging material, the geometry of the package, geometry of product and degree of contact between the product and the container. This model was used to predict the insulating package’s performance by calculating the thermal resistance of a multi-layered wall. Package heat penetration rate was then calculated by considering the basic heat transfer principles covering conduction, convection and radiation. Ice melt test was then used to validate the mathematical model, and the factors affecting the insulating performance, including the geometry of the package and product, were discussed [36, 282]. Finally, the effect of aluminium foil and the variable outside temperature was discussed. It was found that with aluminium foil applied on the outside of the package, the heat penetration rate reduced by 17%, and the percentage decrease was more significant with less wall thickness. However, the explanation was not mentioned. It was also stated that the outside temperature during distribution influenced the performance of the insulating materials. However, larger experimental errors was obtained (in most cases within 30%) [36].

J. Terpak et al. [37] has developed a mathematical model and simulated using MATLAB to investigate the time required for products to reach 32°C when considering heat transfer by conduction, convection and radiation individually and combined. The model started with the thermal energy balance and eventually solved the analytical solution by determining the temperature as a function of time. Despite this transient approach, simplified package geometry and construction were limiting factors that could lead to significant uncertainty. Nevertheless, the model clearly showed that the change of surface emissivity could significantly influence the thermal radiation, and the change of insulation liner thickness resulted in a substantial difference in heat conduction. It is also worth mentioning that aerogel, as a novel material, was utilised in packaging, which could improve the thermal performance of packaging significantly [37]. Unfortunately, little experimental data was obtained to validate the transient model.

J. Singh et al. [283] investigated the thermal insulation performance of packaging designated for delivering pharmaceutical drugs and vaccines. System thermal resistance was calculated using the ice melt test based on G. Burgess's model [282]. Experimental work was carried out by inserting a temperature monitor probe into a product. A phase change material was used to maintain the product at a designated temperature range as long as possible. Twenty different types of packages were designed by varying the thickness and type of insulation material and dimensions of the packages to investigate the factor affecting the insulation performance. The starting temperature of the experiment was not mentioned. It was indicated that the interaction between the R-value and the wall thickness significantly influenced the length of time, and the thermal insulative packages stay in the desired temperature range of 2℃ to 8℃. It was optimal to use low wall thickness except when high R-values accompanied it. This finding could be used as a guide for container manufacturers using greater wall thickness only for high R-values materials.

D. Stubbs et al. [284] developed a numerical model to investigate the effect of quantity and position of gel packs on the period for which maximum product temperature could be maintained below 5℃ and 8℃. The results indicated that the performance of packages was maximised when the product was surrounded by refrigerants.

B. Margeirsson et al. [285] investigated the temperature distribution within the package using computational fluid dynamics (CFD) and verified it experimentally. Thirty-two EPS boxes were built into four layers on a Euro pallet. The results showed that a temperature difference of up to 8.5℃ was recorded for the products. The maximum temperature difference within a single box was approximately 7℃ stored for 6.4 h at a mean ambient temperature of 18.5℃ [285]. This finding suggests that temperature distribution within a package is inconsistent. Therefore, careful design such as positioning the product and phase change materials, container size related to products is needed to minimise the temperature variations.

K. Valtysdittir et al. [286] redesigned a standard rectangular EPS box by increasing the internal corner radius and thinner the wall further away from the corners using CFD methods. Such a design reduced the box weight by 11% compared to the standard EPS box. Meanwhile, the thermal insulation performance was improved significantly, which extended approximately 2 to 3 days longer freshness period and prolonged shelf life up to 1 to 2 days [286]. However, the explanation of the findings was not mentioned.

2.5.5. Conclusion

In this section, an introduction of the insulating package was described, with an overview of the insulating package market. In addition, A number of researches have been focused on investigating the thermal performance of packaging, including analytical models and experimental work. However, the use of aerogel composites in this field is rarely reported. Besides, the factors influencing package insulation performance have not been studied comprehensively. Furthermore, a simplified analytical model accompanied by the ice melt test lead to significant uncertainty; therefore, both the analytical model and experimental work could be improved.

2.6. Conclusions of the literature review

In this chapter, highly insulating materials, including porous geopolymer and aerogel, were reviewed comprehensively. Their reaction mechanism and fabrication process were first described. The research status and their application were then explored. Finally, several knowledge gaps were addressed and restated below.

For geopolymer, the foam expansion mechanism and the expansion rate at different temperature of the geopolymer slurry is rarely reported. This could be used to indicate how different pore structures are obtained by varying the foaming agent. In addition, the thermal performance of the geopolymer can be improved by varying the design parameters. Furthermore, the involvement of the waste glass in geopolymer could improve the mechanical property of geopolymer. However, the effect of waste glass on the thermal property of geopolymer is not commonly mentioned. Finally, the chemical bonding state of the fibre dissolution in alkaline solution via FT-IR has not been studied comprehensively. These will be explored in this thesis.

For aerogel and aerogel composite, some detailed descriptions of the fabrication process of aerogel are rarely reported, for example, the amount of solvent used for ageing and solvent exchange. It has a nonnegligible impact in terms of cost-saving, especially in the UK. The cost for one litre of Ethanol and n-Hexane is approximately £50 and £40, respectively [28, 29]. Therefore, adequate usage of these solvents could lower the manufacturing cost. In addition, the fabrication processes, including ageing temperature and drying process, could be optimised to improve the properties of the aerogel and aerogel composites. Dustiness during handling and processing should also be prevented. In addition, the involvement of recycled glass fibre could maximise environmental benefits. These will be discussed in this thesis.

Aerogel composites presented an excellent thermal insulation performance. Thus, the feasibility of using aerogel composites in packaging is worth investigating to improve the thermal insulation performance of the packagings and reduce plastic pollution. A number of researches have been focused on investigating the thermal performance of packaging, including analytical models and experimental work. However, the use of aerogel composites in this field is rarely reported. In addition, the factors influencing package insulation performance have not been studied comprehensively. Furthermore, a simplified analytical model accompanied by the ice melt test lead to significant uncertainty; therefore, both the analytical model and experimental work could be improved.

3. Fabrication and characterisation of porous geopolymer with excellent thermal performance

As mentioned in the background research, insulation in buildings or any other sector is an energy-efficient strategy leading to lower energy consumption [6]. Porous geopolymer possesses a high potential for commercial insulation applications since it is more economical and environmentally friendly than cement-based foamed concrete [23]. Geopolymer can be fabricated using industrial solid waste (i.e., fly ash and furnace slag), and it produces less carbon dioxide as well as consumes less energy during manufacturing than traditional cement [19, 24, 25]. Therefore, it is worth studying the physical, thermal, and mechanical properties of the geopolymer.

A number of researches have been carried out to investigate the properties of porous geopolymer. Foaming agents and foam stabilizers are the key factors determining the final properties of the material, and it was reported considerably. However, the foam expansion mechanism and the expansion rate at different temperature of the geopolymer slurry is rarely reported. This could be used to indicate how different pore structures are obtained by varying the foaming agent. In addition, the thermal performance of the geopolymer can be improved by varying the design parameters.

In this chapter, the feasibility of synthesizing inorganic porous geopolymer is evaluated using industry by-product fly ash as the raw material. The foaming agent is set as the variable, and the influence of the foaming agent on the properties of the geopolymer is discussed. Pore structure, bulk density, thermal conductivity, and compressive strength test are the critical parameters for characterising the prepared specimens. The effect of foaming agent amount on the foam expansion rate is also investigated, and the foam expansion mechanism is discussed.

3.1. Experimental

In this section, the materials used to synthesise porous geopolymer are listed. The preparation process and the characterisation method are described.

3.1.1. Materials

Coal fly ash (Fineness category N - ≤40% retained on the 45 um sieve according to BS EN450) was provided by Cemex (a member of the UK Quality Ash Association). Sodium silicate solution (SiO_2:Na_2O ≈ 3.345) and NaOH pellet purchased from VWR are used as an alkaline activator (AA). NaOH pellets were premixed with deionized water to obtain a 10M sodium hydroxide solution. Calcium stearate and hydrogen peroxide (H_2O_2, 30 wt%) was supplied by VWR.

3.1.2. Sample preparation

In this work, the amount of H_2O_2 was set as the variables, as shown in Table 3-1. The weight ratio of alkaline activator to fly ash was fixed to 0.9, and the weight ratio of sodium silicate solution to 10M NaOH solution was set to 1.23:1. Figure 3-1 presents the preparation process of a geopolymer. Sodium silicate and NaOH were firstly mixed according to the pre-set ratio using mechanical stir for 2 minutes at 300 rpm to form AA. Fly ash and calcium stearate was then mixed for 3 minutes at 300 rpm to create a dry mixture. The premixed alkaline activator was then poured into the dry mix and continued to stir for 3 minutes at 600 RPM to make a uniform slurry. H_2O_2 was then added into the mixed slurry and stirred for 1 minute to ensure H_2O_2 was well distributed in the slurry. The fresh paste was poured into a mould with half-filled to allow the paste to expand freely and then covered with cling film to avoid moisture moving in or out the mould. A triplet plastic mould of 50 mm × 50 mm × 50 mm was used to fabricate the geopolymers for density and compressive strength measurement, as indicated in Figure 3-2 (a). 80 g of fly ash was used to fabricate three specimens. For thermal conductivity measurement, a rubber mould of 30 cm × 30 cm was used, as indicated in Figure 3-2 (b). 240 g of fly ash was used to fabricate one specimen, and other raw materials were adjusted according to Table 3-1. The mould was then placed on a shaker for 1 minute before transferring into an oven at a temperature of 60°C. After 24 hours, the sample was de-moulded and exposed to the ambient environment for free moisture releasing and further ambient curing for 24 hours.

Table 3-1 Mix proportions of fly ash-based geopolymer

Sample label	Fly ash (g)	AA/Fly ash	Calcium stearate (wt%)	H_2O_2 (wt%)
H0C2	80	0.9	2	0
H2C2	80	0.9	2	2
H4C2	80	0.9	2	4
H6C2	80	0.9	2	6
H8C2	80	0.9	2	8

Note: wt% of calcium stearate and H_2O_2 are calculated by the weight of fly ash

Figure 3-1 Preparation procedure of geopolymer

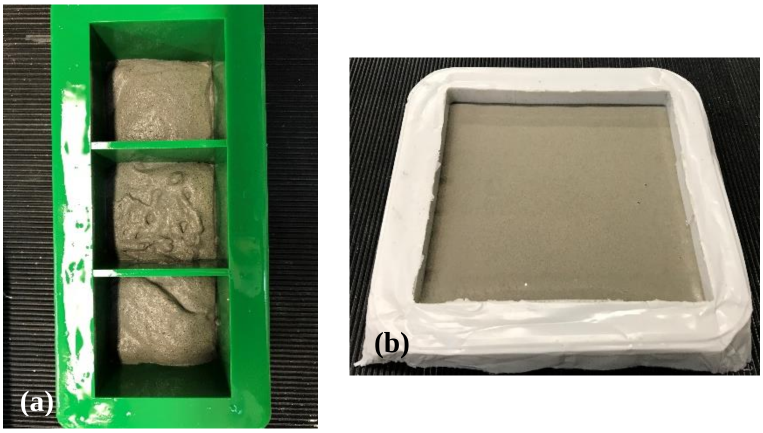

Figure 3-2 (a) triplet plastic mould of 50 mm × 50 mm × 50 mm and (b) rubber mould of 30 cm × 30 cm

3.1.3. Characterisation of geopolymer

3.1.3.1. Density and porosity

The oven-dry density of geopolymer was calculated based on the measurement of the dry mass of the specimen divided by the volume of the sample according to ASTM C513. The specimens were dried in an oven at 110°C for 24 hours and weighed using an electronic balance. The volume was calculated by measuring the length, width, and height with callipers, and each dimension was measured three times across the whole sample range to get an average value. The porosity was calculated based on the following Equation:

$$\varphi_i = 1 - \frac{\rho^i_{bulk}}{\rho^0_{bulk}} \qquad \text{(Equation 3-1)}$$

where φ_i is the porosity; ρ^0_{bulk} is the dry density of the geopolymer without a foaming agent (i.e., 0% H_2O_2); ρ^i_{bulk} is the dry density of the geopolymer at a particular foaming agent amount (i.e., 2%, 4%, 6%, and 8%). It was assumed that ρ^0_{bulk} is the true density of geopolymer, meaning that the prepared geopolymer's porosity is considered 0%. This approximate value is used to estimate the porosity of the porous geopolymer with various foaming agent content for simplicity, despite the fact that it leads to a systemic error of the porosity calculation.

3.1.3.2. SEM imaging

The pore morphology of geopolymers was obtained using a Scanning Electron Microscope (SEM, HITACHI S-3700N) with 15 kV voltage on the fracture of samples without gold coating to discover the influence of synthesizing parameters on pore morphology, as shown in Figure 3-3.

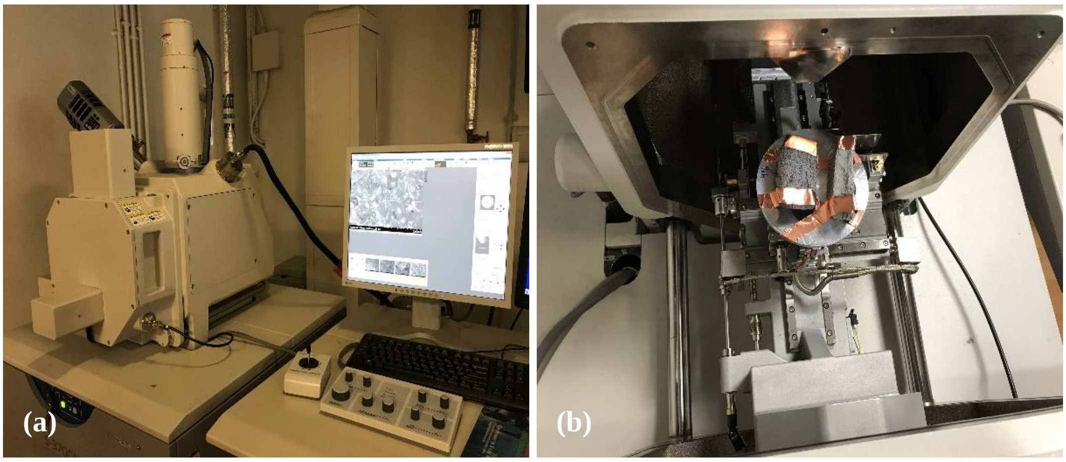

Figure 3-3 (a) Scanning Electron Microscope (SEM, HITACHI S-3700N) and (b) sample loading

3.1.3.3. Thermal conductivity

The Netzsch Heat Flow Meter 436 with a thickness gauge was used to measure the thermal conductivity and thickness of geopolymers accurately, according to ASTM C518-17. The specimens were prepared with a size of 30 cm × 30 cm, and the average thickness of the samples was 1.7 cm. An example of the specimen is illustrated in Figure 3-4 (a). The measurement was carried out at a mean temperature of 20°C, with a temperature difference of 20°C between the hot and cold plates. In this case, the average temperature of the hot and cold plates was 30°C and 10°C, respectively. An external chiller was used to maintain the temperature of the cold plate. Room temperature (20°C) or closer to this temperature is a typical temperature range to characterise the thermal conductivity, which is mentioned in many research [70, 191]. A constant pressure load of 0.7 kPa was applied during all measurements, as shown in Figure 3-4 (b).

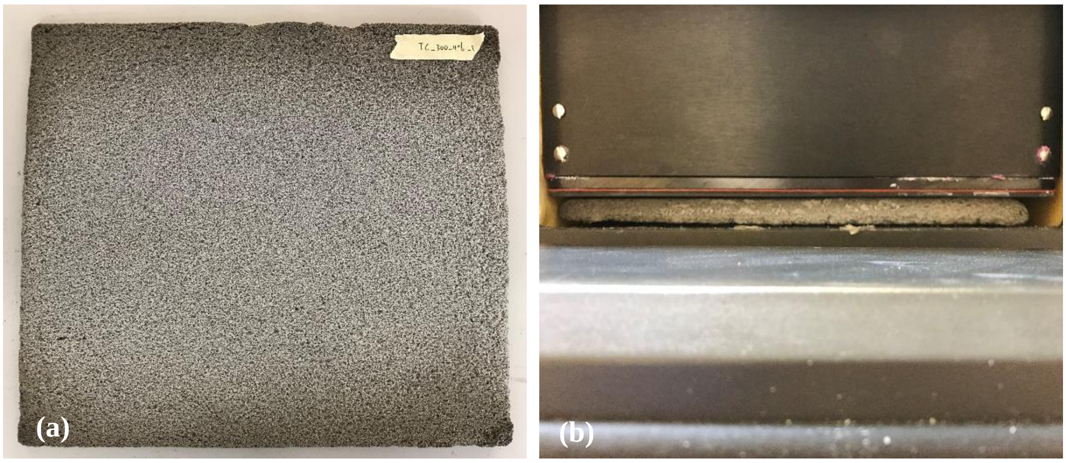

Figure 3-4 (a) Geopolymer with 2% H_2O_2 (b) Sample loading in HFM

3.1.3.4. Compression test

Specimens for compressive strength measurement were cast in triplet plastic moulds of 50 mm × 50 mm × 50 mm, and post-cured for 7 days at ambient conditions before measurement. The 7-day compressive strength measurement was tested using a 50 KN Instron machine with a loading rate of 1 mm/min according to ASTM C513. The gauge length reading accuracy of the machine is ± 0.2%. A minimum of 3 specimens was tested to calculate an average compressive strength and modulus. Several measures were employed to improve the accuracy of the measurement. The samples were polished using sandpaper to obtain a flat surface before testing, as shown in Figure 3-5. It was then transferred to the equipment to make sure the surfaces of the clamps were in parallel with the sample surface. This guaranteed a uniform load applied to the specimens. In addition, a known load (5 N) was applied to the materials before testing (ensure full contact with samples) to minimise the contact error so that the accuracy of the strain measurement is improved.

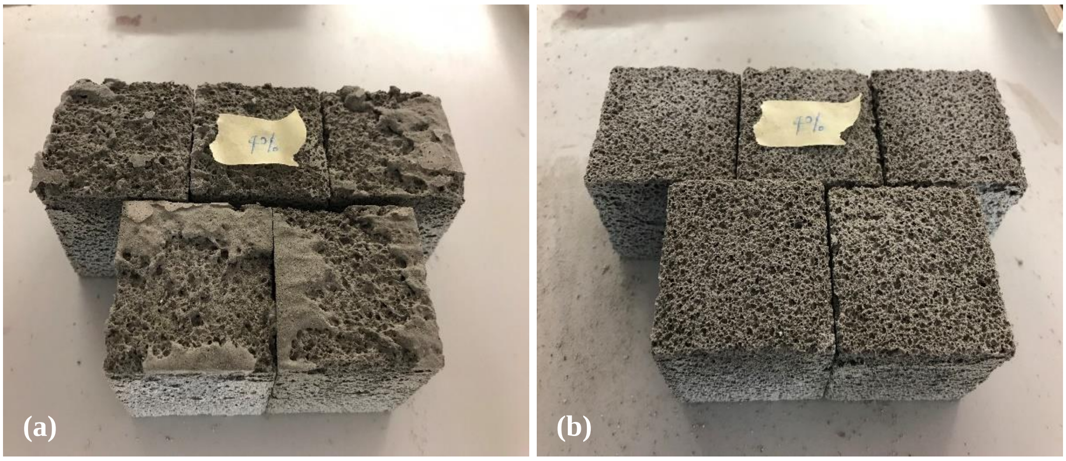

Figure 3-5 Geopolymer with 4% H_2O_2 (a) before and (b) after polishing

3.1.3.5. Water absorption

The water absorption test was conducted by submerging the specimens in water at ambient temperature, according to ASTM C796. For the porous samples, a glass jar was placed on top of the specimens to keep the specimens below the water surface (Figure 3-6). After 24 hours, specimens were removed from the water and allowed excess water to run off (30 seconds) before weighing them using electrical balance. The average mass of water absorbed was calculated by subtracting the oven-dry mass from the specimens' wet mass. The water absorption by mass can be determined using the Equation:

$$Absorption,\ \%\ by\ mass = 100\ \frac{m_w}{m_c} \qquad \text{(Equation 3-2)}$$

where m_w is the mass of water absorbed by geopolymer in 24 hours in g; m_c is the mass of the geopolymer measured in section 3.1.3.1 in g.

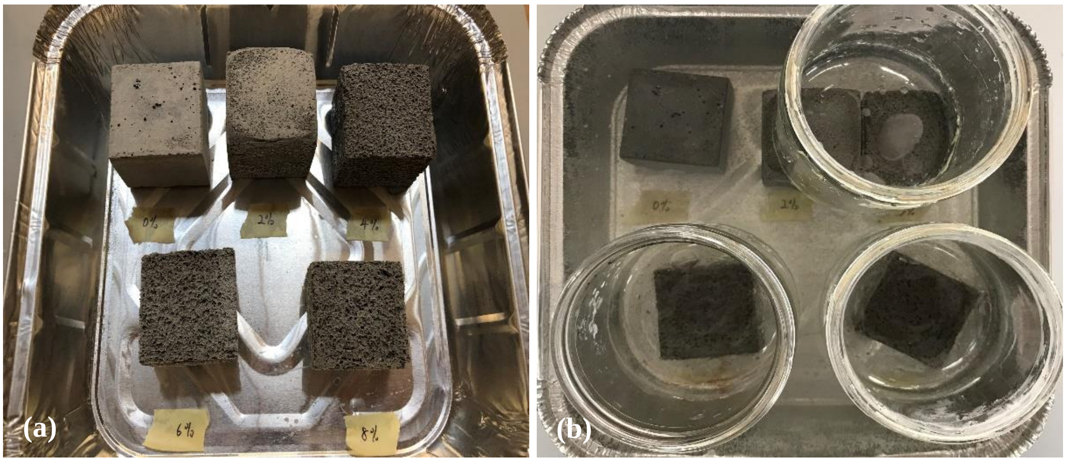

Figure 3-6 Specimens (a) before and (b) during immersion in water

3.1.3.6. Volume expansion

Volume expansion of geopolymer slurry with different amounts of H_2O_2 was tested using a graduated cylinder with a 2 ml scale. The prepared slurry was poured into the cylinder with an initial volume of 20 ml, and the volume change was recorded every 2 minutes until the volume remained constant. Both room temperature and elevated temperature were examined to investigate the foaming rate at different conditions. The elevated temperature was conducted in an oven with a pre-set temperature of 60℃.

3.1.3.7. FTIR analysis

The chemical environments of molecular bonds of geopolymer were determined via Fourier transform infrared analysis (FTIR Agilent Technologies 4100 Exo Scan). The spectral range was set from 4000 to 650 cm^{-1} as there is considerable spectral noise outside this range. A diamond ATR (attenuated total internal reflectance) was used as the diffuse reflectance interface. The samples were crushed and ground into powders for the FTIR test. A minimum of 10 specimens was tested, and the raw data generated were analysed using OriginLab.

3.2. Results and discussion

In this section, the influence of the foaming agent on the properties, including pore structure, bulk density, thermal conductivity, and compressive strength test, of the geopolymer is discussed. The effect of foaming agent amount on the foam expansion rate is also investigated, and the foam expansion mechanism is discussed.

3.2.1. Effect of H_2O_2 content on the pore structure

Figure 3-7 shows the microstructure of porous geopolymers with various amounts of foaming agents. The average pore dimensions were measured and calculated via ImageJ. An average of fifteen pores was measured on each SEM image, and an average of three SEM images was measured for each specimen. It can be seen from Figure 3-7 (a) that the unreacted fly ash particles are presented, and this may be due to the contact area for the reaction being blocked by the excess water molecules, and this, in turn, affected the geopolymerization process between the aluminosilicate and alkaline activator. Besides, the fineness of fly ash also contributes to the dense structure, which helps reduce the formation of microcracks [287]. In contrast, it can be seen from Figure 3-7 (b) to (d) that samples with the addition of H_2O_2 exhibit a porous structure. H_2O_2 is thermodynamically unstable and can be easily decomposed into water and oxygen. The bubble of O_2 is trapped within the paste, expanding and generating void (macropores). The volume expansion of the material depends on the amount of oxygen produced by the reaction shown in Equation 2-3 [68, 71]. Therefore, the pore size becomes larger with foaming agent addition as more oxygen is produced, and it is clearly shown in Figure 3-8. This may result in the pore wall being too thin to resist curing shrinkage, and foam stabilizer may not be sufficient to avoid bubbles coalescing, crushing the pore wall and increasing the connected holes, as clearly shown in Figure 3-7 (d). Besides, with the increase of H_2O_2 addition, the amount of water produced by decomposition increases. Thus, the viscosity of the slurry reduces, and the flow degree increases. During the gas generation process, the ultimate shear stress of aerated slurry rises instantaneously. Thus, the generated bubbles are merged into larger pores in a small range [25].

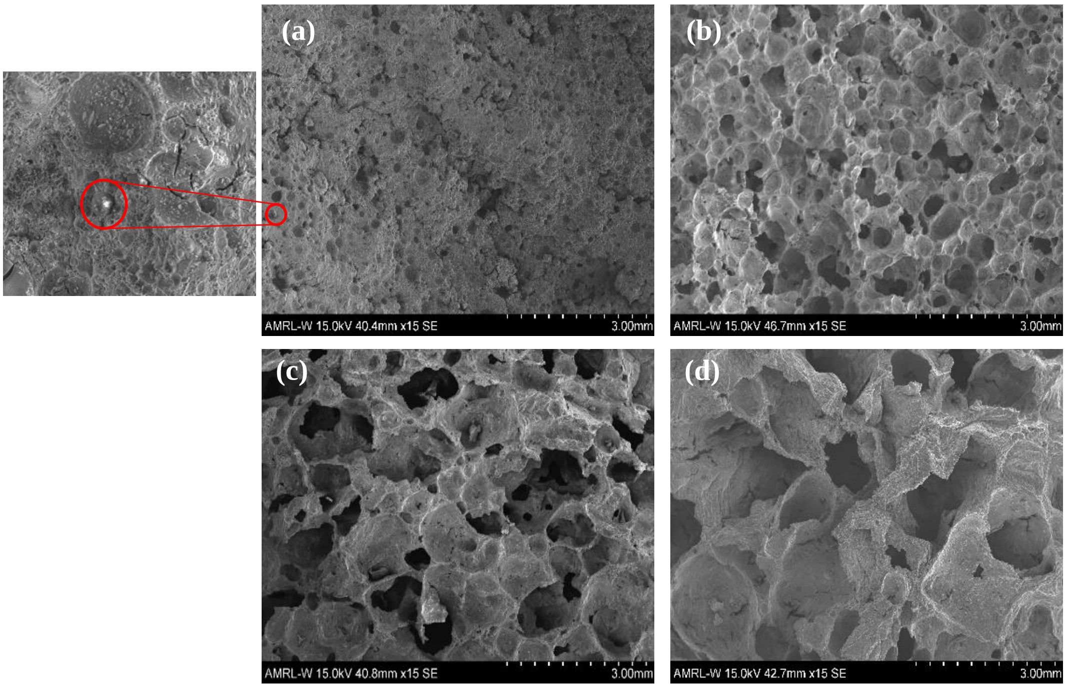

Figure 3-7 SEM image of geopolymer cross-section with (a) 0% (red mark indicates the unreacted fly ash particle), (b) 2%, (c) 4% and (d) 8% H_2O_2 respectively

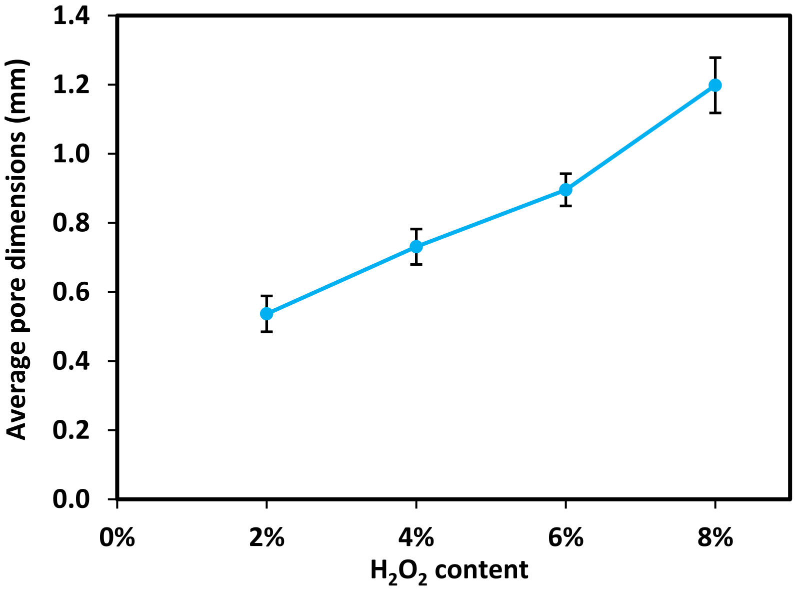

Figure 3-8 Effect of H_2O_2 content on average pore dimensions

3.2.2. Effect of H_2O_2 content on density and porosity

Figure 3-9 shows the effect of H_2O_2 content on the bulk density and porosity of the samples. As expected, the bulk density reduces as the porosity increases with the increment of foam content. It can be predicted from Equation 3-1 that the sample with a small bulk density shows high porosity, and the relationship between bulk density and porosity presents an inverse function. As the H_2O_2 content increases from 0% to 2%, the bulk density drops promptly from 1.17 to 0.38 g/cm^3, a 67% reduction. In contrast, the porosity rises sharply to 67%. This is due to the slurry's foaming capacity being determined directly by foam content [17]. As the amount of H_2O_2 increases further from 2% to 6%, the slurry pores become bigger, as described in section 3.2.1, resulting in a further decrease in density and increase in porosity. However, the changing rate is lower and eventually levels off. This may be attributed to the foams' relatively weak stability before curing, as the air bubbles cannot be trapped within the slurry. Instead, the air bubbles escape from the slurry surface and burst. Moreover, with the increase of H_2O_2 addition, the amount of water produced by deposition increases [25]. The loss of water in the sample causes noticeable shrinkage during the drying process. Thus, the changing rate of density after H_2O_2 content of 4% is not evident relatively to that before 4%. As the amount of H_2O_2 increases further to 8%, a slight increase in density was observed. This may be due to the collapse of the specimen as the bubble shell's strength is not strong enough to hold the immense void. This is described in more detail in section 3.2.4.

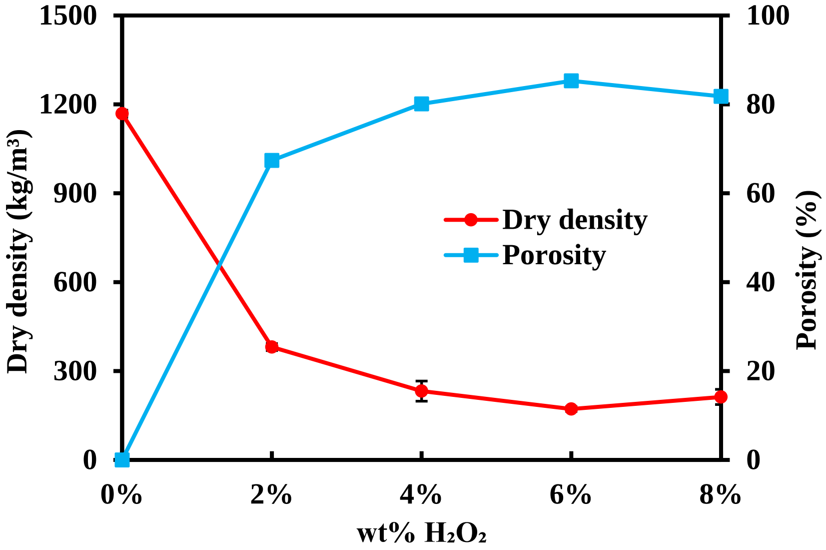

Figure 3-9 Effect of H_2O_2 content on bulk density and porosity of geopolymer

3.2.3. Effect of H_2O_2 content on thermal conductivity

The influence of H_2O_2 addition on the thermal conductivity of the geopolymer is shown in Figure 3-10. When the H_2O_2 content increases, the slope of thermal conductivity shows a similar trend as the density. As the H_2O_2 content increases from 0% to 2%, the thermal conductivity reduces significantly from 156 mW/m.K to 81 mW/m.K, declining nearly 50%. This is due to many unconnected pores being introduced into the geopolymer foam matrix when the foaming agent is present. As a result, the thermal conductivity of the specimens decreases to a large extent. As the H_2O_2 content increases further to 8%, the thermal conductivity reduces slightly and gradually levels off to a minimum value (51 mW/m.K).

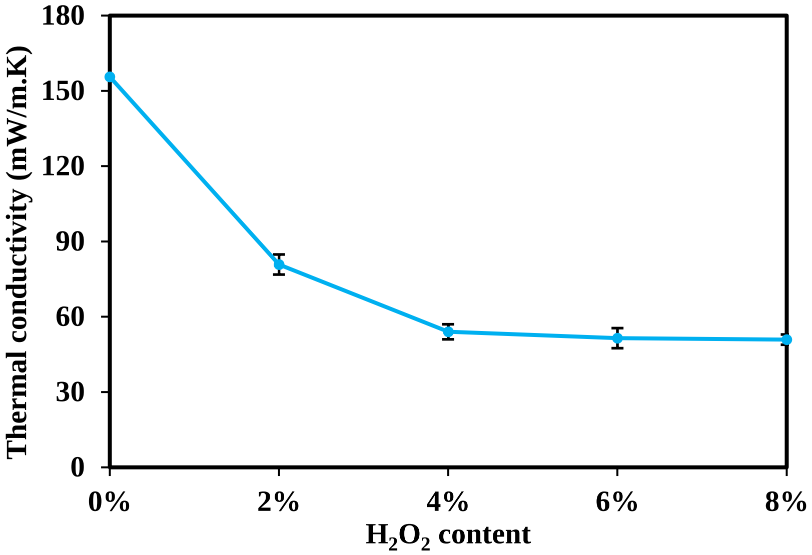

Figure 3-10 Effect of H_2O_2 content on thermal conductivity of geopolymer

Pore characteristics such as porosity, pore size, and distribution significantly impact thermal conductivity, thus the heat transfer of the porous materials [277]. Considering the heat transfer in porous building materials such as geopolymer, the porosity, conductivity of the solid matrix, and the type of the fluid in the pores (water or air) are the main factors influencing the effective thermal conductivity [277]. It was proved that if the solid matrix's thermal conductivity is larger than that of the fluid (air or water), the thermal conductivity decreases with increasing porosity [288]. Similarly, the thermal conductivity increases with increasing porosity if the solid matrix's thermal conductivity is smaller than that of the fluid (air or water) in the pores [288].

The porosity-thermal conductivity relationship of the geopolymer with and without the data point of 0% H_2O_2 content is shown in Figure 3-11. It is suggested that for the specimen with the same material mix proportions, thermal conductivity is inversely proportional to porosity. In both cases, a linear relationship is observed.

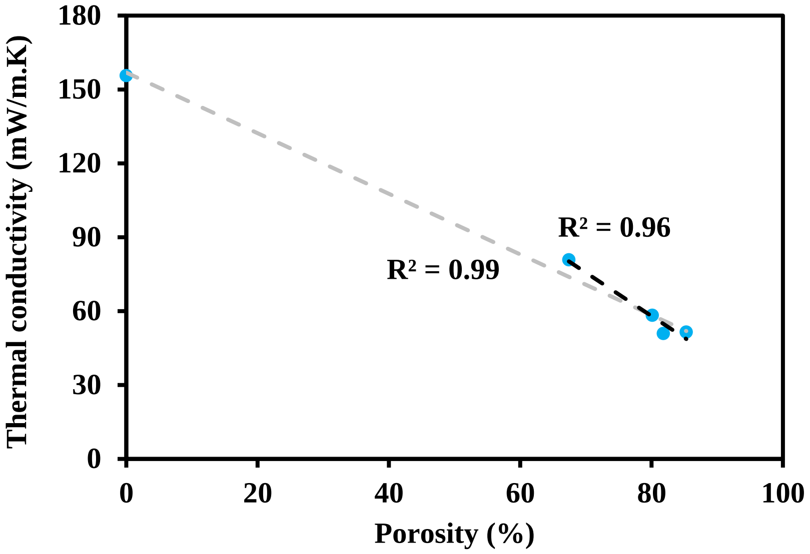

Figure 3-11 Porosity and thermal conductivity relationship of geopolymer with various H_2O_2 content

3.2.4. Effect of H_2O_2 content on volume expansion

Figure 3-12 and Figure 3-13 (a) show the volume expansion of slurry with various H_2O_2 content at room temperature (23°C). It can be seen that the volume is expanded gradually and reaches a constant level after 35 minutes. As the amount of H_2O_2 increases from 2% to 6%, the volume expands significantly from 125% to 220%, whereas further addition of H_2O_2 has no obvious impact on the volume expansion. There are two competing mechanisms during the volume expansion process: one is the expansion due to trapped bubbles; the other is escaped bubbles. The former is responsible for expansion, and the latter reduces the amount of theoretical expansion if all bubbles were to be trapped. As the amount of H_2O_2 increases from 2% to 6%, more oxygen is generated via the decomposition process of H_2O_2, and the bubble of O_2 is trapped within the paste, expanding and generating void (macropores). At this point, the number of trapped bubbles is greater than the escaped bubbles. However, as the amount of H_2O_2 increase further, the bubble generation rate becomes faster. The bubble shell's strength is not strong enough to hold the void, resulting in more bubbles are escaped. As a result, the number of trapped bubbles is equal to or less than the escaped bubbles. Thus, the further addition of H_2O_2 has no obvious impact on the volume expansion.

Figure 3-13 (b) and Figure 3-14 show the volume expansion of slurry with various H_2O_2 content at elevated temperatures (60°C). The volume is expanded almost linearly for all H_2O_2 content initially. The slope gets larger as the amount of H_2O_2 increases from 2% to 6%. The volume expansion increases remarkably from 180% to 450%, whereas further addition of H_2O_2 has no impact on the volume expansion. The volume expansion then gradually levels off after

10 minutes except for the specimen with 8% H_2O_2 content. The volume starts to shrink due to the excessive amount of foaming agent is introduced, and the bubble generation rate becomes faster. The elevated temperature stimulates the deposition rate of H_2O_2, and the air bubbles merge to form a large void [289]. Thus, the volume expansion at the elevated temperature is higher, as shown in Figure 3-15. However, the bubble shell's strength is not strong enough to hold the immense void, and therefore the specimen is collapsed [290]. This reduces the volume expansion for the sample with 8% H_2O_2.

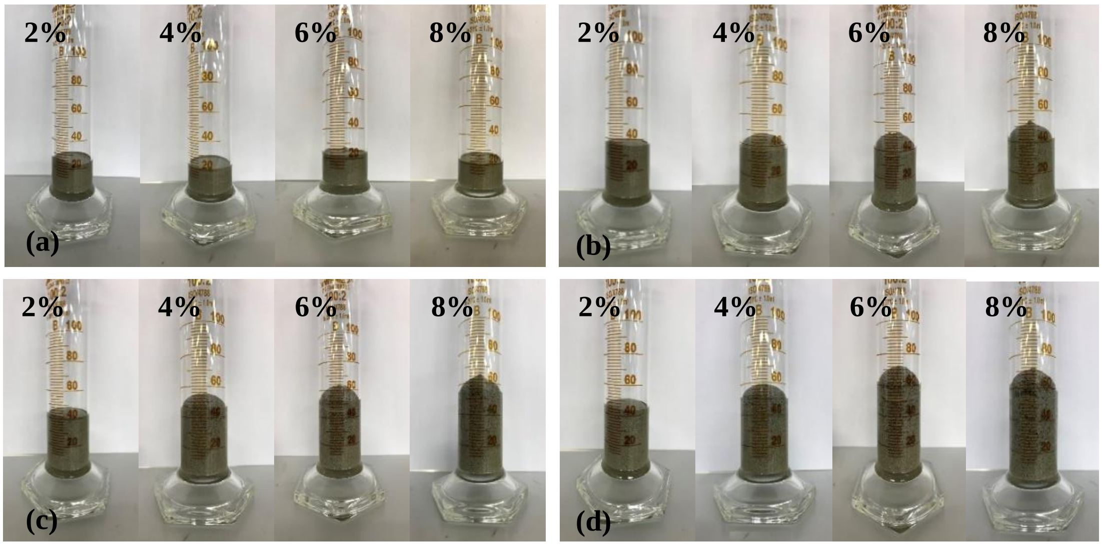

Figure 3-12 Photos of volume expansion of geopolymer slurry with the different amounts of H_2O_2 content (2%, 4%, 6%, and 8%) at (a) initial stage, (b) after 10 minutes, (c) after 20 minutes and (d) after 30 minutes under room environment (23°C)

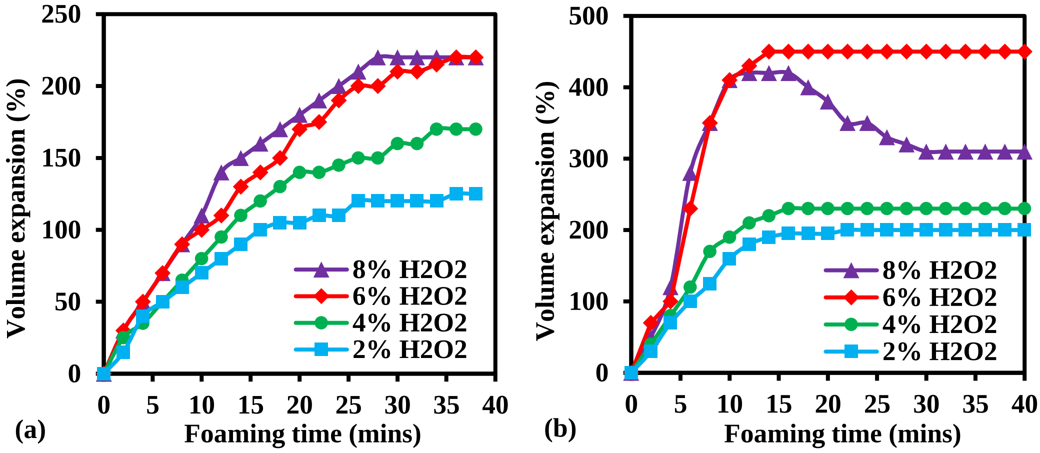

Figure 3-13 Volume expansion result of geopolymer slurry with different amounts of H_2O_2 at (a) room temperature (23°C) and (b) 60°C

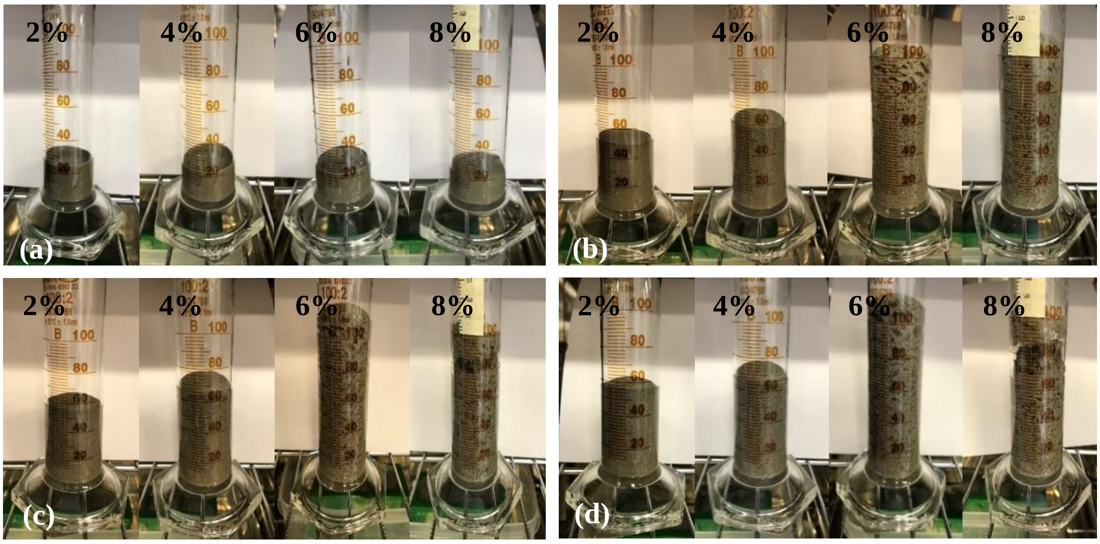

Figure 3-14 Photos of volume expansion of geopolymer slurry with different amounts of H_2O_2 content (2%, 4%, 6%, and 8%) at (a) initial stage, (b) after 10 minutes, (c) after 20 minutes, and (d) after 30 minutes at 60°C

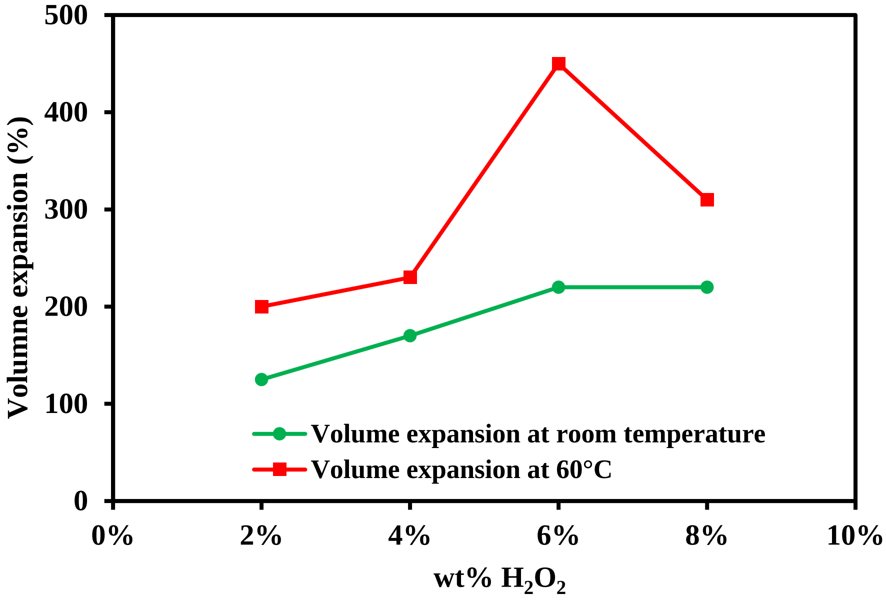

Figure 3-15 Volume expansion comparison of geopolymer slurry with different amounts of H_2O_2 at room temperature (23°C) and at 60°C

3.2.5. Effect of H_2O_2 content on the water absorption rate

The water absorption by mass of geopolymer at different H_2O_2 ranges is shown in Figure 3-16. It can be seen from Figure 3-16 that the amount of H_2O_2 significantly influences the water uptake by the geopolymer. As H_2O_2 content increases from 0% to 2%, the water absorption by mass rises substantially from 37% to 150% of its own mass. This is attributed to the porous structure, and water is filled into the surface pores. It is worth mentioning that a 37% water uptake is observed for the specimen with 0% H_2O_2, and this may be due to the water diffusion into the geopolymer. Once water diffuses into the materials, it is possible to get into 'close' pores, which may have many small cracks. Even if there are not many cracks presented, the water can also diffuse into the pores through pore-pore walls. As the H_2O_2 content increases further to 6%, the water absorption by mass continues to rise to 300% of its own mass. This is because the porosity and pore sizes increase with the addition of H_2O_2, resulting in more water being absorbed. However, when the H_2O_2 content increases to 8%, the water absorption drops. This is because of the reduced porosity as shown in Figure 3-9 and larger pores due to collapsing of pore walls. The water absorption is less because large pores cannot hold pore-filled water due to large gravitational force.

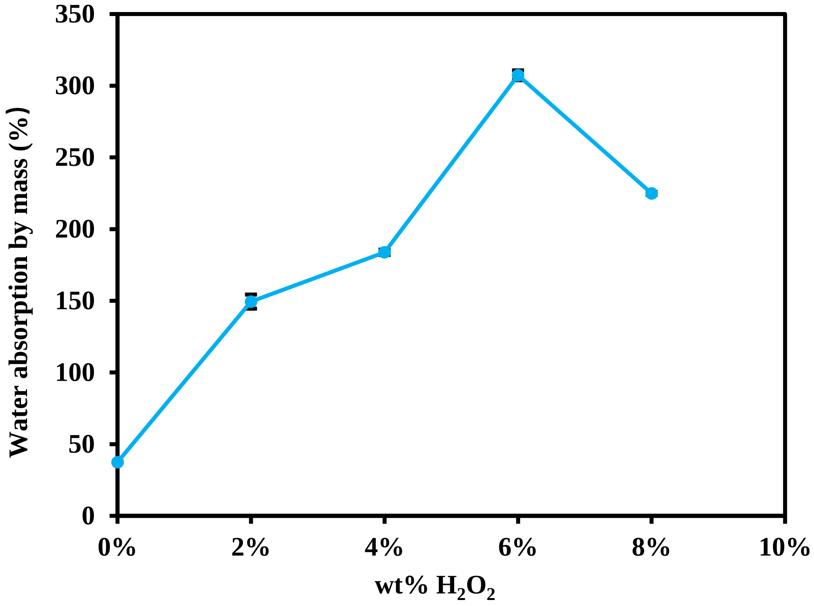

Figure 3-16 Effect of H_2O_2 content on water absorption by the mass percentage of geopolymer

3.2.6. FTIR analysis

The FTIR spectra analysis was used to identify the chemical composition of the inorganic bonds present in the Si- glassy or crystalline phases of fly ash within a geopolymer [74]. Figure 3-17 shows the FTIR spectra of geopolymer with various H_2O_2 content. The broad bands located at approximately 3340 cm^{-1} and 1650-1600 cm^{-1} represent O-H stretching and O-H bending, respectively. These peaks tend to weaken with the addition of H_2O_2 content, and this could attribute to the unreacted alkaline activator presented within the geopolymer. The porosity and pore sizes increase with the addition of H_2O_2, resulting in water to be evaporated more easily. The distinct band near 1000 cm^{-1} is ascribed to Si-O-Al asymmetrical vibration [291]. The Si-O-Si stretching vibration is detected at the wavenumber range of 1300-950 cm^{-}

[1] [292]. The Si-O-Si stretching vibration is more prominent than the O-Si-O bending mode. Therefore, it is logical to use the Si-O-Si to indicate the degree of geopolymerization [293, 294]. The band near 1400 cm^{-1} is related to sodium carbonate via alkali metal hydroxide reaction with atmospheric CO_2 [38].

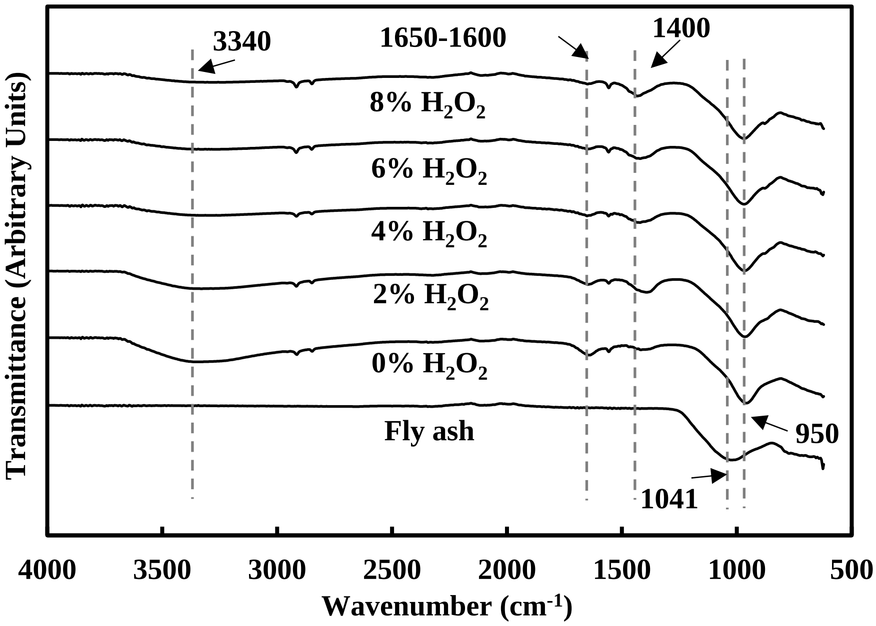

Figure 3-17 FTIR spectra of fly ash and geopolymer with different H_2O_2 content

In addition, the spectrum of fly ash shows broadband in the range of 900-1200 cm^{-1}, which is attributed to the heterogeneous characteristic of fly ash. It is formed by a mixture of the glassy surface layer (SiO_2) and crystalline matrix components such as mullite and quartz [295, 296]. Thus, the resulting band is a broad range of the overlapping peaks with a centre at approximately 1041 cm^{-1}, assigned to the asymmetric stretching vibration of Si-O-T (T = Si or Al) bonds of SiO_4 or AlO_4 tetrahedra. It is worth mentioning that the Si-O-T (T = Si or Al) band position is shifted to lower wavenumbers (950 cm^{-1}) upon polymerization, which indicates a chemical change in the matrix. This shift showed the incorporation of Al into Si-O-Si non-bridging oxygen in the silicon tetrahedral [295, 297]. This confirms the independence of strength development on inherent polymerization [74].

3.2.7. Effect of H_2O_2 content on compressive property

Figure 3-18 shows the 7-day compressive strength of geopolymers with various H_2O_2 content. It can be seen that the involvement of the foaming agent is one of the critical factors affecting the mechanical performance of the samples. When the foaming agent is introduced (2%), the compressive strength decreases significantly from 2.36 to 0.25 MPa, with almost 90% of strength loss due to the porous structure. As the foaming agent's amount increases further to 8%, the compressive strength drops to 0.01 MPa.

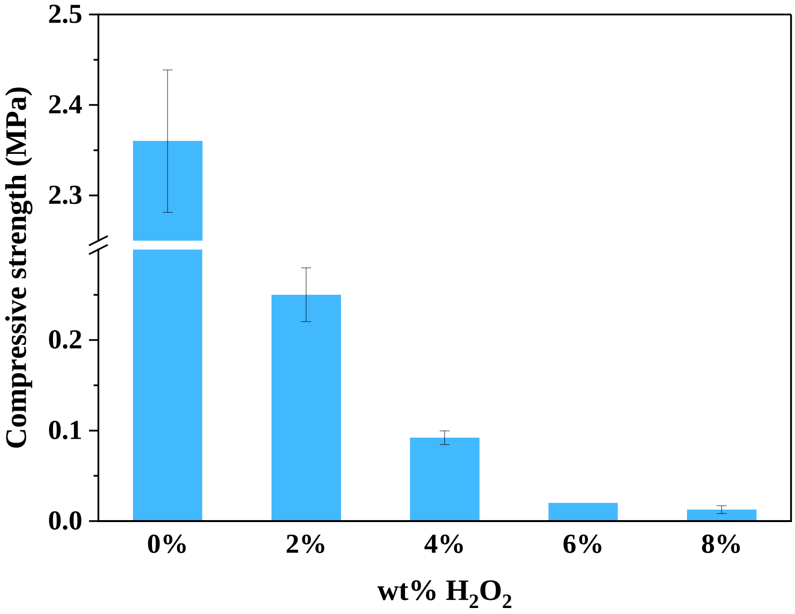

Figure 3-18 Effect of H_2O_2 content on the compressive strength of geopolymer

Figure 3-19 shows the compressive strain at failure and modulus of geopolymers with various H_2O_2 content, and the stress-strain behaviour of geopolymer with various H_2O_2 content is plotted in Figure 3-20. The geopolymer with 0% H_2O_2 content shows a failure strain of 0.002 at the maximum load (2.36 MPa). As the H_2O_2 content increases from 0% to 2%, the failure strain reduced significantly to 0.0012 at the maximum load (0.25 MPa). The failure strain then rises to a similar strain magnitude compared to the geopolymer with 0% H_2O_2 as the H_2O_2 content increases to 4%. As the H_2O_2 content of geopolymer increases further, the strain at the maximum load then fluctuates around 0.002. This suggests that 2% H_2O_2 content is a threshold in terms of the failure strain. Figure 3-19 also shows Young's modulus of geopolymer with various H_2O_2 content. The effect of H_2O_2 content on Young's modulus presents a similar pattern as the compressive strength of geopolymer, as shown in Figure 3-18. When the foaming agent is introduced (2%), Young's modulus decreases significantly from 191 to 34 MPa. As the H_2O_2 content increases from 2% to 8%, the decrease in Young's modulus exhibits an almost linear relationship. The reduction of Young's modulus with increasing H_2O_2 content shows that the resistance to deformation at a given pressure load is decreased.

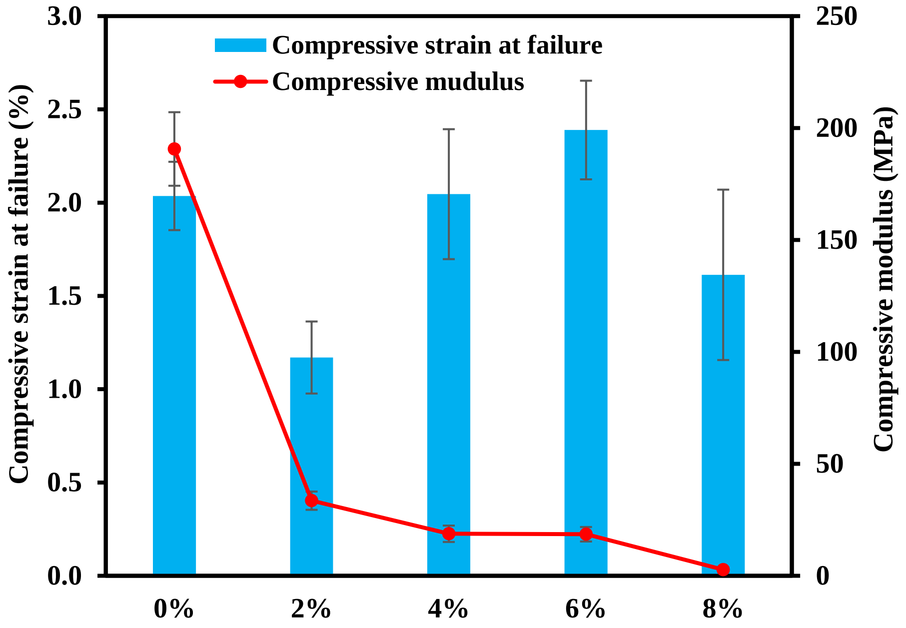

Figure 3-19 Effect of H_2O_2 content on the compressive failure strain and modulus of geopolymer

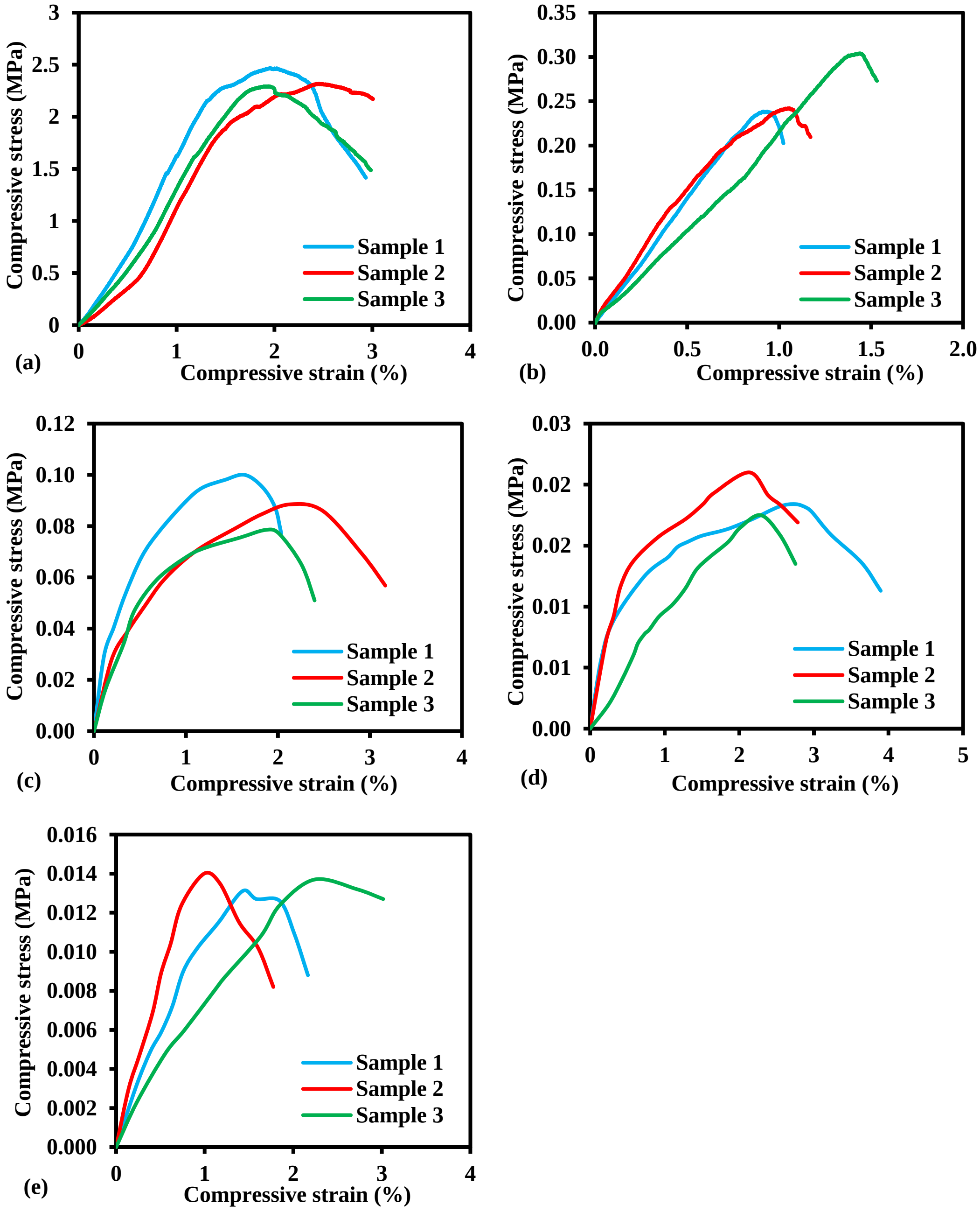

Figure 3-20 Stress-strain curve of geopolymer with (a) 0%, (b) 2%, (c) 4%, (d) 6% and (e) 8% H_2O_2 respectively

The thermal-mechanical relationship of geopolymer is presented in Figure 3-21. It is shown that geopolymer's compressive strength increases almost linearly as geopolymer's thermal conductivity increases. Thus, there should be a trade-off between thermal and mechanical performance, depending on the requirement. There are no specific strength requirements for insulating concrete in ASTM C332, although the thermal conductivity is far below the maximum limit (1.5 W/m.K). By referencing ASTM C869 (standard specification for foaming agents used in making preformed foam for cellular concrete), the minimum compressive strength for cellular concrete made with preformed foam is 1.4 MPa, whereas the thermal requirement is not mentioned. Therefore, the mechanical properties of the specimens still need to be improved.

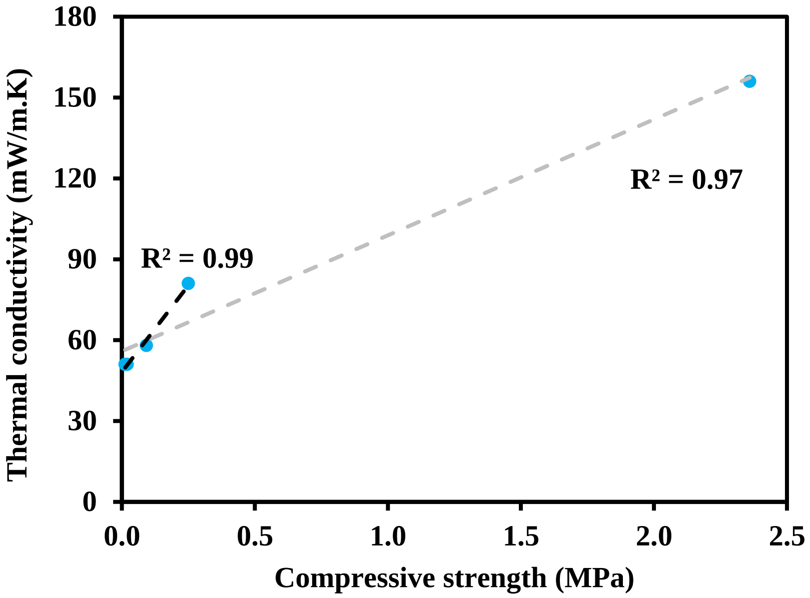

Figure 3-21 Thermal conductivity versus compressive strength of geopolymer with different amounts of H_2O_2 (0%, 2%, 4%, 6%, and 8%)

3.3. Conclusion

In this chapter, the foamed geopolymer was successfully synthesised by varying foaming agent content. Properties such as density, porosity, thermal conductivity, water absorption rate, and compressive strength were investigated. The effect of foaming agent amount on the foam expansion rate was also examined, and the foam expansion mechanism was discussed.

The foaming agent proved to be a critical factor influencing the pore structure, thus, the density, thermal conductivity and the compressive strength of the geopolymer. The calculated porosity reached 83% when the H_2O_2 content was 8%. As the foaming agent content increased from 0% to 8%, the density reduced by 85% to 171 kg/m^3. The effect of H_2O_2 content on thermal conductivity had a similar trend as the density. The lowest thermal conductivity value obtained in this work was 51 mW/m.K at H_2O_2 content of 8%, and a reduction of 67% was obtained when compared to the sample without any foaming agent. The thermal conductivity value is superior to most of the foamed concrete reported. This finding suggests that geopolymer can be an ideal substitute for foamed concrete since it is more economical and environmentally friendly with superior thermal insulation performance compared to foamed concrete.

The volume expansion test indicates two competing mechanisms: one is the expansion due to trapped bubbles; the other is escaped bubbles. As the amount of H_2O_2 increased, more oxygen was generated via the decomposition process of H_2O_2, and the bubble of O_2 was trapped within the paste, expanding and generating void (macropores). At this point, the number of trapped bubbles was greater than the escaped bubbles. However, as the amount of H_2O_2 increased further, the bubble generation rate became faster. The bubble shell's strength was not strong enough to hold the void, resulting in more bubbles were escaped. As a result, the number of trapped bubbles was equal to or less than the escaped bubbles. Thus, the further addition of H_2O_2 had no obvious impact on the volume expansion. The elevated temperature stimulated the deposition rate of H_2O_2, and the air bubbles merged to form a large void. Thus, the volume expansion at the elevated temperature was higher. This finding could be used to indicate how different pore structures are obtained by varying the foaming agent.

4. Fabrication and characterisation of silica aerogel with an improved fabrication process

Apart from porous geopolymer, silica aerogel also shows great potential in thermal insulation application due to its highly porous structure. It gives unique properties such as high specific surface area (500-1500 m^2/g), high porosity (80-99%), low bulk density (0.03-0.35 g/cm^3) [26], extremely low thermal conductivity (12-30 mW/m.K) [22], high acoustic resistance and strong adsorption [22]. The involvement of aerogel in buildings or any other sector could be an energy-efficient strategy leading to lower energy consumption. Therefore, it is worth studying the synthesizing mechanism as well as the characterisation of the materials.

Silica aerogel and its fabrication process have been investigated extensively [27]. The general fabrication process involves sol-gel, ageing, solvent exchange and drying [27]. However, some detailed descriptions of the fabrication process are not commonly mentioned, for example, the amount of solvent used for ageing and solvent exchange. It has a nonnegligible impact in terms of cost-saving, especially in the UK. The cost for one litre of Ethanol and n-Hexane is approximately £50 and £40, respectively. Therefore, adequate usage of these solvents could lower the fabricating cost. In addition, the fabrication processes, including ageing temperature and drying process, could be optimised to improve the properties of the aerogel.

In this chapter, the feasibility of synthesizing silica aerogel is evaluated using a more economical sodium silicate as the precursor. The effect of ageing and solvent exchanging temperature on the pore structure of aerogel are examined. The minimum amount of solvent used to synthesise aerogel is investigated. Properties including morphology, pore structure, bulk density, BET surface area, hydrophobicity, thermal stability and thermal conductivity are examined as the critical parameters for characterising the prepared specimens.

4.1. Experimental

In this section, the materials used to synthesise silica aerogel are listed. The preparation process and the characterisation method are described.

4.1.1. Materials

The precursor used to synthesise aerogel was sodium silicate (34.6 wt%, VWR UK, Na_2O: $SiO_2 \approx 3.43$). Other agents, including HCl (37%), ammonia solution (NH_4OH, 28%), ethanol

(EtOH), n-Hexane (95%) and Chlorotrimethylsilane (TMCS $\geq$ 98% GC), were purchased from VWR UK. Deionised water was supplied by the lab.

4.1.2. Sample preparation

Figure 4-1 illustrates the schematic diagram for the preparation of silica aerogel. Sodium silicate was diluted with deionised water with a 1:3 volume ratio. Hydrolysis of the diluted sodium silicate solution was carried out by adding 6M HCl while stirring, which formed silicic acid sol with a pH of ~2.0. The hydrogel was prepared by adding 2M NH_4OH while stirring to reach a pH of ~5.0. The silica sol was poured into a glass container with a screw lid. Gelation occurred within 10 minutes, and a porous network was formed. EtOH was used for ageing with a 2:1 volume ratio to the gel, and the ageing process was conducted at 45°C for 24 hours. EtOH was replaced by n-Hexane twice in 32 hours at 45°C. The surface modification was carried out by adding the silylating mixture of TMCS: n-Hexane in the volume ratio of 1:4 for 24 hours at 45°C. Then the silylated gel was dried in ambient pressure at 50°C, 80°C, 100°C, and 120°C for 6 hours respectively to obtain hydrophobic silica aerogels. The fabrication process of the silica aerogel is shown in Figure 4-2.

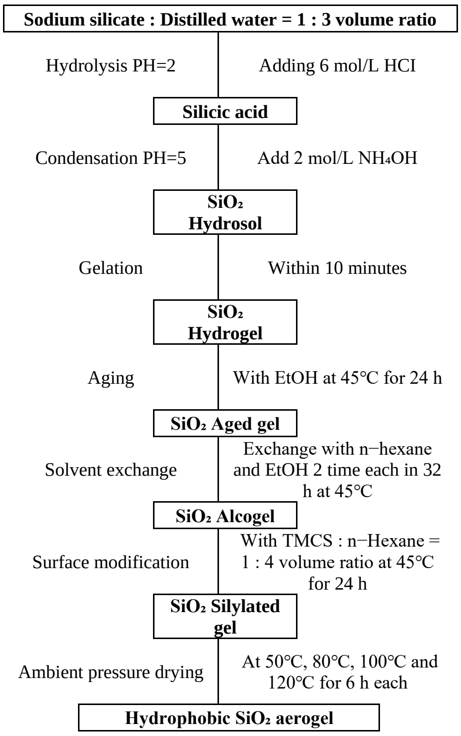

Figure 4-1 Schematic diagram for the preparation of silica aerogel

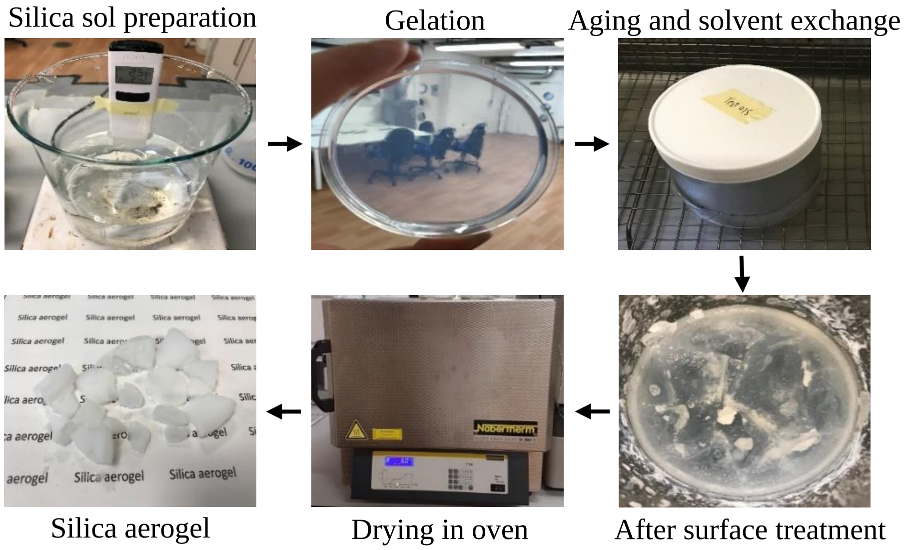

Figure 4-2 Fabrication process of silica aerogel

4.1.3. Sample characterisation

4.1.3.1. Density and porosity

The bulk density of aerogel was calculated using the measured volume of the samples by a calliper and their mass by an electronic balance with an accuracy of ±0.01 g. The aerogel was pre-shaped before the measurement. An average of five measurements was conducted with errors showing a 95% confidence limit.

The porosity of the aerogel was calculated as follow:

$$\varphi_i = \left(1 - \frac{\rho_a}{\rho_s}\right) \times 100\% \qquad \text{(Equation 4-1)}$$

where φ_i is the porosity, ρ_a is the bulk density of aerogel, and ρ_s is the skeleton density of the silica aerogel, generally $\rho_s = 2.2\ \mathrm{g/cm^3}$ [298].

4.1.3.2. SEM imaging

The morphology of aerogel was investigated by Field Emission Scanning Electron Microscope (FE-SEM, HITACHI SU6600) with a voltage of 15 kV (Figure 4-3 (a)). The samples were gold coated using an AGAR sputter coater before analysing (Figure 4-3 (b)).

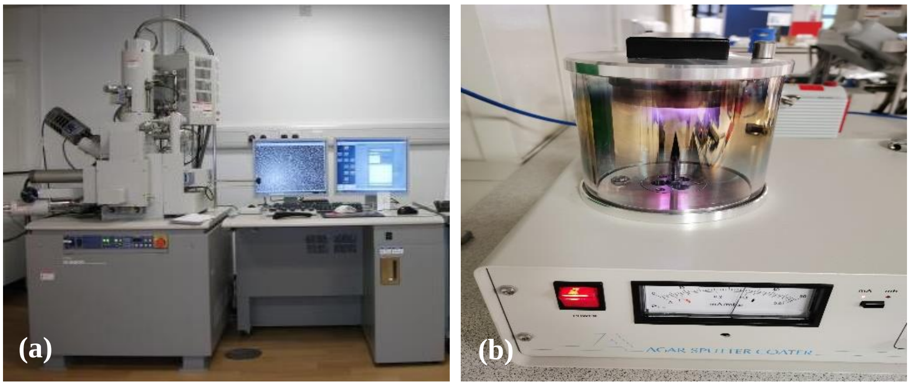

Figure 4-3 (a) Field Emission Scanning Electron Microscope (FE-SEM, HITACHI SU6600), (b) AGAR sputter coater

4.1.3.3. Gas adsorption

Gas adsorption measurements were conducted using a Micromeritics ASAP2420 Surface Area and Porosity Analyser (Figure 4-4). Surface area, pore volume and average pore size were determined via analysis of the cryogenic nitrogen adsorption/desorption isotherm. Approximately 0.1 g of sample was subject to a degas cycle of 30 min at 50°C, followed by 120 min at 110°C, at a pressure of 10 mHg. This process removed any residual solvent or surface contaminants from the samples. Degased samples subsequently underwent a 40 point adsorption cycle between the relative pressures (sample pressure/saturation vapour pressure) of 0.01 and 1, followed by a 30 point desorption cycle between the relative pressures of 1 and 0.1. Sample temperature was maintained at a constant value of -196°C throughout the experiment using a liquid nitrogen bath.

Figure 4-4 Micromeritics ASAP 2420 Surface Area and Porosity Analyser

4.1.3.4. Hydrophobicity test

Contact angle measurements were obtained using Kruss DSA30 (Hamburg, Germany) and HPLC grade water (Merk, Switzerland), as shown in Figure 4-5. The data were analysed in Advance software (Kruss, Germany) using manual fitting of a baseline and shape of the water drop. An average contact angle was calculated based on seven measurements of each sample.

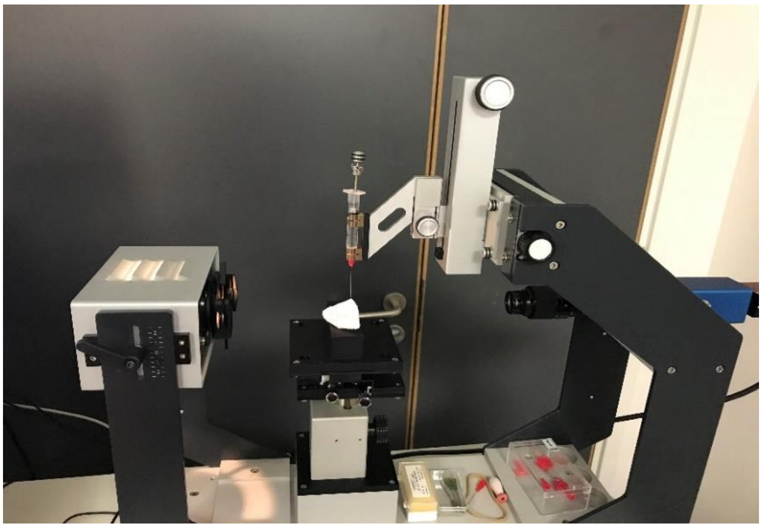

Figure 4-5 Kruss DSA30 (Hamburg, Germany)

4.1.3.5. FT-IR analysis

The chemical environments of molecular bonds of the aerogel were determined via Fourier transform infrared analysis (Agilent Technologies 4100 Exo Scan), as shown in Figure 4-6 (a). The spectral range was set from 4000 to 650 cm^{-1} as there is considerable spectral noise outside this range. A diamond ATR (attenuated total internal reflectance) was used as the diffuse reflectance interface. The aerogel samples were crushed and ground into powders for the FTIR test. The analysis involved the application of pressure to the samples with a clamp to allow full contact with the diamond ATR crystal, as shown in Figure 4-6 (b). A minimum of 10 specimens was tested, and the raw data generated were analysed using OriginLab.

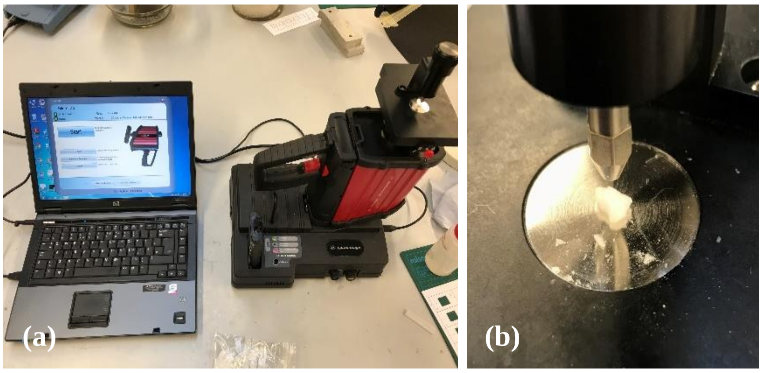

Figure 4-6 (a) Agilent Technologies 4100 Exo Scan (b) detailed view of the sample

4.1.3.6. Thermal gravimetric analysis

Thermal stability, which refers to the temperature up to which the aerogel retains its hydrophobicity, was tested by thermal gravimetric analysis (TGA, TA Instruments Q50), according to ASTM E2550. This is shown in Figure 4-7. The sample was heat-treated in the air from 20°C up to 800°C with a rate of 10°C.min^{-1}.

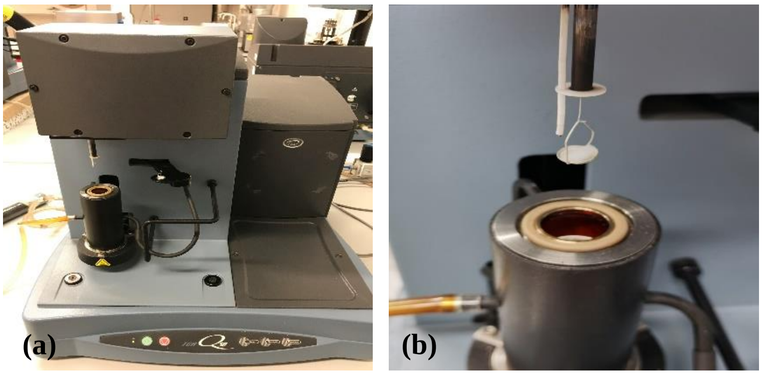

Figure 4-7 (a) TGA, TA Instruments Q50 (b) aerogel sample loading

4.1.3.7. Thermal conductivity

The XIATECH TC3000E was used to measure the thermal conductivity of the aerogel, according to ASTM 1113-2019. It is a transient hot-wire method based on the non-steady-state principle. The hot wire sensor was sandwiched by two layers of samples. The aerogel powder was ground and sieved using a 1250 um mesh, and the aerogel powder was then held in a special sample holder with a dimension of 5 cm × 5 cm ×1 cm, as shown in Figure 4-8. Two batches of aerogels with the same parameters are needed to fill the sample holder. The change of pore structure caused by grinding is not considered here. A Pyrex glass was put on the samples to minimise the airflow around the aerogel samples. Before testing, the device was calibrated by a standard PMMA glass. This was implemented by referencing the standard inspection report of the PMMA glass provided by the equipment manufacturer, ensuring the measurement error was within ±3% of the standard values.

Figure 4-8 XIATECH TC3000E thermal conductivity meter

4.2. Results and discussion

In this section, the effect of ageing and solvent exchanging temperature on the pore structure of aerogel are examined. The minimum amount of solvent used to synthesise aerogel is investigated. Properties including morphology, pore structure, bulk density, BET surface area, hydrophobicity, thermal stability and thermal conductivity of the silica aerogel are examined.

4.2.1.1. Morphology and physical properties

The solvent to gel (amount of sodium silicate, HCl and NH_4OH) volume ratio was first investigated to reduce the amount of expensive solvent (EtOH and n-Hexane) being used. Two factors are used to judge if the materials are synthesised successfully before conducting proper characterisation: the appearance (colour of aerogel) and hydrophobicity. The hydrophobicity was tested by dropping a water droplet on the material surface, and the water droplet will float on the material surface if the aerogel is prepared successfully. Figure 4-9 shows the morphology of aerogel prepared with solvent to gel volume ratio of 1:1, 1.5:1, and 2:1. It can be seen that the aerogel is fabricated successfully when the ratio of solvent to gel is 2:1. When the amount of solvent is less efficient (i.e., 1:1 and 1.5:1), the water inside the gel may not be replaced by the solvent completely. As mentioned in the literature, the key mechanism of ageing and solvent exchange is to minimise the capillary pressure during the drying process. It is shown that the surface tension of most solvents is only a third of that in water, which means that the capillary pressure could be reduced by three times if the water is replaced by those solvents completely during drying [27], according to Equation 2-5. Thus, powder form or small piece is fabricated if water is not replaced by the solvent completely. In addition, hydrophilization agents are insoluble in water, and drying of these mixtures (agent and water) could have a negative impact on the final product. This may be the reason for the yellowish crystalized product being formed. The hydrophobicity test also failed for the sample prepared with less solvent to gel ratios (i.e., 1:1, 1.5:1). Thus, the hydrophobization process is not successful. Therefore, a solvent to gel volume ratio of 2:1 is selected for future sample preparation.

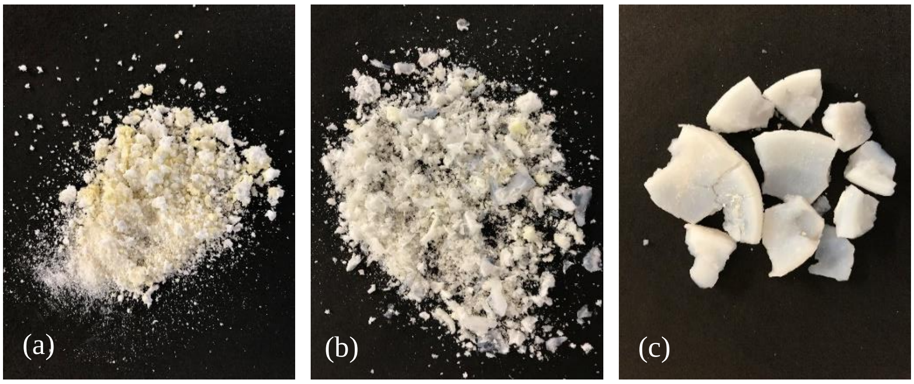

Figure 4-9 The morphology of aerogel prepared with solvent: gel (amount of sodium silicate, HCI, and NH_4OH) volume ratio (a) 1:1, (b)1.5:1, and (c) 2:1

To investigate the influence of ageing temperature on the pore structure of the silica aerogels, the ageing and solvent exchange process of silica gel were conducted at both ambient temperature (23°C) and 45°C. The ageing process was conducted in EtOH for 24 hours, and EtOH was replaced by n-Hexane twice in 32 hours for both cases. The physical properties of both samples are summarised in Table 4-1.

Table 4-1 Physical properties of silica aerogel aged and solvent-exchanged in both room temperature (23℃) and 45℃

Sample	Density (g/cm^3)	Porosity (%)	BET surface area (m^2/g)	Pore volume (cm^3g^{-1})	Pore size (nm)
At 23℃	0.198±0.008	91	461	1.43	13.3
At 45℃	0.184±0.018	91.6	726±3.5	2.78	12.1

It is found that aerogel aged and solvent-exchanged at higher temperatures leads to a lower apparent density, higher specific surface area and pore volume, and finer average pore diameter. This may be because that solvent-exchanging at a higher temperature increases the solvent diffusivity according to the theory of diffusion in gel, resulting in a higher coarsening of the gel network [205]. This promotes the dissolution and reprecipitation of the silica gel

[299]. The further hydrolysis and condensation of unhydrolyzed groups and the esterification of silanols occur as well [299]. In addition, aerogel aged and solvent-exchanged at higher temperatures is more homogeneous and bulk in size, as shown in Figure 4-10. It means that shrinkage of the wet gel during the dry process was reduced when the gel was aged and solvent-exchanged at higher temperatures. This leads to high skeletal strength, high specific surface area and pore volume. The effect of heat-treatment ascribed as the Ostwald ripening process is very similar to the one observed for silica aerogels derived from supercritical drying except using the methanol at T > 240℃ [299]. The silica gel is heated up to a temperature above the critical point, enhancing the backbone strength and reducing the collapse or cracking of silica aerogel during the drying process [299]. Furthermore, increasing the ageing and solvent-exchanging temperature shortens the fabrication time while improving silica aerogels' properties [299].

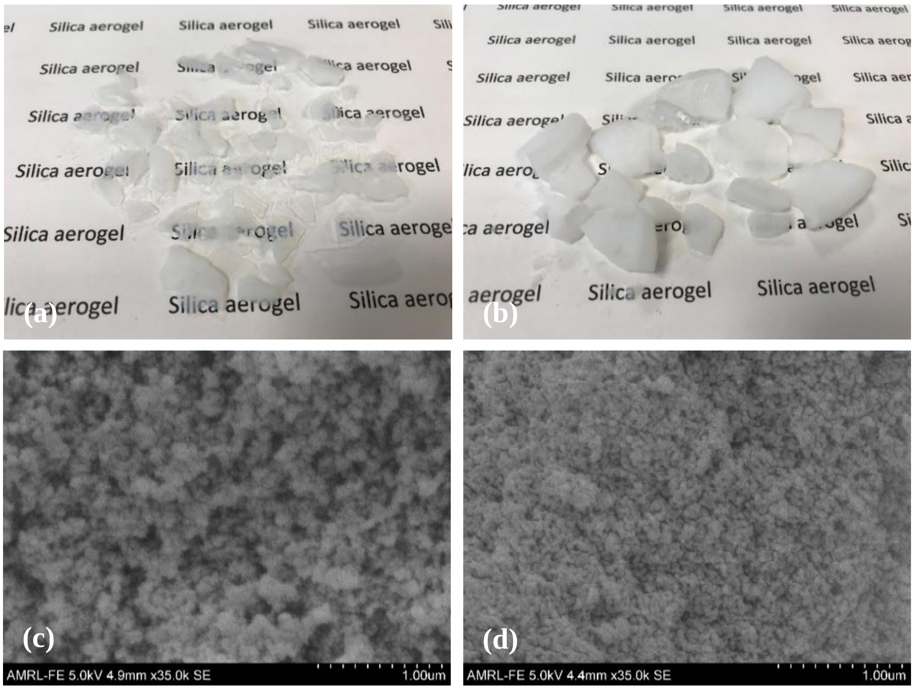

Figure 4-10 the photo and the microstructure of silica aerogel aged and solvent-exchanged at (a) (c) 23℃ and (b) (d) 45℃

Figure 4-10 (c) and (d) display a highly branched polymeric structure of silica aerogel regardless of the influence of ageing and solvent-exchange temperature. However, it can be visualised that larger pores were formed for the aerogel aged and solvent-exchanged at ambient temperature (Figure 4-10 (c), whereas the pores are finer and more uniformly distributed for the ones aged at 45℃ (Figure 4-10 (d)). As a result, higher surface area and pore volume are obtained when aerogel is aged and solvent-exchanged at a higher temperature.

The pore size distribution (PSD) of the samples aged and solvent-exchanged at both ambient (23°C) and 45°C is shown in Figure 4-11 (a). It can be seen that the silica aerogels exhibited meso- and macro-pore size region (2-40 nm) and centred at 12-18.3 nm and 18 nm, corresponding BJH mean pore diameter of 12.1 nm and 13.3 nm, respectively, as shown in Table 4-1. Figure 4-11 (b) shows the N_2 adsorption-desorption isotherm of the silica aerogel aged and solvent exchanged at both ambient and 45°C. It presents a type IV(a) isotherm with a H3 hysteresis loop at $P/P_0 > 0.6$ [300], revealing the mesoporous characteristics of the aerogel. The sharp increase of isotherms in the high relative pressure region ($P/P_0 = 0.95\text{-}1.0$) is due to the liquid condensation suggesting the presence of macropores [191].

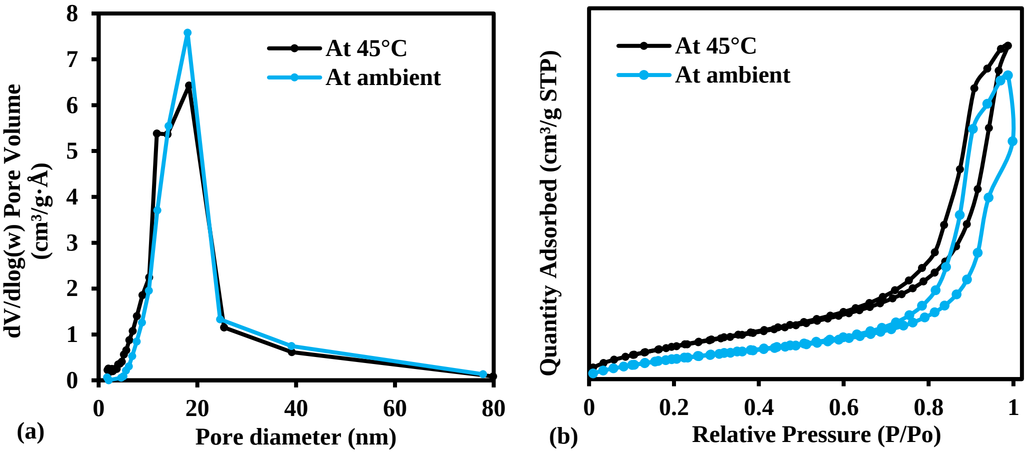

Figure 4-11 (a) Pore size distribution (PSD) and (b) N_2 adsorption-desorption isotherms of aerogel aged and solvent-exchanged at ambient temperature (23°C) and 45°C

4.2.1.2. Hydrophobicity and FT-IR analysis

Figure 4-12 (a) and (b) show the photo and microscopic images of a water droplet on the treated surface of the silica aerogel, respectively. The average water contact angle for aerogel is 129.0 ± 12.9°. This excellent water-repellent property is a result of the treatment of the specimens with TMCS, where the stable methyl groups are responsible for the excellent hydrophobicity of the silica components [20].

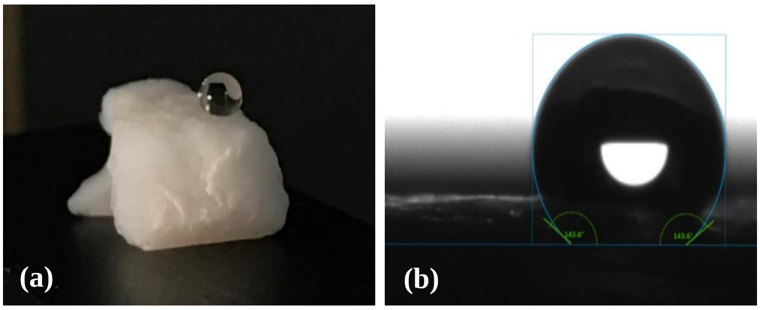

Figure 4-12 (a) Photo of a water droplet on the treated surface of silica aerogel and (b) microscopic image of water contact angle measurement of silica aerogel

The hydrophobicity of aerogel is attributed to the attachment of $-Si(CH_3)_3$ group to the gel surface, which can also be confirmed by the FTIR analysis. Figure 4-13 shows the FTIR spectrum of TMCS-treated silica aerogel. It can be seen that apart from the Si-O-Si (absorption peak at about 755 cm^{-1} and 1050 cm^{-1}), the surface-treated aerogel shows strong absorption peaks at about 850 cm^{-1}, 1260 cm^{-1} and 2980 cm^{-1}, corresponding to $Si\text{-}CH_3$ groups and $-CH_3$ groups [26, 191]. The presence of these absorption peaks confirms the attachment of $-Si\text{-}CH_3$ groups from the TMCS to the silica aerogel surface, indicating that the surface modification process is successful. Moreover, the bonds at ~3450 and ~1650 representing -OH groups disappear after surface modification. The amount of Si-OH groups reduces after the modification process, according to Equation 4-2, which leads to a weaker absorption intensity of -OH [26].

$$(CH_3)_3SiCl + \equiv Si\text{-}OH \rightarrow \equiv Si\text{-}O\text{-}Si(CH_3)_3 + HCl \qquad \text{(Equation 4-2)}$$

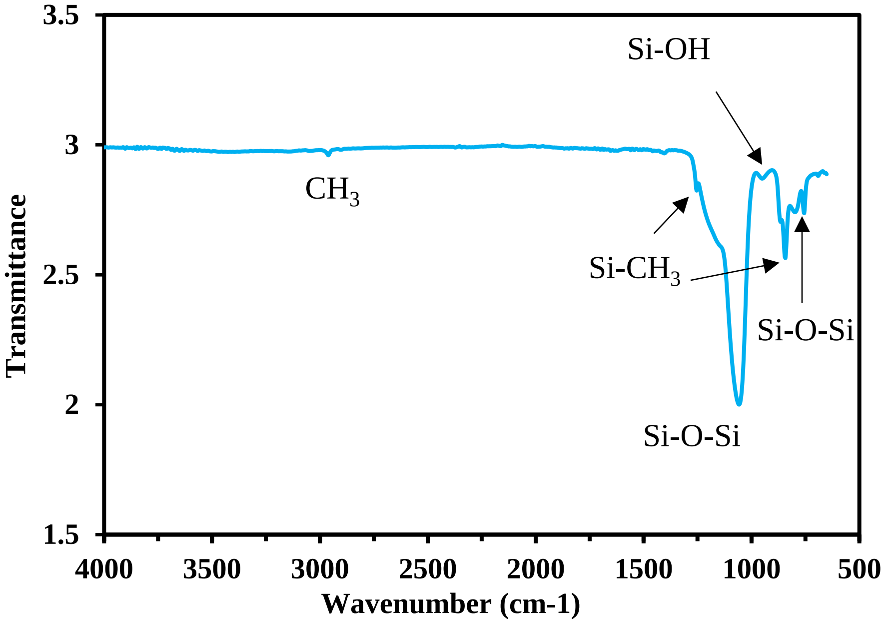

Figure 4-13 FTIR spectrum of TMCS-treated silica aerogel

4.2.1.3. Thermal conductivity

Figure 4-14 and Figure 4-15 show the morphology and thermal conductivity values of aerogel before and after grinding. It is seen that finer particle size leads to a lower thermal conductivity (25.1 mW/m.K), and this value is slightly below the thermal conductivity of the air (i.e., 26 mW/m.K) [301]. It is also worth mentioning that this value is comparable to the literature with similar precursors and drying processes (23.7 to 25.9 mW/m.K) [191, 302].

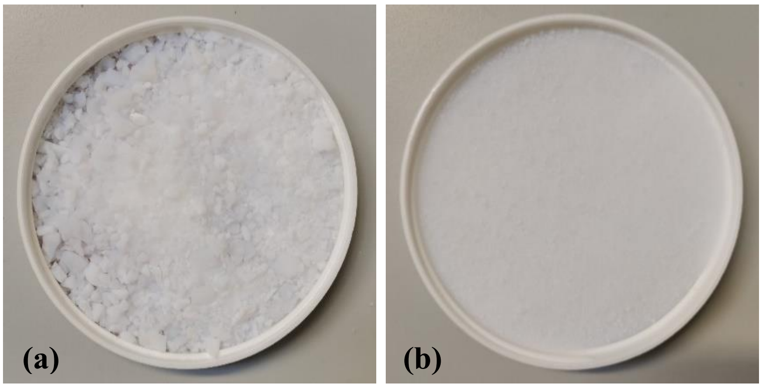

Figure 4-14 In-house silica aerogel (a) before and (b) after grinding

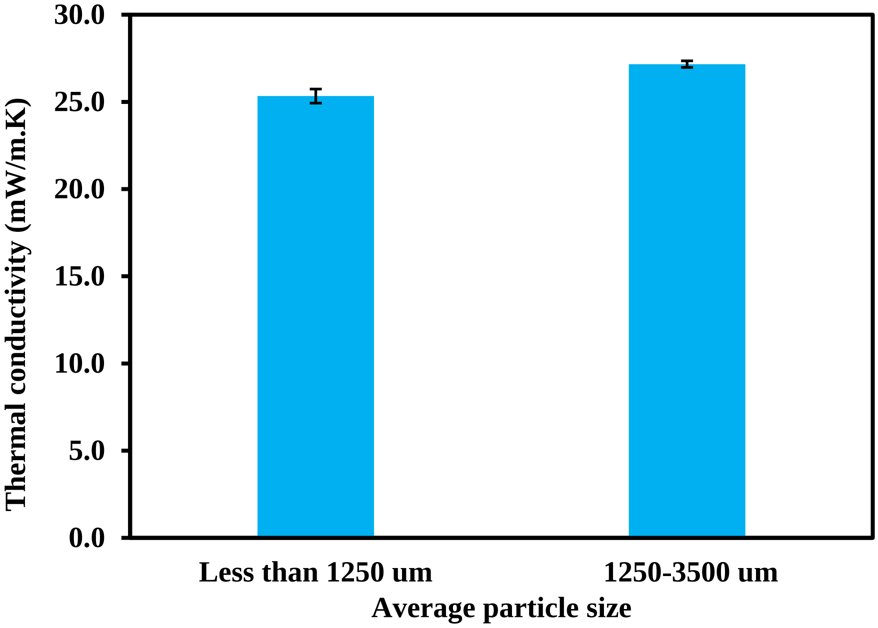

Figure 4-15 Thermal conductivity values of in-house aerogel before and after grinding

During the thermal conductivity measurement of aerogel particles, the air is one of the most significant factors influencing the aerogel’s effective thermal conductivity. Due to the irregular shape of the aerogel particles, the gap between aerogel particles increases with larger particle sizes. Therefore, the bulk density of aerogel particles is reduced [303]. Due to the nano-porous structure, the average pore size of monolithic neat silica aerogels is less than the mean free path, which restricts the free movement of air molecules within the backbone structure. Thus, the convection heat transfer within aerogel is negligible. The thermal conductivity of aerogel particles is a combination effect of air conductivity through gaps among aerogel particles and conductivity of aerogel, and this can be expressed as [304]:

$$\lambda = \frac{\lambda_s \lambda_a}{\lambda_s - (\lambda_a - \lambda_s)\frac{\rho_b}{\rho_s}} \qquad \text{(Equation 4-3)}$$

where λ is the effective thermal conductivity; λ_s is the solid conduction of aerogel; λ_a is the thermal conductivity of air; ρ_b is the bulk density of the aerogel particle, and ρ_s is the skeleton density of the aerogel.

By grinding the aerogel granules, the gap between aerogel particles improves, leading to a lower air conductivity. Thus, the effective thermal conductivity of aerogel decreases, as described in Equation 4-3.

The structure of nano-porous silica aerogels leads to a reduced heat transfer within the gaseous phase compared to the heat transfer within the free-moving gas [301]. Therefore, silica aerogels can achieve effective thermal conductivity values far below the thermal conductivity of the air (i.e., 0.026 W/m.K) at the ambient condition [301].

4.2.1.4. Thermal stability

The TGA curve under the air of the silica aerogel is presented in Figure 4-16. It is shown that a sharp decrease in the TGA curve is presented at a temperature of approximately 400°C due to the oxidisation of the $-CH_3$ group. A slight weight loss before 100°C is observed due to the evaporation of the residual solvent and water molecules [26]. Figure 4-17 displays the hydrophobic performance of surface-treated aerogel before and after the thermal gravimetric analysis. It clearly shows that the aerogel sample sinks into the water after the thermal gravimetric analysis (Figure 4-17 (b)), meaning that the aerogel becomes hydrophilic. This can also be verified using FTIR analysis.

Figure 4-18 shows the FTIR spectrum of TMCS-treated silica aerogel and after heat treatment (800°C). It can be seen that the strong absorption peaks at about 850 cm^{-1}, 1260 cm^{-1} and 2980 cm^{-1}, corresponding to $Si-CH_3$ groups and $-CH_3$ groups, disappeared after thermal treatment at high temperature due to pyrolysis. The heat-treated aerogel becomes hydrophilic; thus, it will absorb water which could diminish the thermal insulation performance.

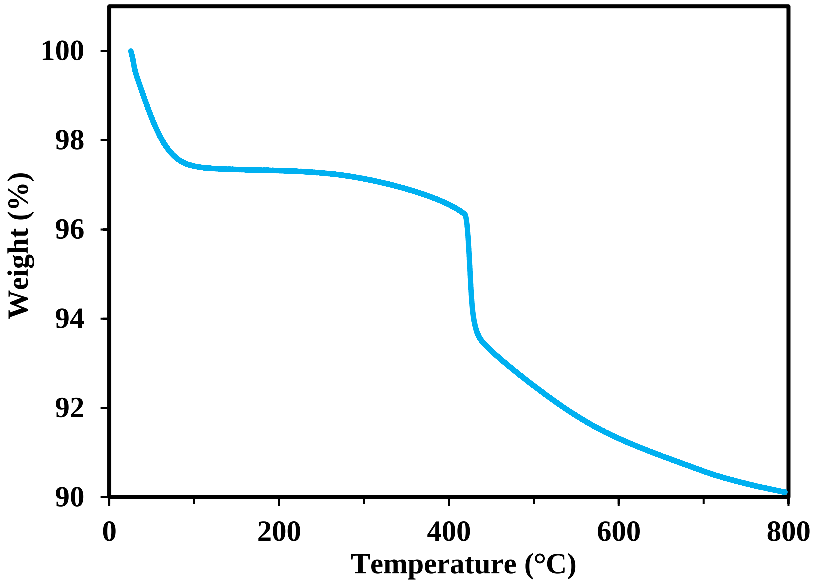

Figure 4-16 TGA curve of silica aerogel

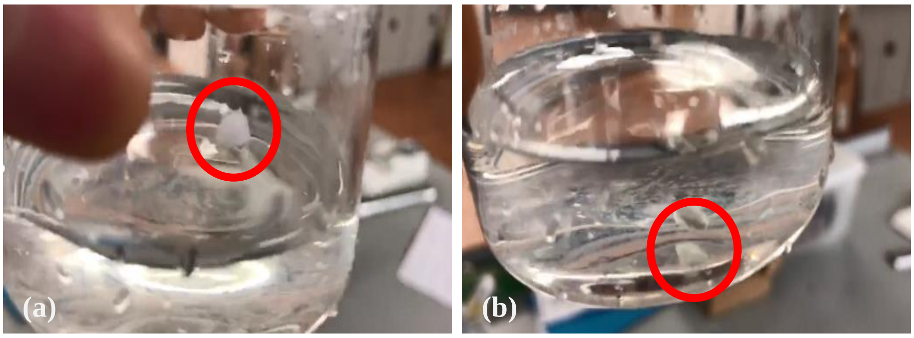

Figure 4-17 aerogel sample (a) floats on the water surface before heat treatment and (b) sinks into the water after heat treatment (800°C)

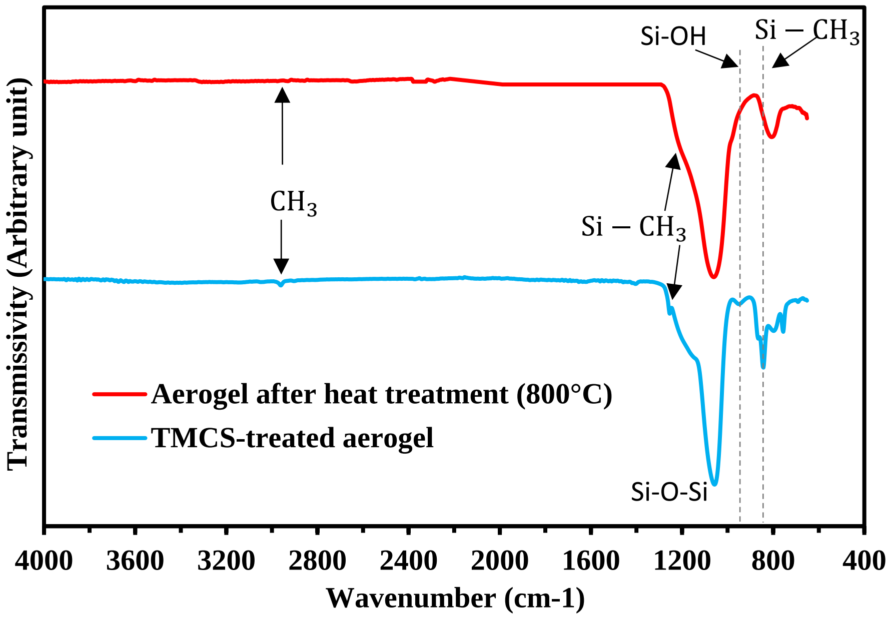

Figure 4-18 FTIR spectrum of TMCS-treated aerogel and aerogel after heat treatment (800°C)

4.3. Conclusion

Waterglass-based silica aerogel was successfully synthesised via ambient pressure drying. The minimum amount of solvent used to synthesise aerogel was investigated. A few detailed fabrication processes, including ageing temperature and drying process, were optimised to improve the properties of the aerogel. The physical property, microstructure, hydrophobicity, thermal conductivity and thermal stability of the aerogel were characterised.

It was experimentally demonstrated that there was a minimum solvent to gel ratio (2:1) to fabricate aerogel successfully. When the amount of solvent was less efficient (i.e., 1:1 and 1.5:1), the water inside the gel may not be replaced by the solvent completely. As a result, large capillary pressure was presented due to the high surface tension of water. Thus, powder form or small piece was fabricated after the drying process. In addition, hydrophilization agents were insoluble in water, and drying of these mixtures (agent and water) could have a negative impact on the final product. This may be the reason for the yellowish crystalized product being formed. The hydrophobicity test also failed for the sample prepared with less solvent to gel ratios (i.e., 1:1, 1.5:1). Thus, the hydrophobization process was not successful. This finding provides guidance for fabricating aerogel with a minimum amount of solvent if the manufacturing cost is considered. The impact of excessive solvent (i.e., 3:1) on the physical properties of aerogel is unknown, but the benefit of using the minimum ratio on the economic aspect is obvious. The fabrication process of aerogel was also optimised. The results indicated that the aerogel aged and solvent-exchanged at a higher temperature (45℃) led to a lower apparent density, higher specific surface area and pore volume, and finer average pore diameter. Ageing and solvent-exchanging at a higher temperature might also have enhanced the backbone strength and reduced the collapse or cracking of silica aerogel during the drying process. The obtained silica aerogel aged at a higher temperature possessed high porosity (91.6%) and a high specific surface area (726 m^2/g). The thermal conductivity test indicated that smaller particle size (<1250 μm) leads to a lower thermal conductivity (25.1 mW/m.K) compared to larger particles (1250 to 3500 μm), and this value was below the thermal conductivity of the air (i.e., 26 mW/m.K) at the ambient condition. This finding indicates that proper optimisation of the fabrication process can improve the properties of silica aerogel, which shows great potential in thermal insulation application.

The mechanical performance of thermal insulation materials should not be ignored. However, it is not mentioned in this chapter, as it is difficult to examine this property due to the fragile nature of aerogel. Thus, fibre reinforcement could be an efficient way to enhance the material structure. In the meanwhile, the thermal insulation performance may also be improved. This will be investigated in the next chapter.

5. Vacuum sealed fibre-reinforced silica aerogel composites with excellent thermal conductivity

The research on optimising aerogels' physical properties, such as pore structure and density, has shown extensive progress. However, the improvement of the strength, fragility and shrinkage rate of the aerogels are unsatisfactory, especially under ambient pressure drying [30]. The involvement of a secondary reinforcement seems to be an efficient way to strengthen the aerogel structure and thus widen its application [31]. Therefore, it is worth investigating the silica aerogel reinforced with fibre.

Fabrication of aerogel composites with embedded fibre is probably the most widely adopted technique in academic research and industrial manufacturing. This is because the involvement of fibre is an effective way to prevent shrinkage during the drying process, especially the ambient drying method. Thus, monolithic aerogel composites can be produced, and the mechanical properties can be improved significantly. However, the challenge is to preserve the insulation properties, minimise the increase of apparent density, and improve the dustiness due to the weak interfacial bonding between the aerogel particle and fibres [22].

In this chapter, glass fibre mats are embedded in silica sol to form fibre reinforced aerogel composites. The fabrication process, including ageing temperature and drying process, is optimised to improve the physical, thermal and mechanical properties of the aerogel composite. The prepared aerogel composite is then vacuum sealed to prevent dustiness during handling, and its influence on thermal conductivity is investigated.

5.1. Experimental

In this section, the materials used to synthesise fibre reinforced aerogel composites are listed. The preparation process and the characterisation method are described.

5.1.1. Materials

The precursor used to synthesise aerogel was sodium silicate (34.6 wt%, VWR UK, Na_2O: $SiO_2 \approx 3.43$). Other agents, including hydrochloric acid (HCl, 37%), ammonia solution (NH_4OH, 28%), ethanol (EtOH), n-Hexane (95%) and Chlorotrimethylsilane (TMCS), were purchased from VWR UK. The polyethene terephthalate (PET) fibre needled blanket (AIRBLEED 10) was supplied by Aerovac systems Keighley Ltd. The density of the material is 55 kg/m^3 with a nominal thickness of 6 mm without compression. The glass fibre (GF) needled mat was purchased from an online store (Mijexhaust Ltd.); the density of the fibre mat is 120 kg/m^3 with a thickness of 10 mm.

5.1.2. Sample preparation

5.1.2.1. The fabrication process of aerogel blanket

Figure 5-1 illustrates the schematic diagram for the preparation of silica aerogel and fibre reinforced aerogel composites. Sodium silicate was diluted with deionised water with a 1:3 volume ratio. Hydrolysis of the diluted sodium silicate solution was carried out by adding 6M HCl while stirring, forming silicic acid sol with a pH of ~2.0. The hydrogel was prepared by adding 2M NH_4OH while stirring to reach a pH of ~5.0. The silica sol was poured into a mould containing a PET blanket or GF mat. The mat was impregnated in the sol for 4 minutes. The excessive silica sol was then poured out, and the quantity was measured using a beaker. The amount of silica sol attached to fibres was calculated by subtracting the amount of sol poured out from the total volume (the volume of sodium silicate, HCl and NH_4OH). Gelation occurred within 30 minutes, and a porous network was formed. EtOH was used for ageing with a 2:1 volume ratio to the gel (the amount of sol attached to fibres). The ageing process was conducted at 45°C in an oven for 24 hours. EtOH was replaced by n-Hexane twice in 32 hours at 45℃. The surface modification was carried out by adding the silylating mixture of TMCS: n-Hexane with a volume ratio of 1:4 for 24 hours at 45°C. Then the silylated gel was dried in ambient pressure at 50°C, 80°C, 100°C, and 120°C for 6 hours respectively to obtain hydrophobic PET or GF-silica aerogel composites. The fabrication process of the GF-aerogel composite is shown in Figure 5-2.

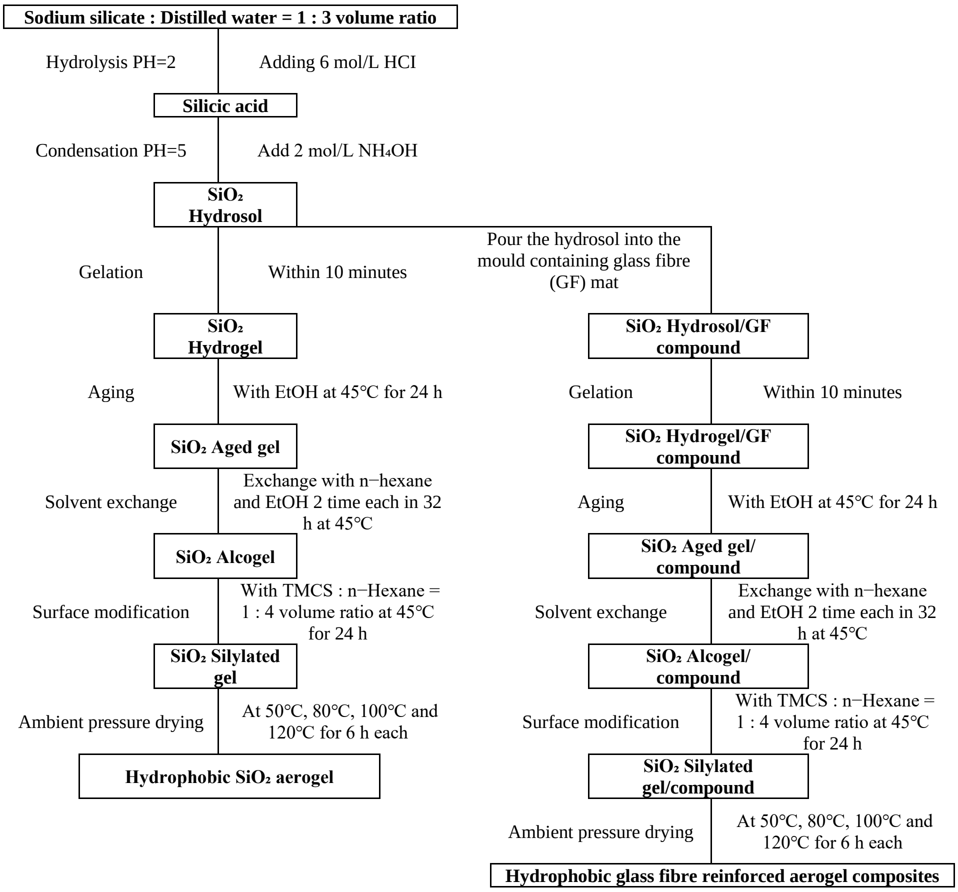

Figure 5-1 Schematic diagram for the preparation of silica aerogel and fibre reinforced aerogel composites

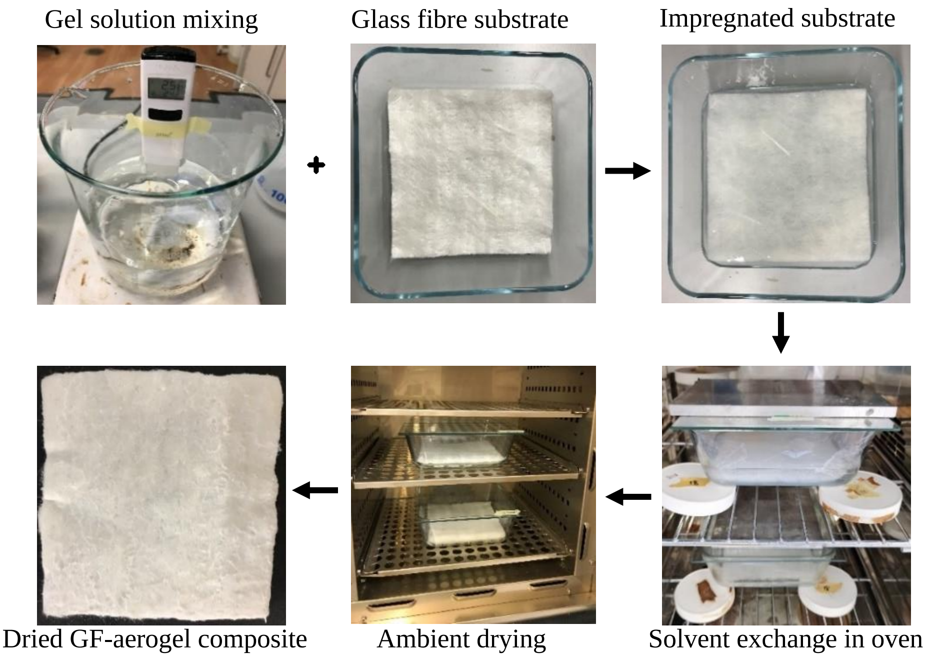

Figure 5-2 Fabrication process of GF-aerogel composites

5.1.2.2. Vacuum sealing of aerogel blanket

It was stated that the thermal conductivity of aerogel composites could be reduced by vacuuming and sealing the blanket [237]. In addition, the sealing of aerogel composites could prevent dust release during handling and processing. It was decided to investigate the benefits of vacuum sealing of the aerogel blankets.

The aerogel composite was placed in a vacuum sealing bag, and the open end of the bag was sealed using a commercial food sealer, as shown in Figure 5-3 (a). A vacuum pump was then used to evacuate the air by inserting a needle into the sealing bag (Figure 5-3 (b)). The vacuum pressure was controlled below -0.8 bar. The needle hole was finally melted using a hair straightener.

Figure 5-3 Photo of (a) sealing and (b) vacuum of a GF-aerogel composite

5.1.3. Sample characterisation

5.1.3.1. Density and porosity

The bulk density of the aerogel composites was calculated using the measured volume of the samples and their mass by an electronic balance with an accuracy of ± 0.01 g. An average of five measurements was conducted with errors showing a 95% confidence limit.

The true density (density of fibre itself without voids in the mat) of the GF mat and PET blanket was measured using a density determination kit, as shown in Figure 5-4. The density determination kit is performed by Archimedes’ principle. This principle states that every solid body immersed in a fluid apparently losses weight by an amount equal to that of the fluid it displaces. The density of the solid can be calculated as follows [305]:

$$\rho = \frac{wa}{wa\text{-}w_l}(\rho_l\text{-}\rho_a)+\rho_a \qquad \text{(Equation 5-1)}$$

where ρ is the density of the sample, w_a is the weight of the sample in air in g, w_l is the weight of the sample in the liquid (deionised water in this case) in g, ρ_l is the density of the water at measured temperature (0.99802 g/cm^3 at 21℃), ρ_a is the density of air (0.0012 g/cm^3) [305].

An average of eight measurements was conducted with errors showing a 95% confidence limit.

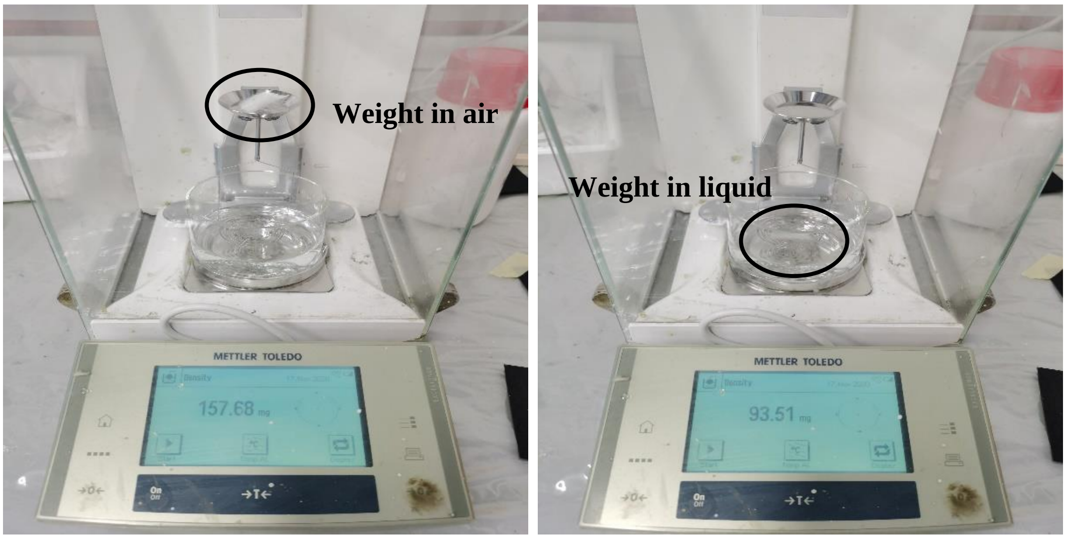

Figure 5-4 True density measurement of glass fibre mat using a density determination kit

The porosity of the aerogel composites was calculated as follow:

$$\varphi_i = \frac{\frac{1}{\rho_a}-\frac{1}{\rho_s}-\frac{1}{\rho_f}}{\frac{1}{\rho_a}} \times 100\% \qquad \text{(Equation 5-2)}$$

where φ_i is the porosity, ρ_a is the bulk density of aerogel composites, ρ_s is the skeleton density of the silica aerogel, generally = 2.2 g/cm^3 [298], and ρ_f is the true density of fibre measured and calculated using Equation 5-1.

5.1.3.2. SEM imaging

The morphology of aerogel composites was investigated by Scanning Electron Microscope (SEM, HITACHI S-3700N) with 5 kV voltage, as shown in Figure 5-5 (a). The samples were gold coated using AGAR sputter coater before analysing.

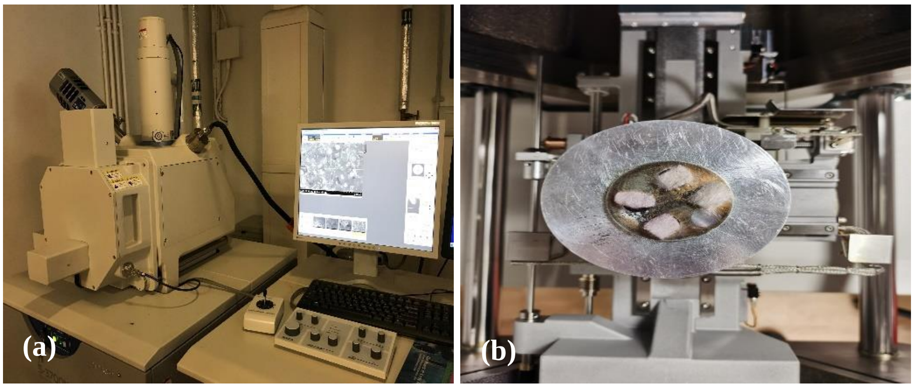

Figure 5-5 (a) Scanning Electron Microscope (SEM, HITACHI S-3700N) and (b) sample loading

5.1.3.3. Gas adsorption

Gas adsorption measurement was conducted according to the procedure described in section 4.1.3.3.

5.1.3.4. Hydrophobicity

Contact angle measurement was conducted according to the procedure described in section 4.1.3.4.

5.1.3.5. FT-IR analysis

The chemical environments of molecular bonds of the aerogel composites were determined via Fourier transform infrared analysis, and it was conducted according to the procedure described in section 4.1.3.5.

5.1.3.6. Thermal gravimetric analysis

The thermal gravimetric analysis was conducted according to the procedure described in section 4.1.3.6.

5.1.3.7. Thermal conductivity

The thermal conductivity test was conducted according to the procedure described in section 3.1.3.3. The specimens were prepared with a size of 18 cm × 18 cm. Standard testing was conducted with a compressive load of 13.8 kPa (2 psi) and a mean temperature of 20°C, with a temperature difference between the hot and cold plates of 20°C. The equipment has a measurement range of 0.002 to 2.0 W/m.K, with an accuracy of ± 1 to 3%. An average of three specimens was prepared and measured to get an average result.

5.1.3.8. Compression and bending test

The mechanical performance of aerogel composites was evaluated by the compression and three-point bending using a 50 kN mechanical tester (Instron 5969, Figure 5-6). The constant loading rate for the compression test was 0.5 mm/min, according to ASTM C165, and the specimen’s size for compression was 50 × 50 × 10 mm, as shown in Figure 5-7 (a). The sample dimensions for three-point bending were 100 × 50 × 10 mm, as shown in Figure 5-7 (b). The support span was set to 60 mm. The sample’s flexural stress, flexural strain and flexural modulus of elasticity can be calculated as:

$$\sigma_f = \frac{3PL}{2wt^2} \qquad \text{(Equation 5-3)}$$

$$\varepsilon_f = \frac{6Dt}{L^2} \qquad \text{(Equation 5-4)}$$

$$E_f = \frac{\sigma f_2 - \sigma f_1}{\varepsilon f_2 - \varepsilon f_1} \qquad \text{(Equation 5-5)}$$

where σ_f is the flexural stress in MPa, ε_f is the flexural strain in the outer surface, E_f is the flexural modulus of elasticity in MPa, P is the applied load in N, L is the support span, setting as 60 mm, D is the maximum deflection of the sample centre in mm, W and t are the width and thickness of the specimen in mm, respectively.

Figure 5-6 50 kN mechanical tester (Instron 5969)

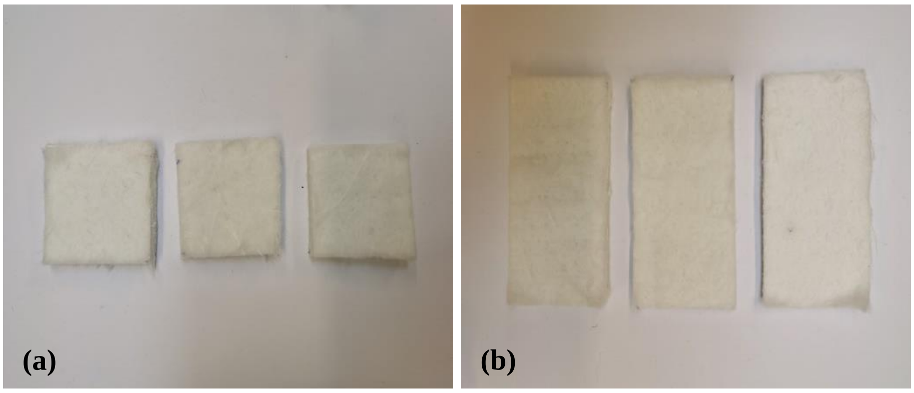

Figure 5-7 GF-aerogel samples for (a) compression test and (b) bending test

5.2. Results and discussion

In this section, the physical, thermal and mechanical properties of the aerogel composite are investigated after optimisation of the fabrication process, including ageing temperature and drying process. The effect of vacuum sealing and variable compressive load on the thermal conductivity of the aerogel composites is discussed.

5.2.1.1. Morphologies and physical properties of aerogel composites

Table 5-1 summarises the physical properties of the aerogel and aerogel composites. The bulk density of the GF mat and PET blanket is calculated as 0.12 g/cm^3 and 0.07 g/cm^3, while the bulk density of the GF-aerogel and PET-aerogel composites increase slightly to 0.17 g/cm^3 and 0.10 g/cm^3, respectively. This is because the voids in the fibre mat are occupied by aerogel. The true density of the PET and GF fibres was determined based on the measurement described in section 5.1.3.1 and calculated using Equation 5-1. The true density of the GF and PET fibre is 2.56 ± 0.08 g/cm^3 and 1.37 ± 0.04 g/cm^3, respectively. The porosity of the composites was calculated based on Equation 5-2 using these measured values.

The specific surface area was obtained by Brunauer-Emmett-Teller (BET) model, and the mean pore diameter was calculated by Barrett-Joyner-Halenda (BJH) method. However, these can only use to obtain the surface area and pore volume for the sample pore size less than 100 nm (mainly aerogel). Since the adsorption capacities were measured according to the mass of the sample (per gram), the composites have less pure silica aerogel compared to the neat silica aerogel with the same weight. Thus, the BET surface area and pore volume of the aerogel composites are much lower compared to the neat silica aerogel. The pore volume was calculated based on the quantity of adsorbed gas at P/P_0=0.99 and the density of liquid nitrogen (0.8081 g/cm^3).

Figure 5-8 (a), (c), (e) and (b), (d), (f) present the photos and the microstructures of PET-aerogel, GF-aerogel, and commercial aerogel blanket (Spaceloft®), respectively. It can be seen from Figure 5-8 (b) and (d) that the silica aerogel matrix adheres to the PET and glass fibre tightly, and the microstructure of the commercial aerogel blankets shown in Figure 5-8 (f) is well-replicated in this work (Figure 5-8 (d)).

Table 5-1 Physical properties of the aerogel and aerogel composites

Sample	Bulk Density (g/cm^3)	Porosity (%)	BET surface area (m^2/g)	Pore volume (cm^3g^{-1})	Pore size (nm)
Aerogel	0.184±0.018	91.6	726±3.5	2.78	12.1
PET-aerogel	0.10±0.001	87.0	195±5.8	0.66	10.2
PET blanket	0.07±0.001	94.9	-	-	-
GF-aerogel	0.17±0.018	85.6	177±7.6	0.75	12.2
GF mat	0.12±0.002	95.5	-	-	-

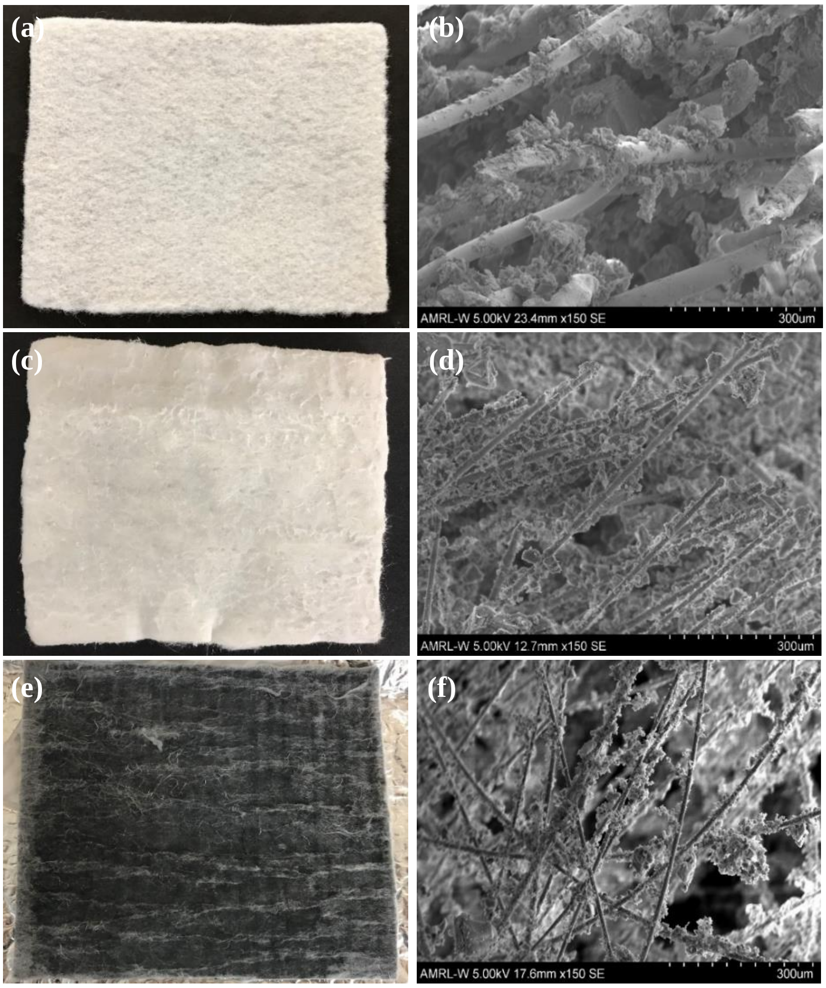

Figure 5-8 (a), (c), (e) the photos and (b), (d), (f) the microstructure of PET-aerogel, GF-aerogel, and commercial aerogel blanket (Spaceloft®), respectively

The pore size distribution (PSD) of the aerogel composites is shown in Figure 5-9 (a). It can be seen that the silica aerogel exhibits meso- and macro-pore size region (2 - 40 nm) and centred at 18 nm, corresponding BJH mean pore diameter of 12.1 nm, as shown in Table 5-1. Both PET-aerogel and GF-aerogel composites have narrower pore size distribution, with a mean pore diameter of 10.2 nm and 12.2 nm, respectively. Figure 5-9 (b) shows the N_2 adsorption-desorption isotherm of the aerogel, GF-aerogel and PET-aerogel composites. It presents a type IV(a) isotherm with a H3 hysteresis loop at $P/P_0 > 0.6$ [300], revealing the mesoporous characteristics of the aerogel. The sharp increase of isotherms in the high relative pressure region ($P/P_0 = 0.95$-1.0) is due to the liquid condensation suggesting the presence of macropore [191]. The fibre-reinforced aerogel composites retain the aerogel nature in terms of the microstructure. The pore sizes are much smaller than the mean free path of air (70 nm) in the atmosphere, which could reduce the heat transfer via the gaseous phase. Thus, the thermal insulation performance of the aerogel composites could be improved.

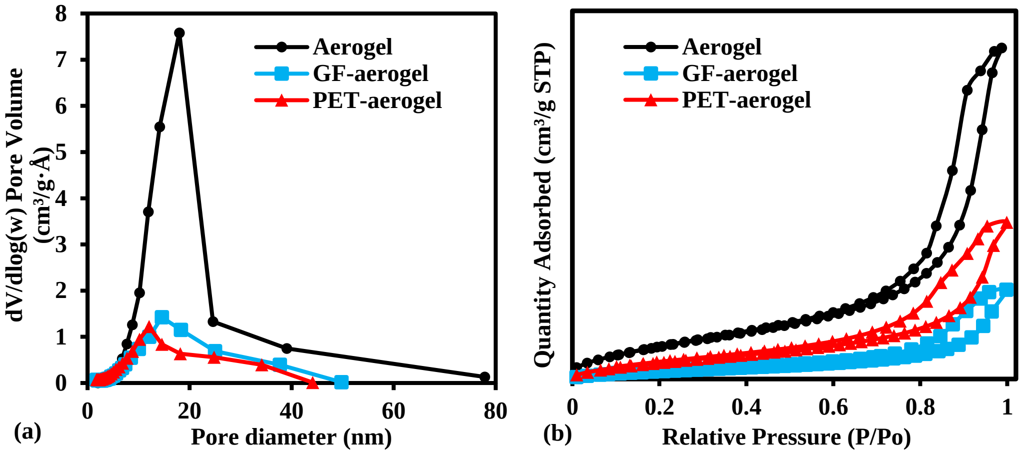

Figure 5-9 (a) Pore size distribution (PSD) and (b) N_2 adsorption-desorption isotherms of aerogel, GF-aerogel, and PET-aerogel composites

5.2.1.2. Hydrophobicity and FTIR spectra of aerogel composites

Figure 5-10 (a), (b) and (c), (d) show the photos and microscopic images of a water droplet on the treated surface of PET-aerogel and GF-aerogel composites, respectively. The average water contact angle is 137.8° ± 14.3° and 121.0° ± 8.8°, respectively. This excellent water-repellent property is stemmed from the treatment of the specimens with TMCS, where the stable methyl groups are responsible for the excellent hydrophobicity of the silica components [20].

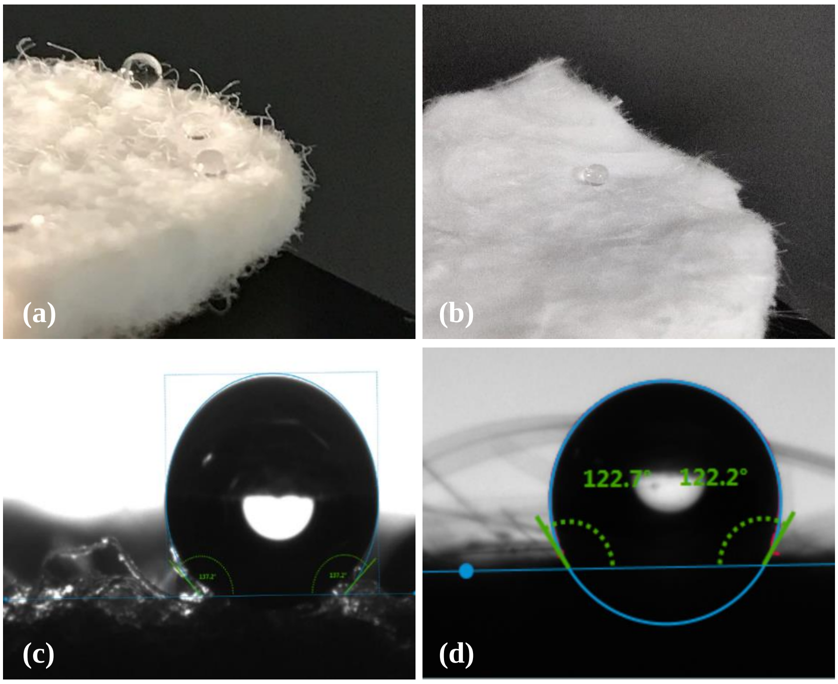

Figure 5-10 (a) (b) the photos of a water droplet on the treated surface and (c) (d) microscopic image of water contact angle measurement of PET-aerogel and GF-aerogel composites, respectively

Figure 5-11 shows the FTIR spectrum of TMCS-treated silica aerogel, glass fibre and TMCS-treated GF-aerogel composites. The band at 1060 cm^{-1} is caused by the symmetric stretching vibrations of Si-O-Si bonds [306], and the peak at 900 cm^{1} shows the characteristics of stretching bands of the Si-OH for E-glass fibre. The surface-treated aerogel and aerogel composites show strong absorption peaks at about 850 cm^{-1}, 1260 cm^{-1} and 2980 cm^{-1}, corresponding to Si-CH_3 groups and -CH_3 groups [26, 191]. The presence of these absorption peaks confirms the attachment of -Si-CH_3 groups from the TMCS to the silica aerogel surface, indicating that the surface modification process was successful. Moreover, the bonds at ~3450 and ~1650 representing -OH groups disappear after surface modification.

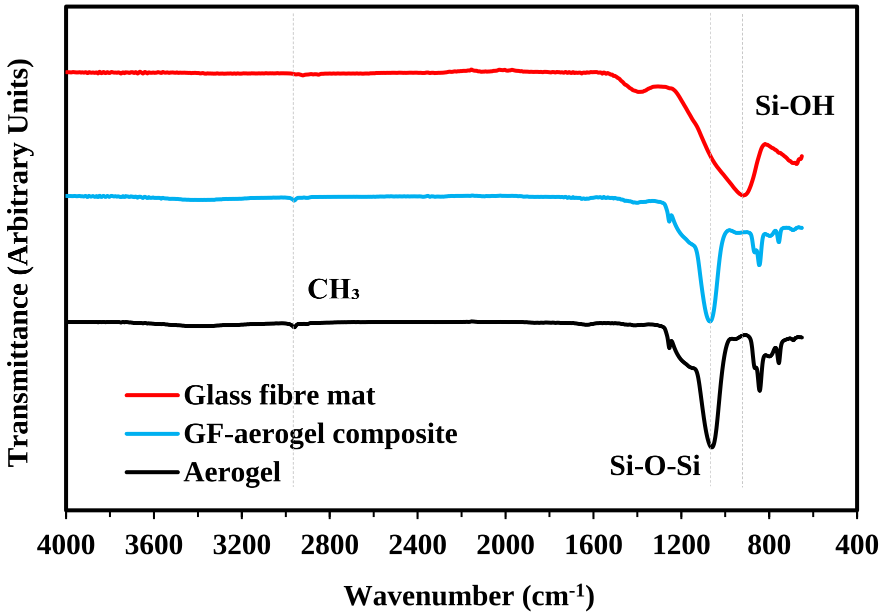

Figure 5-11 FTIR spectrum of glass fibre, TMCS-treated silica aerogel, and TMCS-treated GF-aerogel composite

The FTIR spectrum of silica aerogel, PET fibre and PET-aerogel composite is illustrated in Figure 5-12. Strong absorption peaks at about 712 and 1730 cm^{-1}, corresponding to the interaction of polar ester groups and benzene rings, and stretching of C=O of the carboxylic acid group are well captured within PET-aerogel composite. This indicates that the aerogel is well bonded with the PET fibre. The detailed absorption band of the PET blanket is summarised in Table 5-2 [307].

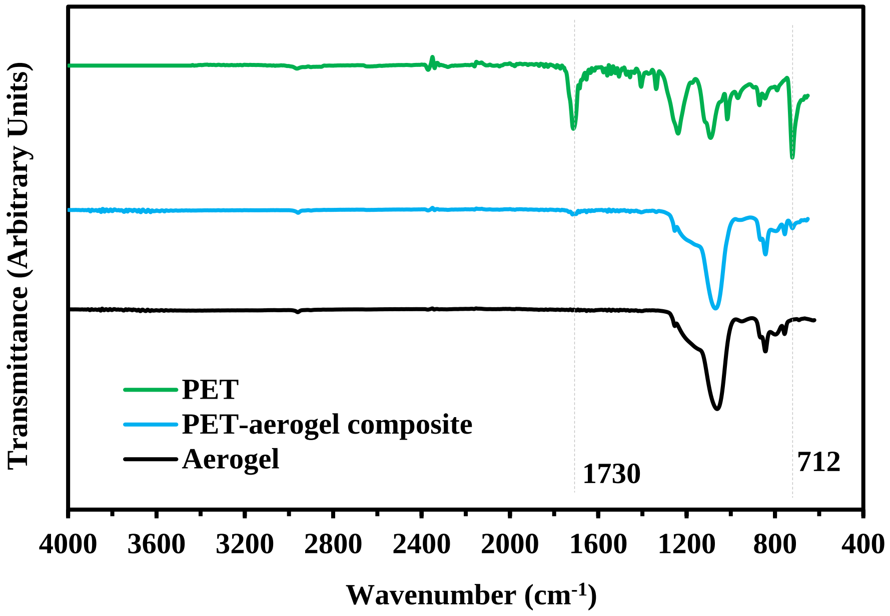

Figure 5-12 FTIR spectrum of silica aerogel, PET fibre and PET-aerogel composites

Table 5-2 Absorption band of PET blanket, reproduced from [307]

Absorption band (cm^{-1})	Bands
2969	C-H, Symmetrical stretching
2350	Axial symmetrical deformation of CO2
1730	Stretching of C=O of carboxylic acid group
1453, 1410 and 1342	Stretching of the C-O group deformation of the O-H group and bending and wagging vibrational modes of the ethylene glycol segment
1240	Terephthalate group (OOCC6H4-COO)
1096 and 1050	Methylene group and vibrations of the ester C-O bond
972 and 872	Aromatic rings 1,2,4,5; Tetra replaced
1960 and 795	Vibrations of adjacent two aromatic H in p-substituted compounds and aromatic bands
712	Interaction of polar ester groups and benzene rings

5.2.1.3. Thermal properties of aerogel composites

5.2.1.3.1. Thermal conductivity of aerogel blankets

Figure 5-13 shows the measured thermal conductivity of PET blanket, GF mat, PET-aerogel and GF-aerogel composites at a mean temperature of 20°C, with a constant loading pressure of 13.8 kPa. A noticeable improvement in thermal conductivity is achieved when aerogel is introduced into the fibre matrix, especially for GF-aerogel composite, where the thermal conductivity drops from 29.6 mW/m.K to 18.4 mW/m.K. A slight improvement can be found for PET-aerogel composites (reduces from 27.4 mW/m.K to 24.3 mW/m.K). It is worth mentioning that the thermal conductivity of both composites is lower than the neat aerogel granule. This behaviour can be explained through the combination heat transfer mechanism of porous materials, including solid conduction by fibre and aerogel particles, gas conduction inside aerogel pores and voids between fibres, convection in voids between fibres, and radiation.

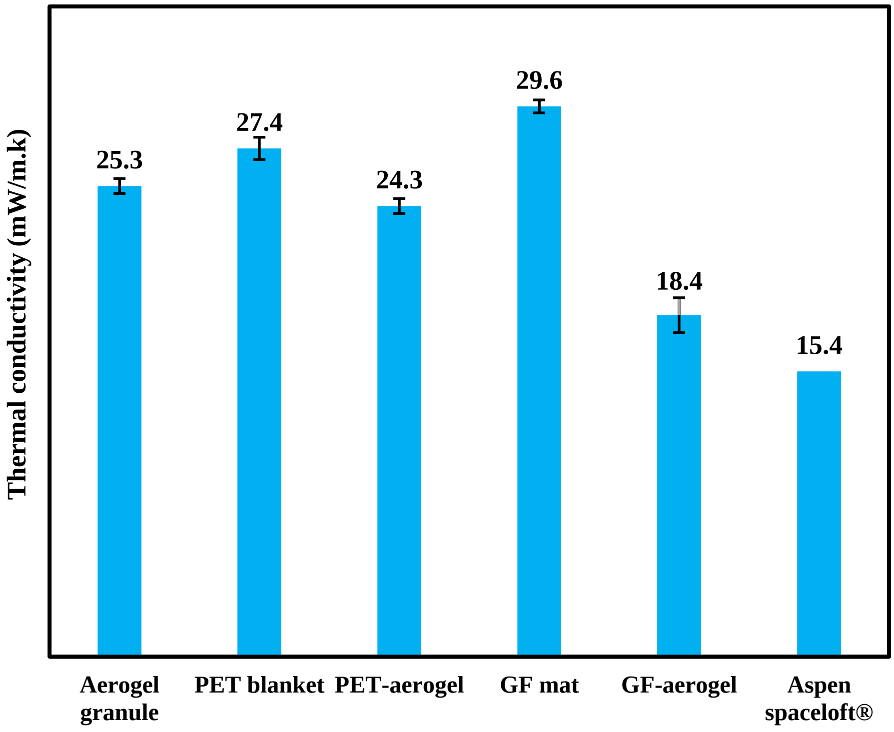

Figure 5-13 Measured thermal conductivity for aerogel granule (prepared in-house), PET blanket, PET-aerogel, glass fibre mat, GF-aerogel, and commercial Aspen Spaceloft® blanket at a constant pressure load of 13.8 kPa, with a mean temperature of 20°C

In porous insulating materials, the total effective heat transfer is dominated by the contribution of the non-convective gas within the hollow spaces or pores [308]. The gas conductivity in a porous medium is determined by the number of gas molecules as a transfer medium as well as by the number of 'walls' on the way from the hot to the cold side [308]. It is stated that convection in a porous medium can be neglected if the material's pores are less than 4 mm [309, 310]. A reduction in insulating material's gas thermal conductivity is achieved by either reducing the pressure or introducing a nano-structured core material [220]. By reducing the pressure, the number of gas particles in a given volume of space is reduced; thus, the mean free path between collisions of particles is increased [220]. When the pore diameter of the material becomes less than the mean free path of gas molecules, such as in aerogels, the molecules will only collide with the pore surface without transferring energy, known as the Knudsen Effect [220]. The heat transfer in the solid grain of aerogel should flow mainly through phonons or localised oscillations [310]. As the solid grain sizes of aerogel are in the range of 2-5 nm, the phonon-grain boundaries scattering occupies the main position and lowers the phonon mean free path in aerogel; thus, the solid thermal conductivity is reduced [310].

5.2.1.3.2. Thermal conductivity of vacuum-sealed aerogel blankets

Figure 5-14 shows the comparison of thermal conductivity of aerogel composite under ambient and vacuum at a mean temperature of 20°C, with a constant loading pressure of 13.8 kPa. A noticeable reduction of the thermal conductivity can be found for the GF-aerogel sample. The thermal conductivity decreases from 18.4 mW/m.K to 13.8 mW/m.K, with 25% reduction. This value is superior to the commercial Aspen aerogel blanket at ambient condition (15.4 mW/m.K). As mentioned previously, the heat transfer of fibre reinforced aerogel composites consist of solid conduction, gaseous conduction and radiation. It was stated that the most effective way of improving the thermal insulation properties of materials is to reduce the gaseous thermal conductivity [220]. When a vacuum system is introduced, the number of gas particles in a given volume of space is reduced or eliminated; thus, the mean free path between collisions of particles is increased [220]. When the pore diameter of the material becomes less than the mean free path of gas molecules, the molecules will only collide with the pore surface without transferring energy (Knudsen Effect). Therefore, the heat transfer by the gas phase present within the composite is minimised. Thus, a lower thermal conductivity value can be achieved.

It can also be found from Figure 5-14 that only a 3% reduction of the thermal conductivity is obtained for the PET-aerogel sample. As mentioned previously, a slight decrease in thermal conductivity is obtained when aerogel is reinforced by a PET blanket (reduces from 27.4 mW/m.K to 24.3 mW/m.K) under the ambient condition. This may be because the porosity of the GF mat (95.5%) is slightly higher than the PET blanket (94.9%), as shown in Table 5-1. It leads to a higher mass percentage of aerogel in the GF-aerogel composite as more voids can be occupied by aerogel. Thus, the reduction in thermal conductivity of GF-aerogel is higher than the PET-aerogel composite.

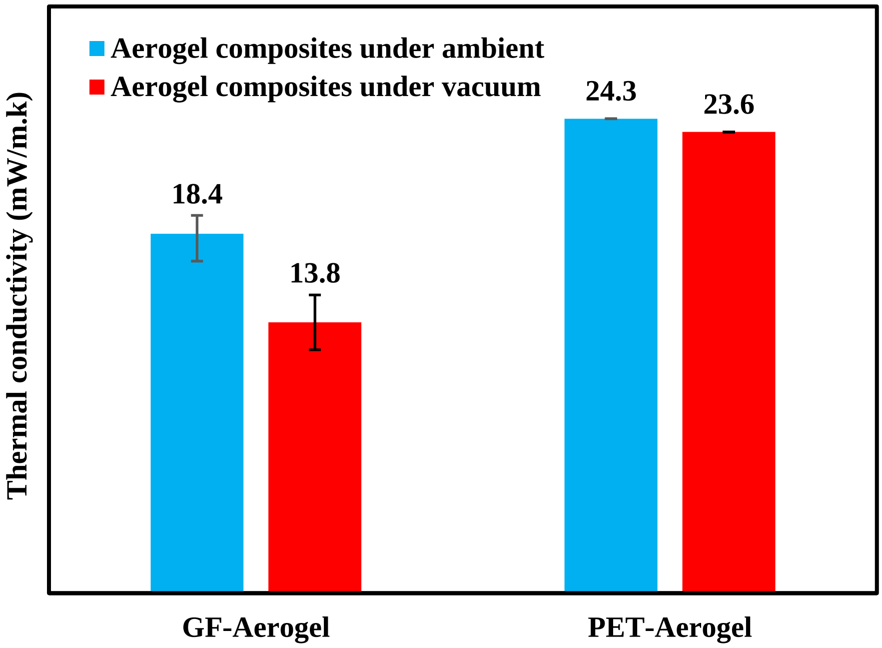

Figure 5-14 The comparison of thermal conductivity of GF-aerogel and PET-aerogel under ambient and vacuum at a mean temperature of 20°C, with a constant loading pressure of 13.8 kPa

5.2.1.3.3. Thermal conductivity of aerogel composites at various pressure loads

The thermal conductivity of glass fibre reinforced aerogel composite against various loading pressure is shown in Figure 5-15. The result shows that lower thermal conductivity is achieved with higher pressure, with a logarithmic order, and there is no sign of level-off with continuing increasing pressure. However, the applied load is limited by the apparatus. The thermal conductivity of GF-aerogel composite can reach as low as 18.6 mW/m.k at a pressure of 15 kPa, which is significantly lower than conventional organic foams (i.e. EPS, 35 mW/m.k). As mentioned previously, gas conductivity is the dominant heat transfer path. Compressing the composites blanket results in a change in its microstructure; thus, the porosity varies with compression. Assuming that the volume of fibres and aerogel particles (solid volume) does not change at each loading step, only the pore volume decreases [311]. Based on the mathematical model developed in Hoseini [311], the porosity of the GF-aerogel composite decreases slightly as the pressure load increases. As the composite is compressed, densification likely occurs as a result of a better entanglement of clusters, leading to a decrease in the pore size located between clusters [280]. This suppresses gas conduction heat transfer due to fewer collisions between gas molecules and an increasing number of elastic collisions between gas molecules and pore wall [312]. Thus, the thermal conductivity decreases with increasing pressure load.

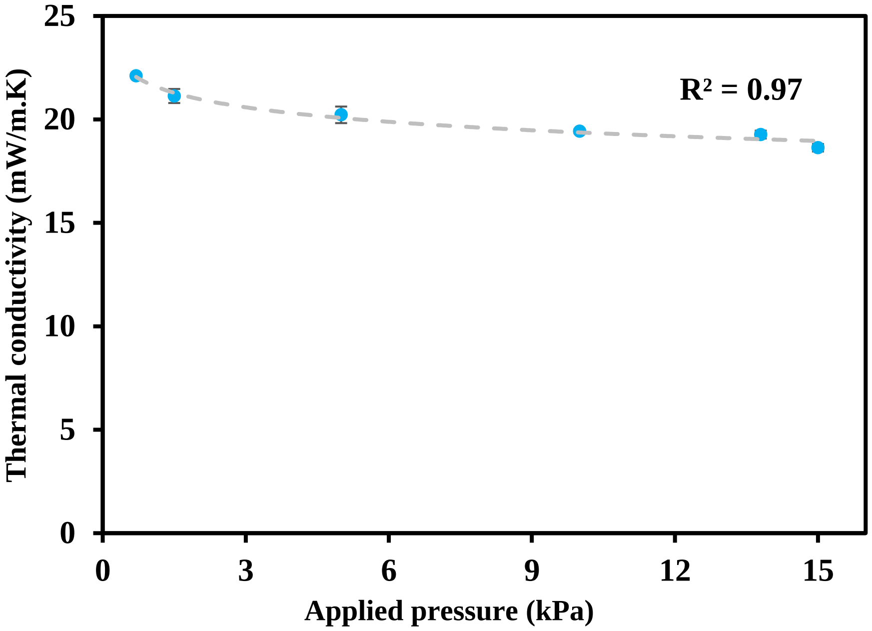

Figure 5-15 Thermal conductivity of glass fibre reinforced aerogel composite at various loading pressure with a mean temperature of 20°C

5.2.1.3.4. Thermal stability

The TG curve of synthesised silica aerogel, PET-aerogel and GF-aerogel composites is shown in Figure 5-16. A slight weight loss before 100℃ is observed due to the evaporation of the residual solvent and water molecules [26]. No apparent weight loss can be seen for the glass fibre mat due to its pure inorganic composition. By introducing inorganic glass fibre, the aerogel composite maintained almost 95% of its weight, where only 5% of the weight is lost at 800°C. The synthesised glass fibre reinforced aerogel composite achieves excellent thermal stability at a high temperature. For PET-aerogel composites, it remains thermally stable up to 300°C which significantly limit their use. It is also worth mentioning that the GF-aerogel composite made in this project is more thermally stable at a higher temperature than the commercial aspen aerogel blanket.

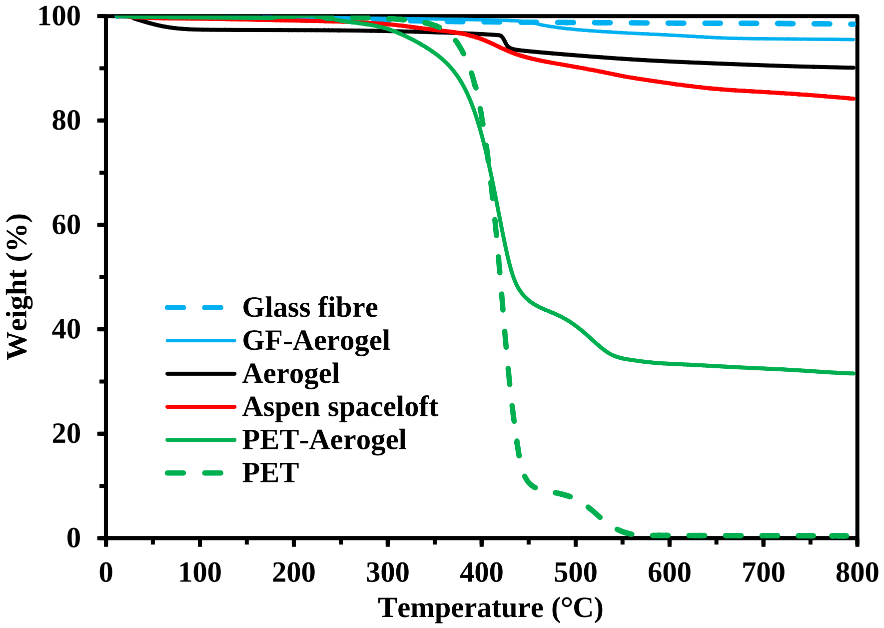

Figure 5-16 TGA curve of PET blanket, PET-aerogel, GF mat, GF-aerogel composite, and commercial Aspen blanket

5.2.1.4. Mechanical properties of aerogel composites

Figure 5-17 (a) - (d) show the photos of the neat PET blanket, PET-aerogel composite, GF mat, and GF-aerogel composite during the compression test. The average compressive strength is summarised in Figure 5-18. Fibre-reinforced aerogel composites exhibit excellent compressive performance than the specimen without aerogel, especially for GF-aerogel composite. A three-fold improvement in compressive strength (4.7 kPa) is achieved at 25% strain compared to the neat glass fibre mat (1.12 kPa). This can be explained using the stress-strain curve shown in Figure 5-19.

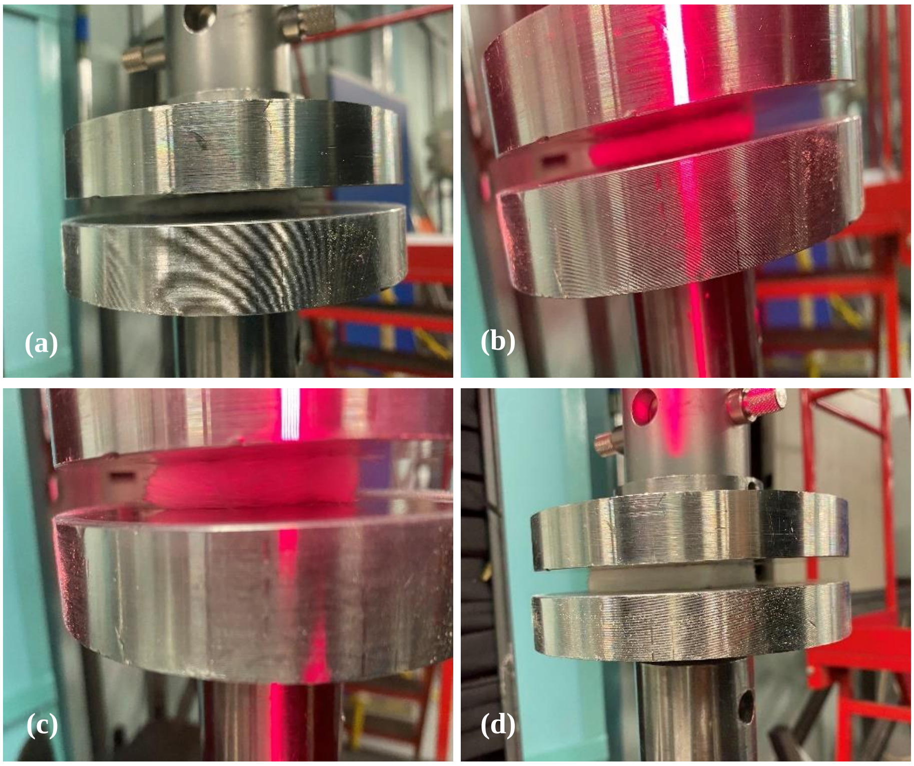

Figure 5-17 Photos of (a) PET blanket, (b) PET-aerogel composite, (c) GF mat, (d) GF-aerogel composite during the compression test

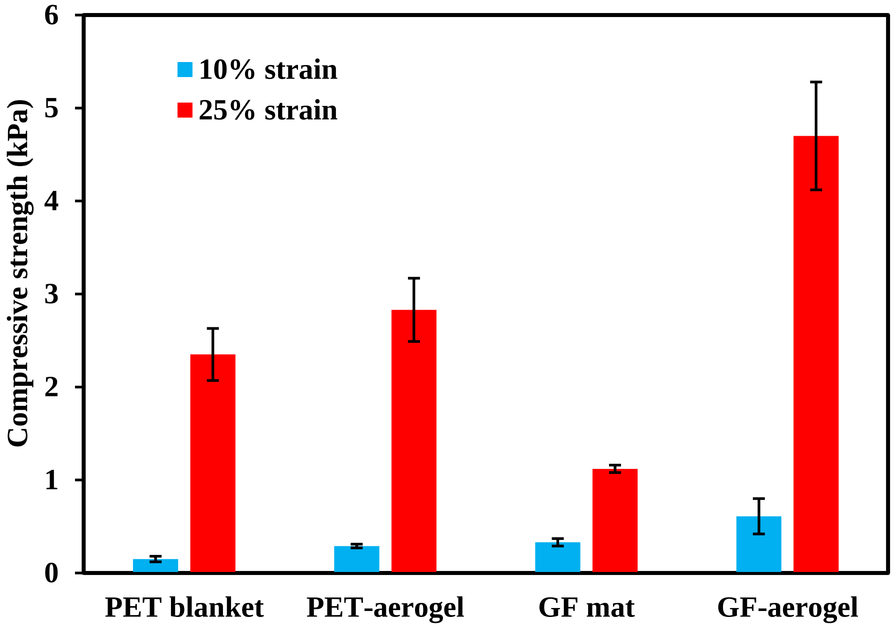

Figure 5-18 Compressive strength of PET blanket, PET-aerogel composite, glass fibre mat, and GF-aerogel composite at 10% and 25% strain

Figure 5-19 shows the stress-strain curve of GF mat, GF-aerogel, PET blanket, and PET-aerogel composites. In general, the stress-strain curve of GF-aerogel and PET-aerogel can be divided into four different stages: the contact stage, the linear stage, the yielding stage, and the densification stage [191]. At the contact stage, the strain varied from 0% to 15% is caused by the uneven surface of the specimens. The strain in the range of 20% to 25% represents the linear stage, where the slope of the curve remains unchanged. The nanopores of silica aerogel act as the main load capacity part, while the fibres are only responsible for the structural integrity of the composites [313]. The linear stage between the composites and the neat fibre is well distinguished in Figure 5-19. The strain in the range of 25% to 40% shows the yielding and densification stage, where the stress increases significantly. At the yield stage, fibres act as the main load capacity part, resulting in a rapid increase in stress. At the densification stage, the significant increase in stress is mainly due to the collapse of aerogel and gradual densification of the porous structure [313].

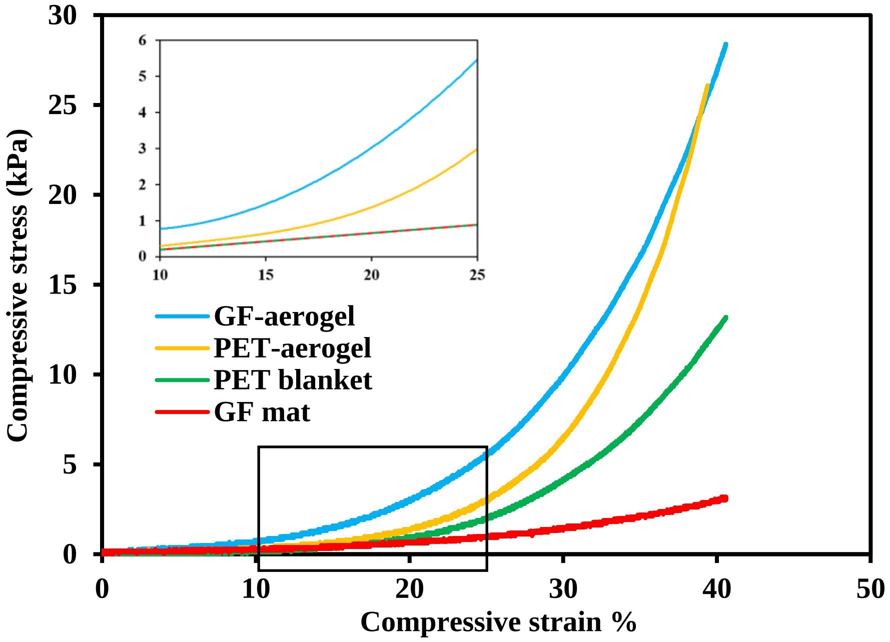

Figure 5-19 The compressive stress-strain curves of GF mat, GF-aerogel, PET blanket, and PET-aerogel composite

From the inset shown in Figure 5-19, the strain from 20% to 25% of PET-aerogel and GF-aerogel shows preferable linearity corresponding to the linear stage. Thus, Young's modulus is calculated based on the strain of 20% ($\varepsilon_{20\%}$) and 25% ($\varepsilon_{25\%}$) and the corresponding compressive stress ($\sigma_{20\%}$ and $\sigma_{25\%}$). The calculated compressive modulus of PET blanket, PET-aerogel, GF mat, and GF-aerogel is summarised in Table 5-3 and Figure 5-20. It can be seen clearly that the introduction of aerogel presents an increase in Young's modulus, especially for the GF-aerogel composite. A five-fold improvement in modulus (45.33 kPa) is achieved compared to the neat glass fibre mat (9.07 kPa), whereas the increase of modulus of

PET-aerogel is 24% compared to the neat PET blanket. This shows that the involvement of aerogel in the fibre matrix enhances the resistance to compressive deformation at a given pressure load.

Table 5-3 Compressive stress at the strain of 20% and 25% and the calculated Young's modulus of the samples

Sample	$\sigma_{20\%}$ (kPa)	$\sigma_{25\%}$ (kPa)	Young's modulus (kPa)
PET blanket	1.03±0.19	2.35±0.22	26.33±0.94
PET-aerogel	1.20±0.08	2.83±0.29	32.60±4.11
GF mat	0.67±0.05	1.12±0.05	9.07±0.94
GF-aerogel	2.43±0.45	4.70±0.67	45.33±4.71

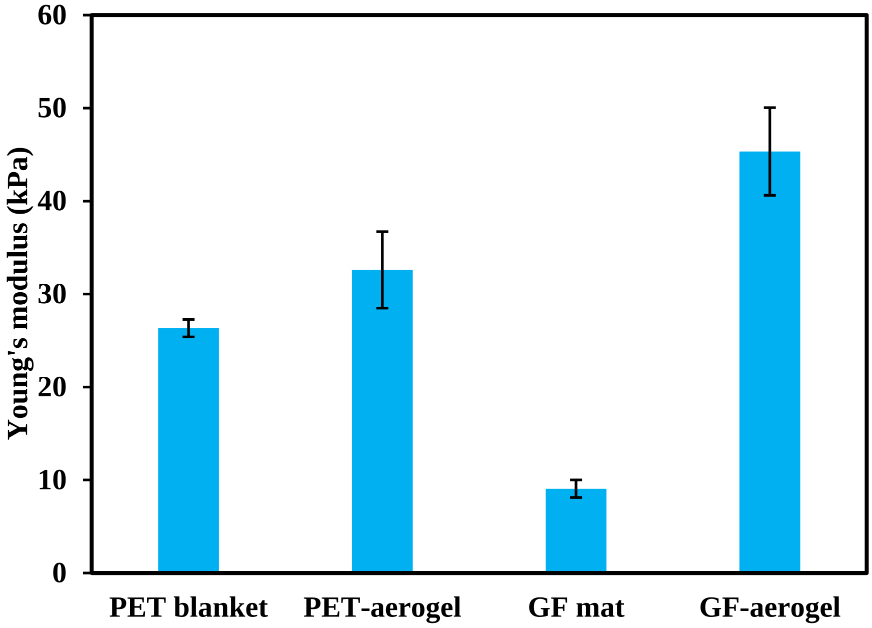

Figure 5-20 Compressive modulus of PET blanket, PET-aerogel composite, GF mat, and GF-aerogel composite

Figure 5-21 (a) - (d) show the photos of neat PET blanket, PET-aerogel composite, GF mat, and GF-aerogel composite during 3-point bending test. The average flexural strength is summarised in Figure 5-22. It is evident that fibre reinforced aerogel composite shows excellent flexural performance than that of the specimen without aerogel, especially for glass fibre reinforced aerogel composite. Nearly three-fold improvement in flexural strength is achieved at 25% strain compared to the neat GF mat. This is well indicated in the stress-strain curve shown in Figure 5-23. The strain from 0% to 10% in Figure 5-23 indicates a linear stage where the slope of the curve remains unchanged. This is used to calculate Young's modulus of the sample. The strain from 10% to 25% shows a non-linear stage with a declining slope, meaning that the resistance to deformation tends to decrease. This is due to the layers split of the composites as the top side surface is in compression where the bottom side surface is in tension.

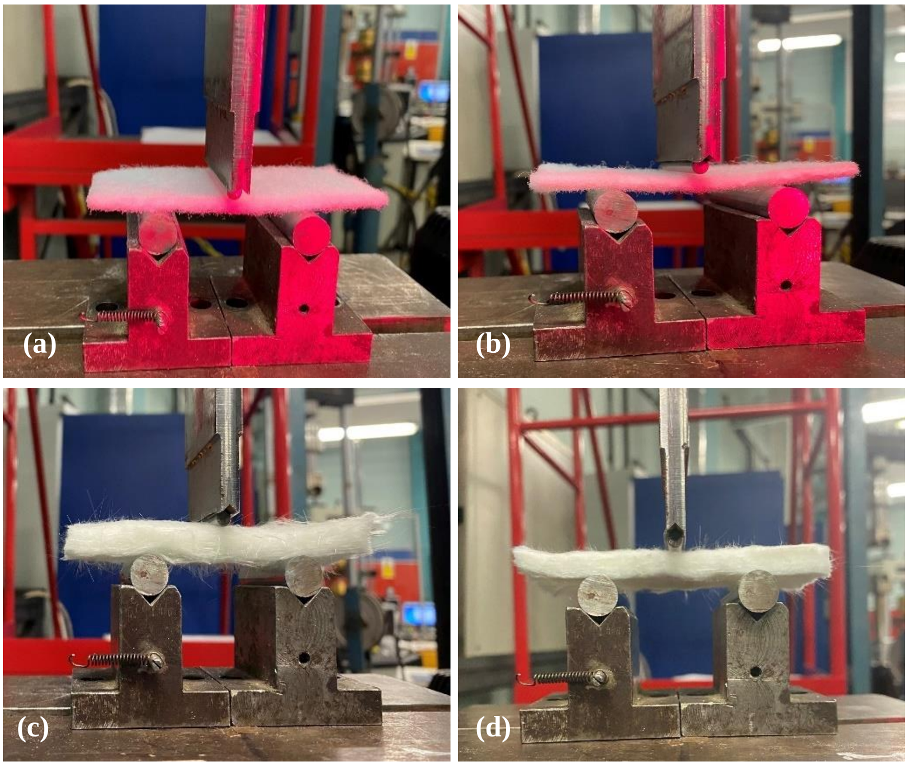

Figure 5-21 Photos of (a) PET blanket, (b) PET-aerogel composite, (c) GF mat, (d) GF-aerogel composite during 3-point bending test

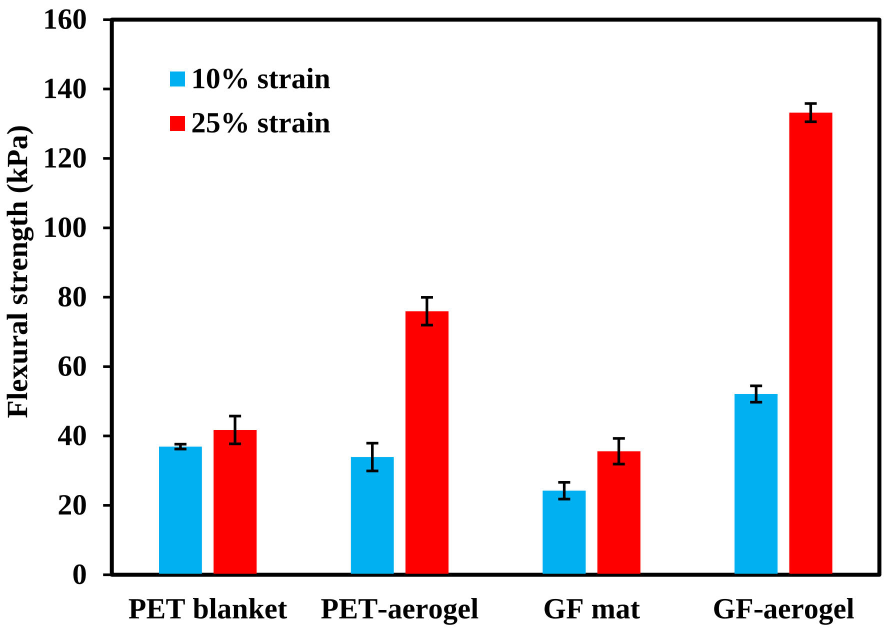

Figure 5-22 Flexural strength of PET blanket, PET-aerogel composite, glass fibre mat, and GF-aerogel composite at 10% and 25% strain

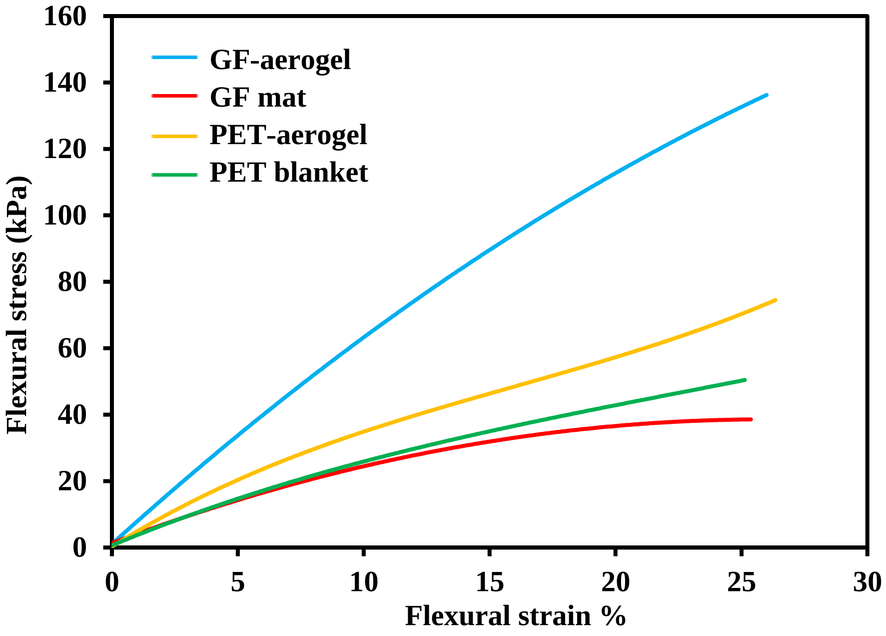

Figure 5-23 The flexural stress-strain curves of GF mat, GF-aerogel, PET blanket, and PET-aerogel composite

The calculated flexural modulus of PET blanket, PET-aerogel, GF mat, and GF-aerogel is summarised in Figure 5-24. It can be seen clearly that the introduction of aerogel presents an increase in the flexural modulus, especially for the GF-aerogel composite. A two-fold improvement in modulus (606 kPa) is achieved compared to the neat glass fibre mat (253 kPa), whereas the increase of modulus of PET-aerogel is 38% compared to the neat PET blanket. This shows that the involvement of aerogel in the fibre matrix enhances the resistance to flexural deformation at a given pressure load.

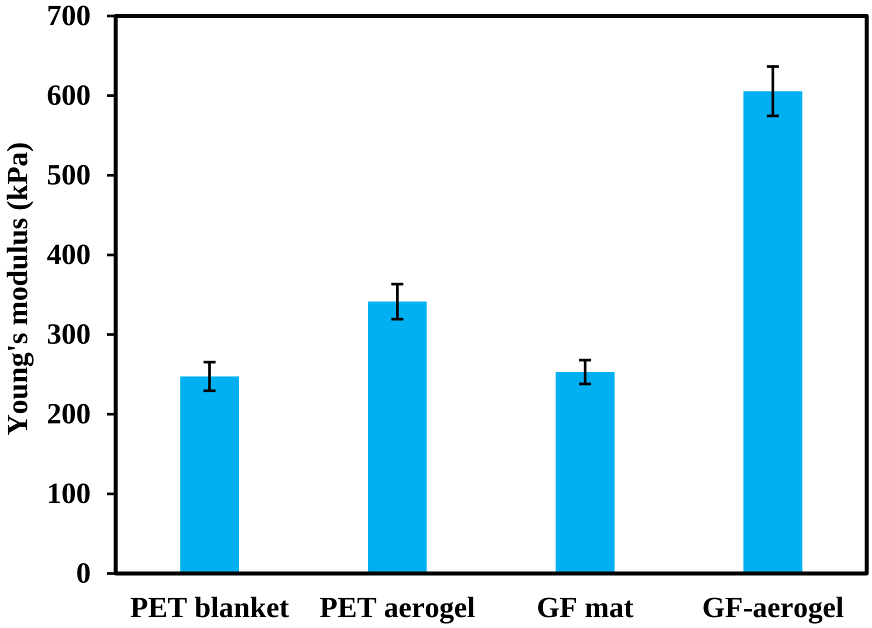

Figure 5-24 Flexural modulus of PET blanket, PET-aerogel composite, GF mat, and GF-aerogel composite

5.4. Conclusion

In this chapter, PET and glass fibre mats were embedded in silica sol to form fibre reinforced aerogel composites. The fabrication process, including ageing temperature and drying process, was optimised to improve the physical, thermal and mechanical properties of the aerogel composite. The prepared aerogel composite was then vacuum sealed to prevent dustiness during handling, and its influence on thermal conductivity was investigated.

The GF-aerogel composites obtained from the optimised process showed excellent thermal conductivity (18.4 mW/m.K at a pressure load of 13.8 kPa). It is worth mentioning that vacuum sealing of the aerogel composites did not only prevent dustiness during handing but also improves the thermal performance. The thermal conductivity could be further reduced to 13.8 mW/m.K by vacuum sealing the GF-aerogel composite. This finding suggests a more efficient way of fabricating aerogel composite with maximum benefit (lowering the thermal conductivity and preventing dustiness during handing). The influence of the pressure load on the thermal conductivity of the GF-aerogel composites was also investigated. The result showed that lower thermal conductivity was achieved with higher pressure, and there was no sign of level-off if the load pressure continued to increase. This might attribute to the microstructure change under compression. The GF-aerogel composites also possessed excellent thermal stability. The aerogel composites maintained almost 95% of their weight, where only 5% of the weight was lost at 800°C. The compression and bending tests proved that the aerogel composites could endure considerable compressive and flexural strain without structural destruction. These outstanding characteristics indicate that GF-aerogel composites have great potential in the thermal insulation field, especially for a moderate temperature environment (i.e., less than 800℃).

6. Eco-friendly geopolymer and aerogel composites reinforced with recycled glass fibre

The fabrication and characterisation of geopolymer have been investigated in previous chapters. The mechanical performance of the prepared geopolymer could be further improved. Besides, an increasing amount of waste glass has been produced nowadays due to the widespread use of glass in different applications [32]. The glass products are non-biodegradable; thus, recycling and reusing glass are attractive, which could significantly contribute to the prevention of environmental pollution [32]. Therefore, It is worth investigating the involvement of recycled glass fibre in the geopolymer.

Waste glass, as a partial mineral precursor, has been investigated extensively in the fly ash-based geopolymer system [32-34]. The mechanical property of geopolymer generally improved with the addition of waste glass. However, the effect of waste glass on the thermal property of geopolymer is not commonly mentioned. In addition, the chemical structure of fibre dissolved in alkaline solution via FT-IR have not been studied comprehensively.

In this section, recycled glass fibre (rGF) is introduced into the geopolymer. The rGF is partially or fully dissolved in sodium hydroxide solution to form the alkaline activator. The effect of rGF content on the mechanical and thermal properties of geopolymer is examined. In addition, the chemical environments of molecular bonds of the fibre dissolution in alkaline solution via FT-IR are investigated.

6.1. Geopolymer with recycled glass fibres

6.1.1. Experimental

In this section, the materials used to synthesise geopolymer with rGF are listed. The preparation process and the characterisation method are described.

6.1.1.1. Materials

The glass fibres were recycled in-house according to the procedure described in section 6.1.1.2. The original fibres were E-glass fibres supplied by Hexcel Reinforcements UK Ltd. Coal fly ash (Fineness category N - ≤40% retained on the 45 μm sieve according to BS EN450) was provided by Cemex (a member of the UK Quality Ash Association). Sodium silicate solution

(SiO2: Na2O ≈ 3.345) and NaOH pellet purchased from VWR are used as an alkaline activator (AA). NaOH pellets were premixed with deionized water to obtain a 10M sodium hydroxide solution. Calcium stearate and hydrogen peroxide (H_2O_2, 30 wt%) was supplied by VWR.

6.1.1.2. Sample preparation

The fibre recycling process is shown in Figure 6-1. The glass fibre reinforced epoxy composites (GF-EP) were prepared in-house, as described in Pender [258]. The composites were first granulated using Zerma Granulator by Summit Systems Ltd, with a screen size of 5 mm. The granulated composites were then heat-treated in a furnace at 570°C. The obtained glass fibres had an average fibre length of 2 mm based on fibre length distribution analysis [258].

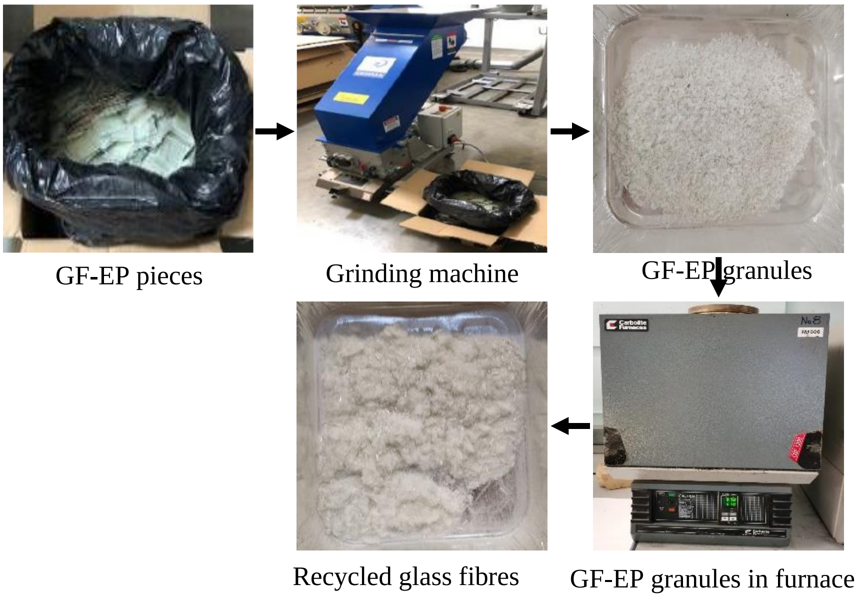
GF-EP pieces

Grinding machine

GF-EP granules

Recycled glass fibres

GF-EP granules in furnace

Figure 6-1 Fibre recycling process

Figure 6-2 presents the fibre dissolution process. 0 to 25 g rGF with an increment of 5 g was mixed with 100 ml 10M NaOH solution. The mixed solution was magnetically stirred at 95°C for 24 hours at a speed of 600 rpm. The hot plate was set to 125°C to obtain a solution temperature of 95°C, and this was measured using a K-type thermocouple. An insulation layer (aluminium foil and PET blanket) was applied around the plastic container to minimise heat loss. The solution was then filtered using filter paper, and the filtered paste was dried at 110℃ for 2 hours. The filtered solution and the solid from drying out the filtered (meaning what is left on the filter paper) were characterised using FTIR analysis. The unfiltered mix solution was used as the alkaline activator to synthesise geopolymer according to the procedure described in section 3.1.2. All parameters were remained the same apart from the alkaline activator, as described in Table 6-1.

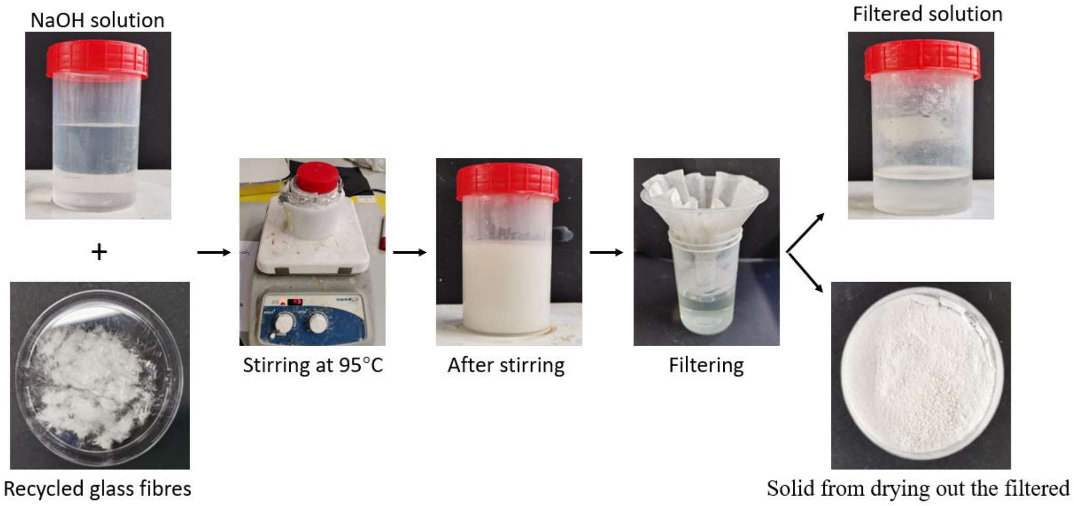

Figure 6-2 rGF dissolution process

Table 6-1 The description of various alkaline activator

Sample ID	Sample description (Alkaline activator)
SS + NaOH	Mixture of commercial sodium silicate and 10M NaOH solution
SS + 5g rGF	5g of rGF dissolve in 100ml 10M NaOH solution and mix with commercial sodium silicate solution
SS + 10g rGF	10g of rGF dissolve in 100ml 10M NaOH solution and mix with commercial sodium silicate solution
SS + 15g rGF	15g of rGF dissolve in 100ml 10M NaOH solution and mix with commercial sodium silicate solution
SS + 20g rGF	20g of rGF dissolve in 100ml 10M NaOH solution and mix with commercial sodium silicate solution
SS + 25g rGF	25g of rGF dissolve in 100ml 10M NaOH solution and mix with commercial sodium silicate solution

6.1.1.3. Sample characterisation

6.1.1.3.1. Density and porosity

The oven-dry density and porosity of geopolymer were characterised according to the procedure described in section 3.1.3.1.

6.1.1.3.2. SEM imaging

The pore morphology of geopolymer was characterised according to the procedure described in section 3.1.3.2.

6.1.1.3.3. Thermal conductivity

The thermal conductivity measurement was conducted according to the procedure described in section 3.1.3.3.

6.1.1.3.4. Compression test

The compressive strength measurement was conducted according to the procedure described in section 3.1.3.4.

6.1.1.3.5. FTIR analysis

The FTIR analysis of the filtered solution and the solid from drying out the filtered was conducted according to the procedure described in section 3.1.3.7.

6.1.2. Results and discussion

In this section, the effect of rGF content on the mechanical and thermal properties of geopolymer is examined. In addition, the chemical bonding state of the fibre dissolution in alkaline solution via FT-IR is investigated.

6.1.2.1. Morphology and physical properties

Figure 6-3 shows the dry density and porosity of geopolymer alkaline activated by sodium silicate with various rGF content. It can be seen that the dry density of geopolymer increases with the increasing amount of rGFs in the alkaline activators up to 15 g rGF. This is mainly due to the unreacted solid particles presented during the fibre dissolution process. A higher amount of rGFs leads to higher unreacted/undissolved residual fibres, as shown in Figure 6-4. In addition, as the rGFs content increases to 15 g, the reaction mechanism may reach a saturation state, meaning that there is a considerable amount of rGFs undissolved. This is well presented in the SEM image shown in Figure 6-5. As the rGFs content increases further to 20 g, a significant amount of fibre clusters is generated due to the presence of excessive fibres and inefficient stirring, as shown in Figure 6-4. This is also well presented in the SEM image shown in Figure 6-6. However, there is no noticeable effect on the porosity with the addition of rGF content.

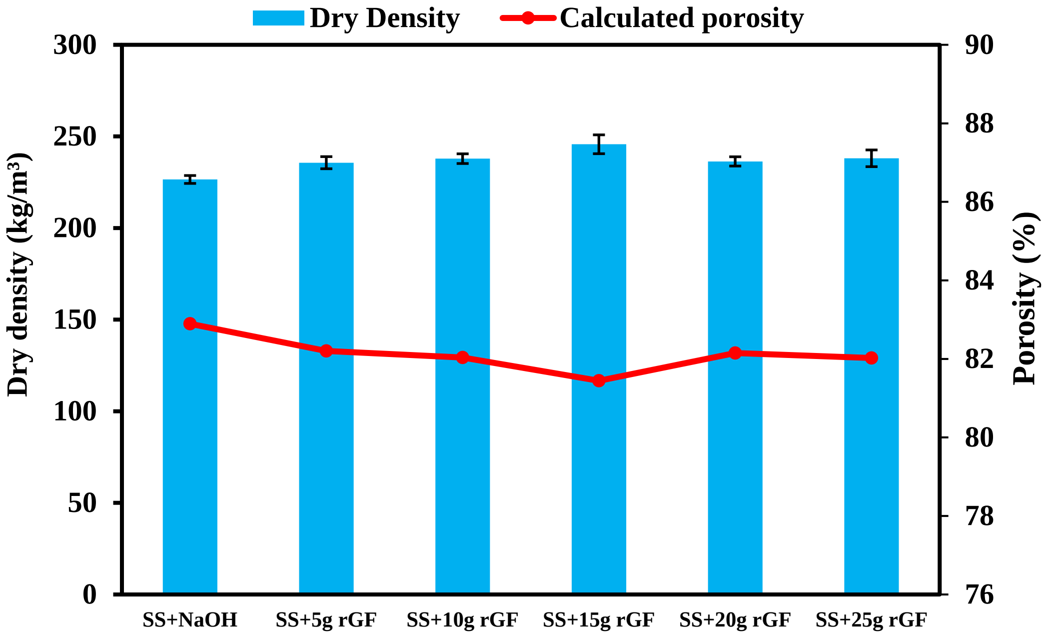

Figure 6-3 Dry density and porosity of geopolymer alkaline activated by SS with various rGF content

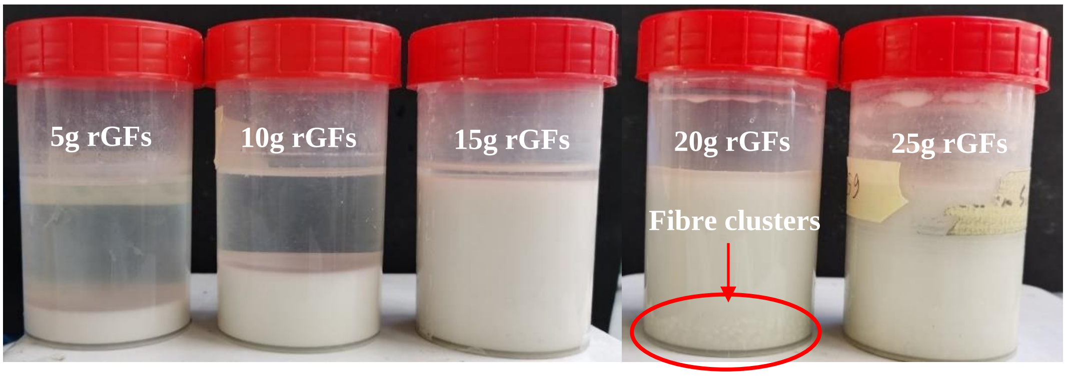

Figure 6-4 Photo of 5g, 10g, 15g, 20, and 25 g rGFs after dissolving in 100ml NaOH solution

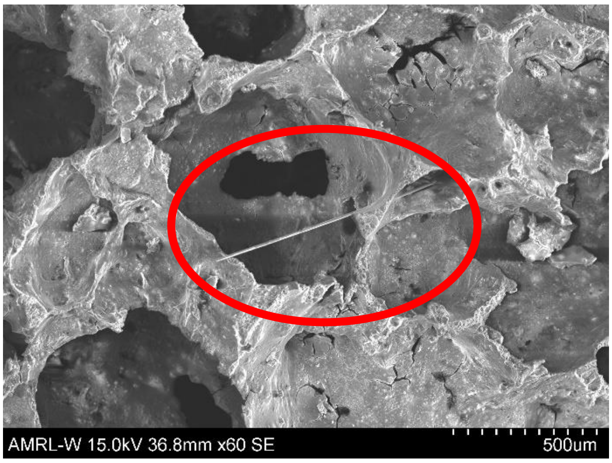

Figure 6-5 SEM image of geopolymer alkaline activated by SS+15g rGF showing undissolved fibre

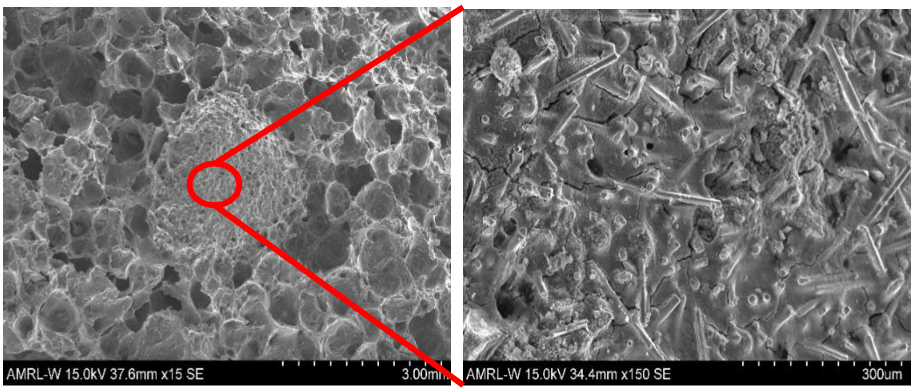

Figure 6-6 SEM image of geopolymer alkaline activated by SS+20g rGF showing fibre clusters

The SEM images of geopolymer activated by SS+NaOH, SS+5g rGF, SS+10g rGF, SS+15g rGF, SS+20g rGF and SS+25g rGF are shown in Figure 6-7 (a) - (f), respectively. The main reaction product in the alkaline activation of fly ash is an amorphous polymer, an aluminosilicate hydrate (N-A-S-H gel) whose chemical composition and microstructure vary depending on the nature of the activator used [254]. At the macroscopic level, the pore size appears to reduce with fewer connection holes as the amount of rGFs increases, as shown in Figure 6-8.

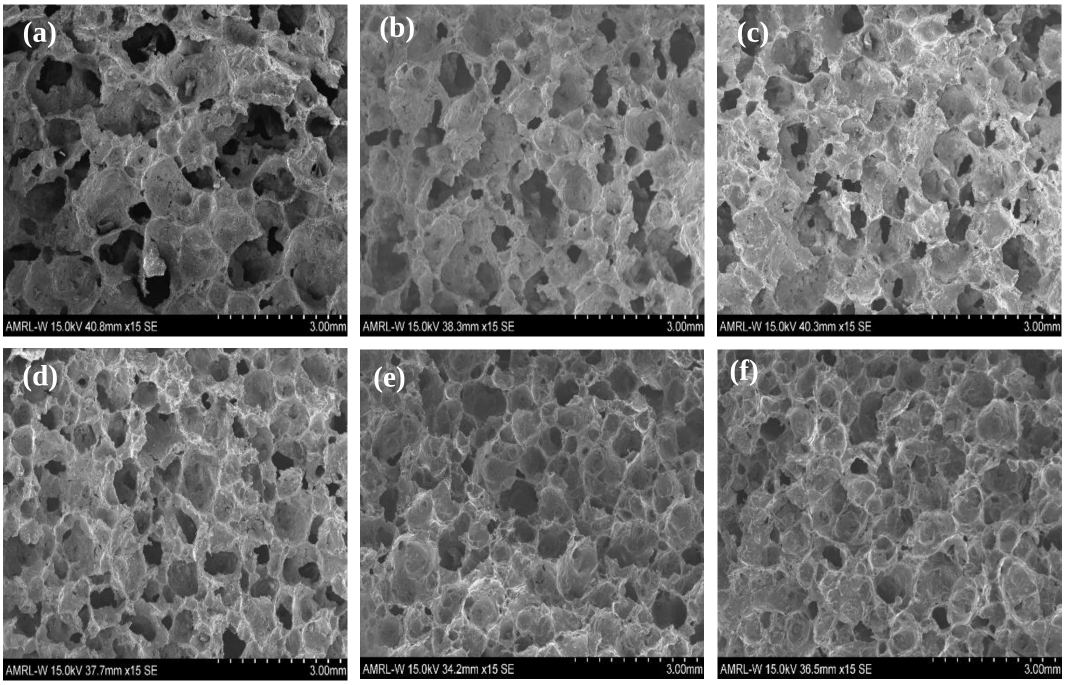

Figure 6-7 SEM images of geopolymer activated by (a) SS+NaOH, (b) SS+5g rGF, (c) SS+10g rGF, (d) SS+15g rGF, (d) SS+20g rGF, and (f) SS+25g rGF, respectively

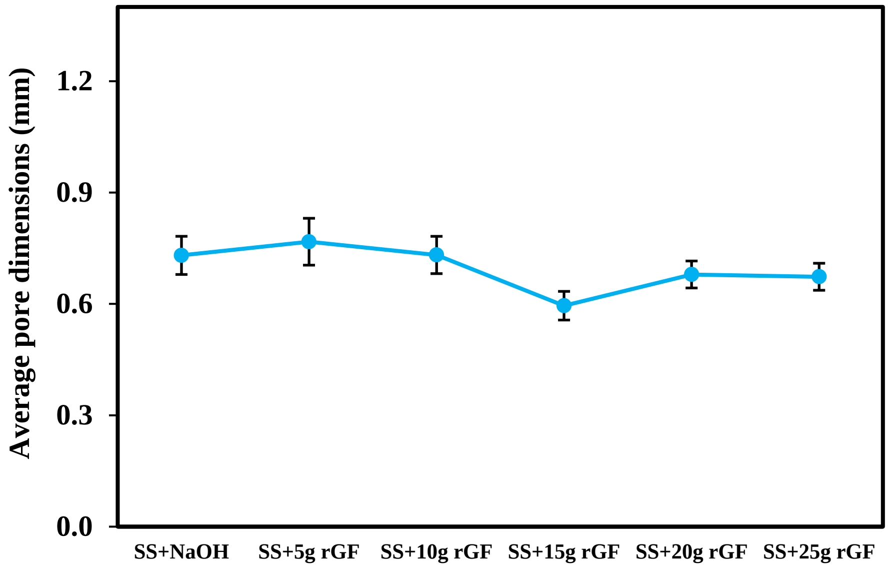

Figure 6-8 Average pore dimensions of geopolymer alkaline activated by SS with various rGF content

6.1.2.2. Thermal conductivity

Figure 6-9 shows the thermal conductivity of geopolymer alkaline activated by SS with various rGF content. In general, there is no significant influence on thermal conductivity with the addition of rGF, despite the fact that the thermal conductivity of geopolymer activated by 20 g rGF content increases to 65 mW/m.K. This is suggested as an outlier. The thermal conductivity-porosity relationship shown in Figure 6-10 also supports this suggestion. The heat transfer in porous building materials such as geopolymer, the porosity, conductivity of the solid matrix (particle), and the type of the fluid in the pores (water or air) are the main factors influencing the effective thermal conductivity [277]; although the pore size seems to reduce with fewer connection holes as the amount of rGFs increases. The porosity remains almost unchanged regardless of the rGF content, as it was well proved that the amount of H_2O_2 significantly influenced the porosity of geopolymer. The addition of rGF, thus the density, has no noticeable impact on the thermal conductivity of geopolymer when ignoring the outlier.

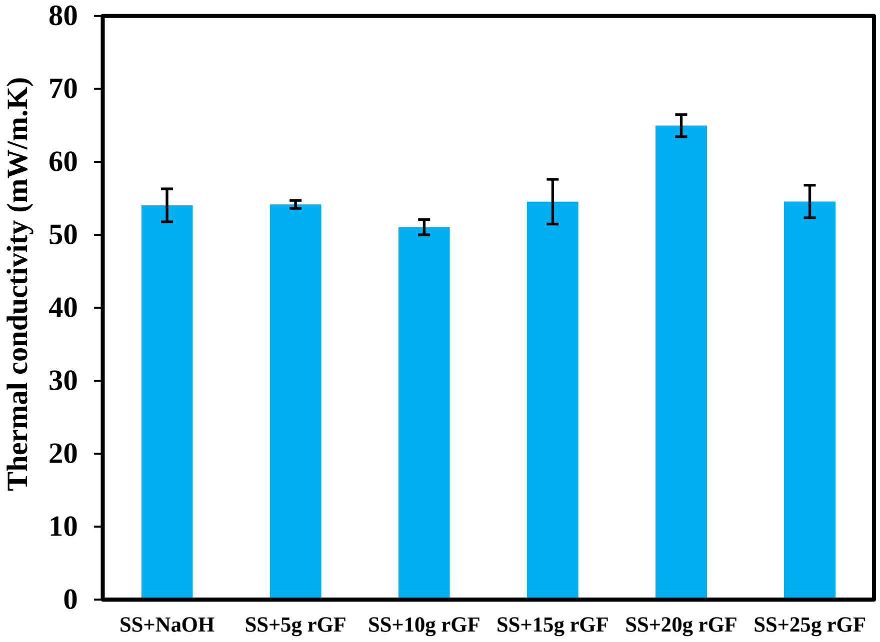

Figure 6-9 Thermal conductivity of geopolymer alkaline activated by SS with various rGF content

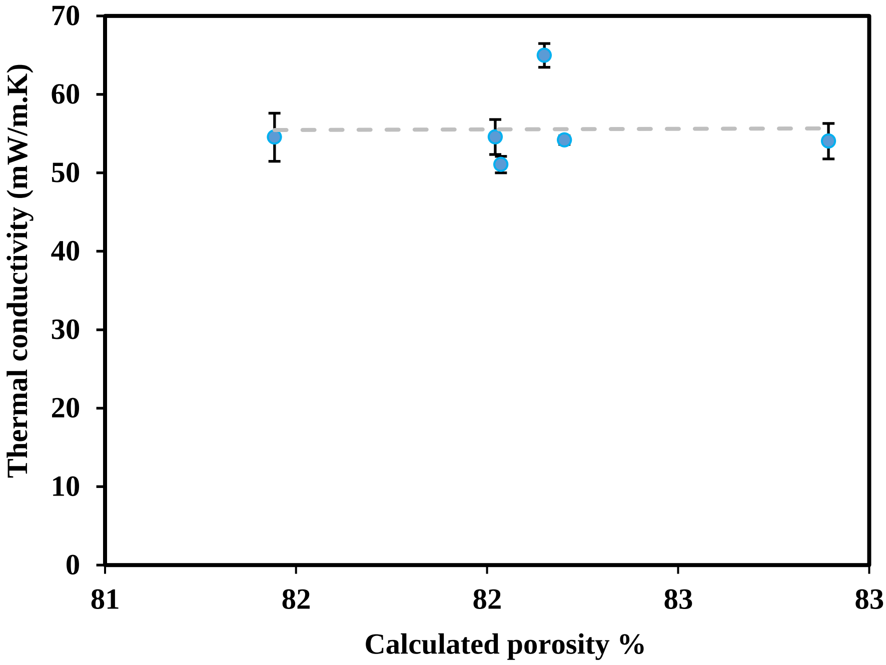

Figure 6-10 Calculated porosity and thermal conductivity relationship of geopolymer with rGF

6.1.2.3. Compressive property

The compressive strength of geopolymer alkaline activated by SS with various rGF content is shown in Figure 6-11. A linear increase in compressive strength is observed as the number of rGFs dissolved in NaOH solution increases up to 15g rGF. The compressive strength increased from 92 to 165 kPa, with a 79% improvement. As the amount of rGFs increases, the content of Si in the system rises, so as the SiO_2/Na_2O ratio. The variation in the SiO_2/Na_2O ratio may lead to a change in the degree of polymerisation. It has been shown in other work that the higher the ratio, the greater the connectivity among silicon atoms. Thus, the degree of polymerisation increases [254]. Therefore, the compressive strength of geopolymer is improved with the addition of rGF. However, As the addition of rGF increases further to 20 g, the compressive strength of geopolymer starts to reduce. As mentioned earlier, only a portion (32.29 g) of the prepared NaOH+ 20 g rGFs solution (150.39 g) was used to fabricate three specimens (50 × 50 × 50 mm), meaning that some of the precipitated fibre clusters may not be used to fabricate the sample. The actual fibre dissolves in NaOH solution may be less than the specimen made with less rGFs, so as the SiO_2/Na_2O ratio. Thus, the connectivity among silicon atoms is also reduced, leading to a lower degree of polymerisation. As a result, the compressive strength drops to 128 kPa when the rGF content increases to 25 g.

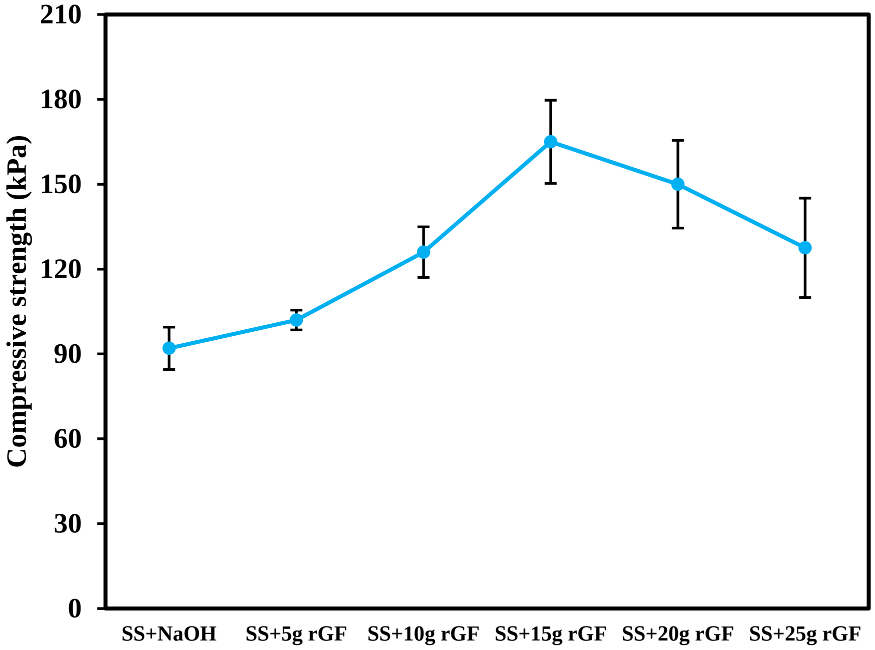

Figure 6-11 Compressive strength of geopolymer alkaline activated by SS with various rGF content

Figure 6-12 shows the compressive strain at failure of geopolymers alkaline activated by SS with various rGF content. The stress-strain behaviour of geopolymer with various rGF content is plotted in Figure 6-13. The geopolymer without rGF shows a failure strain of 0.0021 at the maximum load (92 kPa), and the addition of rGF generally has a lower failure strain than the geopolymer without rGF. However, the stress-strain curve shown in Figure 6-13 shows that the geopolymer with any rGF content presents a higher peak than the one without rGF. This indicates that the involvement of rGF is beneficial for increasing the compressive strength.

Figure 6-12 also shows Young’s modulus of geopolymers alkaline activated by SS with various rGF content. The effect of rGF content on Young’s modulus presents a similar pattern as the compressive strength of geopolymer, as shown in Figure 6-11. When the rGF content increases from 5 to 15 g, Young’s modulus increases from 12.2 to 22.6 MPa. As the rGF content increases further to 25 g, Young’s modulus tends to decrease. The increase of Young’s modulus at 15 g rGF shows that the resistance to deformation at a given pressure load is increased.

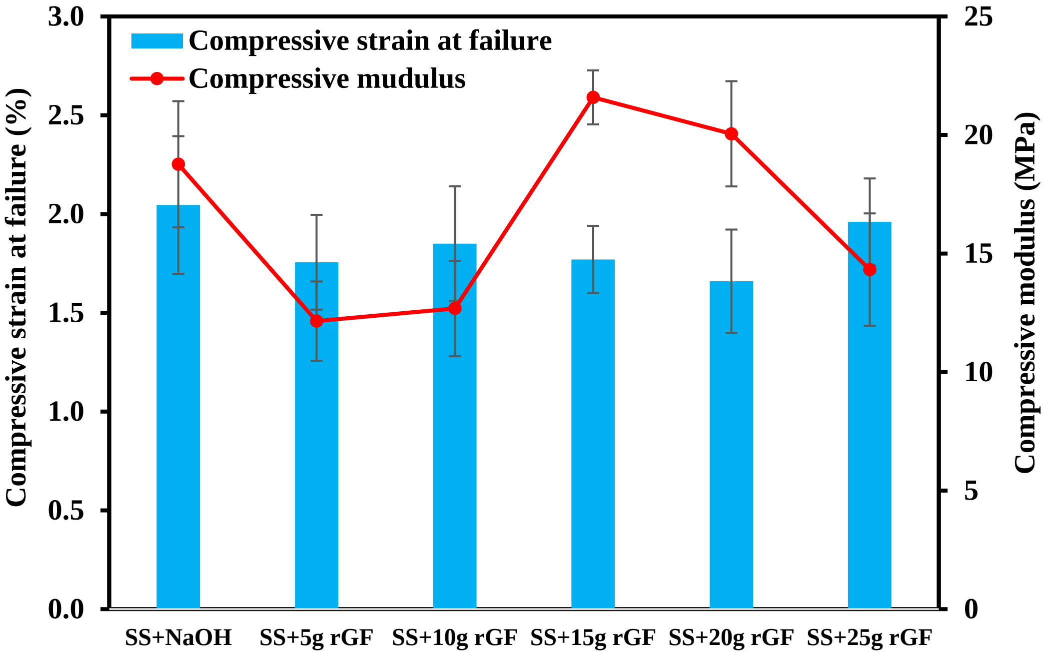

Figure 6-12 Compressive strain at failure and compressive modulus of geopolymer alkaline activated by SS with various rGF content

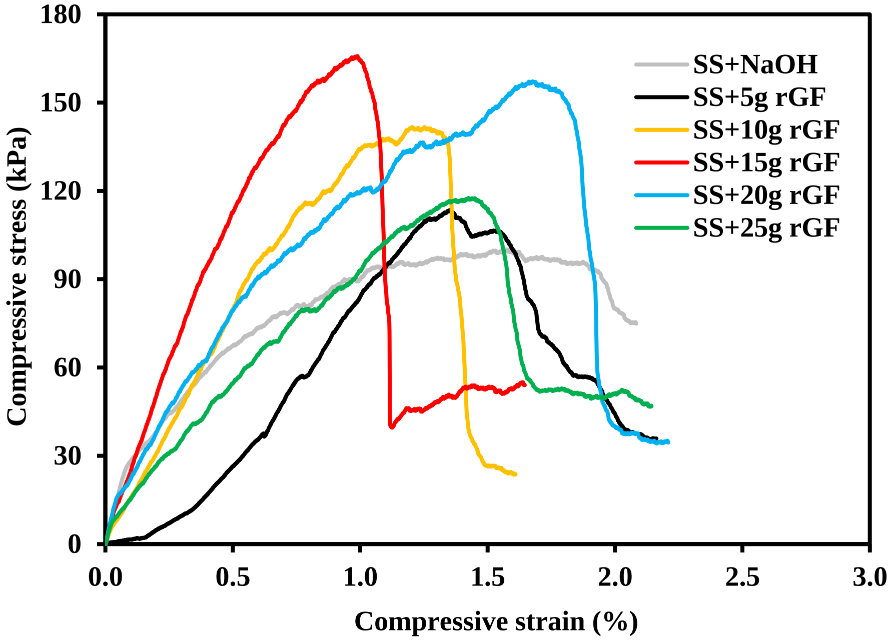

Figure 6-13 An example of the stress-strain curve of geopolymer alkaline activated by SS with various rGF content

The porosity-compressive strength relationship of the geopolymer with rGF is shown in Figure 6-14. In general, the compressive strength decreases with increasing porosity. A small change in porosity (from 81% to 83%) could have a noticeable reduction in the compressive strength (165 kPa to 92 kPa).

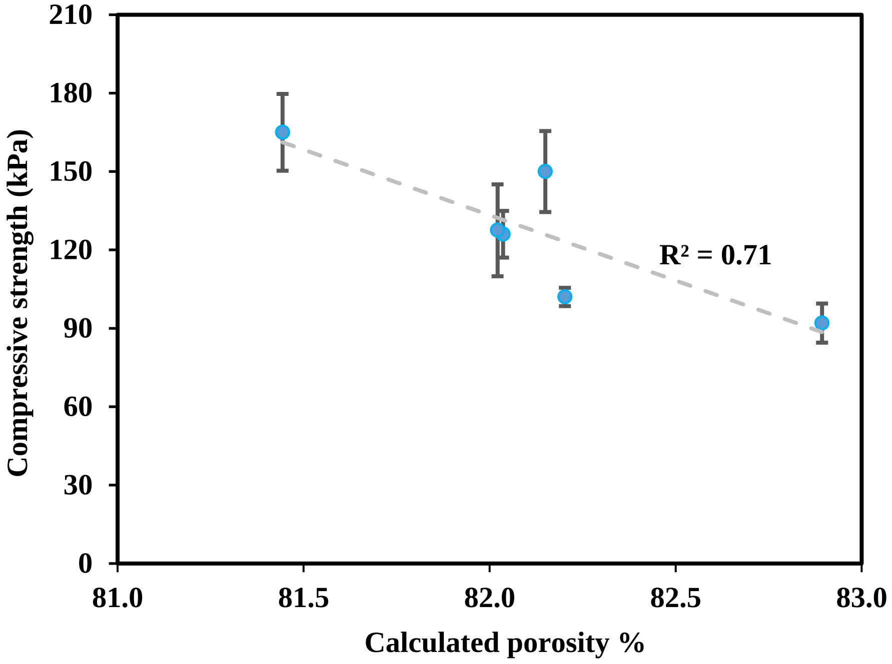

Figure 6-14 Dry density and compressive strength relationship of geopolymer

6.1.2.4. FTIR analysis

Figure 6-15 shows the FTIR spectra of DI H_2O, 10M NaOH solution, commercial sodium silicate solution, and the filtered solution prepared in this work. The peaks at about 650 cm^{-1}, 1600 cm^{-1} and 3300 cm^{-1} are assigned to the hydroxyl groups of adsorbed and bound water [314]. The Si-O-Na absorption stretch is indicated at about 1000 cm^{-1}. No apparent difference in the spectra of NaOH solution and filtered solution can be observed, apart from the wavelength in the range of 800 cm^{-1} to 1000 cm^{-1}. This range is critical in determining the chemical structure of the solutions. In order to study the detailed chemical structure of the prepared samples, the commercial sodium silicate solution and prepared filtered and unfiltered solution was dried at 150 °C for one hour to obtain dry solids and crushed to powder, as shown in Figure 6-16.

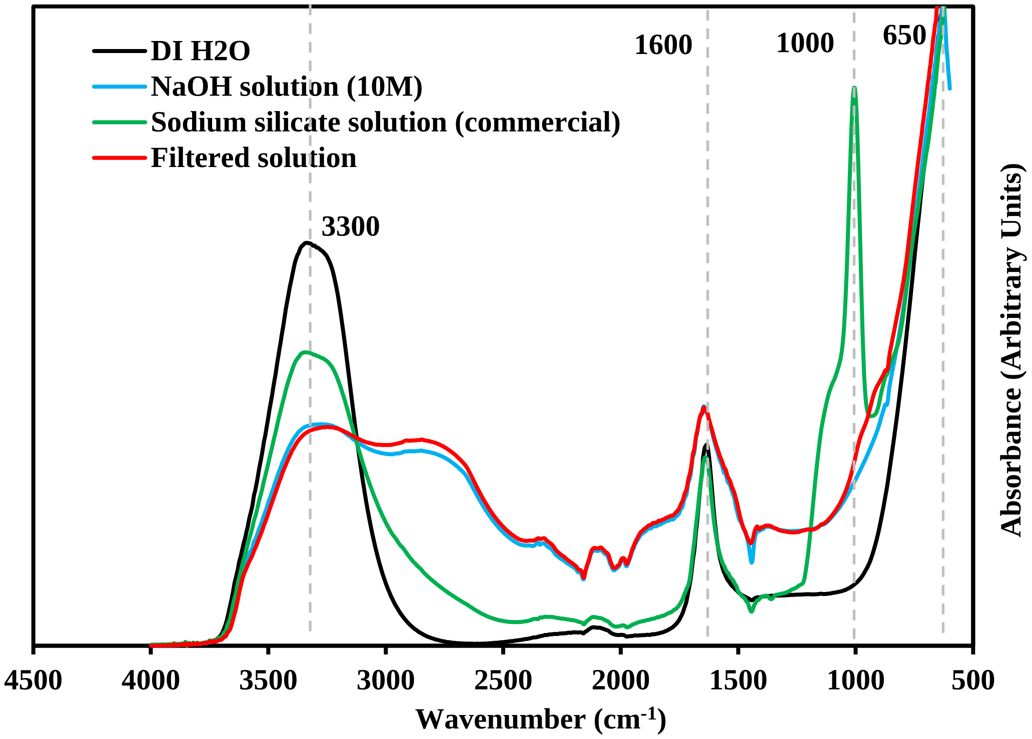

Figure 6-15 FTIR spectra of DI H_2O, 10M NaOH solution, commercial sodium silicate solution, and the filtered solution prepared in this work

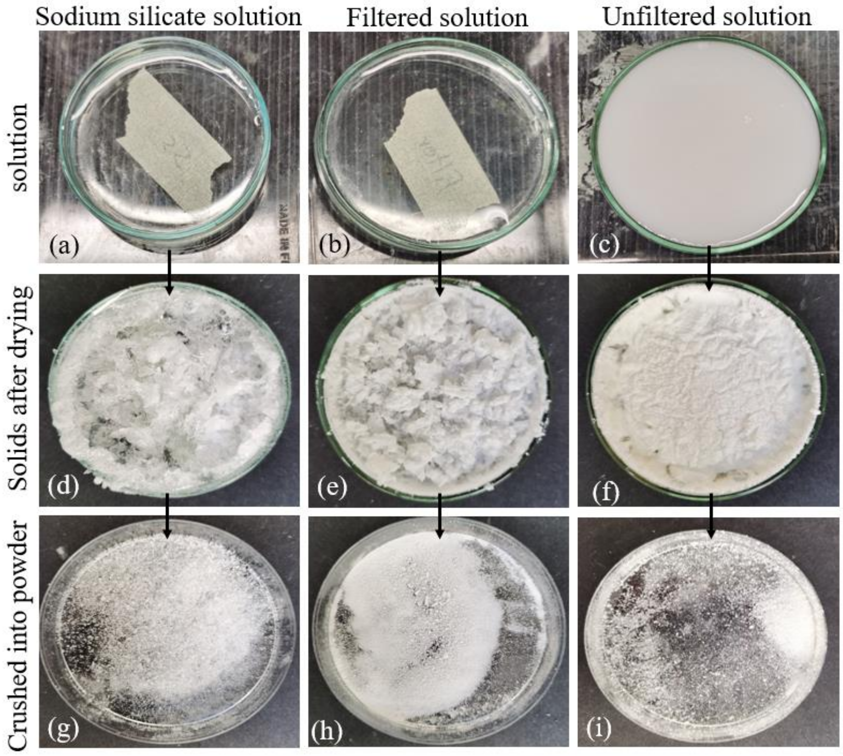

Figure 6-16 Photos of sodium silicate solution, filtered solution and unfiltered solution before drying (a) – (c), solids after drying (d) – (f), and crushed powder (g) – (i)

Figure 6-17 shows the FTIR spectra of the solid from drying out the filtered (meaning what is left on the filter paper), solid from drying out sodium silicate, solid from drying out the unfiltered solution, and solid from drying out filtered solution. The peaks at 1423 cm^{-1} and around 2900 cm^{-1} is attributed to sodium carbonate [315]. The bicarbonate salt structure observed in this peak range could be formed between APS (silane) on glass fibres and carbon dioxide. However, APS should have been oxidized from the fibre after heat treating at 570°C. It is most likely that these absorbances appear due to organic contaminants (carbon dioxide) on the glass from handling or the atmosphere. Moreover, Sairah [316] demonstrated that the intensity of the peak at around 2900 cm^{-1} decreased sharply due to the oxidisation of APS after heat treating the fibres. This peak appeared again in the NaOH treated fibres more prominently than in as received fibres. It was suggested that it might be due to the interaction between organic contaminants and alkali to form a carboxylic species [316].

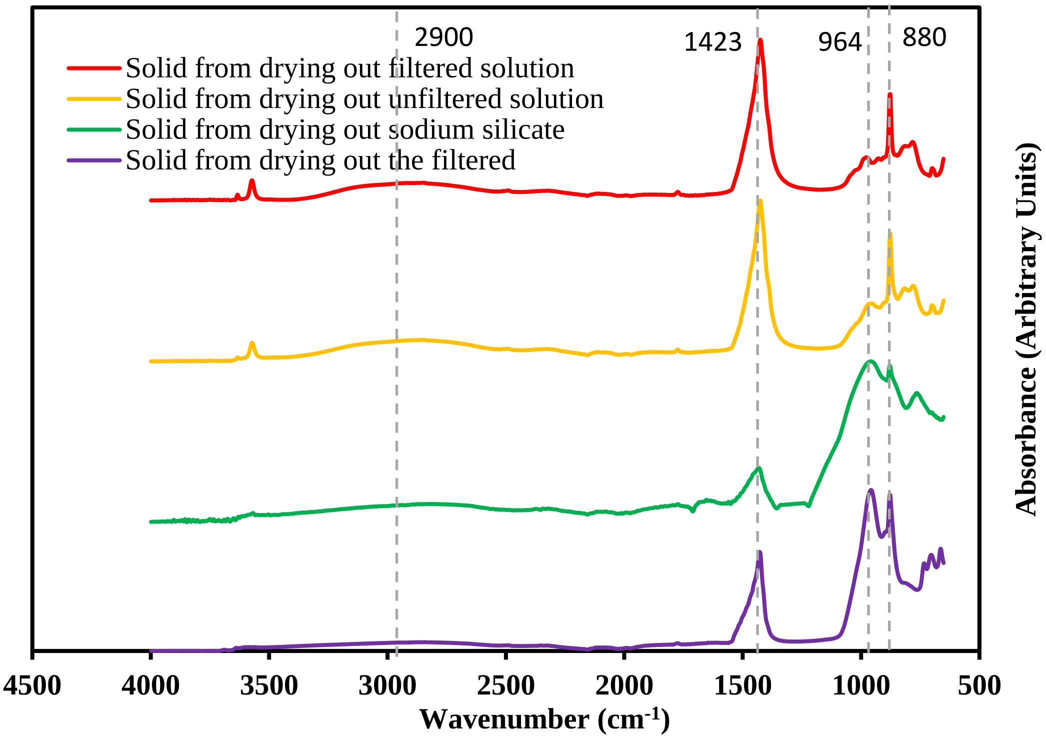

Figure 6-17 FTIR spectra of solid from drying out the filtered (meaning what is left on the filter paper), solid from drying out sodium silicate, solid from drying out the unfiltered solution, and solid from drying out filtered solution. All solutions were dried in an oven at 150°C for 1 hour

The Si-O-Na absorption stretch is indicated at 964 cm^{-1} [317], where this peak is observed at 1000 cm^{-1} for the commercial sodium silicate solution. The intensity of this peak is much weaker in the filtered and unfiltered solution than in the filtered dry solid. This suggests that the Si-O-Na is hardly dissolvable in an aqueous solution, and it could be due to part of sodium ions being wrapped in the crystal interior [314]. The addition of alkali cations in silicates destroys the silicate polymerised network. As a result, the Na observed in IR spectra shifts to a lower wavenumber of the main peaks associated with Si-O-Si bonds stretching and bending [315]. The inclusion of alkali metal cations breaks down the Si-O-Si bonds to form Si-O-M (where M is the alkali metal cations), and Si connects with non-bridging oxygen (NBO) [315]. The research suggested that a higher concentration of NBO groups could be observed with the addition of alkali concentration in the silica network [315]. This improves the dissolution of silica and its availability to form Si-rich structures [315].

The peak observed at about 3500 cm^{-1} in the solid from drying out the filtered and unfiltered solution is suggested as unreacted NaOH [315]. New Si-O-Si stretching bands appear at about 710 cm^{-1} and 880 cm^{-1}, which are attributed to the aggregation of tetrahedral and hence formed Si-O-Si [314]. It is worth mentioning that the strong peaks presented at wavenumber position

964 to 878 cm^{-1} may suggest as anhydrous sodium metasilicate, which is composed of a chain of Si-O tetrahedra, each sharing two oxygens with adjacent Si-O groups [315].

The qualitative analysis of the dry solid is well implemented via FTIR. It can be concluded that the chemical structure of the obtained dry solid shows a disordered sodium silicate structure with a considerable amount of reactive NBO groups. It is concentrated on the solid surface, allowing a faster dissolution and availability for the reaction of Si [315].

6.1.3. Conclusion

The feasibility of introducing recycled glass fibre (rGF) into the geopolymer system was investigated. The rGFs were dissolved in sodium hydroxide solution to form the alkaline activator. The effect of rGF content on the physical properties, thermal and mechanical performance was discussed. In addition, the chemical structure of the fibre dissolution in alkaline solution via FT-IR was investigated.

The addition of rGF showed that the dry density of geopolymer increased (227 kg/m^3 to 246 kg/m^3) with the increasing amount of rGFs in the alkaline activators up to 15 g. The density then started to drop, whereas the porosity remained almost unchanged regardless of the rGF content (between 81% and 83%). Besides, the addition of rGF had no noticeable impact on the thermal conductivity of geopolymer (51.1 to 54.6 mW/m.K) when ignored the outlier since the porosity tends to dictate the thermal behaviour of porous material. Furthermore, the FTIR analysis showed that the chemical structure of the obtained dry solid had a disordered sodium silicate structure. Finally, a linear increase in compressive strength was observed as the number of rGFs dissolved in NaOH solution increased up to 15g rGFs. The compressive strength increased from 92 to 165 kPa, with a 79% improvement. However, further increase of rGF content led to a reduction of the compressive strength.

The involvement of rGF in geopolymer significantly increase the strength without diminishing the thermal performance. In addition, a considerable amount of recycled glass fibre is being reused. This paves a promising way to maximise environmental benefits and shows great potential in the thermal insulation field.

6.2. Aerogel with recycled glass fibres

The fabrication and characterisation of aerogel composites have been investigated in previous chapters. The fibre reinforced aerogel composite could be more economical and environmentally friendly. Today, an increasing amount of waste glass has been produced due to the widespread use of glass in different applications [32]. The glass products are non-biodegradable; thus, recycling and reusing glass are attractive, which could significantly contribute to the prevention of environmental pollution [32]. Therefore, It is worth investigating the involvement of recycled glass fibre in aerogel composites.

The fabrication of short recycled glass fibre (rGF) mats and incorporating the prepared rGF mat with aerogel are scarcely reported. Needle-punching, as a more eco-friendly and lower energy consumption process, has been widely used to fabricate fibre mats compared to chemical bonding and thermal bonding [35]. However, it may be challenging to process short and low strength rGFs, as the fibres need to be long enough to sustain the repositioning force. Sizing, as a chemical bond technique, shows great potential in manufacturing rGF mat due to its ability to enhance the chemical bonding between glass fibre. Therefore, the feasibility of fabricating the rGF mats and incorporating the prepared rGF mat with aerogel is investigated.

In this chapter, recycled glass fibre (rGF) is introduced into aerogel composites. The rGF is used to fabricate the glass fibre mat via wet deposition and chemical bonding process to support the aerogel network. The mechanical and thermal performance of the rGF-aerogel composites is characterised and compared with the aerogel composite reinforced with a commercial glass fibre blanket (prepared in the previous chapter).

6.2.1. Experimental

In this section, the materials used to synthesise fibre mat and aerogel composites are listed. The preparation process and the characterisation method are described.

6.2.1.1. Materials

The chopped glass fibres (cGF, PPG 8069) were supplied by the PPG Fibreglass Company. The fibres were received non-dried with a sizing that is optimised for dispersion in aqueous media. The nominal fibre diameter is 10 μm, and the nominal fibre length is 9 mm. The density of the fibre is 2.55 g/cm^3.

The polypropylene fibres (Armafloc DA3/6) were supplied by Goonvean Fibres Ltd. The polypropylene fibres are chopped with a nominal length of 6 mm, and the density of the fibre is 0.91 g/cm^3.

The rGFs were recycled in-house, as described in Pender [245]. An end-of-life offshore wind turbine blade was cut into regular pieces using a water jet cutter before being thermally recovered. The average fibre length after recycling is 6.8 mm, and the density of the fibre is 2.65 ±0.1 g/cm^3.

(3-Aminopropyl)triethoxysilane (APS) was used as the coupling agent to bind glass fibres, and it was supplied by Sigma-Aldrich UK. It was diluted with deionized water with a 1:99 mass ratio. The precursor used to synthesise aerogel was sodium silicate (34.6 wt%, VWR UK, Na_2O: SiO_2 = 3.43). Other agents, including hydrochloric acid (HCl, 37%), ammonia solution (NH_4OH, 28%), ethanol (EtOH), n-Hexane (95%) and Chlorotrimethylsilane (TMCS), were purchased from VWR UK.

6.2.1.2. Sample preparation

Figure 6-18 shows the fabrication process of a GF/PP mat. A pre-determined amount of GF/PP was first mixed via the wet deposition method. The GF or GF/PP fibres were stirred in water suspension at 1200 RPM for 10 minutes before draining the water. The obtained wet mats were dried in an oven with a set temperature of 110℃ for 4 hours. For the samples with pure rGFs, an additional heating process (570°C) was carried out to remove surface residuals (mainly carbon after the recycling process). The coupling agent (APS) was then sprayed using a spray container on both sides of the mat and redried at 110℃ for 20 minutes to obtain the fibre mat.

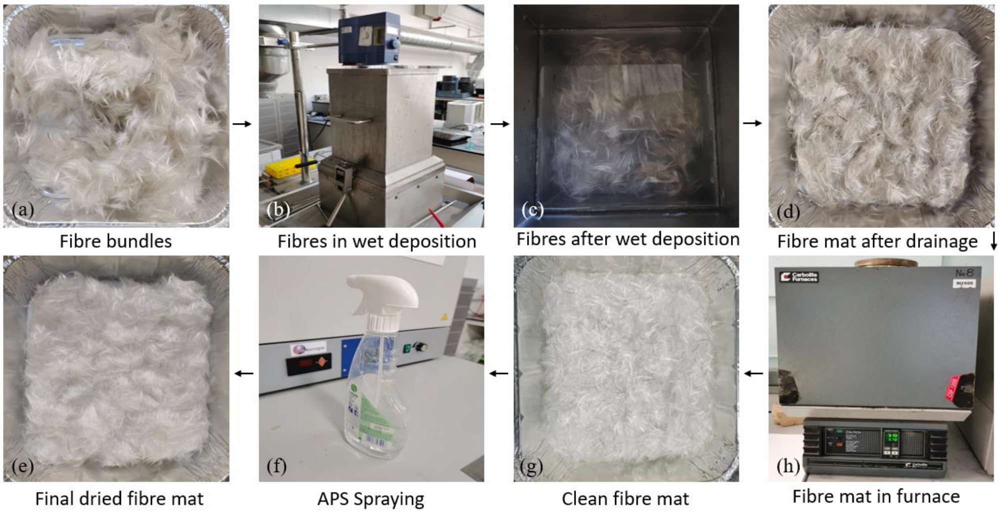

Figure 6-18 Fabrication process of GF/PP mat

The obtained fibre mats are shown in Figure 6-19, and they were then used as the fibre matrix to synthesise fibre reinforced silica aerogel composites following the procedure described in section 5.1.2.

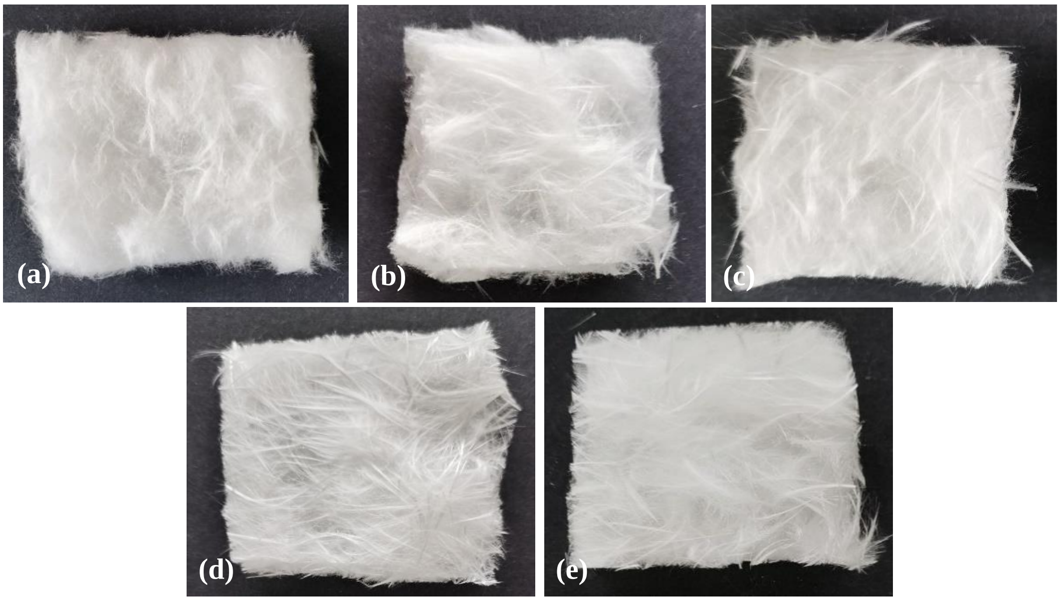

Figure 6-19 Fibre mat (5 × 5 cm) made with mass ratios of cGF: PP (a) 3:7, (b) 5:5, (c) 7:3, (d) neat cGF and (e) neat rGF, respectively

6.2.1.3. Sample characterisation

6.2.1.3.1. Density and porosity

The bulk density of the aerogel composites was calculated using the measured volume of the samples and their mass by an electronic balance with an accuracy of 0.01 g.

The porosity of the aerogel composites was calculated as follow:

$$Porosity=\frac{\frac{1}{\rho_a}-\frac{1}{\rho_s}-\frac{1}{\rho_g}}{\frac{1}{\rho_a}}\times 100\% \qquad \text{(Equation 6-1)}$$

where ρ_a is the bulk density of aerogel composites, ρ_s is the skeleton density of the silica aerogel, generally ρ_s = 2.2 g/cm^3 [298], and ρ_g is the density of fibre. The density of mixed fibre is calculated based on the proportion of the fibres.

6.2.1.3.2. SEM imaging

The morphology of aerogel composites was investigated according to the procedure described in section 5.1.3.2.

6.2.1.3.3. Gas adsorption

Gas adsorption measurement was conducted according to the procedure described in section 5.1.3.3.

6.2.1.3.4. Hydrophobicity

The hydrophobicity test was conducted according to the procedure described in section 5.1.3.4.

6.2.1.3.5. FT-IR analysis

The chemical environments of molecular bonds of the aerogel composites were determined via Fourier transform infrared analysis, and it was conducted according to the procedure described in section 5.1.3.5.

6.2.1.3.6. Thermal gravimetric analysis

The Thermal stability test was conducted according to the procedure described in section 5.1.3.6.

6.2.1.3.7. Thermal conductivity

The XIATECH TC3000E was used to measure the thermal conductivity of the aerogel composites, according to ASTM 1113-2019. It is a transient hot-wire method based on the non-steady-state principle. The measuring accuracy is ± 3%. The hot wire sensor was sandwiched by two layers of samples with a sample size of 5 cm × 5 cm. A Pyrex glass was put on the samples to ensure a uniformly distributed load was applied. A cylindrical weight (500g) was put on the pyrex glass to ensure the sensor was well contacted with both sample surfaces, as shown in Figure 6-20. The pressure load was calculated to be 2.7 kPa. Before testing, the device was calibrated by a standard PMMA glass.

Figure 6-20 XIATECH TC3000E thermal conductivity meter

6.2.1.3.8. Compression test

The compression tests were conducted according to the procedure described in section 5.1.3.8.

6.2.2. Results and discussion

In this section, the effect of the cGF/PP ratio on the physical properties, thermal and mechanical performance was first investigated. The mechanical and thermal performance of the rGF-aerogel composites is then characterised and compared with the aerogel composite reinforced with a commercial glass fibre blanket (prepared in the previous chapter).

6.2.2.1. Morphology and physical properties

Figure 6-21 shows the effect of the cGF/PP ratio on bulk density and porosity of the aerogel composites. In general, the bulk density shows an increasing trend as the number of cGF increases. This is because cGF has a much higher density (2.55 g/cm^3) than PP (0.91 g/cm^3). However, a considerable error is presented due to the irregular shape of the samples resulting in a measurement error of the sample dimensions. This leads to a considerable error for calculating the density shown in Figure 6-21. It is also indicated that the effect of the cGF/PP ratio has no obvious impact on the porosity of the composite, and the porosity for all samples is greater than 87%. The sample with the lowest density (GF/PP ratio of 3:7) does not correlate with the highest porosity, and this may be because the porosity is calculated based on the density of the composites, density of glass fibre and PP fibre as indicated in Equation 6-1. Thus, measurement errors could build-up, leading to an error in calculating the porosity.

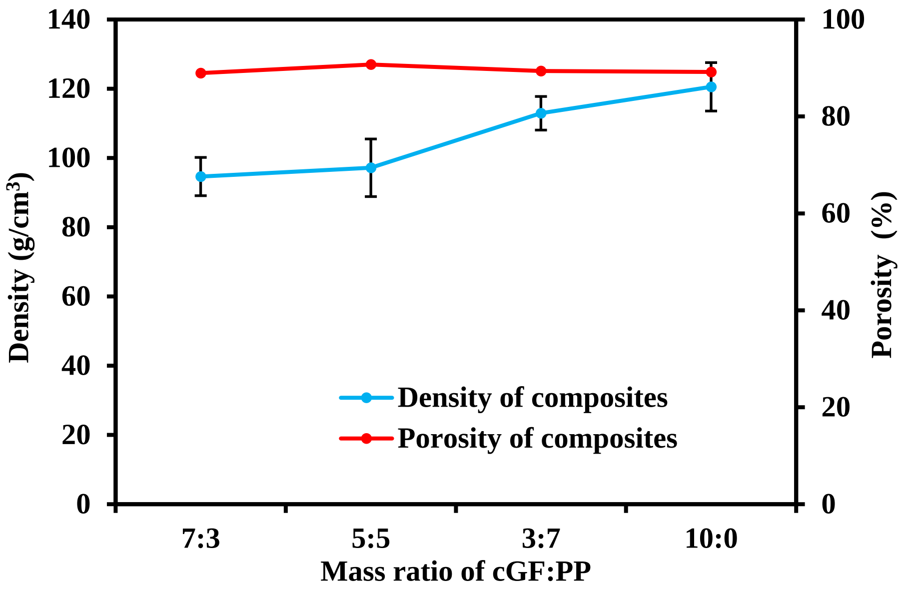

Figure 6-21 Effect of cGF/PP ratio on the density and porosity of aerogel composites

Table 6-2 summarises the physical properties of GF-aerogel made with the commercial needle-punched blanket (as described in chapter 5), in-house cGF mat, and in-house rGF mat. It can be seen that the GF-aerogel made with the commercial needle-punched blanket has the largest density and lowest porosity among those three composites. It is well known that the BET only characterises pores smaller than 100 nm. However, much of the porosity in aerogel blanket, unlike in aerogel itself, is attributed to large pores. Thus, the BET results cannot characterise full pores in the aerogel blanket. The BET surface area per unit mass of all aerogel blankets is much lower than the neat aerogel, as the mass of the aerogel blanket consists of fibre mass and aerogel mass. The cGF-aerogel composite has the lowest density, whereas the BET surface area and pore volume are significantly lower than the others. This may be because the connection between aerogel and fibres is low (as seen in the SEM images below), limiting the reduction of gel shrinkage during the drying process. The aerogel particles could easily fall off during handling. Thus, less mass percentage of aerogel could be presented within the samples, leading to a significant low BET surface area and pore volume per unit mass. The rGF-aerogel composite possesses excellent physical properties. The BET surface area and pore volume are almost doubled compared to the GF-aerogel made with the commercial blanket while a lower density is maintained. It is worth mentioning that the APS sprayed on the in-house rGF mat does not cause the same problem as commercial sizing did (in-house cGF mat). This may be because a much diluted APS solution was used (1 %wt) and the amount of APS applied on the mat is low (not throughout all fibres).

Table 6-2 Physical properties of the aerogel, GF-aerogel (with a commercial needle-punched blanket), cGF-aerogel (with in-house cGF mat), and rGF-aerogel (with in-house rGF mat) composites

Sample	Density (g/cm^3)	Porosity (%)	BET surface area (m^2/g)	Pore volume (cm^{3}g^{-1})	Pore size (nm)
Aerogel	0.184±0.018	91.6	726	2.78	12.1
GF-aerogel with commercial blanket	0.170±0.018	85.6	184	0.75	12.2
cGF-aerogel with in-house cGF mat	0.121±0.007	89.2±1.4	65	0.32	15.9
rGF-aerogel with in-house rGF mat	0.134±0.008	89.6±1.4	311	1.22	12.3

Figure 6-22 and Figure 6-23 show the morphology and SEM images of synthesised aerogel composites reinforced with mat mass ratios of cGF: PP at (a) 3:7, (b) 5:5, (c) 7:3, (d) neat cGF and (e) neat rGF, respectively. It can be seen from Figure 6-23 (a) to (c) that an increasing proportion of glass fibre (smaller diameter) is well captured in the SEM images. In addition, the comparison between Figure 6-23 (d) and (e) seems to indicate that the aerogel composite reinforced with rGF exhibits better connectivity between aerogel and fibre compared to the one with cGF. This is also well observed during the impregnating process, as shown in Figure 6-24. In Figure 6-24, the rGF mat is well impregnated in the sol, whereas the cGF mat is appeared as ‘white colour (colour of the fibre)’ and float on the sol surface. This means that the sol is not easy to ‘coat’ on cGF fibres, although the sol can still flow into the voids within the mat. Nevertheless, a considerable amount of aerogel is presented in the voids between fibres for all samples.

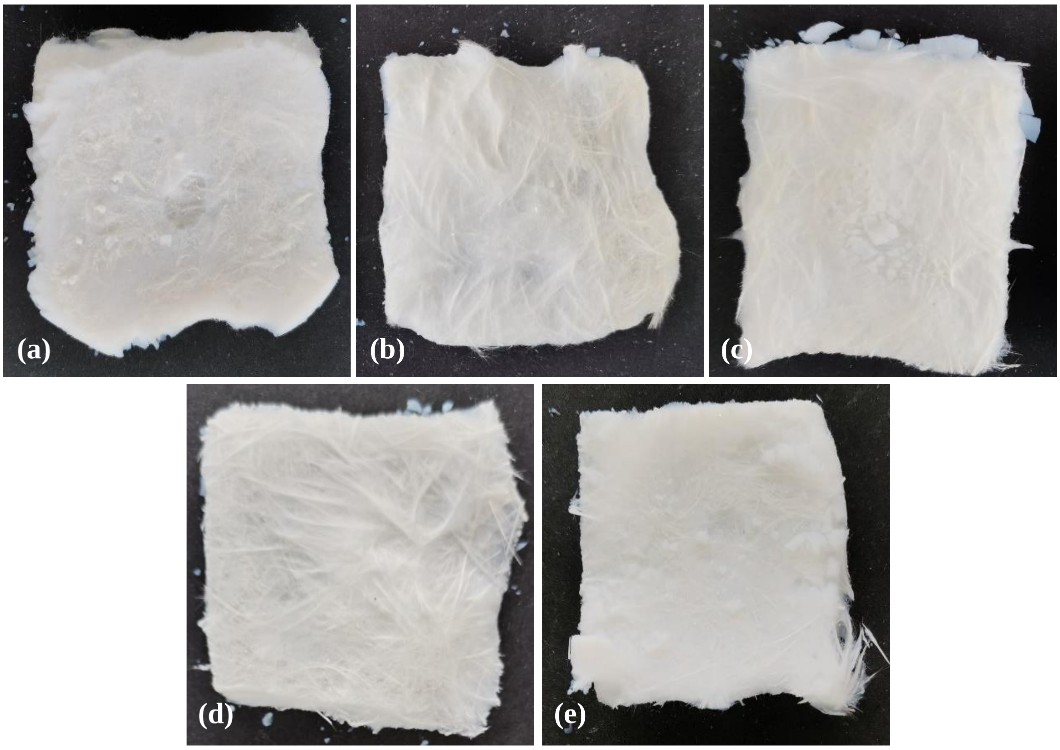

Figure 6-22 Morphology of synthesised aerogel composites reinforced with mat mass ratios of cGF: PP (a) 3:7, (b) 5:5, (c) 7:3, (d) neat cGF and (e) neat rGF, respectively

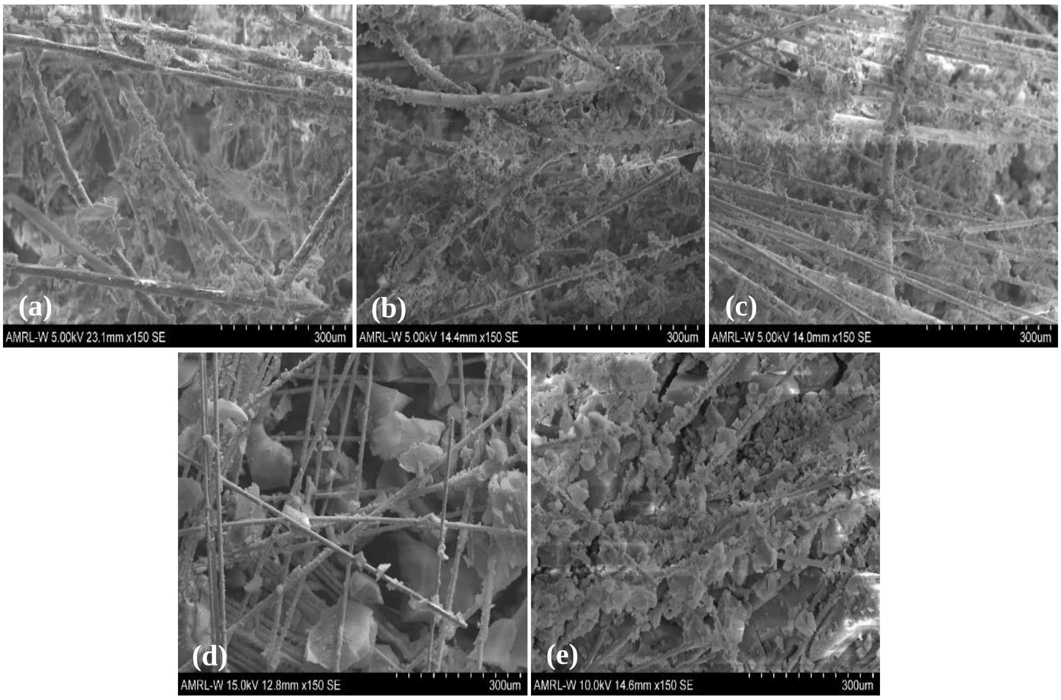

Figure 6-23 Microsturcture of synthesised aerogel composites reinforced with mat mass ratios of cGF: PP (a) 3:7, (b) 5:5, (c) 7:3, (d) neat cGF and (e) neat rGF, respectively

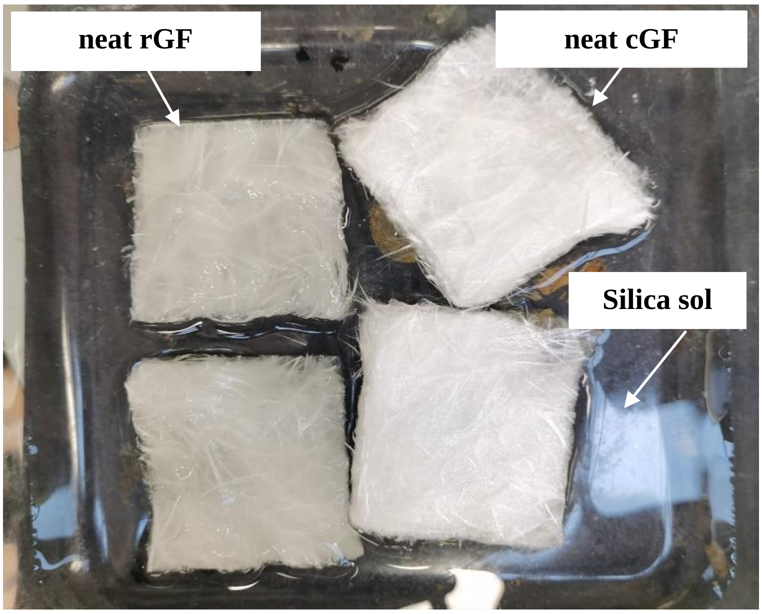

Figure 6-24 Photo of neat rGF and neat cGF mat impregnate in silica sol

The pore size distribution (PSD) of the cGF-aerogel and rGF-aerogel composites are shown in Figure 6-25 (a). It can be seen that the cGF-aerogel and rGF-aerogel composites have finer pore size distribution, with a mean pore diameter of 15.9 nm and 12.3 nm, respectively. The higher the peak, the higher the pore volume of the average pore diameter. Figure 6-25 (b) shows the N_2 adsorption-desorption isotherm of the cGF-aerogel and rGF-aerogel composites. They present a type IV(a) isotherm with a H3 hysteresis loop at $P/P_0 > 0.6$ [300], revealing the mesoporous characteristics of the aerogel. The sharp increase of isotherms in the high relative pressure region ($P/P_0 = 0.95$-1.0) is due to the liquid condensation suggesting the presence of macropore [191]. The fibre-reinforced aerogel composites retain the aerogel nature in terms of the microstructure. The pore sizes are much smaller than the mean free path of air (70 nm) in the atmosphere, which significantly reduces the heat transfer via the gaseous phase. Thus, the thermal insulation performance can be improved [191].

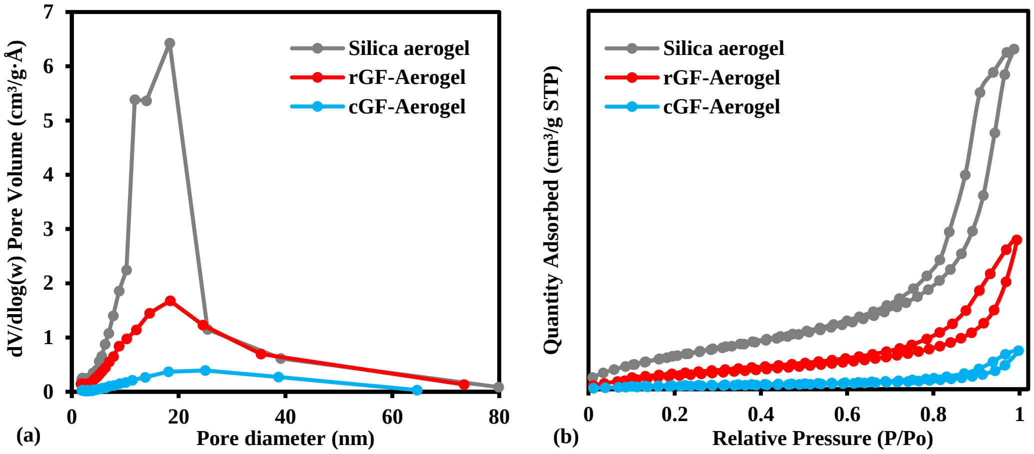

Figure 6-25 (a) Pore size distribution (PSD) and (b) N_2 adsorption-desorption isotherms of rGF-aerogel and cGF-aerogel composites

6.2.2.2. Hydrophobicity and FTIR analysis

Figure 6-26 (a) - (e) and Figure 6-27 (a) - (e) show the photo and microscopic images of a water droplet on the treated surface of aerogel composites reinforced with mat mass ratios of cGF: PP at (a) 3:7, (b) 5:5, (c) 7:3, (d) neat cGF and (e) neat rGF, respectively. The average contact angle is presented in Figure 6-28. It can be seen that the average contact angle is between 128° to 147°. This excellent water-repellent property is stemmed from the treatment of the specimens with TMCS, where the stable methyl groups are responsible for the excellent hydrophobicity of the silica components [20].

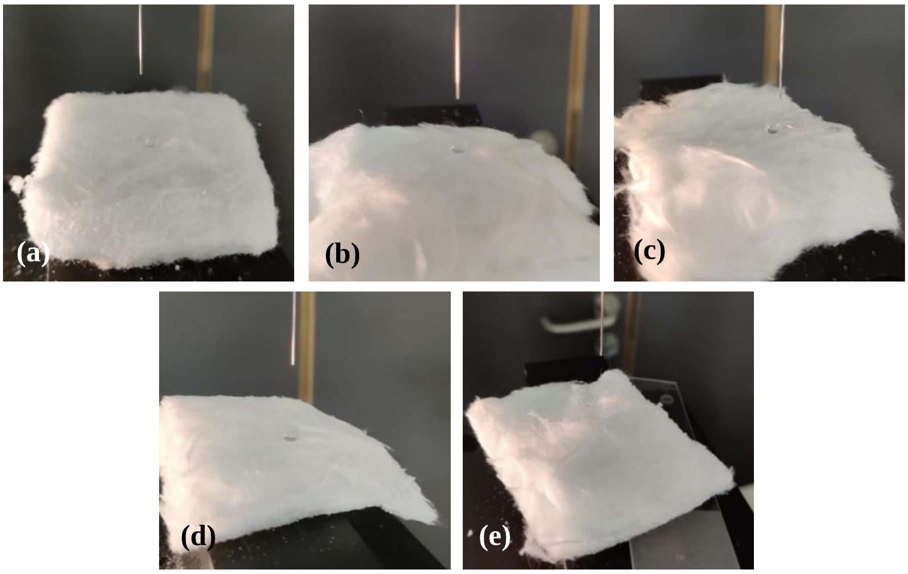

Figure 6-26 The photos of a water droplet on the treated surface of aerogel composites reinforced with mat mass ratios of cGF: PP at (a) 3:7, (b) 5:5, (c) 7:3, (d) neat cGF and (e) neat rGF, respectively

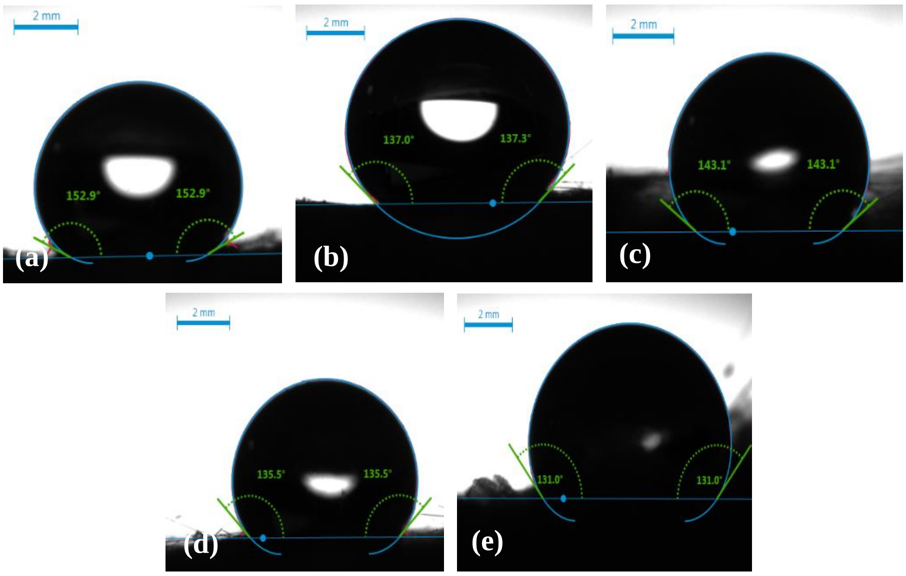

Figure 6-27 The microscopic images of water contact angle measurement of aerogel composites reinforced with mat mass ratios of cGF: PP at (a) 3:7, (b) 5:5, (c) 7:3, (d) neat cGF and (e) neat rGF, respectively

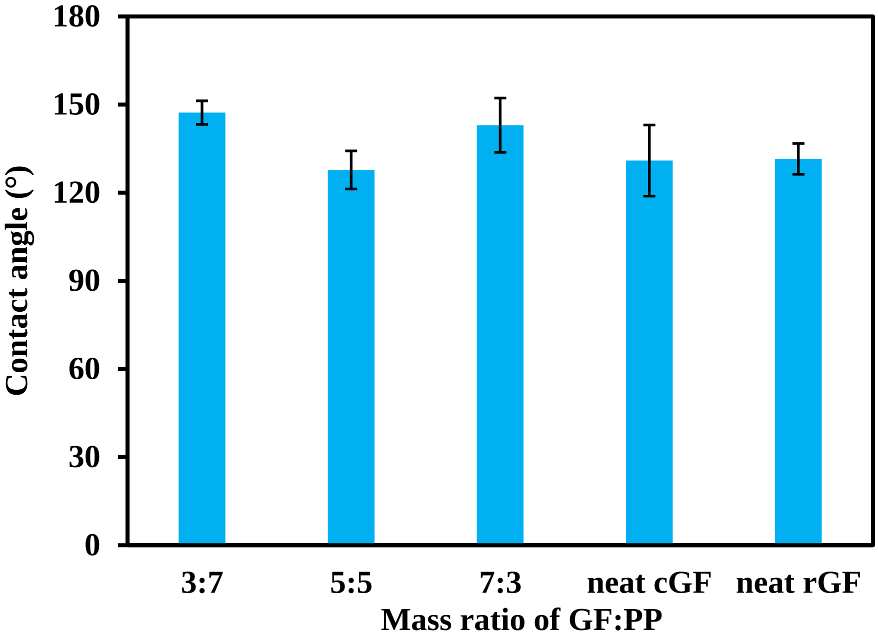

Figure 6-28 Average contact angle of aerogel composites reinforced with mat mass ratios of cGF: PP at (a) 3:7, (b) 5:5, (c) 7:3, (d) neat cGF and (e) neat rGF, respectively

The hydrophobicity of aerogel is attributed to the attachment of -Si(CH$_3$)$_3$ group to the gel surface, which can also be confirmed by the FTIR analysis. Figure 6-29 shows the FT-IR spectrum of fibre mat with different GF/PP mass ratios. It can be seen that apart from the Si-O-Si (absorption peak at about 755 cm^{-1} and 1050 cm^{-1}), all aerogel composites show strong absorption peaks at about 850 cm^{-1}, 1260 cm^{-1} and 2980 cm^{-1}, corresponding to Si-CH$_3$ groups and -CH_3 groups [26, 191]. The presence of these absorption peaks confirms the attachment of -Si-CH_3 groups from the TMCS to the aerogel composite surface, indicating that the surface modification process was successful. Moreover, the bonds at ~3450 and ~1650 representing -OH groups disappear after surface modification.

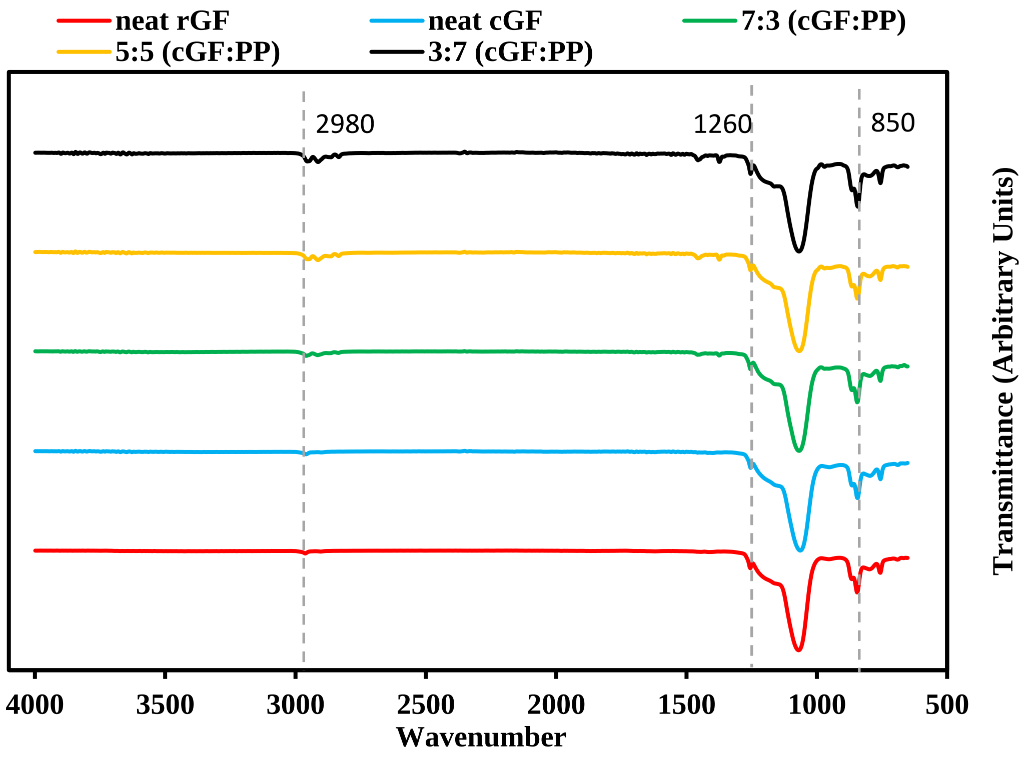

Figure 6-29 FTIR spectrum of aerogel composites reinforced with various fibre mat mass ratios (GF/PP)

6.2.2.3. Thermal properties

The example of the TG curve of synthesised aerogel composites reinforced with various fibre mat mass ratios (GF/PP) is shown in Figure 6-30. It is evident that a higher percentage of cGF leads to better thermal stability. For the composites reinforced with fibre mat mass ratios of 3:7, 5:5 and 7:3, they remain thermally stable up to 210°C due to the thermal degradation of PP fibres. For the composite reinforced with neat cGF and neat rGF, a decrease in the gravity curve is presented at a temperature of approximately 400°C due to the oxidisation of the -CH_3 group [26]. The aerogel composite reinforced with both in-house cGF and rGF mat maintained over 93% of its weight, where only up to 7% of the weight is lost at 800°C. It is worth mentioning that the composite made with rGF has slightly better stability than the one made with neat cGF. Nevertheless, the aerogel composites reinforced with neat glass fibre achieve excellent thermal stability at a high temperature.

The mass percentage of the aerogel was calculated by subtracting the mass of the fibre mat from the aerogel composite, and the mass percentage of PP and glass fibres were calculated based on the mass ratio in the fibre mat. This is based on the assumption that the mass of water is neglible due to hydrophobic aerogel used. Figure 6-31 displays the mass percentage of aerogel, GF, and PP fibre within the aerogel composites. Since PP is thermally degraded completely at 800°C, the remaining weight percentage after thermal treatment shown in Figure 6-30 is in good agreement with the mass percentage of aerogel composites indicated in Figure 6-31.

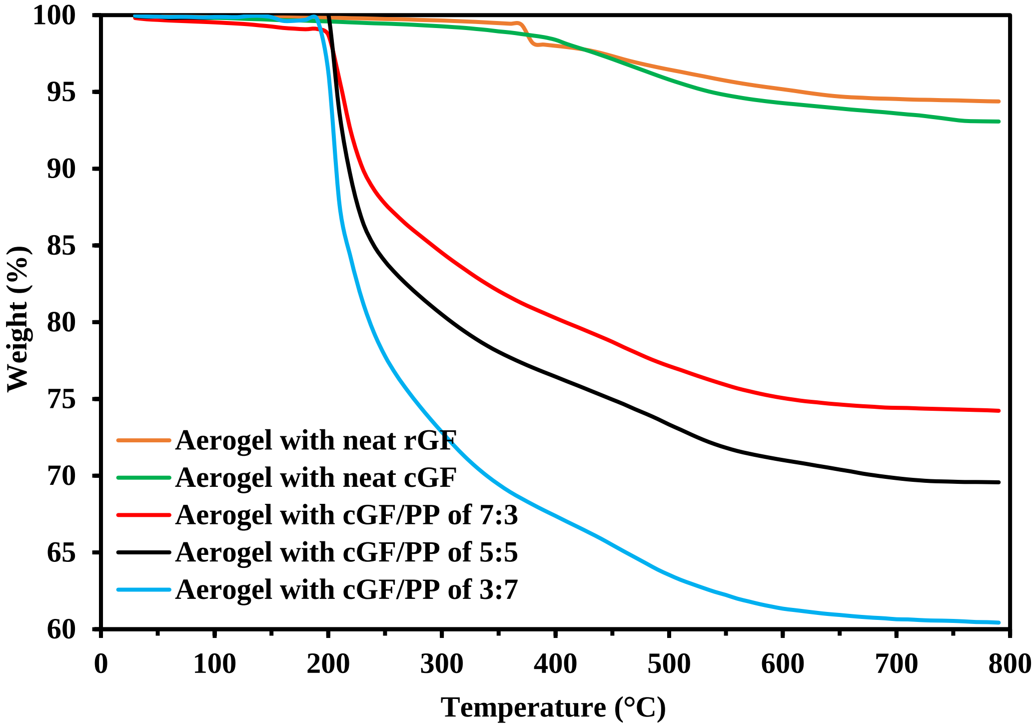

Figure 6-30 TGA curve of synthesised aerogel composites reinforced with various fibre mat mass ratios (GF/PP)

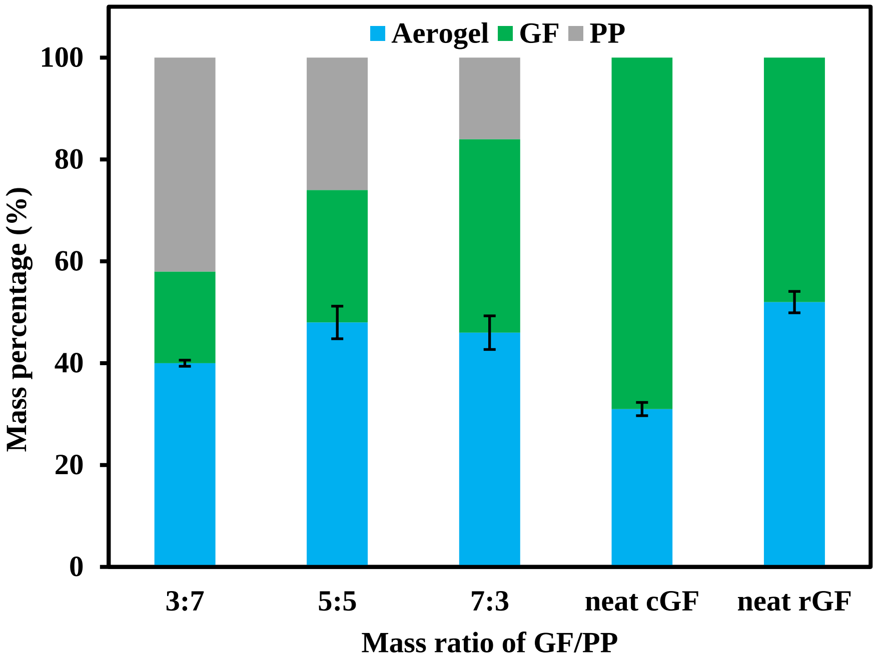

Figure 6-31 Mass percentage of aerogel, GF, and PP fibre within the aerogel composites

Figure 6-32 shows the effect of the cGF/PP mass ratio on the thermal conductivity of neat GF/PP mat and aerogel composites. A linear relationship between the cGF/PP ratio and thermal conductivity for cGF/PP mat is observed (blue data points). Glass fibres have a higher conductivity compared to PP fibres, meaning that heat transfer via solid conduction increases with increasing glass fibre amount. As a result, the thermal conductivity of the cGF/PP mat increases from 33 mW/m.K to 39.4 mW/m.K. The effect of the cGF/PP mass ratio on the thermal conductivity of aerogel composites shows an opposite trend. The thermal conductivity of the aerogel composites is found to decrease with increasing glass fibre amount, as seen in Figure 6-32. The thermal conductivity value reaches the lowest (25 mW/m.K) when aerogel is reinforced with pure cGF. An improvement of 37% is gained compared to pure cGF. Heat transfer in the porous composite material is a complex process, as it involves the combination of solid conduction, gaseous conduction, and radiation. The change of the cGF/PP mass ratio could influence all of these mechanisms. Therefore, it cannot simply describe these trends from any heat transfer mechanism.

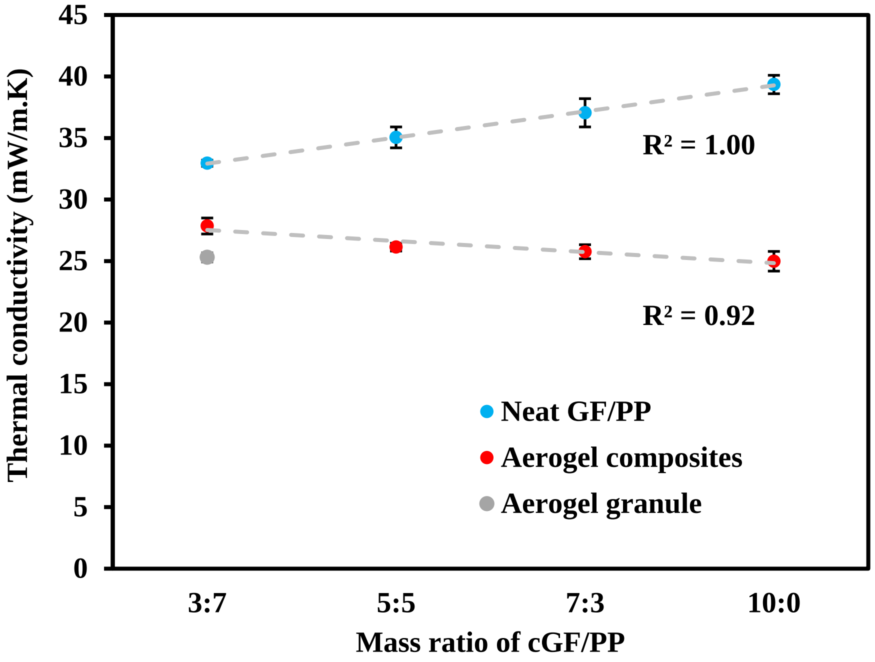

Figure 6-32 Effect of cGF/PP mass ratio on the thermal conductivity of neat GF/PP mat and aerogel composites

Figure 6-33 shows the thermal conductivity comparison of GF-aerogel reinforced with cGF and rGF. It can be seen that the aerogel composite reinforced with rGF has a superior thermal conductivity (23.8 mW/m.K) compared to the one reinforced with cGF (25.0 mW/m.K), although the neat rGF mat has a slightly higher thermal conductivity compared to neat cGF mat. As mentioned in section 6.2.2.1, aerogel composite reinforced with rGF exhibits excellent connectivity between aerogel and fibre compared to cGF. This could minimise the direct contact between fibres, leading to lower solid conduction. Besides, the mass percentage of aerogel within the rGF-aerogel is more significant than the cGF-aerogel, as mentioned in Figure 6-31. This may reduce the gaseous thermal conductivity as more voids are replaced by aerogel. Thus, the thermal conductivity of rGF-aerogel is improved.

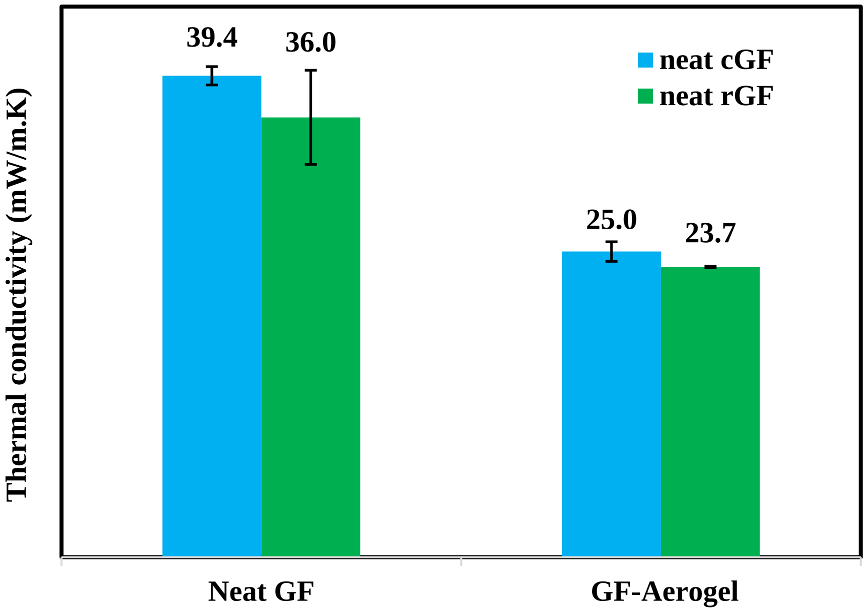

Figure 6-33 The thermal conductivity comparison of GF-aerogel reinforced with cGF and rGF

6.2.2.4. Mechanical properties

Figure 6-34 shows the effect of the cGF/PP mass ratio on the compressive strength of aerogel composites. A linear relationship between the cGF/PP ratio and compressive strength is observed at both 10% and 25% strain. Glass fibres are much stiffer compared to PP fibres, meaning that the ability of load resistance rises with increasing glass fibre amount. As a result, the compressive strength of the composites increases from 0.649 kPa to 2.097 kPa at 25% strain, and an improvement of 220% is achieved. The stress-strain curve of the aerogel composites reinforced with various cGF content is shown in Figure 6-35. The stress-strain curve of aerogel composites can be divided into four different stages: the contact stage, the linear stage, the yielding stage, and the densification stage [191]. The strain in the range of 15% to 25% shows the yielding and densification stage, where the stress increases significantly. At the yield stage, fibres act as the main load capacity part, resulting in a rapid increase in stress. Since the glass fibres are much stiffer than the PP fibres, the increase in the stress is greater with increasing cGF content.

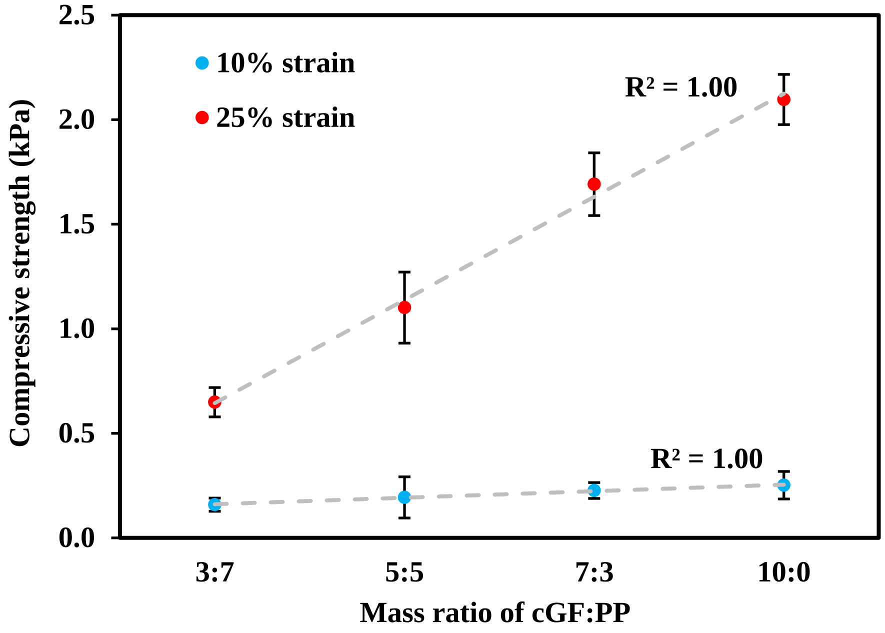

Figure 6-34 Effect of the cGF/PP mass ratio on the compressive strength of aerogel composites

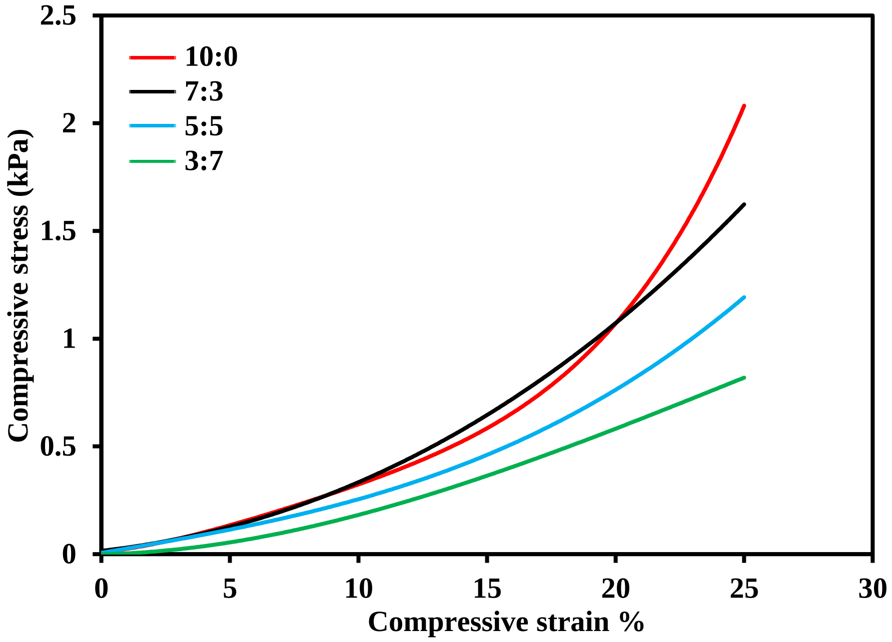

Figure 6-35 The compressive stress-strain curves of aerogel composites reinforced with various fibre mat mass ratios (GF/PP)

The compressive strength comparison and the stress-strain curve of cGF-aerogel, rGF-aerogel, and GF-aerogel made with the commercial blanket (as described in chapter 5) are shown in Figure 6-36 and Figure 6-37, respectively. It can be seen that the aerogel composites reinforced with rGF exhibit greater compressive strength than the ones reinforced with cGF. The stress-strain curve of GF-aerogel can be divided into four different stages: the contact stage, the linear stage, the yielding stage, and the densification stage [191]. At the contact stage, the strain varied from 0% to 10% is caused by the uneven surface of the specimens. The strain in the range of 20% to 25% represents the linear stage, where the slope of the curve remains unchanged, and it is well distinguished in Figure 6-37 (red line against the blue line). The nanopores of silica aerogel act as the main load capacity part, while the fibres are only responsible for the structural integrity of the composite [313]. The strain after 25% shows the yielding and densification stage, where the stress increases significantly. At the yield stage, fibres act as the main load capacity part, resulting in a rapid increase in stress. The SEM images in Figure 6-23 seem to indicate that the aerogel composite reinforced with rGF exhibits better connectivity between aerogel and fibre compared to the one with cGF. This leads to a high load resistance during compression. Thus, the mechanical performance of rGF-aerogel is improved. As a result, the compressive strength of the rGF-aerogel increases from 2.1 kPa to 5.8 kPa, with 170% of improvement, even though the stiffness of neat rGFs reduced significantly after the thermal recycling process [245, 246]. It is also worth mentioning that the rGF-aerogel possesses higher compressive strength than the aerogel reinforced with the commercial needle punched GF mat. The reason is unclear at this point, and further work is required.

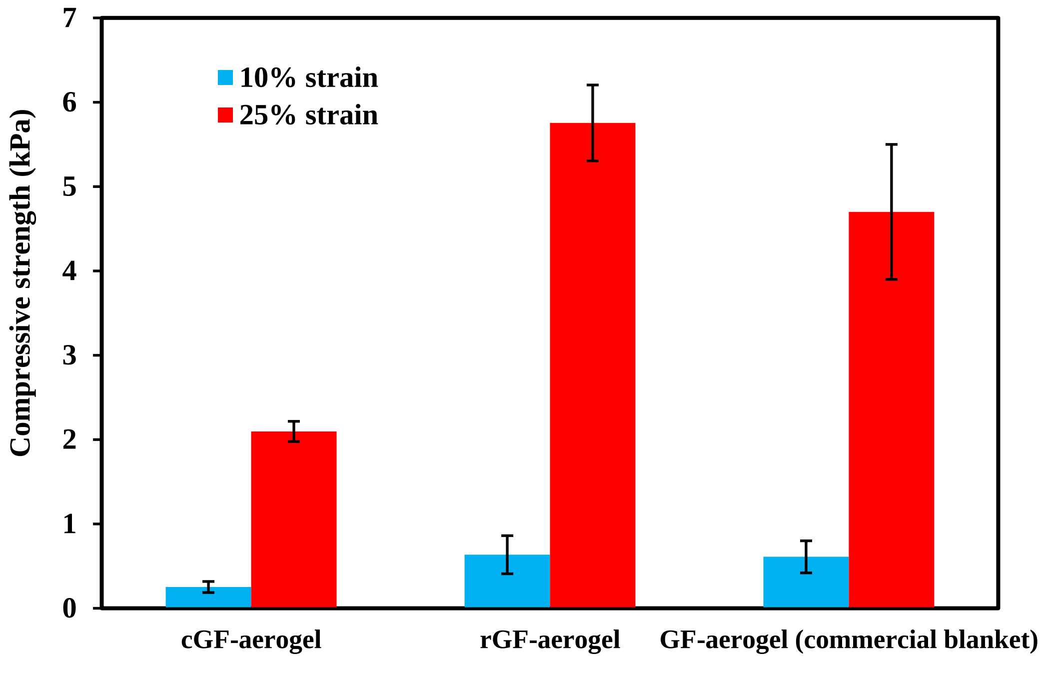

Figure 6-36 The compressive strength comparison of cGF-aerogel, rGF-aerogel, and GF-aerogel made with the commercial blanket

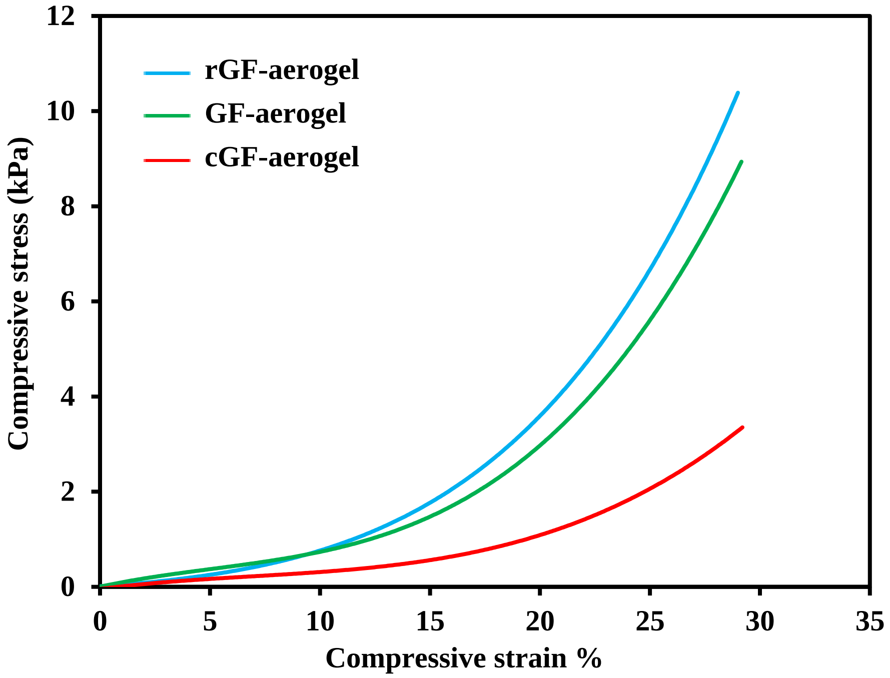

Figure 6-37 The compressive stress-strain curves of cGF-aerogel, rGF-aerogel, and GF-aerogel made with the commercial blanket

The strain from 20% to 25% of aerogel composites shows preferable linearity corresponding to the linear stage. Thus, Young's modulus is calculated based on the strain of 20% and 25% and the corresponding compressive stress. The calculated compressive modulus of rGF-aerogel, cGF-aerogel and GF-aerogel made with commercial GF blanket is summarised in Figure 6-38. It can be seen clearly that the rGF-aerogel shows a superior compressive modulus than the cGF-aerogel, with a two-fold improvement. This shows that the rGF-aerogel has a much higher resistance to compressive deformation at a given pressure load than the cGF-aerogel. It is also worth mentioning that the rGF-aerogel possesses a higher compressive modulus than the aerogel reinforced with the commercial needle punched GF mat. The reason is unclear at this point, and further work is required.

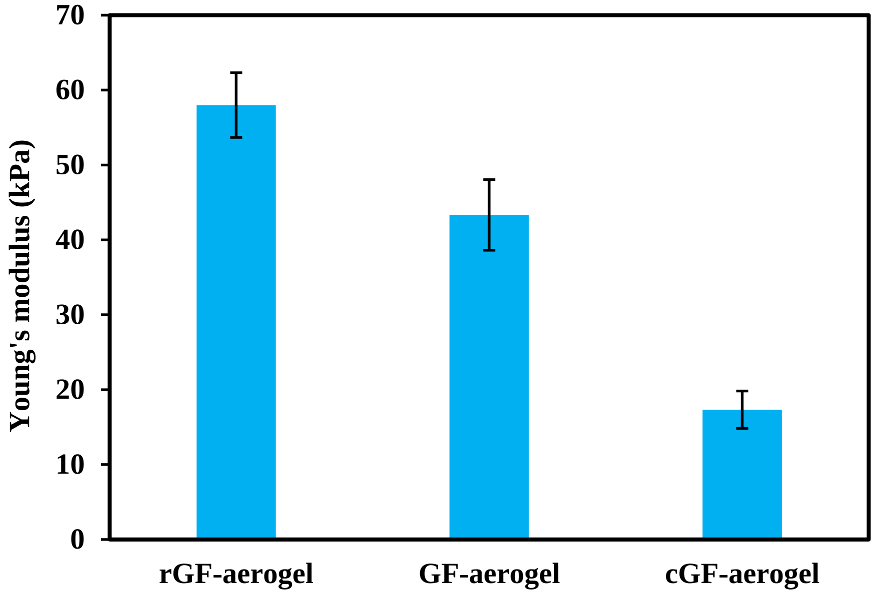

Figure 6-38 Compressive modulus of rGF-aerogel and GF-aerogel made with the commercial blanket and cGF-aerogel

6.2.3. Conclusion

The feasibility of introducing recycled glass fibre (rGF) into the aerogel system was investigated. Glass fibre mat was first fabricated via wet deposition and chemical bonding, and it was then used to support the aerogel network. The mechanical and thermal performance of the rGF-aerogel composites was characterised and compared with the aerogel composite reinforced with a commercial glass fibre blanket (prepared in the previous chapter).

The effect of the cGF/PP ratio on the physical properties, thermal and mechanical performance was first investigated. The results showed that bulk density possessed an increasing trend as the number of cGF increased, whereas the porosity had no apparent difference. The obtained samples showed an excellent water-repellent property with a maximum contact angle of 147° due to the treatment with TMCS. The hydrophobicity of samples was also confirmed by the FTIR analysis. Besides, a linear relationship between the cGF/PP ratio and thermal conductivity for cGF/PP mat was observed, while the thermal conductivity of the aerogel composites decreased with increasing cGF amount. The thermal conductivity value reached the lowest (25 mW/m.K) when aerogel was reinforced with neat cGF. An improvement of 37% was gained compared to the cGF mat. The effect of the cGF/PP ratio on compressive strength also showed a linear relationship at both 10% and 25% strain. The compressive strength of the composites increased from 0.65 kPa to 2.10 kPa at 25% strain, and an improvement of 220% was achieved. These findings provide valuable suggestions when two or more fibres are selected to fabricate fibre mat and reinforced aerogel composites to meet a particular requirement (i.e., flexibility, heat resistance, or good insulation).

Recycled glass fibre mat was then successfully fabricated via wet deposition and chemical bonding process. In this process, less amount of coupling agent was used by spraying it on the fibre surface. This finding provides valuable suggestions for the preparation of recycled short fibre mats.

The prepared rGF-aerogel had a low thermal conductivity (23.8 mW/m.K). Besides, the rGF-aerogel possessed higher compressive strength (5.8 kPa at 25% strain) than the aerogel reinforced with the commercial needle punched GF mat (4.7 kPa at 25% strain, prepared in chapter 5). Although the thermal conductivity of the rGF-aerogel is slightly higher than the aerogel reinforced with the commercial needle punched GF mat (18.3 mW/m.K), it still paves a promising way to maximise environmental benefits and shows great potential in the thermal insulation field.

7. The potential application of aerogel composites in thermal insulating packaging

It was experimentally demonstrated that the aerogel composites showed an excellent thermal insulation performance in previous chapters. In the packaging industry, conventional insulation materials may no longer satisfy the requirement of temperature control during package delivery due to increasing market demand for long-haul transportation of fresh goods (e.g. foods and medicine). Besides, Synthetic (plastic) materials have become a significant problem to the environment nowadays as they can lead to contamination of a wide range of natural terrestrial, freshwater and marine habitats [20]. Therefore, the feasibility of using aerogel composites in packaging is worth investigating to improve the thermal insulation performance of the packagings and reduce plastic pollution.

A number of researches have been focused on investigating the thermal performance of packaging, including analytical models and experimental work. However, the use of aerogel composites in this field is rarely reported. In addition, the factors influencing package insulation performance have not been studied comprehensively. Furthermore, a simplified analytical model accompanied by the ice melt test lead to significant uncertainty; therefore, both the analytical model and experimental work could be improved.

In this chapter, the thermal insulation performance of a typical shipping container with different insulation materials, including aerogel composites, is evaluated. An optimised mathematical model is derived and used to analyse the effect of packaging parameters on insulative performance. The novel aspect of this model is incorporating two mathematical models described in the literature to improve the accuracy of the calculated results [36, 37]. Some crucial factors, such as surface emissivity and thermal conductivity of materials, were measured experimentally instead of using literature value to improve the accuracy of the model. A number of experiments are then set up to validate the optimised model comprehensively. The effect of parameters, including surface emissivity, insulation thickness, insulation materials, amount of coolants and surrounding temperatures, on package insulative performance is investigated.

7.1. Analytical modelling

In order to investigate the feasibility of using aerogel composites in packaging, an analytical model has been optimised based on the previously developed model to understand heat flow in the passively insulated package [318]. The analytical model is based on thermal energy balance. This balance presents a synthesis of elementary thermal processes such as accumulation of heat, heat transfer and conversion of heat into another form of energy [37]. The novel aspect of this model is incorporating two mathematical models described in the literature to improve the accuracy of the calculated results [36, 37].

Starting with the basic energy balance Equation:

$$Q_{in}\text{-}Q_{out}=\Delta U \qquad \text{(Equation 7-1)}$$

where Q_{in} is the energy transferred into the system via heat transfer in watts, Q_{out} is the energy transferred out of the system via heat transfer in Watts, and ΔU is the internal energy change in the system, i.e. total heat flow across a packaging in watts.

Assuming that energy is only transferred into the system, Equation 7-1 can be written as:

$$Q_{in}=\Delta U \qquad \text{(Equation 7-2)}$$

The basic balance Equation has the next form

$$\frac{dQ}{dt} = \Delta U = Q_{in} \qquad \text{(Equation 7-3)}$$

The heat change rate across the system can be written as:

$$\frac{dQ}{dt} = m.c.\frac{dT}{dt} \qquad \text{(Equation 7-4)}$$

In this packaging model, it is assumed that the mass of both product and coolant are considered; therefore, Equation 7-4 is written as:

$$\frac{dQ}{dt} = (m_1.C_1 + m_2.C_2).\frac{dT}{dt} \qquad \text{(Equation 7-5)}$$

where m_1 is the mass of product in kg, C_1 is the specific heat capacity of product in J/kg.K, m_2 is the mass of coolant in kg, C_2 is the specific heat capacity of coolant in J/kg.K, and $\frac{dT}{dt}$ is the temperature change per time unit in K/s.

Heat flow across a packaging can be written as both Equation 7-6 and 7-7 [36]:

$$Q_{in}=HPR \times \Delta T \qquad \text{(Equation 7-6)}$$

$$Q_{in} = \frac{\Delta T}{R_Q} \qquad \text{(Equation 7-7)}$$

where HPR is the heat penetration rate in W/K, ΔT is the temperature difference between inside and outside of the system in K, and R_Q is the total thermal resistance in K/W, resulting from conduction, convection and radiation.

Therefore, the relationship between heat penetration rate and total thermal resistance crossing the system can be derived as (know as the thermal mass of packaging):

$$R_Q = \frac{1}{HPR} \qquad \text{(Equation 7-8)}$$

7.1.1. The thermal resistance of a multi-layered wall (RW)

Figure 7-1 demonstrates a one-dimensional diagram of a multi-layered wall. Air spaces separate liners. The liner surface temperature at both sides is labelled as '*T*', and the liner's thickness is marked as '*th*' with the numerical subscript system shown [36].

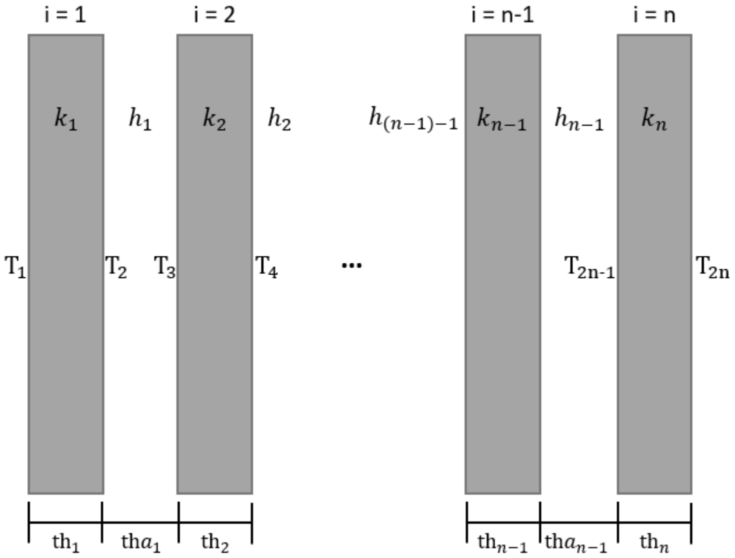

Figure 7-1 Example of a multilayer wall, reproduced from [36]

The thermal resistance of the multi-layered wall (RW) can be calculated by applying the concept of a thermal network [36]:

$$RW = \sum_{i=1}^{n} \frac{th_i}{k_i} + \sum_{i=1}^{n-1} \frac{1}{h_i} \qquad \text{(Equation 7-9)}$$

where n is the number of layers, k_i is the thermal conductivity of layer i in W/m.K, th_i is the thickness of layer i in meter, and h_i is the overall convection and radiation heat transfer coefficient of surface i in W/m^{2}K.

Increasing RW raises the resistance to heat penetration and makes the wall a better insulator [36]. A major question concerning heat transfer through air spaces in the multi-layered wall is whether heat flows by conduction or convection [36]. It is stated that when the thickness of the air space is smaller than 13 mm, most of the heat transfer in these air spaces is dominated by conduction regardless of the material surface temperature. Equation 7-9 can be described as Equation 7-10 based on the earlier study [36]. However, in this project, it is assumed that there is no significant air space between each layer (much less than 13 mm). Thus the thickness of air space (tha1, tha2 and tha3) is assumed to be zero.

$$RW = \sum_{i=1}^{N} R_i th_i + 0.039tha1 + 0.037tha2 + \sum_{i=1}^{N_3} \frac{0.217tha3_i}{5.918+tha3_i} \qquad \text{(Equation 7-10)}$$

where N is the number of layers, R_i is the R-value per millimetre for i *th* layer in m^2.K/W.mm, th_i is the thickness of layer i in mm, *tha1* is the total thickness of those air spaces where both bounding surfaces are covered with aluminium foil in mm, *tha2* is the total thickness of those air spaces where only one bounding surface is covered with aluminium foil in mm, N_3 is the number of the air spaces without foil on either bounding surface, and $tha3_i$ is the thickness of i *th* non-foiled air space in mm.

The RW for multi-layered walls can be calculated via Equation 7-10. An example of the multi-layered wall system is shown in Figure 7-2. For this wall construction, there are two layers with one air space.

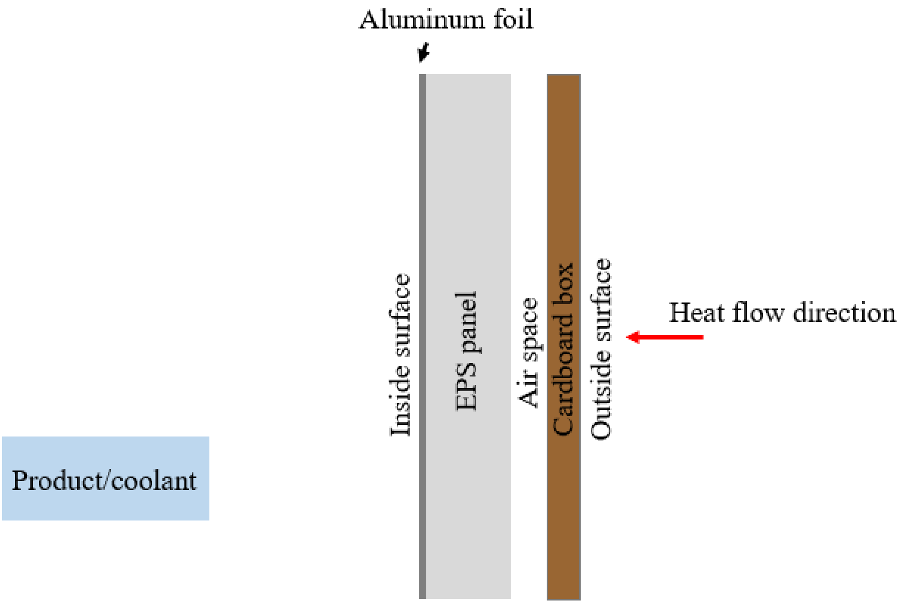

Figure 7-2 An example of the multi-layered wall system

7.1.2. Heat penetration rate

Heat penetration rate (HPR) is used to quantify the insulating ability of a package, and it is the rate in watts at which heat penetrates the container per degree of the temperature difference between the outside and inside air [36]. A diagram of a typical insulating package is illustrated in Figure 7-3. In this design, the coolant is considered as the product.

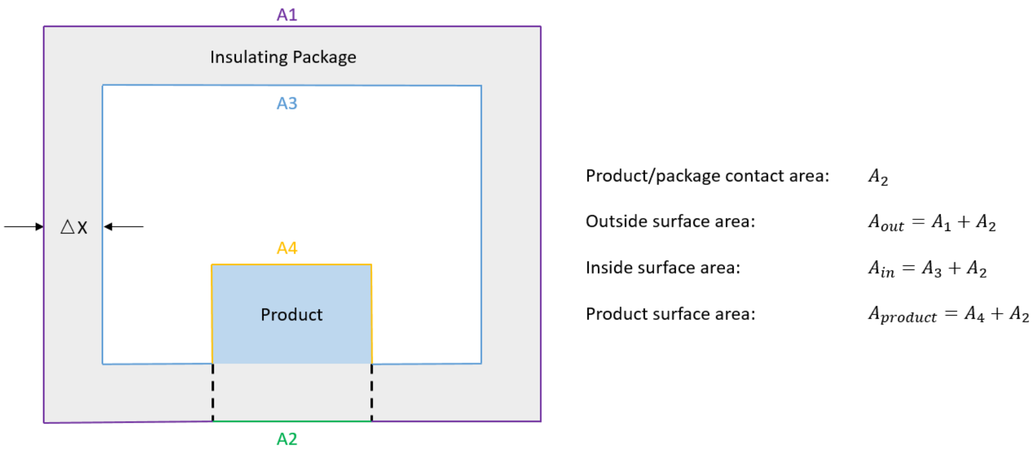

Figure 7-3 Illustration of a typical insulating package, reproduced from [36]

The HPR for the insulating package can be calculated using the procedure described in [36]. The surface area A_1, A_2, A_3, and A_4 is first calculated. Outside surface emissivity (ε_{out}), inside surface emissivity (ε_{in}) and product surface emissivity ($\varepsilon_{product}$) is then measured using an infrared thermometer. Outside surface radiative heat transfer coefficient is obtained using Equation 7-11 [36]:

$$h_{out}=1.778+5.198\ \varepsilon_{out} \qquad \text{(Equation 7-11)}$$

where h_{out} is the outside surface heat transfer coefficient in W/m^2.K, and ε_{out} is the outside surface emissivity.

Inside surface radiative heat transfer coefficient is calculated using Equation 7-12 [36]:

$$h_3=3.557\frac{A_4}{A_3+A_4}+\frac{4.600}{\frac{A_3\;1}{A_4\varepsilon_{in}}+\frac{1}{\varepsilon_{product}}-1} \qquad \text{(Equation 7-12)}$$

where h_3 is the inside surface heat transfer coefficient in W/m^2.K, ε_{in} is the inside surface emissivity, A_3 equals to $A_{in}-A_2$ in m^2, and A_4 equals to $A_{product}-A_2$ in m^2.

The heat penetration rate is finally determined using Equation 7-13 [36]:

$$HPR=\frac{1}{\frac{1}{h_{out}A_{out}}+\frac{1}{\frac{1}{\frac{1}{h_3A_3}+\frac{RW}{\sqrt{A_1A_3}}}+\frac{A_2}{RW}}} \qquad \text{(Equation 7-13)}$$

where HPR is the heat penetration rate in W/K, A_{out} is the outside surface area in m^2, $\varepsilon_{product}$ is the product surface emissivity, A_1 equals to $A_{out}-A_2$ in m^2, A_2 is the product/package contact surface in m^2, and RW is the thermal resistance of the multi-layered wall in m^2.K/W.

7.1.3. Analytical solution

The ordinary linear differential equation of first order is obtained by substituting Equation 7-5 and 7-7 in Equation 7-3:

$$R_Q\ (m_1.C_1+m_2.C_2)\ \frac{dT}{dt}+T_i= T_E \qquad \text{(Equation 7-14)}$$

where R_Q is the total thermal resistance in K/W, which is the combination of conduction, convection and radiation, m_1 is the mass of the product in kg, C_1 is the specific heat capacity of product in J/kg.K, m_2 is the mass of the coolant in kg, C_2 is the specific heat capacity of coolant in J/kg.K, $\frac{dT}{dt}$ is the temperature change per unit time in K/s, T_i is the initial temperature of the product in K, and T_E is the exterior surrounding temperature in K.

The analytical solution describing the temperature change inside the package as a function of time can finally be written as:

$$T(t)=(T_i-T_E)\ e^{-\frac{t}{R_Q\ (m_1.C_1+m_2.C_2)}}+T_E \qquad \text{(Equation 7-15)}$$

Several assumptions have been applied when developing the model. Firstly, conduction is considered as a dominating mechanism for heat transfer in a perfectly closed package surrounded by negligible fluid displacement. Furthermore, it is assumed that there is no significant air gap between insulation materials and cardboard box and temperature change of coolant, and the transported product will change at the same rate with time. Finally, the uniform temperature distribution is assumed at any given time for the coolant and the product in the package. The key input parameters for this model are package dimensions, thickness and thermal conductivity of an insulation liner, the mass of coolants, material surface emissivity and surrounding temperature. These parameters can be varied within the model to predict the insulating performance of a packaging design, which is the main novel aspect of the developed model.

In the present work, the package insulating performance was characterised by the maximum insulation time (MIT), which was defined as the time required for coolant temperature increase from -20°C to 5°C. Previous research has proven that 5°C tends to be an upper limit temperature for the transportation of perishable goods (e.g. fish) [262, 319]. When phase change materials (e.g. ice) were present inside the package, the latent heat of fusion of coolant must be taken into account to calculate the MIT. During the phase change, the temperature was set to be constant in this work, and the amount of time required to complete the phase change was calculated when total heat flow reached the latent heat determined by the amount of coolant and its specific latent heat. Before and after the phase change, Equation 7-15 was used to determine the product's temperature changes. The total time associated with the sensible heat was obtained by implementing a 'for' loop function of Equation 7-15 in MATLAB to calculate the package internal temperature every second elapse. The novel aspect of this model is incorporating two mathematical models described in the literature to improve the accuracy of the calculated results [36, 37]. The total thermal resistance ($R_{Q)}$ in Equation 7-15 is calculated via Equation 7-8 and Equation 7-13. The model also calculated the amount of energy being added and total heat flow across packaging walls to identify when phase change should commence and finish. As a result, a complete temperature-time profile before, during and after coolant phase change was obtained. MIT was obtained at a temperature of 5°C.

7.2. Experimental validation of the analytical model

The heat flow mechanism in the passively insulated package is well presented via the analytical model. A number of experiments are then set up to validate the optimised model comprehensively. The initial temperature of the coolant/product is -21°C, where the maximum insulation time (MIT) is obtained at a temperature of 5°C. The surrounding temperature of the packages is set to be a variable. The novel aspect of this experiment is to use an aerogel blanket as an insulated liner. The factors influencing the MIT of the insulated packages are also studied comprehensively. The material used and the measurement strategy are first outlined.

7.2.1. Materials

Single corrugated cardboard boxes with dimensions 25.6 × 20.5 × 21.2 cm and 38.1 × 25.4 × 25.4 cm with a thickness of 2.68 mm were obtained from Packaging Now Ltd. PE liners and packaging grade EPS liners (10-12 g/L) were purchased from an online store. Food catering aluminium foil was supplied by Kirkland. Kingspan TF70 PIR boards were provided by Encon Insulation Ltd. Aerogel blanket of 1 cm thickness was purchased from Aerogel UK Ltd. Mylar bags (PET film sandwiched by aluminium foil) were obtained from Fresherpack Ltd. Two 100 g, 200 g and 400 g Thermos ice packs (99.4% H_2O) purchased from Miage Ltd were used in order to keep the volume and shape of coolants constant throughout all experiments. Envelope-shaped packages were provided by the sponsor, and the dimensions are summarised in Table 7-1.

Table 7-1 The specification of the envelope package

Envelope Code	Outer Dimensions (cm)		
	Length	Width	Thickness of each layer
Small	30	25	1.1
Medium	45	25	1.1
Large	60	25	1.1

7.2.2. Measurement of maximum insulation time (MIT)

7.2.2.1. Measurement of MIT of a typical shipping box

Experiments were carried out with cardboard boxes fitted with pre-cut liners of different insulation materials, as shown in Figure 7-4. The morphology of the insulation materials is shown in Figure 7-5, and the average thickness of the insulation materials is summarised in Table 7-2. Two layers of AB liners had to be used to achieve an insulation thickness similar to other insulation materials. The measurement of thermal insulation performance of the packages was carried out according to ASTM D3103 -14. The lab environment was controlled at a temperature of 22°C ± 3°C and relative humidity of 50% ± 5%. The coolants were preconditioned in a freezer with a temperature of -21°C for 48 hours before positioning inside the box, as shown in Figure 7-4. A temperature sensor named EL-21CFR-TP-LCD (shown in Figure 7-6) with an accuracy of ±0.1°C was used, and the sensor probe with a diameter of 0.4 cm and length of 2.5 cm was sandwiched between the two ice packs (the temperature variation of different sensor location was investigated in section 7.3.1.1). The sensor records the package internal temperature every second elapse. Once the insulation lid was put on, the box was sealed. The package was then placed in an oven to initiate the MIT test. The oven was pre-heated to the desired temperature (variable described in section 7.3.1.4) for two hours before the box was put in the oven. An additional temperature sensor was used to monitor the oven temperature with an accuracy of ± 0.5°C. The basic operation procedure is demonstrated in Figure 7-7. All MIT measurements were repeated three times to obtain an average value.

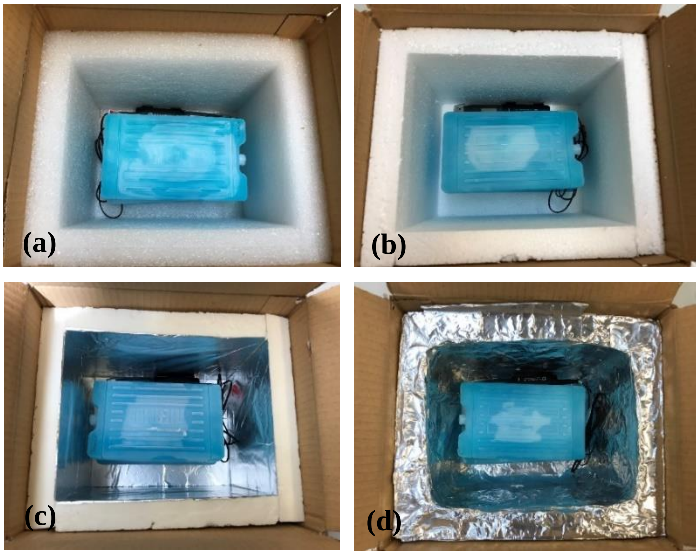

Figure 7-4 Package prototype with various insulation lining materials including (a) PE (b) EPS (c) PIR with aluminium foil (d) aerogel blanket with aluminium foil

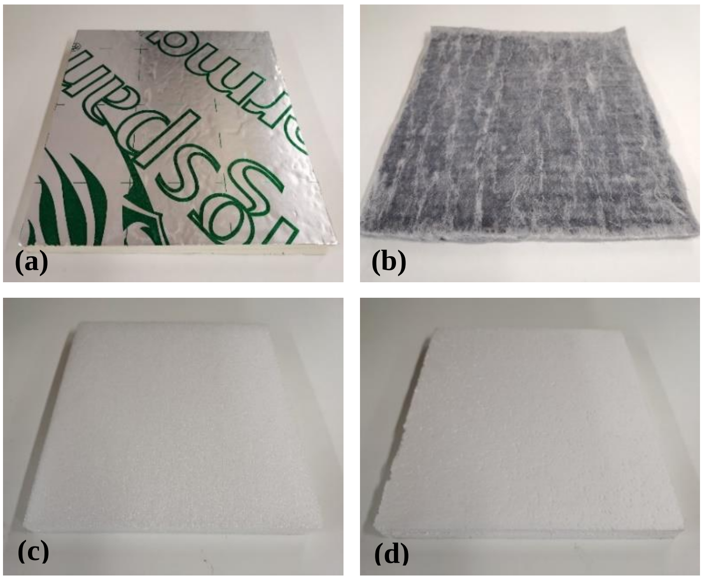

Figure 7-5 Morphology of the insulation materials (a) PIR panel, (b) aerogel blanket, (c) PE foam and (d) EPS panel

Table 7-2 Measurement of thermal conductivity and thickness at 20°C with a pressure load of 2 kPa

Material	**Ave. thermal conductivity (mW/mk)**	**Ave. thickness (mm)**
Polyisocyanurate	24.6 ±0.04	25.42 ±0.01
Aerogel blanket	16.2 ±0.02	9.42 ±0.02
Polyethylene	61.0 ±0.18	27.45 ±0.03
Expanded Polystyrene	42.5 ±0.06	24.38±0.02
Cardboard box	43.9 ±0.46	2.68 ±0.01

Figure 7-6 Thermistor data logger EL-21CFR-TP-LCD, reproduced from [320]

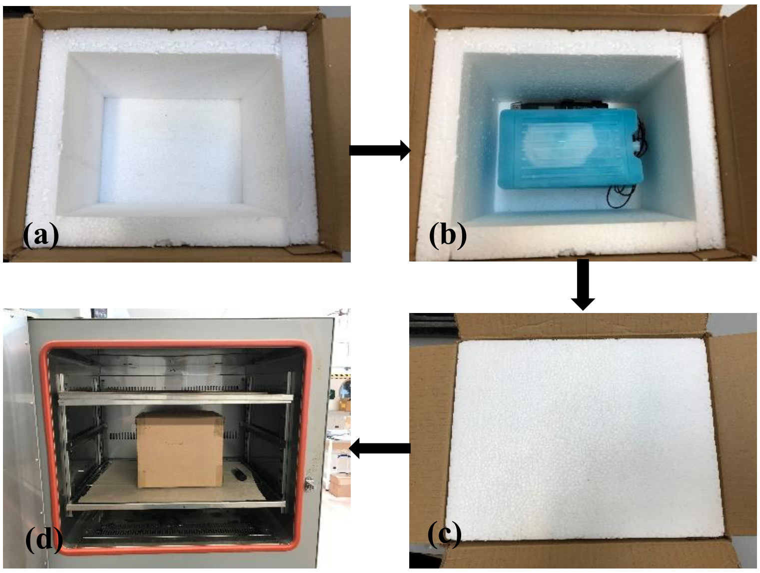

Figure 7-7 Procedure of measurement of package insulation performance (a) cardboard boxes fitted with pre-cut liners (PE in this case), (b) temperature sensor probe sandwiched between the two ice packs, (c) insulation lid put on and (d) box sealed and placed in an oven at a designated temperature

7.2.2.2. Measurement of MIT for a typical shipping envelope

A similar procedure was adopted for measuring the MIT of an envelope-shaped package. Instead of a rectangular ice pack, ice sheets were used to fit in the envelope package. The encapsulated ice sheets were immersed in water for 10 minutes to absorb enough water before conditioning in the freezer. A thermistor data recorder with four-probe sensors named EL-SGD 43 ATP (shown in Figure 7-8) was used to monitor temperature change at a different position within the envelope. The mass of each ice sheet after frozen was recorded before the MIT test. Once the ice sheets and the sensor probes were positioned, the envelope was sealed. The basic operation procedure is demonstrated in Figure 7-9.

Figure 7-8 Thermistor data logger EL-SGD 43 ATP, reproduced from [321]

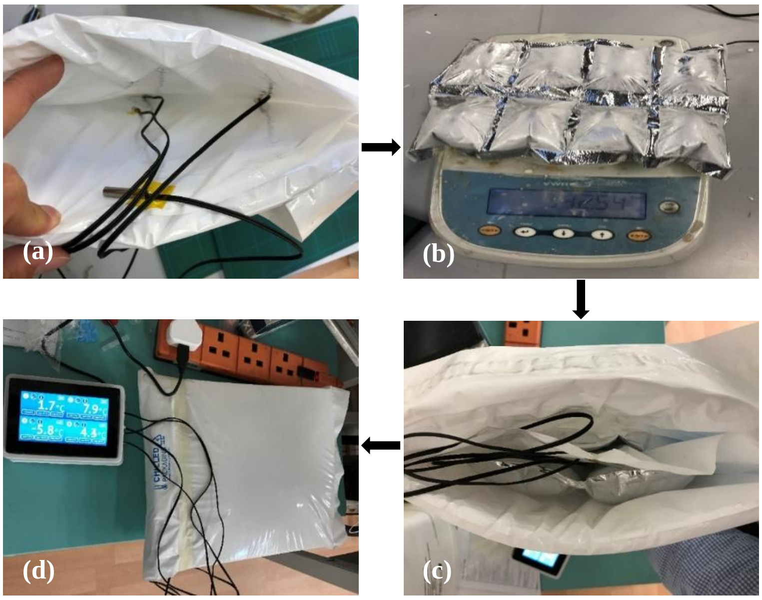

Figure 7-9 Procedure of measurement of package insulation performance (a) sensor probe located at the designated position, (b) ice sheet weighted, (c) ice sheets positioned and (d) test initiated

Several parameters were investigated in this part, including the effect of the ice sheets amount and envelope size on MIT and the temperature distribution within the envelope. Besides, real seafood products were also introduced to monitor the temperature change at the product's surface.

7.2.3. The positioning of the temperature sensor

As coolant inside the package is the primary temperature regulator in the passive insulated package, it is paramount to measure its temperature change with elapsed time accurately. Consequently, the time-temperature variation obtained with different sensor positioning was first examined to identify the temperature difference within the box, as shown schematically in Figure 7-10.

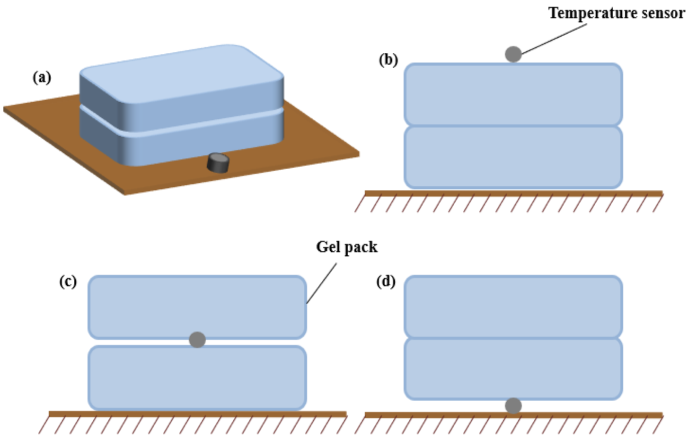

Figure 7-10 Illustration of temperature sensor position to the ice pack within a box (a) at the side (b) on the top (c) sandwiched in between and (d) at the bottom of ice packs

In Figure 7-10 (a), the temperature sensor was placed at the edge of ice packs; in this case, the temperature around the ices packs was monitored. In Figure 7-10 (b), the temperature sensor was placed on top of the ice packs to measure the ice pack's free surface temperature. In Figure 7-10 (c), the temperature sensor was placed in between the ice packs to measure the bulk temperature of the ice pack. In Figure 7-10 (d), the temperature sensor was placed at the bottom of the ice packs to measure the ice pack's non-free surface temperature. The PE insulated package was used in these cases, and the MIT measurement was conducted at room temperature.

Similar to the typical box, four-sensor probes located in the envelope-shaped package are illustrated in Figure 7-11. In this case, the PE insulated package was used, and the MIT measurement was conducted at room temperature.

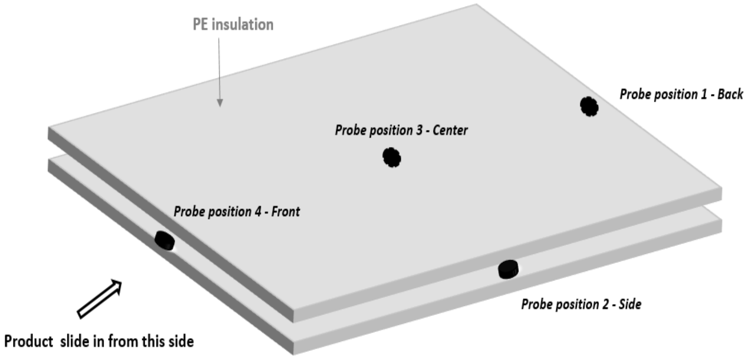

Figure 7-11 Illustration of temperature sensor position within a shipping envelope

7.2.4. Measurement of surface emissivity

7.2.4.1. Emissivity measurement theory

Surface emissivity measurement was carried out according to the procedure described in Luo and Sun [322]. The basic theory needs to be understood to proceed with the measurement. The Principle of emissivity is that each body with a temperature above absolute zero emits electromagnetic radiation from its surface [323]. The maximum rate of radiation per unit of area is from an ideal surface (a blackbody) which can be expressed as:

$$Q_b(T) = \sigma T^4 \qquad \text{(Equation 7-16)}$$

A blackbody is an idealized perfect emitter and absorber of radiations. However, the real surface is not an ideal emitter, so radiation from a real surface is less than the blackbody:

$$Q_{emit} = \varepsilon \sigma T^4 \qquad \text{(Equation 7-17)}$$

where ε is the coefficient of emissivity of the material, which is the ratio of emissive power of a body to the emissive power of a black body at the same temperature.

When radiation energy impacting a surface, a fraction will be absorbed, reflected, and transmitted:

$$\alpha + \rho + \tau = 1 \qquad \text{(Equation 7-18)}$$

where α is the coefficient of absorptivity, ρ is the coefficient of reflectivity, and τ is the coefficient of transmissivity of a material.

Kirchhoff’s law:

$$\alpha=\varepsilon \qquad \text{(Equation 7-19)}$$

For opaque surfaces, it is assumed that no energy will be transmitted; therefore, the radiation energy reflected by the object can then be written as:

$$\rho=1\text{-}\varepsilon \qquad \text{(Equation 7-20)}$$

A thermal imager can be used to measure the surface emissivity of materials. The total radiation received by the infrared detector within the thermal imager includes the radiation reflected from the object and the radiation emitted by the surroundings. These radiations pass through the atmospheric attenuation and are captured by the detector [322]. This is illustrated in Figure 7-12.

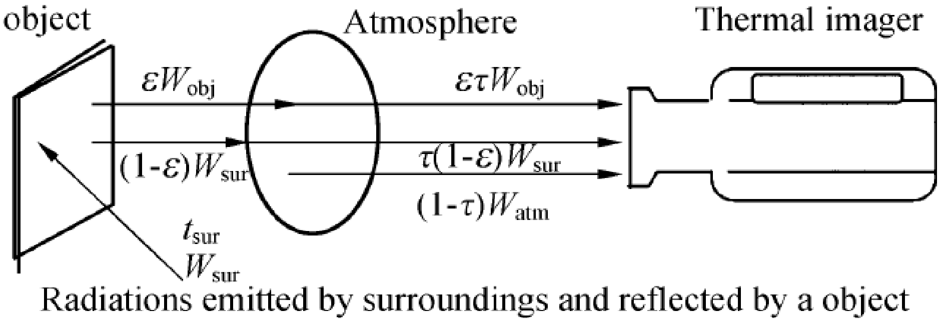

Figure 7-12 Illustration of radiation received by the thermal imager, reproduced from [322]

The total radiation W_{tot} received by the detector can be written as:

$$W_{tot}=\varepsilon\tau W_{obj}+(1\text{-}\varepsilon)\tau W_{sur}+(1\text{-}\tau)W_{atm} \qquad \text{(Equation 7-21)}$$

where ε is the object surface emissivity, τ is the atmospheric transmittance, $1\text{-}\tau$ is the average atmospheric emissivity within detect range, $\varepsilon\tau W_{obj}$ is the radiation energy emitted by an object, $(1-\varepsilon)\tau W_{sur}$ is the radiation emitted by surrounding and reflected by the object, and $(1-\tau)W_{atm}$ is the radiation emitted by the atmosphere.

Rearrange Equation 7-21 as:

$$\varepsilon=\frac{W_{tot}\text{-}\tau W_{sur}\text{-}(1\text{-}\tau)W_{atm}}{\tau W_{obj}\text{-}\tau W_{sur}} \qquad \text{(Equation 7-22)}$$

Indoor atmosphere transmittance is close to 1 (i.e. τ=1). Equation 7-22 can then be written as:

$$\varepsilon=\frac{W_{tot}\text{-}W_{sur}}{W_{obj}\text{-}W_{sur}} \qquad \text{(Equation 7-23)}$$

W_{tot} can be obtained by set ε =1, then Equation 7-21 becomes:

$$W_{tot}= \tau' W'_{obj}+(1-\tau')W_{atm} \qquad \text{(Equation 7-24)}$$

For the indoor environment, $\tau'=\tau=1$, then $W_{tot}=W'_{obj}$, Equation 7-23 becomes:

$$\varepsilon=\frac{W'_{obj}-W_{atm}}{W_{obj}-W_{sur}} \qquad \text{(Equation 7-25)}$$

$W= \sigma T^4$, and assume $T_{atm}=T_{sur}$, Equation 7-25 can be written as:

$$\varepsilon=\frac{T'^4_{obj}-T^4_{sur}}{T^4_{obj}-T^4_{sur}} \qquad \text{(Equation 7-26)}$$

where T_{sur} is the temperature of the surrounding environment, T_{obj} is the temperature of the object, and T'_{obj} is the temperature of the object when ε =1.

7.2.4.2. Measurement of surface emissivity

Material surface emissivity was measured experimentally, as indicated in Figure 7-13. The sample was placed on a hot plate with a pre-set temperature of 50°C to create more than at least a 10°C difference than the surrounding temperature, as required in ASTM E1933-14. A K-type thermocouple was used to detect material surface temperature (T_{obj}) as well as the surrounding air temperature (T_{sur}). For the thicker materials, including PE, EPS, PIR and AB, the materials were placed on the hot plate for 1 hour to reach the steady-state temperature, and this was checked frequency using the K-type thermocouple. An Infrared (IR) thermometer named Keysight U5857A was used to detect surface temperature (T'_{obj}) when emissivity was set to 1. The Infrared thermometer measures objects' surface temperatures by sensing the infrared radiation emitted by the object's surface. These measured temperatures were used to calculate the surface emissivity (ε) of the sample by Equation 7-26. Figure 7-14 (a) to (c) show the experimental setup for measuring the surface emissivity of aluminium foil, composite foil (detached from PIR board) and PE foam, respectively. Experiments were also carried out to validate the influence of inner surface emissivity on package performance by applying mylar film and aluminium foil on the same PE insulated package at a surrounding temperature of 40°C. This is shown in Figure 7-15.

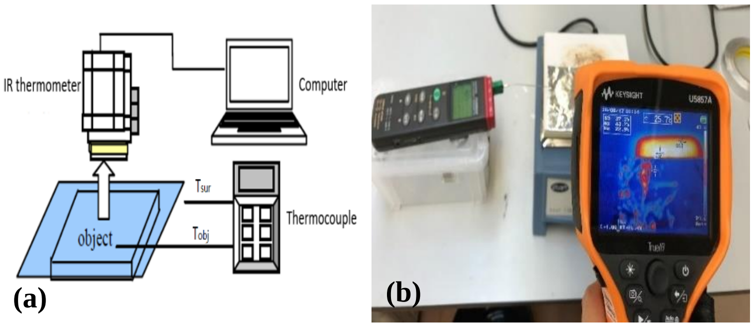

Figure 7-13 (a) simple layout diagram (b) photo of the experimental set-up for the surface emissivity measurement

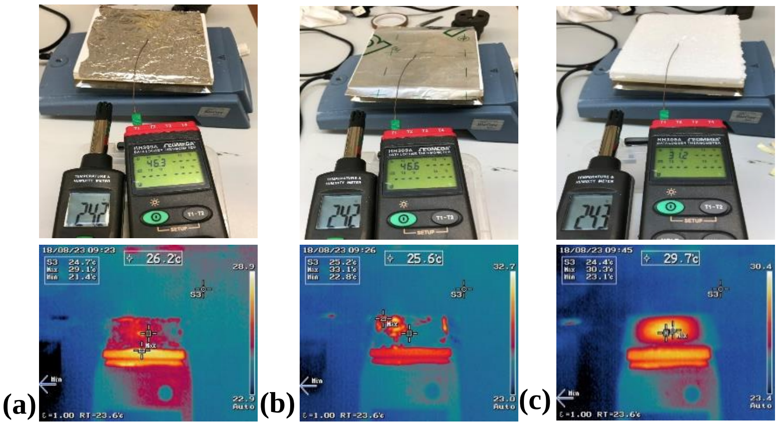

Figure 7-14 Measurement of material surface emissivity including (a) aluminium foil (b) composite foil detached from PIR and (c) PE foam

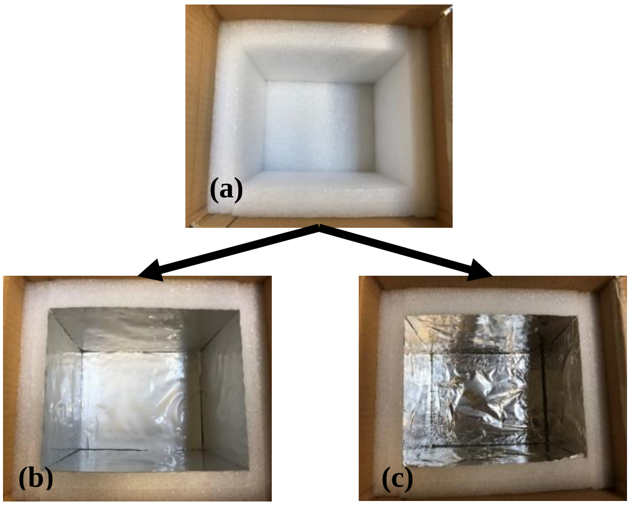

Figure 7-15 Photo of (a) Original PE insulated package (b) mylar film and (c) aluminium film on the inner surface of a PE insulated package

7.2.5. Measurement of thermal conductivity

The Netzsch Heat Flow Meter 436 with thickness gauge, as shown in Figure 7-16, was used to measure the thermal conductivity and thickness of insulation materials accurately according to ASTM C518-17. The mass and dimensions of each insulation material were recorded and used in the software to determine the density. The measurement was carried out at various temperatures with a temperature difference between the hot and cold plates of 20 °C, and a constant pressure load of 2 kPa was applied during all measurements.

Figure 7-16 Netzsch Heat Flow Meter 436

7.3. Result and discussion

7.3.1. Thermal insulative performance of a typical shipping box

In this section, the effect of parameters, including surface emissivity, insulation thickness, insulation materials, amount of coolants and surrounding temperatures, on package insulative performance of a typical shipping box is investigated.

7.3.1.1. Effect of temperature measurement

Figure 7-17 shows a comparison of the time-temperature profile obtained from a temperature sensor positioned at the edge of ice packs (Figure 7-17 (a)), on top of the ice packs (Figure 7-17 (b)), sandwiched between two ice packs (Figure 7-17 (c)), and at the bottom of ice packs (Figure 7-17 (d)), respectively. It can be seen from Figure 7-17 (b) that the surface temperature of the ice pack increases rapidly and continuously. As a result, the surface temperature reaches 5°C in 1.5 hours. A similar trend is obtained when the sensor is positioned at the edge of ice packs (Figure 7-17 (a)). These temperatures can be used to represent the inner surrounding temperature of the container. On the contrary, when the sensor is sandwiched between the two ice packs and at the bottom of the ice packs, the phenomenon of latent heat is clearly illustrated, as shown in Figure 7-17 (c) and (d). In Figure 7-17 (c) and (d), the temperature-time profile can be divided into three distinct stages. The first stage shows a rapid temperature increase before it reaches the melting temperature of the ice packs. This is followed by a prolonged stage for ice melting with little temperature change in the container. Upon completion of this phase change, the temperature experiences another rapid increase towards the external temperature. It is evident that the MIT is dominated by the second stage controlled by the PCM in the package.

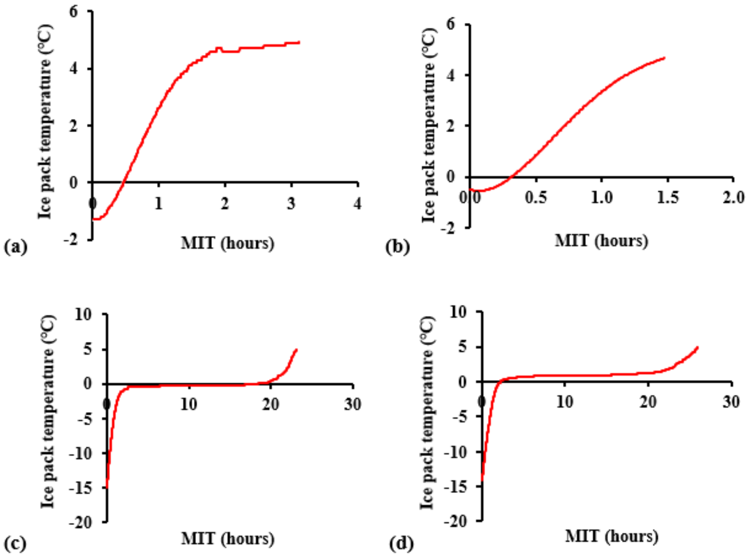

Figure 7-17 Effect of temperature sensor position (a) at the edge, (b) at the top surface, (c) sandwiched in between, and (d) at the bottom of ice packs on the measurement of ice pack temperature as a function of time

For all future experiments, the sensor position layout that is shown in Figure 7-17 (c) will be adopted for the following reason. The results that are shown in Figure 7-17 (c) and (d) clearly define three different stages of temperature-time behaviour that do not appear in Figure 7-17 (a) and (b). Figure 7-17 (c) is more representative of how the delivery product is positioned with respect to ice packs (i.e., sandwiched or surrounded by ice packs). A temperature sensor is less affected by natural convection inside the package during the measurement.

7.3.1.2. Effect of surface emissivity on maximum insulation time

Figure 7-18 shows the results for the surface emissivity of different materials used in this work. It is well known that materials with a highly reflective surface, such as aluminium foil and PIR composite foil, have much lower emissivity values than rough and low reflective surfaces such as EPS and PE. It can also be seen from Figure 7-18 that the measured results for surface emissivity are in good agreement with the literature value [324-326]. However, this property is also affected by surface colour and topography. In this work, directly measured values were chosen for the model to evaluate the influence of emissivity on MIT in order to improve the accuracy of the results produced by the model.

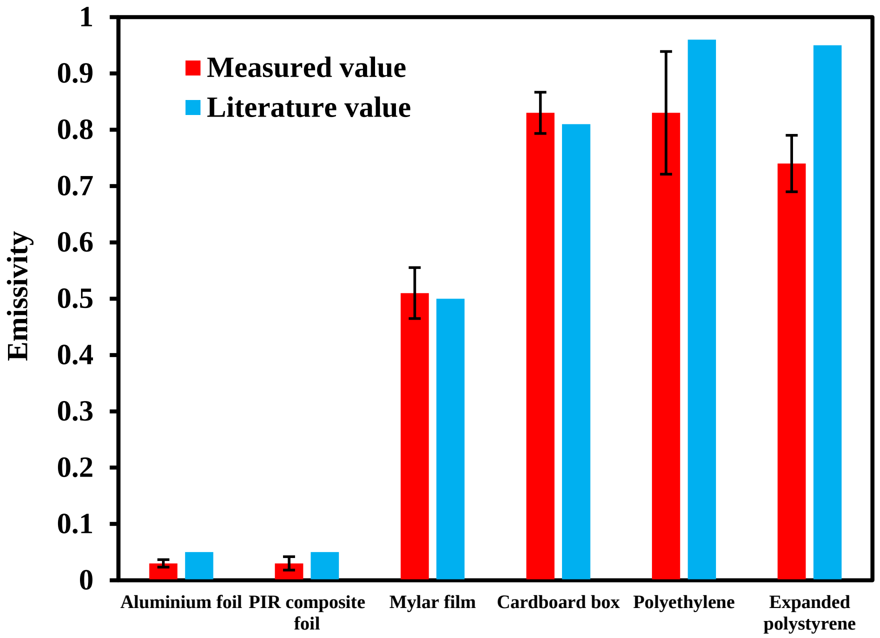

Figure 7-18 Material surface emissivity comparison between literature and measured values

The effect of internal surface emissivity on MIT at a surrounding temperature of 40°C is presented in Figure 7-19. The analytical model indicates that as package interior surface emissivity value increases from 0.03 to 1, a reduction of almost 40% is expected to obtain from the MIT. Surface emissivity is the crucial factor to radiation heat transfer, as described by Stefan-Boltzmann law. An increase in surface emissivity will lead to less reflected heat and increased heat energy transfer through the container wall. It can also be seen from Figure 7-19 that a good agreement between the calculated and measured values is achieved with approximately 10% discrepancy. As a result, a 46% increase in MIT is obtained with aluminium foil applied on PE inner surface compared to the original PE insulated package. This agrees with the observation achieved in other studies [37].

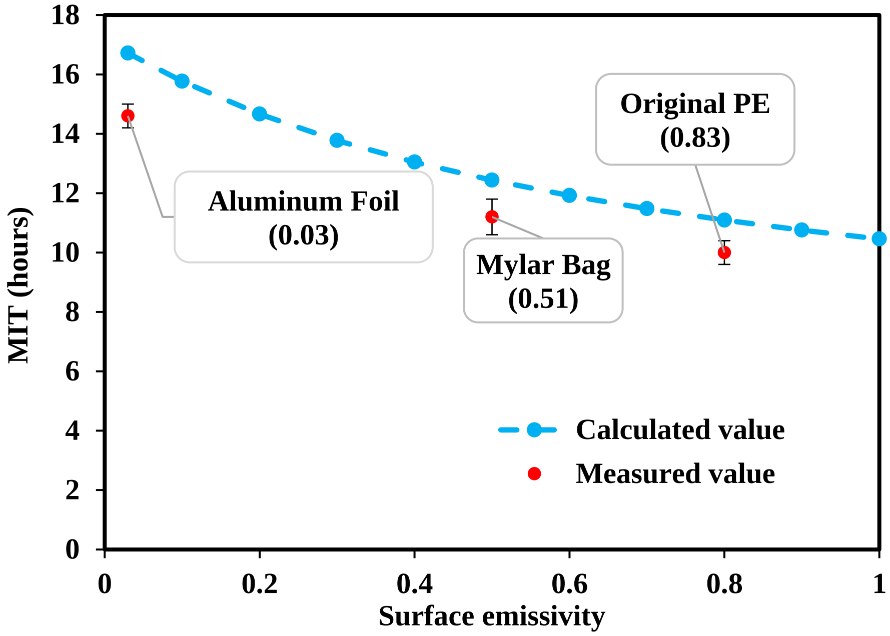

Figure 7-19 Effect of internal surface emissivity on MIT at a surrounding temperature of 40°C using PE insulated package

7.3.1.3. Effect of insulation materials on maximum insulation time

Figure 7-20 presents the calculated MIT as a function of the insulation liner's thermal conductivity at a surrounding temperature of 20°C. The thermal conductivity of the insulation liner and the external box is considered separately. When assessing the effect of the thermal conductivity of insulation liner on the MIT, the thickness and thermal conductivity for the external box remain constant. It can be seen from Figure 7-20 that MIT tends to drop rapidly with the increase of wall thermal conductivity and the rate of MIT change decreases gradually as the wall conductivity increases. This trend continues until the MIT levels off and remains unaffected by the wall conductivity. It is well expected that MIT will decrease as packaging walls become more thermally conductive. However, the overall behaviour of MIT is affected by both wall thickness and thermal conductivity. Since the cardboard box thickness (2.68 mm) is significantly less than the PE liner thickness (27.45 mm), the effect of thermal conductivity on the MIT will be much less prominent for the cardboard box than the insulation liner, as shown in Figure 7-20. For a given wall thickness, its insulation effect will diminish as the wall becomes more and more heat conductive. It follows that the plateau in Figure 7-20 represents the MIT provided only by the box/insulation liner when the insulation liner/box becomes very conductive.

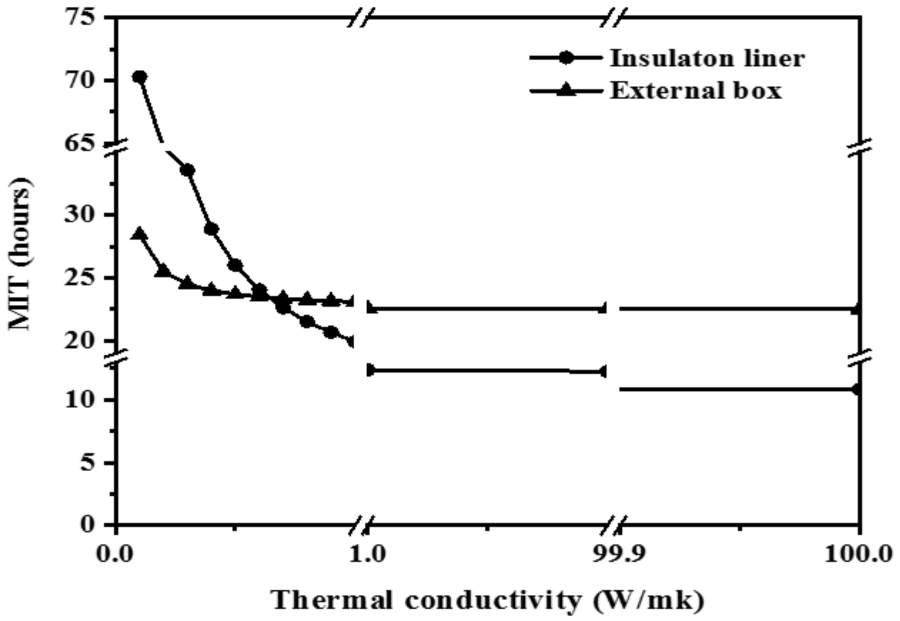

Figure 7-20 Effect of thermal conductivity of insulation liner and external box on calculated MIT at a surrounding temperature of 20°C

Figure 7-21 shows the influence of insulation thickness on MIT. It is evident that the MIT increases as the insulation liner becomes thicker; however, in practice, liner thickness may be restricted either by the dimensions of packages or cost. As mentioned previously, the MIT is affected by both the wall conductivity and thickness. This becomes evident when Equation 7-15 is rearranged into:

$$t = -R_q * \left(C_{p1} * m_1 + C_{p2} * m_2\right) * \ln\left(\frac{T_{(t)} - T_e}{T_i - T_e}\right) \qquad \text{(Equation 7-27)}$$

It can be seen that more time is required to raise the product temperature when the total thermal resistance increases. As the calculation of MIT is partly based on the convolution of Equation 7-27, the higher thermal resistance leads to a faster increase in MIT. This also means that the effect of different liner materials on their insulating performance will be enlarged as their thickness increases, as shown in Figure 7-21.

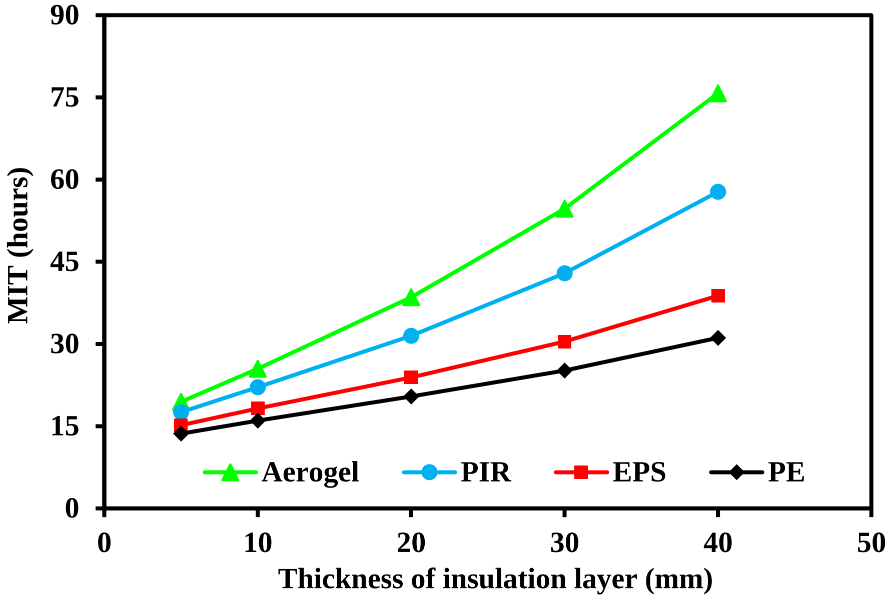

Figure 7-21 Effect of insulation thickness on calculated MIT for insulation material including aerogel blanket, PIR panel, EPS panel and PE foam at a surrounding temperature of 20°C

Since the MIT for EPS panel and PE foam is in a similar range, as indicated in Figure 7-21, and it is also well shown that EPS panel is more commonly used for package insulation, as listed in Appendix-A. Thus, the MIT for EPS panel is set as the baseline for future measurement.

Figure 7-22 (a) to (d) show the comparison between the calculated and measured MIT obtained from a package with a liner of EPS panel, foiled EPS panel, foiled PIR panel and foiled aerogel blanket respectively, at a surrounding temperature of 30°C. For all cases, the temperature-time behaviour exhibits the three distinct stages described earlier, and there is a good agreement between the modelling and experimental results. In particular, the test results for stage 1 and a large part of stage 2 are well-matched by the theoretical prediction. In contrast, the transition between different stages experiences a sharp turn with the modelling results but is typically smooth for the test results. Such discrepancy is mainly due to the modelling assumption of uniform temperature at any given time. In reality, there should be a non-uniform temperature distribution in thick walls and contained bulk products. As the ice pack temperature was measured by the sensor sandwiched between two ice packs, the measured temperature is likely to be slightly higher than that at the centre of an equivalent monolithic ice pack in the model. This may explain why the temperature rise after the phase change appeared sooner from the measurement than the model, as shown in Figure 7-22. However, this does not account for the opposite observation at the beginning of the phase change. Nevertheless, Figure 7-22 shows a good agreement overall between the tests and the model, and the difference is less than 11%.

A large error is found in Figure 7-22 (d) for the aerogel-insulated package, and this is probably because the insulation performance of the ABs was somewhat compromised by the potential air gap between two individual blankets.

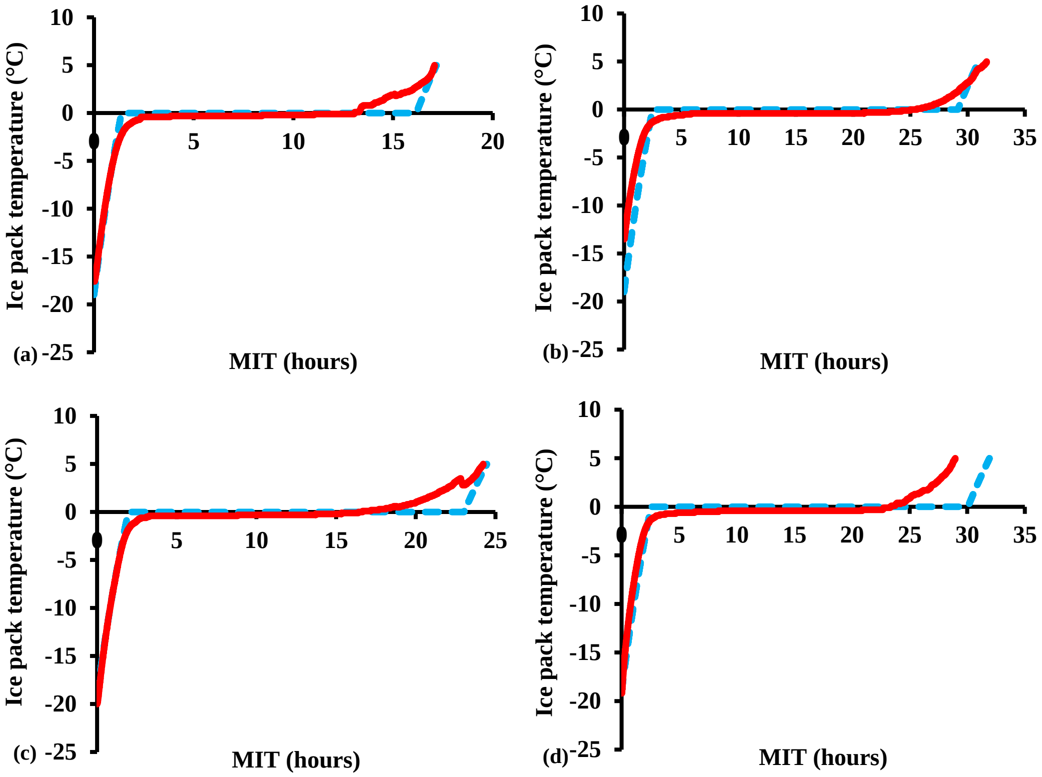

Figure 7-22 Comparison of calculated (dashed blue line) and measured (solid red line) MIT of packages insulated with (a) EPS panel (b) foiled EPS panel (c) foiled PIR panel (d) foiled aerogel blanket at a surrounding temperature of 30°C

The comparison of the MIT normalised by the thickness of each liner material is summarised in Figure 7-23. For the packages with high-performance insulation materials such as foiled PIR and AB, an increase of 28% and 47% in the MIT per unit thickness is achieved, respectively, compared to the foiled EPS insulated package. Furthermore, an improvement of 79% and 106% in the MIT per unit thickness is obtained for foiled PIR and AB insulated packages compared to the EPS insulated package. It can also be seen from Figure 7-23 that an excellent agreement between theoretical and experimental results is obtained. However, all practical results have a slightly less MIT than the theoretical prediction meaning that the model tends to underestimate the total heat flux across the package marginally. One of the reasons could be that convection was not considered in the numerical model. Satisfactory repeatability of the experimental results is also achieved with a maximum standard deviation of 0.7.

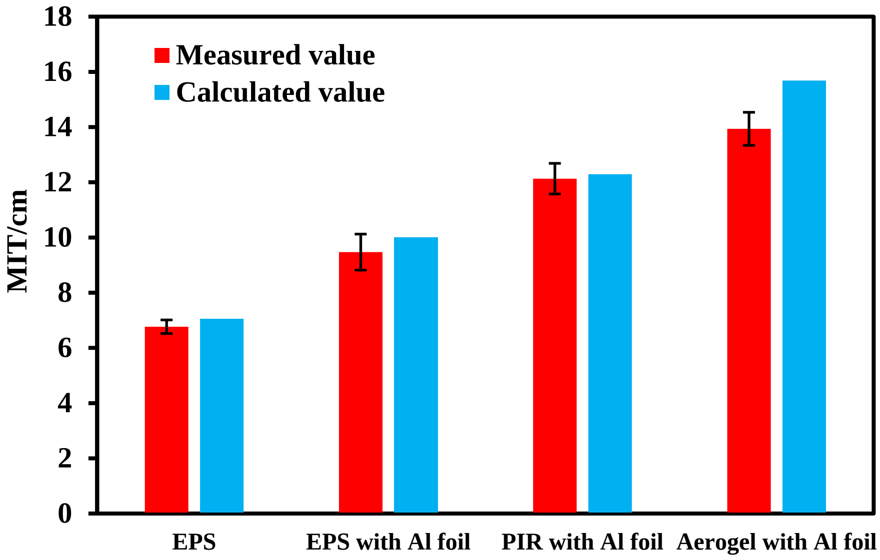

Figure 7-23 Comparison of calculated and measured MIT per unit thickness for packages insulated with different materials at a surrounding temperature of 30°C

However, such significant improvement is based on the high cost of materials. Table 7-3 lists the estimated cost to make one insulated package. The material cost is based on the small-scale purchase online, and it should be lowered for bulk orders. It can be seen clearly from Table 7-3 that the cost for an aerogel insulated package is 26 times more than a traditional EPS insulated package to achieve twice the MIT (without normalisation by thickness). The MIT for PIR is almost the same as the aerogel blanket. However, similar to EPS, PIR is also a plastic material that breaches the global plastic reduction challenge. It is well indicated that the cost per MIT for the aerogel blanket is significantly higher than the others, which shows the importance of lowering the product cost to replace or partially replace the plastic materials in the thermal insulation field.

Table 7-3 Estimated retail cost and insulating performance using different liner materials

Material	**Unit price (£/m^2)**	**Thickness (mm)**	**Material used per box m^2**	**Amount of box made per 1 m^2**	**Price of cardboard (£)**	**Price per box (£)**	**MIT (hour) at 20°C**	**Cost/MIT (£/hour)**
PE	8.24	27	0.22	4	0.9	3.0	23.1	0.13
EPS	1.6	25	0.22	4	0.9	1.3	24.0	0.05
PIR	20.76	25	0.22	4	0.9	6.1	46.0	0.13
Aerogel	65.83	10	0.44*	2	0.9	33.8	46.4	0.73

* Two layers of AB liners had to be used to achieve an insulation thickness similar to other insulation materials

7.3.1.4. Effect of surrounding temperature on maximum insulation time

Figure 7-24 shows the measured MIT per unit thickness of different insulation materials as a function of surrounding temperatures. As expected, an increase in outside temperature results in a decrease in the MIT due to higher heat flux entering the package. The temperature dependence of the MIT in Figure 7-24 follows a logarithmic relation, which is predicted by the governing Equation for calculating the MIT in Equation 7-27. This has a significant implication to packaging design for insulating performance as the results from Figure 7-24 indicates that maintaining a low temperature around an insulated package can bring about significant MIT benefit. This is the case, particularly when the package is insulated with high-performance insulation materials such as aerogel. In addition, the positive effect of reflective foil on the MIT is found to be sustained over the temperature range, as shown in Figure 7-24.

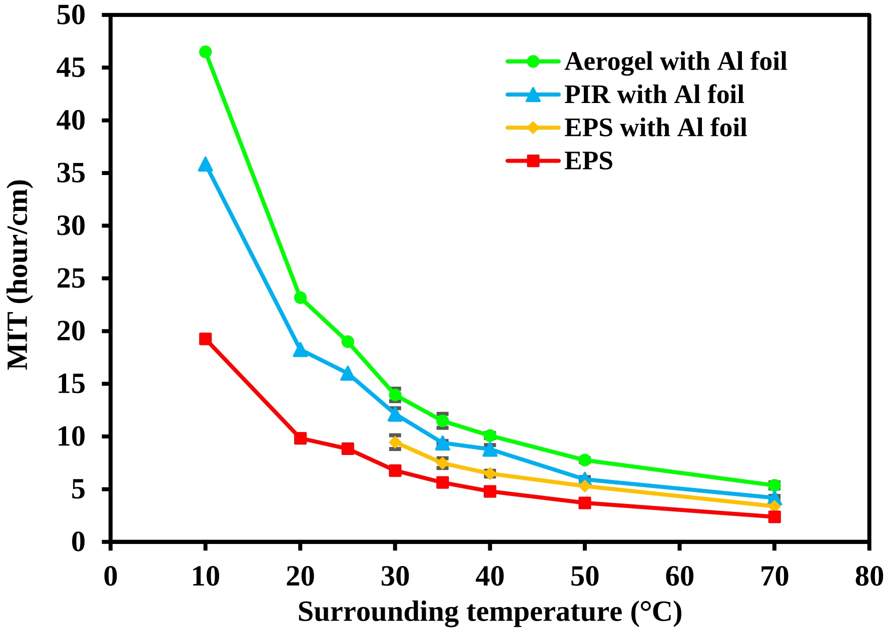

Figure 7-24 Comparison of measured MIT per unit thickness at different surrounding temperatures for packages insulated with various materials

The calculated and measured MIT for packages with different insulation materials at different surrounding temperatures are plotted in Figure 7-25. Once again, an excellent agreement between calculated and measured values can be found over the temperature range investigated in this work.

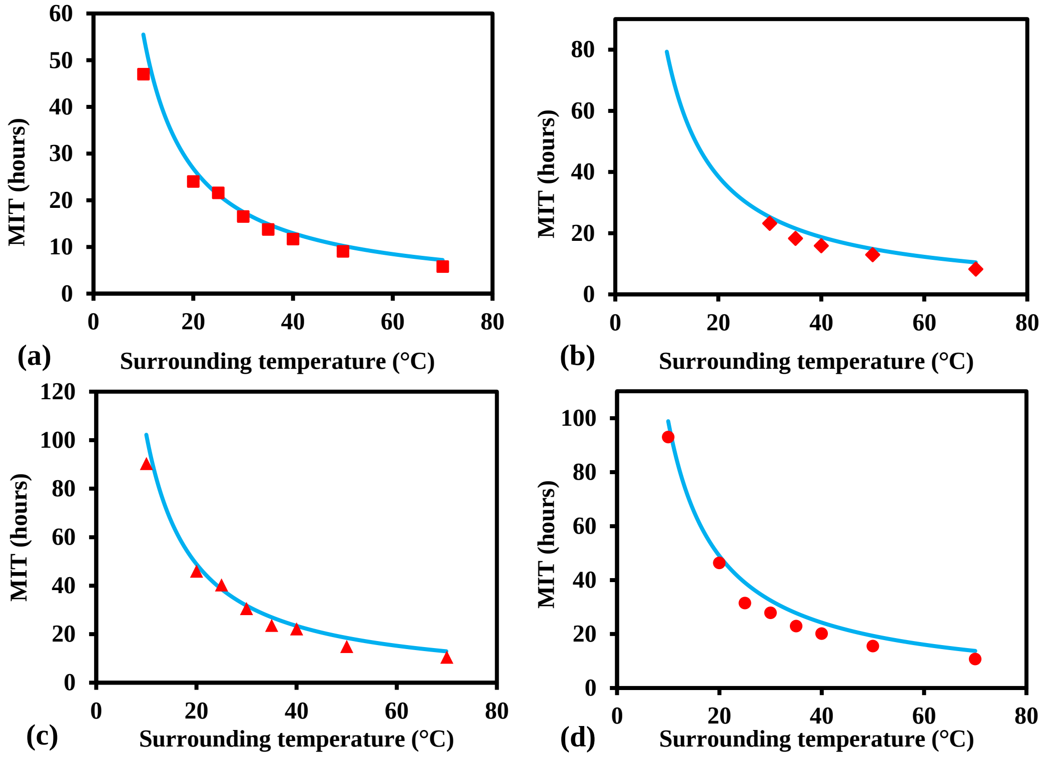

Figure 7-25 Comparison of calculated (solid line) and measured (data points) MIT as a function of sounding temperature for packages insulated with (a) EPS panel (b) foiled EPS panel (c) foiled PIR panel, and (d) foiled aerogel blanket

7.3.1.5. Effect of package dimensions on maximum insulation time

Figure 7-26 demonstrates the calculated and measured MIT of EPS and PIR insulated packages with two different package dimensions, 25.6 × 20.5 × 21.2 cm and 38.1 × 25.4 × 25.4 cm with a thickness of 2.68 mm at a surrounding temperature of 25°C. It can be seen clearly from Figure 7-26 that an increase in package dimension results in a decrease in MIT for both EPS and PIR insulated packages. This is due to the increase in package internal surface area resulting in a decrease in the internal surface heat transfer coefficient, as described in Equation 7-12. This leads to a rise in the heat penetration rate. Therefore, MIT is reduced. It can also be seen from Figure 7-26 that a satisfactory agreement between calculated and measured values is obtained for both EPS and PIR insulated packages.

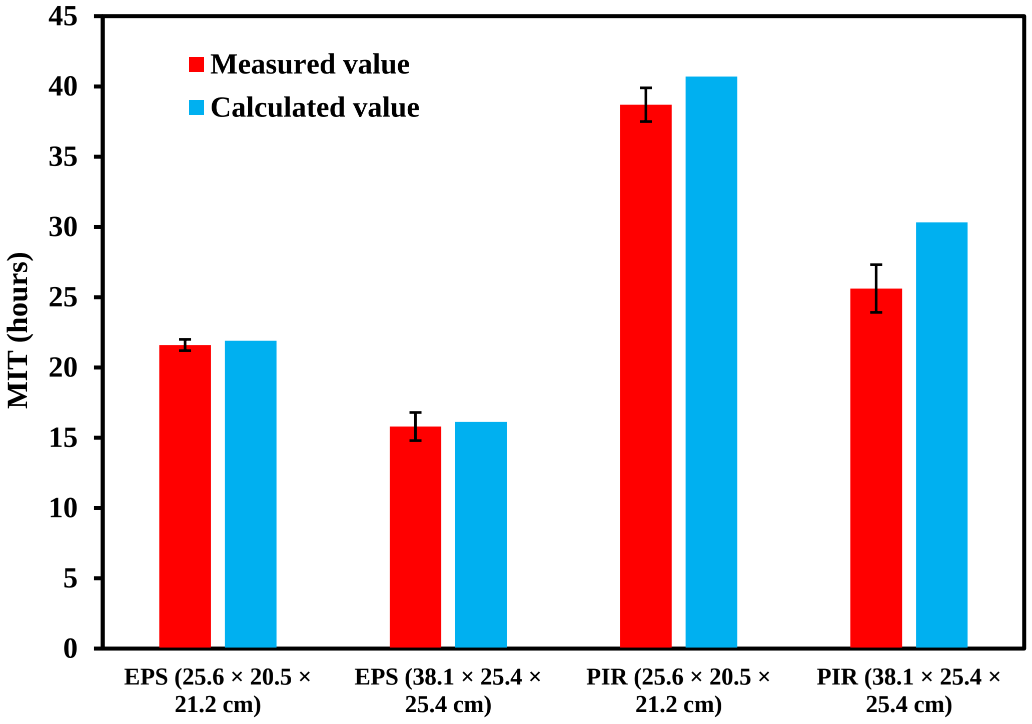

Figure 7-26 Comparison of the calculated and measured MIT of EPS and PIR insulated packages with two different package dimensions at a surrounding temperature of 25°C

7.3.1.6. Effect of coolant weight on maximum insulation time

Figure 7-27 demonstrates the MIT of the PIR insulated package with various amounts of coolants at a surrounding temperature of 25°C. It can be seen clearly that the coolant weight has a significant influence on MIT. A 100% increase in MIT is gained when the coolant weight increases from 200 g to 800 g. More volume of coolant means more thermal energy can be absorbed, and the phase changing process can be extended significantly. However, the shipping cost will be more expensive with an increase in coolant weight. The comparison of the calculated and measured MIT with different amounts of coolant weight can also be seen in Figure 7-27. An excellent agreement is obtained when 800 g of coolant is used. The error increases when the coolant amount is reduced, especially for the experiment with 200 g of coolant. As mentioned in section 7.2.3, the probe sensor is located between two ice packs, meaning that the sensor may be partially exposed to air. The smaller-sized ice packs (200 g) are exposed to air much more than the larger ones (800 g). This can be the reason for increasing error as the size of coolants reduces.

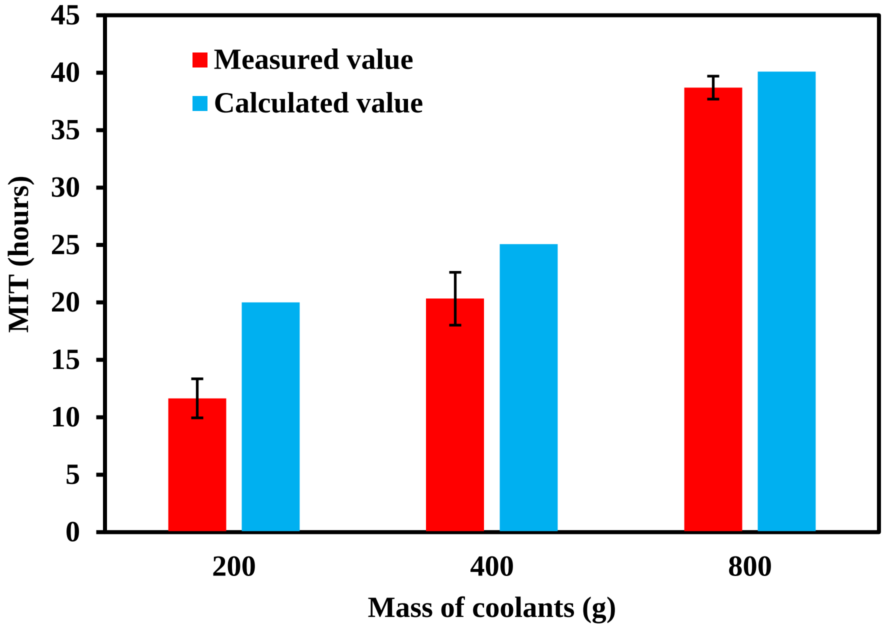

Figure 7-27 Comparison of the calculated and measured MIT of PIR insulated package with different amounts of coolants at a surrounding temperature of 25°C

7.3.2. Thermal insulative performance of typical shipping envelopes

In this section, the effect of parameters, including the amount of coolants, envelope size, surrounding temperatures, type of insulation material, on package insulative performance of typical shipping envelopes is investigated. The effect of temperature measurement on actual seafood products is then examined.

7.3.2.1. Effect of number of ice sheets on maximum insulation time

Figure 7-28 shows the effect of coolants amount on medium-sized envelope package on MIT. It is evident that without any coolant, the temperature increases rapidly until it reaches room temperature, as shown in the blue line in Figure 7-28. The performance can be improved significantly by putting one ice sheet into the package. As mentioned in section 7.3.1.1, the temperature-time profile can be divided into three distinct stages. The first stage shows a rapid temperature increase before it reaches the melting temperature of the ice sheets. This is followed by a prolonged stage for ice melting with little temperature change in the container. During the phase changing process (i.e., from ice to water), energy is consumed from the surrounding environment, and the temperature does not change during this process, as can be seen from both orange and green lines in Figure 7-28. Upon completion of this phase change, the temperature experiences another rapid increase towards the external temperature. As a result, The MIT for the envelope with two ice sheets is twice as much as the package with one ice sheet, and this is due to more phase change materials absorbing more heat energy, and the phase changing process is prolonged.

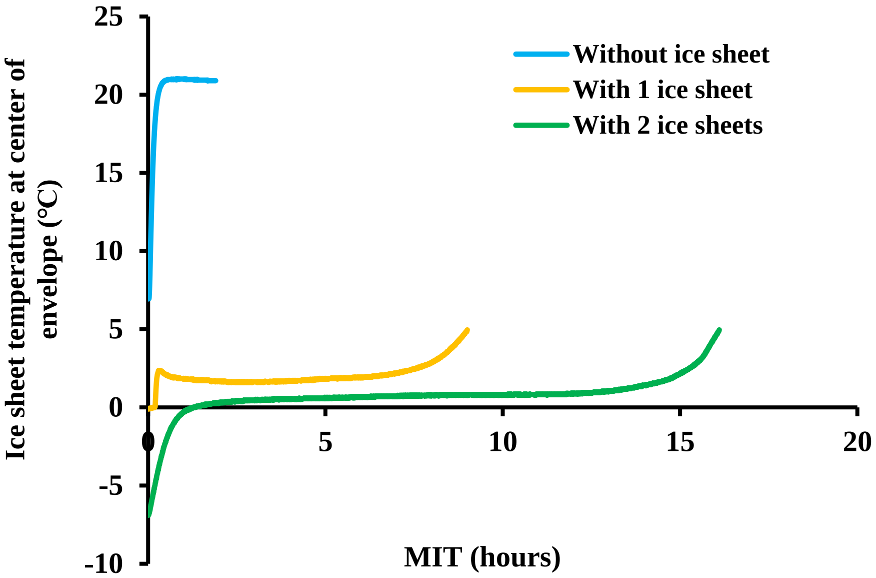

Figure 7-28 Comparison of various number of ice sheets on MIT with the medium envelope at room temperature

7.3.2.2. Effect of temperature measurement

The temperature distribution within the medium envelope package without ice sheet, with one and with two ice sheets, are indicated in Figure 7-29 (a) to (c), respectively, and the illustration of temperature sensor position within a shipping envelope is shown in Figure 7-29 (d). As expected, the temperature distribution (position 1 to position 4) within the envelope is consistent without the ice sheet since there is no additional cooling source for the ice melting stage to occur, as indicated in Figure 7-29 (a). Figure 7-29 (b) was to measure the ice sheet's free surface temperature, similar to the situation described in Figure 7-10 (b). However, the internal surface area of the envelope is much smaller than the box described in section 7.3.1. The probe sensor is mostly surrounded by the ice sheet. Thus, the prolonged stage for ice melting with little temperature change in the envelope is observed. As a result, it takes 9 hours for the centre of the envelope to reach 5°C. Figure 7-29 (c) clearly illustrates the phenomenon of latent heat and the three distinct stages. As a result, it takes 16.6 hours for the centre of the envelope to reach 5°C, almost doubled the MIT than the envelope with one ice sheet (Figure 7-29 (b)).

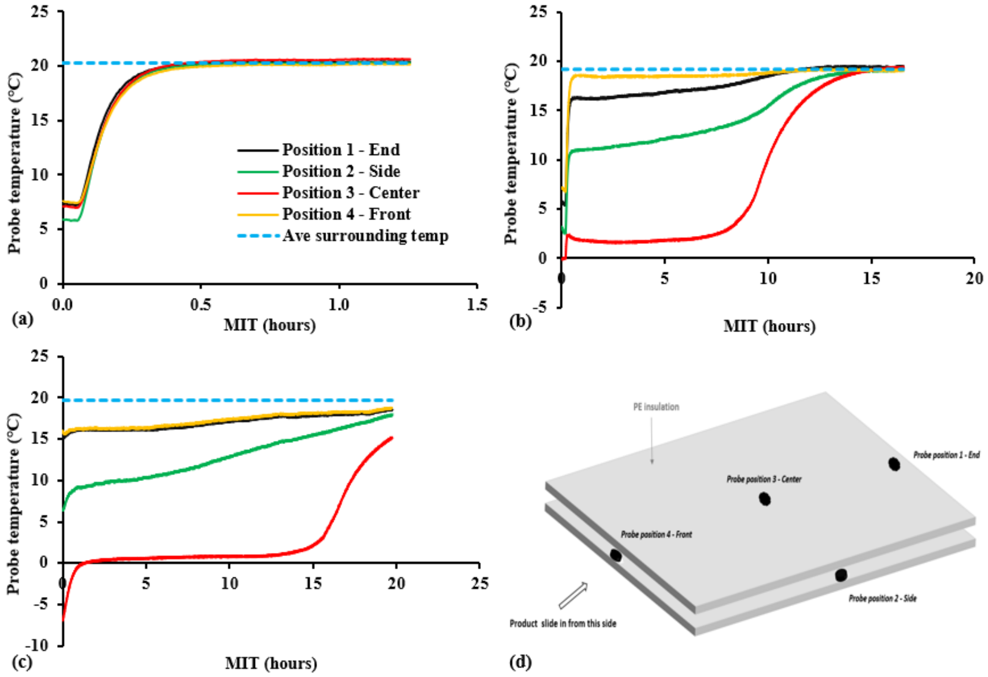

Figure 7-29 Temperature distribution within the medium PE insulated envelope (a) without ice sheet, (b) with one and (c) with two ice sheets at room temperature, and (d) illustration of temperature sensor position within a shipping envelope

7.3.2.3. Effect of envelope size on maximum insulation time

The performance comparison for different sizes of envelopes is summarised in Figure 7-30. Length is the only difference in dimensions, as mentioned in Table 7-1. The result shows that the envelope’s size has no noticeable difference in MIT for both cases (with one and with two ice sheets). This may be because, for a larger envelope, the size of the ice sheet is relatively small compared to that of the envelope (shown in Figure 7-31 and Table 7-4). As a result, the effective internal area remains the same as the smaller envelope, and the internal heat transfer coefficient calculated from Equation 7-12 will also remain the same. Therefore, the effect of envelope size on MIT is limited.

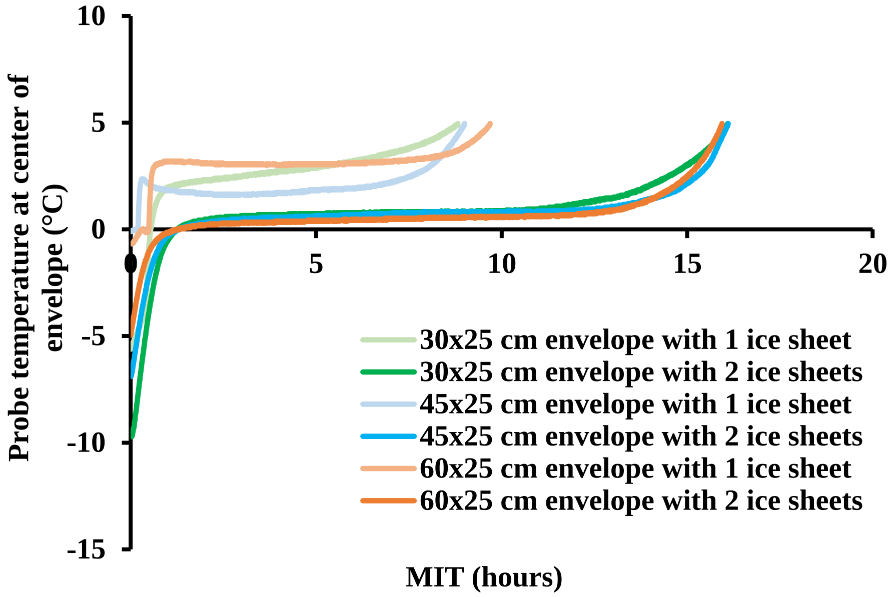

Figure 7-30 Performance comparison for different sizes of envelopes with one and with two ice sheets

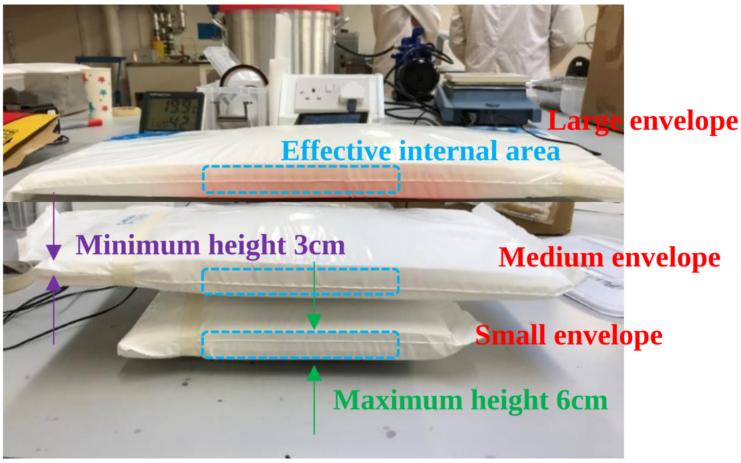

Figure 7-31 Photos of a small (30×25 cm), medium (45×25 cm) and large (60×25 cm) envelope

Table 7-4 Side area for the envelopes and ice sheet

Product	Side area (length × width) in cm^2
Small envelope (30×25 cm)	750
Medium envelope (45×25 cm)	1125
Large envelope (60×25 cm)	1500
Ice sheet (24×17 cm)	408

7.3.2.4. Effect of surrounding temperature on maximum insulation time

Figure 7-32 shows the calculated and measured MIT of different envelope sizes as a function of surrounding temperatures. As expected, an increase in outside temperature results in a decrease in the MIT for all envelopes due to higher heat flux entering the envelope. The temperature dependence of the MIT in Figure 7-32 follows a logarithmic relation, which is predicted by the governing Equation for calculating the MIT in Equation 7-27. This has a significant implication to packaging design for insulating performance as the results from Figure 7-32 indicates that maintaining a low temperature around an insulated package can bring about significant MIT benefit. However, the influence of various surrounding temperatures on MIT further proves that there is no apparent difference in measured MIT for the 30×25 cm, 45×25 cm and 60×25 cm envelope, which can be seen in Figure 7-32. In contrast, the numerical prediction still shows a decrease in MIT when the size of the package increases. In the numerical model, the package is assumed to be a rectangular shape regardless of the presence of the ice sheets. This means the larger internal surface area of the large envelope has a lower internal heat transfer coefficient (Equation 7-12). This leads to an increase in the heat penetration rate. Therefore, MIT is reduced with an increasing heat penetration rate. In reality, the effective internal area of the medium and large envelope is more or less the same as the smaller envelope. This is due to the side area of the ice sheet is much smaller than the side area of envelopes, and the internal heat transfer coefficient calculated from Equation 7-12 will also remain the same. Thus, there is no noticeable difference in MIT for different envelope sizes. However, a good agreement between calculated and measured MIT can still be obtained for the small envelope.

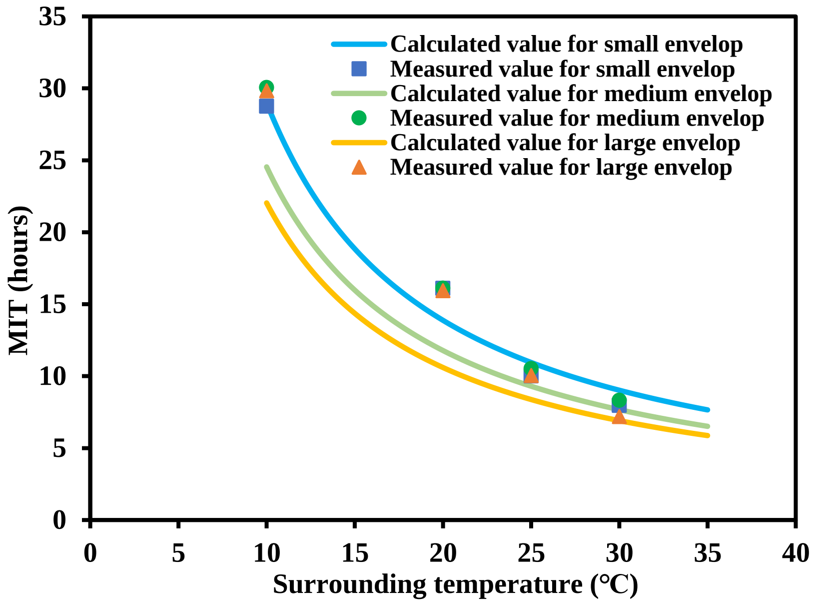

Figure 7-32 Comparison of calculated (solid line) and measured (data points) MIT as a function of sounding temperature for different envelope sizes

7.3.2.5. Effect of insulation materials on maximum insulation time

The MIT comparison of PE and AB insulated envelope is summarised in Figure 7-33. It is shown clearly that an average improvement of 60% for MIT can be achieved by replacing the original PE with AB of the same thickness; this is simply due to the lower thermal conductivity value of AB. An excellent agreement between calculated and measured values can be found over the temperature range investigated in this work.

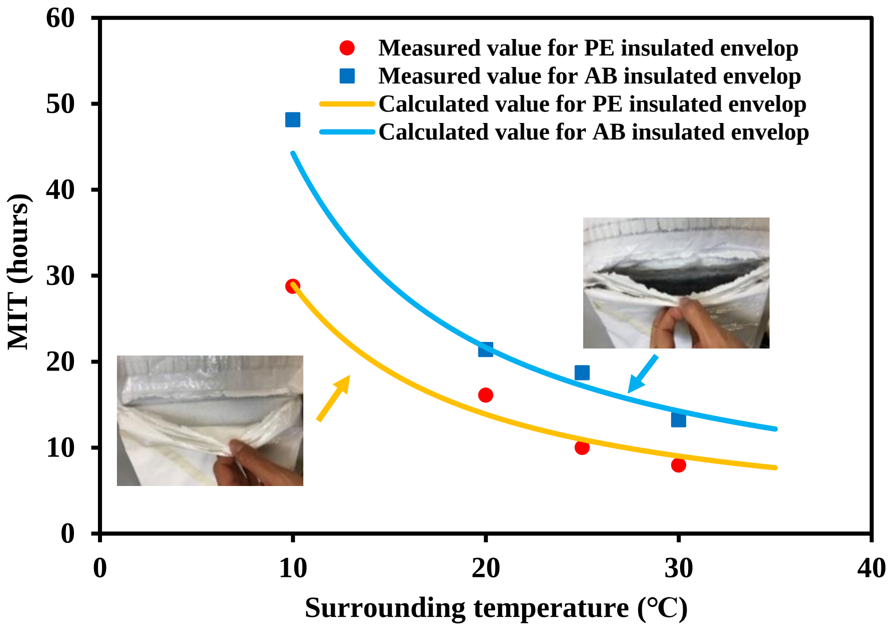

Figure 7-33 Comparison of calculated (solid line) and measured (data points) MIT as a function of sounding temperature for envelope packages with different insulation liner

7.3.2.6. Effect of temperature measurement on actual seafood product

One pack of seafood is used to investigate the temperature profile of an actual seafood product, and the locations of the temperature sensor are shown in Figure 7-34. In this case, the sensor probe is in direct contact with seafood. The seafood was stored in a fridge with an actual temperature of 8.9 ± 1.2°C before measurement. For the experiment with one ice sheet, the seafood top side faces the ice sheet, whereas, for the case with two ice sheets, the product is sandwiched by them. The experiment results with one and two ice sheets are shown in Figure 7-35 (a) and (b), respectively. It is evident that with the presence of two gel pack sheets, the MIT is prolonged and the temperature profile at each sensor position is consistent. The temperature profile does vary with the sensor position for the experiment with one ice pack sheet. The temperature at the back of the product remains above 5°C at all times. It is also shown that the temperature profile at the edge and centre is consistent at the beginning. The temperature rises quicker at the edge than the centre of the product. This may be because the sensor probe is more exposed to air at the edge than at the centre of the product, resulting in a shorter ice melting stage at the edge of the product.

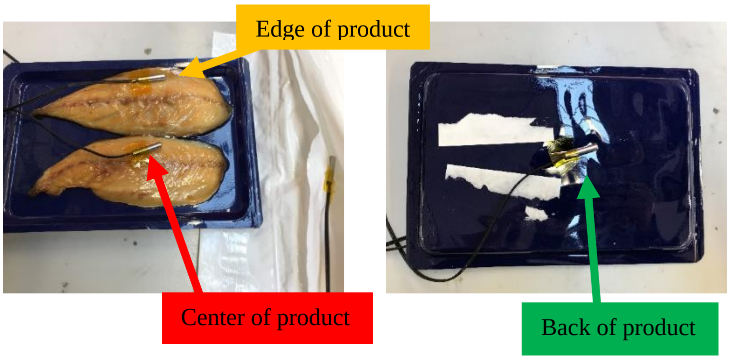

Figure 7-34 Position of sensor probes on product

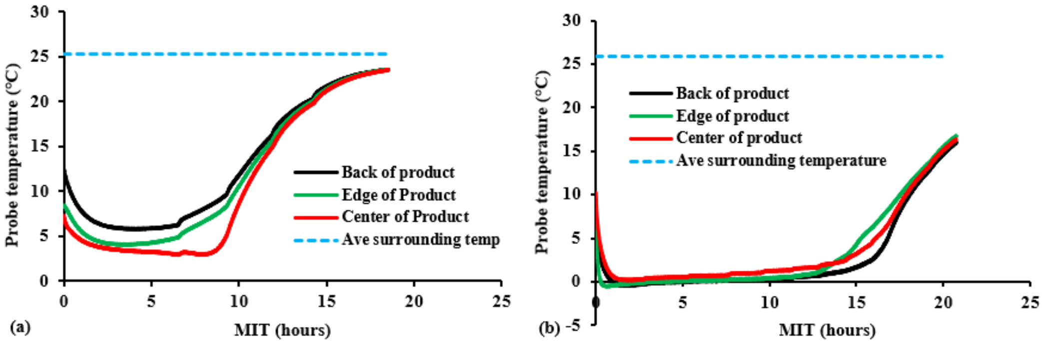

Figure 7-35 Temperature distribution within the small AB insulated envelope (a) with one ice sheet and (b) with two ice sheets at room temperature

The performance comparison with and without seafood products is indicated in Figure 7-36. Two ice sheets are used in both cases, and the temperature profile at the centre of the envelope is compared. The result shows that MIT is less with the presence of an actual product. This may be because to reach thermal equilibrium, part of the energy is consumed by the product to drop to zero degrees. The product’s initial temperature is still higher (around 10°C), even though it is pre-conditioned in the fridge before the experiment. Whereas the initial temperature for the case without seafood product is -10°C, and this represents the surface temperature of the ice sheet. Another reason could be that with the presence of a product, the air gap between two ice sheets is more significant than the case without any product, which stimulates the heat exchange process. Nevertheless, the prolonged stage for ice melting with little temperature change in the envelopes and the rapid increase towards the external temperature stage is well observed.

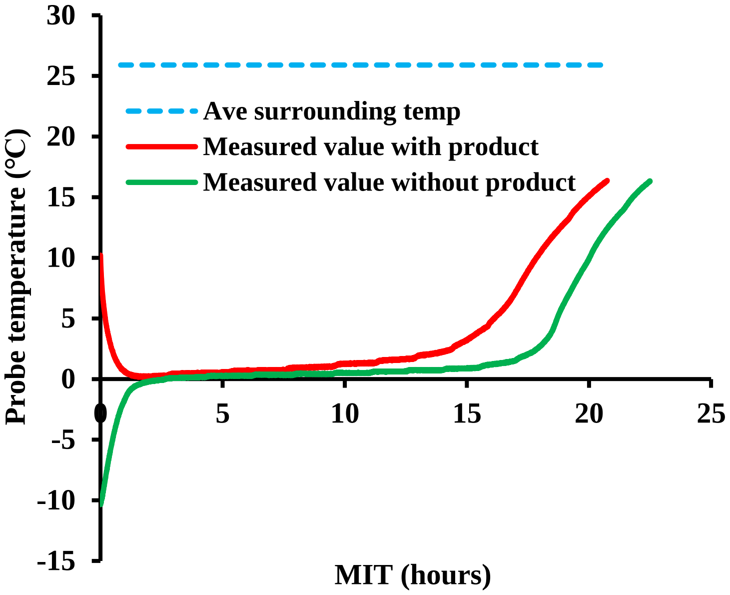

Figure 7-36 Temperature profile with and without actual seafood product with small AB insulated envelope at room temperature

7.4. Conclusion

In this chapter, the insulating performance of multilayered wall packages and the envelope-shaped package were investigated using experimental measurement and a transient thermal model. The effect on the MIT required for the ice packs to reach 5°C was studied of a range of factors including surface emissivity, insulation thickness, insulation materials, amount of coolants and surrounding temperatures.

Internal surfaces with lower emissivity proved to be a very cost-effective approach for improving packaging insulation performance. 46% and 40% increase of the MIT were obtained by applying the aluminium foil to the PE and EPS liners, respectively. Insulation thickness was another critical design factor for packaging performance in passive temperature control as MIT had a nonlinear relationship with insulation thickness. A similar phenomenon was also observed with regard to the influence of the surrounding temperature on MIT. Even with high-performance insulation materials, considerable MIT per thickness of insulation could be achieved only when the external temperature was maintained around room temperature (i.e., 23°C).

Aerogel blanket, as a high thermal insulation material, was used to investigate the feasibility of using such materials in the packaging industry. The result showed that much higher MIT could be achieved by using insulation materials with low thermal conductivity. For instance, a 106% increase in the MIT per unit thickness of insulation liner was obtained by replacing conventional EPS with a foiled aerogel blanket. This finding suggests that aerogel composites have a great potential to satisfy the requirement of temperature control during package delivery for long-haul transportation of fresh goods. However, the high price is the main challenge and must be reduced to compete with traditional insulation materials.

The optimised transient thermal model demonstrated the ability to describe three distinctive stages for temperature-time behaviour in insulated packages with coolant. The model was capable of accurately quantifying the contribution from latent heat and sensible heat, respectively. Comparison of modelling and experimental results showed a satisfactory agreement across all the design factors for the packaging insulation performance. The graphical user interface was developed to simplify the simulation process and ease to use, as shown in Appendix-B. This finding suggests that the model can be utilised as a cost-effective tool for packaging design concerning passive temperature control with improved accuracy.

8. Conclusion and future work

In this chapter, the aims of the thesis are restated, and an overview of the conclusions is described. Future research that can be implemented based on the results and outcomes of this work is proposed.

8.1. Conclusions of the thesis

Low cost, more environmentally friendly, and excellent thermal insulation performance are critical factors in commercializing insulation materials. This thesis aimed to investigate the potential for fabricating low-cost and more environmentally friendly insulation materials while maintaining their thermal insulation performance. The possibility of using aerogel composites for a range of situations, such as insulated packaging and thermal insulation of dwellings, were also discussed. To achieve this, five objectives are outlined:

1. Evaluate the performance of fly ash-based geopolymer.
2. Discuss the performance of silica aerogel granules.
3. Assess the performance of fibre-reinforced silica aerogel composites.
4. Evaluate the feasibility of using recycled glass fibre in geopolymer and aerogel systems.
5. Examine the thermal performance of aerogel composites in the packaging industry.

8.1.1. Fabrication and characterisation of inorganic porous geopolymer with excellent thermal performance

In chapter 3, the feasibility of synthesizing inorganic porous geopolymer was evaluated using industry by-product fly ash as the raw material. The foaming agent was set as the variable, and the influence of the foaming agent on the properties of the geopolymer was discussed. Pore structure, bulk density, thermal conductivity, and compressive strength test were the critical parameters for characterising the prepared specimens. The effect of foaming agent amount on the foam expansion rate was also investigated, and the foam expansion mechanism was discussed.

The foaming agent proved to be a critical factor influencing the pore structure, thus, the density, thermal conductivity and the compressive strength of the geopolymer. The calculated porosity reached 83% when the H_2O_2 content was 8%. As the foaming agent content increased from 0% to 8%, the density reduced by 85% to 171 kg/m^3. The effect of H_2O_2 content on thermal conductivity had a similar trend as the density. The lowest thermal conductivity value obtained in this work was 51 mW/m.K at H_2O_2 content of 8%, and a reduction of 67% was obtained when compared to the sample without any foaming agent. The thermal conductivity value is superior to most of the foamed concrete reported. This finding suggests that geopolymer can be an ideal substitute for foamed concrete since it is more economical and environmentally friendly with superior thermal insulation performance compared to foamed concrete.

The volume expansion test indicates two competing mechanisms: one is the expansion due to trapped bubbles; the other is escaped bubbles. As the amount of H_2O_2 increased, more oxygen was generated via the decomposition process of H_2O_2, and the bubble of O_2 was trapped within the paste, expanding and generating void (macropores). At this point, the number of trapped bubbles was greater than the escaped bubbles. However, as the amount of H_2O_2 increased further, the bubble generation rate became faster. The bubble shell’s strength was not strong enough to hold the void, resulting in more bubbles were escaped. As a result, the number of trapped bubbles was equal to or less than the escaped bubbles. Thus, the further addition of H_2O_2 had no obvious impact on the volume expansion. The elevated temperature stimulated the deposition rate of H_2O_2, and the air bubbles merged to form a large void. Thus, the volume expansion at the elevated temperature was higher. This finding could be used to indicate how different pore structures are obtained by varying the foaming agent.

8.1.2. Fabrication and characterisation of silica aerogel with an improved fabrication process

In chapter 4, the feasibility of synthesizing silica aerogel was evaluated using a more economical sodium silicate as the precursor. The effect of ageing and solvent exchanging temperature on the pore structure of aerogel were examined. The minimum amount of solvent used to synthesise aerogel was investigated. Properties including morphology, pore structure, bulk density, BET surface area, hydrophobicity, thermal stability and thermal conductivity were examined as the critical parameters for characterising the prepared specimens.

It was experimentally demonstrated that there was a minimum solvent to gel ratio (2:1) to fabricate aerogel successfully. When the amount of solvent was less efficient (i.e., 1:1 and 1.5:1), the water inside the gel may not be replaced by the solvent completely. As a result, large capillary pressure was presented due to the high surface tension of water. Thus, powder form or small piece was fabricated after the drying process. In addition, hydrophilization agents were insoluble in water, and drying of these mixtures (agent and water) could have a negative impact on the final product. This may be the reason for the yellowish crystalized product being formed. The hydrophobicity test also failed. Thus, the hydrophobization process was not successful. This finding provides guidance for fabricating aerogel with a minimum amount of solvent if the manufacturing cost is considered. The impact of excessive solvent (i.e., 3:1) on the physical properties of aerogel is unknown, but the benefit of using the minimum ratio on the economic aspect is obvious.

The fabrication process of aerogel was also optimised. The results indicated that the aerogel aged and solvent-exchanged at a higher temperature (45℃) led to a lower apparent density, higher specific surface area and pore volume, and finer average pore diameter. Ageing and solvent-exchanging at a higher temperature might also have enhanced the backbone strength and reduced the collapse or cracking of silica aerogel during the drying process. The obtained silica aerogel aged at a higher temperature possessed high porosity (91.6%) and a high specific surface area (726 m^2/g). The thermal conductivity test indicated that smaller particle size (<1250 μm) leads to a lower thermal conductivity (25.1 mW/m.K) compared to larger particles (1250 to 3500 μm), and this value is below the thermal conductivity of the air (i.e., 26 mW/m.K) at the ambient condition. This finding indicates that proper optimisation of the fabrication process can improve the properties of silica aerogel, which shows great potential in thermal insulation application.

8.1.3. Vacuum sealed fibre-reinforced silica aerogel composites with excellent thermal conductivity

In chapter 5, glass fibre mats were embedded in silica sol to form fibre reinforced aerogel composites. The fabrication process, including ageing temperature and drying process, was optimised to improve the physical, thermal and mechanical properties of the aerogel composite. The prepared aerogel composite was then vacuum sealed to prevent dustiness during handling, and its influence on thermal conductivity was investigated.

The GF-aerogel composites obtained from the optimised process showed excellent thermal conductivity (18.4 mW/m.K at a pressure load of 13.8 kPa). It is worth mentioning that vacuum sealing of the aerogel composites did not only prevent dustiness during handing but also improve the thermal performance. The thermal conductivity could be further reduced to 13.8 mW/m.K by vacuum sealing the GF-aerogel composite. This finding suggests a more efficient way of fabricating aerogel composite with maximum benefit (lowering the thermal conductivity and preventing dustiness during handing). The influence of the pressure load on the thermal conductivity of the GF-aerogel composites was also investigated. The result showed that lower thermal conductivity was achieved with higher pressure, and there was no sign of level-off if the load pressure continued to increase. This might attribute to the microstructure change under compression. The GF-aerogel composites also possessed excellent thermal stability. The aerogel composites maintained almost 95% of their weight, where only 5% of the weight was lost at 800°C. The compression and bending tests proved that the aerogel composites could endure considerable compressive and flexural strain without structural destruction. These outstanding characteristics indicate that GF-aerogel composites have great potential in the thermal insulation field, especially for a moderate temperature environment (i.e., less than 800°C).

8.1.4. Eco-friendly geopolymer and aerogel reinforced with recycled glass fibre

The feasibility of introducing recycled glass fibre (rGF) into the geopolymer system was investigated. The rGFs were dissolved in sodium hydroxide solution to form the alkaline activator. The effect of rGF content on the physical properties, thermal and mechanical performance was discussed. In addition, the chemical structure of the fibre dissolved in alkaline solution via FT-IR was investigated.

The addition of rGF showed that the dry density of geopolymer increased (227 kg/m^3 to 246 kg/m^3) with the increasing amount of rGFs in the alkaline activators up to 15 g. The density then started to drop, whereas the porosity remained almost unchanged regardless of the rGF content (between 81% and 83%). Besides, the addition of rGF had no noticeable impact on the thermal conductivity of geopolymer (51.1 to 54.6 mW/m.K) when ignored the outlier since the porosity tends to dictate the thermal behaviour of porous material. Furthermore, the FTIR analysis showed that the chemical structure of the obtained dry solid had a disordered sodium silicate structure. Finally, a linear increase in compressive strength was observed as the number of rGFs dissolved in NaOH solution increased up to 15g rGFs. The compressive strength increased from 92 to 165 kPa, with a 79% improvement. However, further increase of rGF content led to a reduction of the compressive strength.

The involvement of rGF in geopolymer significantly increase the strength without diminishing the thermal performance. In addition, a considerable amount of recycled glass fibre is being reused. This paves a promising way to maximise environmental benefits and shows great potential in the thermal insulation field.

The feasibility of introducing recycled glass fibre (rGF) into the aerogel system was investigated. Glass fibre mat was first fabricated via wet deposition and chemical bonding process, and it was then used to support the aerogel network. The mechanical and thermal performance of the rGF-aerogel composites was characterised and compared with the aerogel composite reinforced with a commercial glass fibre blanket (prepared in the previous chapter).

The effect of the commercial glass fibre (cGF) to polypropylene (PP) fibre ratio on the physical properties, thermal and mechanical performance was first investigated. The results showed that bulk density possessed an increasing trend as the number of cGF increased, whereas the porosity had no apparent difference. The obtained samples showed an excellent water-repellent property with a maximum contact angle of 147° due to the treatment with TMCS. The hydrophobicity of samples was also confirmed by the FTIR analysis. Besides, a linear relationship between the cGF/PP ratio and thermal conductivity for neat cGF/PP mat was observed, while the thermal conductivity of the aerogel composites decreased with increasing cGF amount. The thermal conductivity value reached the lowest (25 mW/m.K) when aerogel was reinforced with neat cGF. An improvement of 37% was gained compared to the cGF mat. The effect of the cGF/PP ratio on compressive strength also showed a linear relationship at both 10% and 25% strain. The compressive strength of the composites increased from 0.65 kPa to 2.10 kPa at 25% strain, and an improvement of 220% was achieved. These findings provide valuable suggestions when two or more fibres are selected to fabricate fibre mats and to reinforce aerogel composites to meet a particular requirement (i.e., flexibility, heat resistance, or good insulation).

Recycled glass fibre mat was then successfully fabricated via wet deposition and chemical bonding process. In this process, less amount of coupling agent was used by spraying it on the fibre surface. This finding provides valuable suggestions for preparing recycled short fibre mats via wet deposition and chemical bonding processes.

The prepared rGF-aerogel had a low thermal conductivity (23.8 mW/m.K). Besides, the rGF-aerogel possessed higher compressive strength (5.8 kPa at 25% strain) than the aerogel reinforced with the commercial needle punched GF mat (4.7 kPa at 25% strain, prepared in chapter 5). Although the thermal conductivity of the rGF-aerogel is slightly higher than the aerogel reinforced with the commercial needle punched GF mat (18.3 mW/m.K), it still paves a promising way to maximise environmental benefits and shows great potential in the thermal insulation field.

8.1.5. The potential application of aerogel composites in thermal insulating packaging

In chapter 7, the thermal insulation performance of a typical shipping container with different insulation materials, including aerogel composites, was evaluated. An optimised mathematical model was derived and used to analyse the effect of packaging parameters on insulative performance. The novel aspect of this model was incorporating two mathematical models described in the literature to improve the accuracy of the calculated results. Some crucial factors, such as surface emissivity and thermal conductivity of materials, were measured experimentally instead of using literature value to improve the accuracy of the model. A number of experiments were then set up to validate the optimised model comprehensively. The effect of parameters, including surface emissivity, insulation thickness, insulation materials, amount of coolants and surrounding temperatures, on package insulative performance was investigated.

Internal surfaces with lower emissivity proved to be a very cost-effective approach for improving packaging insulation performance. 46% and 40% increase of the MIT were obtained by applying the aluminium foil to the PE and EPS liners, respectively. Insulation thickness was another critical design factor for packaging performance in passive temperature control as MIT had a nonlinear relationship with insulation thickness. A similar phenomenon was also observed with regard to the influence of the surrounding temperature on MIT. Even with high-performance insulation materials, considerable MIT per thickness of insulation could be achieved only when the external temperature was maintained around room temperature (i.e., 23°C).

Aerogel blanket, as a high thermal insulation material, was used to investigate the feasibility of using such materials in the packaging industry. The result showed that much higher MIT could be achieved by using insulation materials with low thermal conductivity. For instance, a 106% increase in the MIT per unit thickness of insulation liner was obtained by replacing conventional EPS with a foiled aerogel blanket. This finding suggests that aerogel composites have a great potential to satisfy the requirement of temperature control during package delivery for long-haul transportation of fresh goods. However, the high price is the main challenge and must be reduced to compete with traditional insulation materials.

The optimised transient thermal model demonstrated the ability to describe three distinctive stages for temperature-time behaviour in insulated packages with coolant. The model was capable of accurately quantifying the contribution from latent heat and sensible heat, respectively. Comparison of modelling and experimental results showed a satisfactory agreement across all the design factors for the packaging insulation performance. The graphical user interface was developed to simplify the simulation process and ease to use, as shown in Appendix-B. This finding suggests that the model can be utilised as a cost-effective tool for packaging design concerning passive temperature control with improved accuracy.

8.2. Future work

In this research, a significant amount of experimental work was carried out to address the project objectives. Although satisfactory results were achieved, there are areas where further research can be targeted. In this section, potential optimisation of the current experiments and new concepts that can be conducted in the future are discussed.

8.2.1. Fabrication and characterisation of inorganic porous geopolymer with excellent thermal performance

The influence of foaming agents on porous geopolymer’s properties was well demonstrated via the investigation of pore structure, bulk density, thermal conductivity, volume expansion, and compressive strength of the prepared specimens. Despite the fact that a comprehensive study of the structure-property relationship of geopolymer was carried out, several parameters can be optimised to improve the accuracy of the experimental results, mechanical properties of the geopolymer and lower the cost.

It was assumed that the true density of the solid geopolymer is the drying density of the geopolymer without a foaming agent. This leads to a systemic error of the porosity calculation using Equation 3.1, and this error is not negligible. Thus, the accuracy of the porosity calculation can be improved by measuring the true density of the solid geopolymer using Archimedes principle.

There are many ways to improve the mechanical properties of geopolymers. The most efficient way is to introduce fibre (without dissolution in alkaline solution) as a structural matrix to form fibre reinforced geopolymer composites. The recycled glass fibre may be a superior option to enhance mechanical properties while lowering the product cost. It was also well explored in the literature that the aluminosilicate solid and alkaline activator ratio, sodium silicate and sodium hydroxide ratio, and sodium hydroxide concentration significantly impact the material properties (see section 2.1.3.2.2). Thus, the effect of these parameters on the mechanical-thermal property relationship is worth investigating.

8.2.2. Fabrication and characterisation of silica aerogel with an improved fabrication process

Waterglass-based silica aerogel was successfully synthesised via ambient pressure drying. The physical properties, microstructure, hydrophobicity, thermal stability, and thermal conductivity of the aerogel were characterised. Due to the fragile nature of the aerogel, it is practically challenging to examine the properties, such as the mechanical properties, as specified sample dimensions are required. Therefore, the application of aerogel is restricted.

The chances of the different aerogel-based products to be transferred to the market depend upon further reduction of production cycle time and, thus, the production cost [202]. Therefore, a fundamental understanding of the thermodynamics and kinetics of the solvent exchange and the drying process is needed. Moreover, the translation into the corresponding multiscale modelling is also necessary. Furthermore, the choice of the solvent, its interaction with the matrix and its influence on the drying process should be investigated further [202]. Although a few novel fabrication processes have been reported, which claimed that production time and the solvent used, can be reduced significantly [302, 327]. These processes need to be further verified to see the possibility of large-scale production.

Meanwhile, the current synthesis path can be optimised by varying deionized water (DI·H_2O) to Na_2SiO_3 volume ratio, the molar concentration of HCl and NH_4OH, and drying methods, aiming to improve the microstructure of aerogel.

8.2.3. Vacuum sealed fibre-reinforced silica aerogel composites with excellent thermal conductivity

In chapter 5, PET and glass fibre reinforced silica aerogel composites were successfully synthesised via ambient pressure drying. Although the GF-aerogel composites offered an excellent thermal insulation performance (18.4 mW/m.K at a pressure load of 13.8 kPa), the influence of heat treatment at high temperature on the thermal insulation performance is unknown. The application of aerogel composite may need excellent thermal stability at a higher temperature while maintaining its structural integrity. Therefore, it would be beneficial to measure the mechanical and thermal properties of the aerogel composites after being heat-treated (i.e., greater than 500°C).

It is well known that the outstanding thermal insulation performance of silica aerogel and composites highly depends on their nano-porous structure. Therefore, it will be beneficial to predict any change of the silica network (i.e. enlargement of pores) during the fabrication process so that the negative effect on the insulation performance can be prevented [22]. Molecular modelling will be an effective technique to fully assess the influence of fibres' presence during gelation and correlate the porous nanostructure features with the type and properties of fibres as well as the possible chemical interaction between the two phases [22].

8.2.4. Eco-friendly geopolymer and aerogel reinforced with recycled glass fibre

In chapter 6, recycled glass fibre (rGF) was introduced into the geopolymer and aerogel system. Within the geopolymer system, rGF was dissolved in sodium hydroxide solution to form the alkaline activator. This is used to improve the mechanical strength of the geopolymer. Within the aerogel system, rGF is used to fabricate the glass fibre mat to support the aerogel network.

The involvement of rGFs significantly improved the strength of geopolymer without diminishing the thermal performance. As a result, the compressive strength increased from 0.07 to 0.17 MPa, with a 143% improvement. However, by referencing ASTM C869 (standard specification for foaming agents used in making preformed foam for cellular concrete), the minimum compressive strength for cellular concrete made with preformed foam is 1.4 MPa. Thus, further improvement is needed to enhance mechanical performance. This can be achieved by introducing a physical foaming method (preformed foam) and optimizing the synthesizing parameters such as ash/alkaline activator ratio and sodium hydroxide/sodium silicate ratio.

The involvement of rGFs in the aerogel system showed that the rGF-aerogel had a superior thermal conductivity (23.8 mW/m.K) compared to the one reinforced with cGF (25.0 mW/m.K). Meanwhile, the compressive strength of the rGF-aerogel increased from 2.1 kPa to 5.8 kPa, with a 170% of improvement. The rGF-aerogel possesses a higher compressive modulus than the aerogel reinforced with the commercial needle punched GF mat. The reason is unclear at this point, and further work is required. Besides, the application of aerogel composite may need excellent thermal stability at a higher temperature while maintaining its structural integrity. Fibre sizing (APS) usually decomposes after 450°C; therefore, it would be beneficial to investigate the microstructure, mechanical and thermal performance of the aerogel composites after heat treatment (i.e., greater than 500°C).

8.2.5. The potential application of aerogel composites in thermal insulating packaging

In chapter 7, a transient thermal model simulating the insulating performance of multi-layered wall packages and the envelope-shaped package were developed and experimentally verified. Although the comparison of modelling and experimental results shows an excellent agreement across all the design factors for the packaging insulation performance, the simplified analytical model accompanied by the ice melt test leads to considerable uncertainty. Therefore, both the analytical model and experimental work can be improved.

Several assumptions have been applied when developing the model. Firstly, conduction is considered as a dominating mechanism for heat transfer in a perfectly closed package surrounded by negligible fluid displacement. In fact, both convection and radiation should be taken into account during the physical shipping process, especially at a higher surrounding temperature. Terpak et al. [37] suggested a faster temperature rise could be obtained when considering only heat transfer by conduction. The influence of convection and radiation was depended on the changing factors during simulation. These include the thickness of the insulation, the surface emissivity of the material and the amount of coolant. The change in emissivity led to a change in radiation and combination heat transfer. The temperature rise could be 25 times slower when the surface emissivity of the material is reduced from 1.0 to 0.04. As a result, the time for the temperature rise was halved via the combination heat transfer [37]. Therefore, it will be beneficial to involve convection and radiation heat transfer within the numerical model.

Furthermore, it is assumed that there is no significant air gap between insulation materials and cardboard. A systematic error could be presented. This was clearly demonstrated when two layers of aerogel blanket liners were used to achieve an insulation thickness similar to other insulation materials, as shown in Figure 7-25 (d). The air space between the layers was classified into categories to calculate the thermal resistance of the multi-layered wall, as described in Equation 7-10. This implies that the air space between layers is unavoidable in the model, although measuring these gaps is practically challenging.

Finally, it was well proved that the surface emissivity of a material is one of the most crucial factors influencing the package’s thermal insulation performance. Therefore, it is favourable to investigate the effects of surface emissivity on package insulative performance in more detail. This includes the location of highly reflective materials in the package, e.g., inside and outside the package and around the product.

Reference

[1] I. E. A. (IEA), "World Energy Outlook 2020," 2020.

[2] I. E. A. (IEA), "Global Energy Review 2021 - Assessing the effects of economic recoveries on global energy demand and CO2 emissions in 2021," 2021.

[3] IPCC, "Climate Change 2021: The Physical Science Basis. Contribution of Working Group I to the Sixth Assessment Report of the Intergovernmental Panel on Climate Change," 2021.

[4] W. W. Fund, "2 °C is Too Much," 2005.

[5] E. Cuce, P. M. Cuce, C. J. Wood, and S. B. Riffat, "Toward aerogel based thermal superinsulation in buildings: A comprehensive review," *Renewable and Sustainable Energy Reviews,* vol. 34, pp. 273-299, 2014.

[6] L. Aditya *et al.*, "A review on insulation materials for energy conservation in buildings," *Renewable and Sustainable Energy Reviews,* vol. 73, pp. 1352-1365, 2017.

[7] D. M. S. Al-Homoud, "Performance characteristics and practical applications of common building thermal insulation materials," *Building and Environment,* vol. 40, no. 3, pp. 353-366, 2005/03/01/ 2005.

[8] K. A. Al-Sallal, "Comparison between polystyrene and fiberglass roof insulation in warm and cold climates," *Renewable Energy,* vol. 28, no. 4, pp. 603-611, 2003/04/01/ 2003.

[9] G. Dixon, T. Abdel-Salam, and P. Kauffmann, "Evaluation of the effectiveness of an energy efficiency program for new home construction in eastern North Carolina," *Energy,* vol. 35, no. 3, pp. 1491-1496, 2010/03/01/ 2010.

[10] T. N. A. I. M. A. (NAIMA), "Energy Efficiency Through Insulation: The Impact on Global Climate Change," in *The Second Conference of the Parties to the Climate Convention*, Geneva, Switzerland, 1996.

[11] A. M. Papadopoulos, "State of the art in thermal insulation materials and aims for future developments," *Energy and Buildings,* vol. 37, no. 1, pp. 77-86, 2005/01/01/ 2005.

[12] Z. Zhang, J. L. Provis, A. Reid, and H. Wang, "Geopolymer foam concrete: An emerging material for sustainable construction," *Construction and Building Materials,* vol. 56, pp. 113-127, 2014.

[13] M. Singh and M. Garg, "Perlite-based building materials — a review of current applications," *Construction and Building Materials*, vol. 5, no. 2, pp. 75-81, 1991/06/01/ 1991.

[14] B. Chu, "Preparation and Properties of Low Thermal Conductivity Insulation Foams Materials Based on Fly Ash," Master, Materials Science and Engineering, China University of Geosciences, 2018.

[15] W. Villasmil, L. J. Fischer, and J. Worlitschek, "A review and evaluation of thermal insulation materials and methods for thermal energy storage systems," *Renewable and Sustainable Energy Reviews,* vol. 103, pp. 71-84, 2019.

[16] N.-N. Shao, Z. Liu, Y.-Y. Xu, F.-L. Kong, and D.-M. Wang, "Fabrication of hollow microspheres filled fly ash geopolymer composites with excellent strength and low density," *Materials Letters,* vol. 161, pp. 451-454, 2015.

[17] Y. Huang, L. Gong, L. Shi, W. Cao, Y. Pan, and X. Cheng, "Experimental investigation on the influencing factors of preparing porous fly ash-based geopolymer for insulation material," *Energy and Buildings,* vol. 168, pp. 9-18, 2018.

[18] C. Bai and P. Colombo, "Processing, properties and applications of highly porous geopolymers: A review," *Ceramics International,* vol. 44, no. 14, pp. 16103-16118, 2018.

[19] N.-n. Shao, Y.-b. Zhang, Z. Liu, D.-m. Wang, and Z.-t. Zhang, "Fabrication of hollow microspheres filled fly ash based foam geopolymers with ultra-low thermal conductivity and relative high strength," *Construction and Building Materials,* vol. 185, pp. 567-573, 2018.

[20] S. Salomo, T. X. Nguyen, D. K. Le, X. Zhang, N. Phan-Thien, and H. M. Duong, "Advanced fabrication and properties of hybrid polyethylene tetraphalate fiber–silica aerogels from plastic bottle waste," *Colloids and Surfaces A: Physicochemical and Engineering Aspects,* vol. 556, pp. 37-42, 2018.

[21] X. Wu, Y. Zhang, P. Yuan, and S. Liao, "Research Progress and Applications of Geopolymer," (in Chinese), *Bulletin of the Chinese ceramic society (in Chinese),* vol. 35, no. 12, 2016.

[22] T. Linhares, M. T. Pessoa de Amorim, and L. Durães, "Silica aerogel composites with embedded fibres: a review on their preparation, properties and applications," *Journal of Materials Chemistry A,* vol. 7, no. 40, pp. 22768-22802, 2019.

[23] A. Hassan, M. Arif, and M. Shariq, "Use of geopolymer concrete for a cleaner and sustainable environment – A review of mechanical properties and microstructure," *Journal of Cleaner Production,* vol. 223, pp. 704-728, 2019.

[24] L. K. Turner and F. G. Collins, "Carbon dioxide equivalent (CO2-e) emissions: A comparison between geopolymer and OPC cement concrete," *Construction and Building Materials,* vol. 43, pp. 125-130, 2013.

[25] F. Xu, G. Gu, W. Zhang, H. Wang, X. Huang, and J. Zhu, "Pore structure analysis and properties evaluations of fly ash-based geopolymer foams by chemical foaming method," *Ceramics International,* vol. 44, no. 16, pp. 19989-19997, 2018.

[26] S. He, D. Huang, H. Bi, Z. Li, H. Yang, and X. Cheng, "Synthesis and characterization of silica aerogels dried under ambient pressure bed on water glass," *Journal of Non-Crystalline Solids,* vol. 410, pp. 58-64, 2015.

[27] A. C. Pierre and A. Rigacci, "SiO2 Aerogels," in *Aerogel Handbook*, M. A. Aegerter, N. Leventis, and M. M. Koebel, Eds.: Spinger Science+Business Media, LLC, 2011, pp. 21-45.

[28] A. UK. (2021). *Retail price for Ethanol absolute, VLSI*. Available: https://uk.vwr.com/store/product/20430052/ethanol-absolute-vlsi

[29] F. Scientific. (2021). *Retail price for n-Hexane*. Available: https://www.fishersci.co.uk/shop/products/n-hexane-environmental-grade-95-thermo-scientific/p-4408263#?keyword=n-hexane

[30] K. A. D. Obrey, K. V. Wilson, and D. A. Loy, "Enhancing mechanical properties of silica aerogels," *Journal of Non-Crystalline Solids,* vol. 357, no. 19-20, pp. 3435-3441, 2011.

[31] H. Zhao and Y. Xu, "Advances in research on strengthening and toughening of silica aerogels," (in Chinese), *Inorganic chemicals industry,* vol. 51, no. 1, pp. 12-15, 2019.

[32] C. Bai, H. Li, E. Bernardo, and P. Colombo, "Waste-to-resource preparation of glass-containing foams from geopolymers," *Ceramics International,* vol. 45, no. 6, pp. 7196-7202, 2019.

[33] S. Zhang, A. Keulen, K. Arbi, and G. Ye, "Waste glass as partial mineral precursor in alkali-activated slag/fly ash system," *Cement and Concrete Research,* vol. 102, pp. 29-40, 2017.

[34] T. Tho-In, V. Sata, K. Boonserm, and P. Chindaprasirt, "Compressive strength and microstructure analysis of geopolymer paste using waste glass powder and fly ash," *Journal of Cleaner Production,* vol. 172, pp. 2892-2898, 2018.

[35] R. Senthil Kumar, S. Sundaresan, and K. Gowri, "Needle Punching Process – A Technological Review."

[36] S.-J. Choi and G. Burgess, "Practical Mathematical Model to Predict the Performance of Insulating Packages," *Packaging Technology and Science,* vol. 20, pp. 369-380, 2007.

[37] J. Terpak, J. Kukurugya, and M. Pitonak, "Simulation Model for Analisis of Thermal Processes in Thermo-Insulating Food Packaging," presented at the 13th International Carpathian Control Conference (ICCC), 2012.

[38] Y. Huang, L. Gong, Y. Pan, C. Li, T. Zhou, and X. Cheng, "Facile construction of the aerogel/geopolymer composite with ultra-low thermal conductivity and high mechanical performance," *RSC Advances*, vol. 8, no. 5, pp. 2350-2356, 2018.

[39] D. Zhang and D. Wang, "Research status of geopolymer concrete," (in Chinese), *Materials Review A: Overview,* vol. 32, no. 5, 2018.

[40] D. N. Huntzinger and T. D. Eatmon, "A life-cycle assessment of Portland cement manufacturing: comparing the traditional process with alternative technologies," *Journal of Cleaner Production,* vol. 17, no. 7, pp. 668-675, 2009.

[41] E. Gartner, "Industrially interesting approaches to “low-CO2” cements," *Cement and Concrete Research,* vol. 34, no. 9, pp. 1489-1498, 2004.

[42] W. Ni, E. Wang, and J. Zhou, "Geopolymer - the green binding material in 21st centruy," (in Chinese), *Advanced Materials Industry,* vol. 6, pp. 24-28, 2003.

[43] G. Zhu, "Preparation and properties of fly ash/metakaolin geopolymer materials," Master, JingDezhen Ceramic Institute, 2014.

[44] Y. Jia, "Preparation and Properties of Na-fly ash geopolymer," China University of Mining and Technology, 2009.

[45] V. F. F. Barbosa and K. J. D. MacKenzie, "Thermal behaviour of inorganic geopolymers and composites derived from sodium polysialate," *Materials research bulletin,* vol. 38, no. 2, pp. 319-331, 2003.

[46] A. Palomo, A. Maclas, and M. T. Blanco, "Physical, chemical and mechanical characterization of geopolymer," presented at the 9th International Congress on the Chemistry of Cement, India, 1992.

[47] J. Xu, Y. Zhou, and X. Tang, "Study on the solidication of heavy metals by fly ash based geopolymers," (in Chinese), *Journal of building materials,* vol. 9, no. 3, 2006.

[48] J. Davidovits, "Properties of geopolymer cements," in *1st international conference on alkaline cements and concretes*, Ukraine, 1994, pp. 131-149: Geopolymer Institute.

[49] J. C. Swanepoel and C. A. Strydom, "Utilisation of fly ash in a geopolymeric material," *Applied Geochemistry,* vol. 17, pp. 1143-1148, 2002.

[50] M. M. A. Abdullah, K. Hussin, M. Bnhussain, K. N. Ismail, and W. M. W. Ibrahim, "Mechanism and Chemical Reaction of Fly Ash Geopolymer Cement- A Review," *International Journal of Pure and Applied Sciences and Technology,* vol. 6, no. 1, pp. 35-44, 2011.

[51] x. Ye, X. Ma, J. He, and J. Zhu, "The Studies on Microstructure of Geopolymer," (in Chinese), *Fly ash comprehensive utilization*, vol. 2, 2016.

[52] (2012, 20/07/2021). *Examples of geopolymer frameworks*. Available: https://www.geopolymer.org/science/examples-geopolymer-frameworks/

[53] C.-K. Ma, A. Z. Awang, and W. Omar, "Structural and material performance of geopolymer concrete: A review," *Construction and Building Materials,* vol. 186, pp. 90-102, 2018.

[54] J. Lv, "Preparation and performance analyzation of fly ash based geopolymer," Master, Xian Northwest University, 2009.

[55] H. Xu, "Geopolymerisation of aluminosilicate minerals," Doctoral, Chemical Engineering, University of Melbourne, 2002.

[56] P. Duan, C. Yan, and W. Zhou, "Influence of partial replacement of fly ash by metakaolin on mechanical properties and microstructure of fly ash geopolymer paste exposed to sulfate attack," *Ceramics International,* vol. 42, no. 2, pp. 3504-3517, 2016.

[57] N. Toniolo and A. R. Boccaccini, "Fly ash-based geopolymers containing added silicate waste. A review," *Ceramics International,* vol. 43, no. 17, pp. 14545-14551, 2017.

[58] *EN450-1 Fly ash for concrete Part1 Definition, specifications and conformity criteria*, 2005.

[59] *C618-Standard Specification for Coal Fly Ash and Raw or Calcined Natural Pozzolan for Use in Concrete*, 2019.

[60] A. Fernández-Jiménez and A. Palomo, "Characterisation of fly ashes. Potential reactivity as alkaline cements☆," *Fuel*, vol. 82, no. 18, pp. 2259-2265, 2003.

[61] P. Duxson, S. W. Mallicoat, G. C. Lukey, W. M. Kriven, and J. S. J. van Deventer, "The effect of alkali and Si/Al ratio on the development of mechanical properties of metakaolin-based geopolymers," *Colloids and Surfaces A: Physicochemical and Engineering Aspects*, vol. 292, no. 1, pp. 8-20, 2007.

[62] L. Le-ping, C. Xue-min, Q. Shu-heng, Y. Jun-li, and Z. Lin, "Preparation of phosphoric acid-based porous geopolymers," *Applied Clay Science*, vol. 50, no. 4, pp. 600-603, 2010.

[63] A. Palomo, M. W. Grutzeck, and M. T. Blanco, "Alkali-activated fly ashes A cement for the future," *Cement and Concrete Research*, vol. 29, pp. 1323-1329, 1999.

[64] Z. Yahya, M. M. A. B. Abdullah, S. Z. A. Talib, and R. A. Razak, "Comparative study on early strength of sodium hydroxide (NaOH) activated fly ash based geopolymer," in *Green Construction and Engineering Education for Sustainable Future*, 2017: American Institute of Physics.

[65] H. Xu and J. S. J. Van Deventer, "The geopolymerisation of alumino-silicate minerals," *International Journal of Mineral Processing*, vol. 59, no. 3, pp. 247-266, 2000.

[66] D. K. Panesar, "Cellular concrete properties and the effect of synthetic and protein foaming agents," *Construction and Building Materials*, vol. 44, pp. 575-584, 2013.

[67] R. M. Novais, R. C. Pullar, and J. A. Labrincha, "Geopolymer foams: An overview of recent advancements," *Progress in Materials Science*, vol. 109, p. 100621, 2020.

[68] G. Masi, W. D. A. Rickard, L. Vickers, M. C. Bignozzi, and A. van Riessen, "A comparison between different foaming methods for the synthesis of light weight geopolymers," *Ceramics International*, vol. 40, no. 9, pp. 13891-13902, 2014.

[69] G. Masi, W. D. A. Rickard, M. C. Bignozzi, and A. van Riessen, "The Influence of Short Fibres and Foaming Agents on the Physical and Thermal Behaviour of Geopolymer Composites," *Advances in Science and Technology*, vol. 92, pp. 56-61, 2014.

[70] T. Li, Z. Wang, T. Zhou, Y. He, and F. Huang, "Preparation and properties of magnesium phosphate cement foam concrete with H2O2 as foaming agent," *Construction and Building Materials*, vol. 205, pp. 566-573, 2019.

[71] S. Petlitckaia and A. Poulesquen, "Design of lightweight metakaolin based geopolymer foamed with hydrogen peroxide," *Ceramics International*, vol. 45, no. 1, pp. 1322-1330, 2019.

[72] P. Liu *et al.*, "Foam stabilizing mechanism of calcium stearate and its effects on pore structure of foam cement thermal insulation board," (in Chinese), *Journal of Central South University (Science and Technology)*, vol. 49, no. 5, 2018.

[73] Y.-F. Cao, Z. Tao, Z. Pan, and R. Wuhrer, "Effect of calcium aluminate cement on geopolymer concrete cured at ambient temperature," *Construction and Building Materials*, vol. 191, pp. 242-252, 2018.

[74] Y. Cui, D. Wang, J. Zhao, D. Li, S. Ng, and Y. Rui, "Effect of calcium stearate based foam stabilizer on pore characteristics and thermal conductivity of geopolymer foam material," *Journal of Building Engineering*, vol. 20, pp. 21-29, 2018.

[75] Q. Li *et al.*, "The role of calcium stearate on regulating activation to form stable, uniform and flawless reaction products in alkali-activated slag cement," *Cement and Concrete Composites*, vol. 103, pp. 242-251, 2019.

[76] M. Wang, H. Du, A. Guo, R. Hao, and Z. Hou, "Microstructure control in ceramic foams via mixed cationic/anionic surfactant," *Materials Letters,* vol. 88, pp. 97-100, 2012.

[77] A. A. Hilal, N. H. Thom, and A. R. Dawson, "On entrained pore size distribution of foamed concrete," *Construction and Building Materials,* vol. 75, pp. 227-233, 2015.

[78] Z. Zhang and H. Wang, "The Pore Characteristics of Geopolymer Foam Concrete and Their Impact on the Compressive Strength and Modulus," *Frontiers in Materials,* vol. 3, 2016.

[79] J. W. Gooch, "Calcium Stearate," in *Encyclopedic Dictionary of Polymers*, J. W. Gooch, Ed. New York, NY: Springer New York, 2011, pp. 111-111.

[80] G. C. Sawicki, "Impact of surfactant composition and surfactant structure on foam control performance," *Colloids and Surfaces A: Physicochemical and Engineering Aspects,* vol. 263, no. 1-3, pp. 226-232, 2005.

[81] T. N. Hunter, E. J. Wanless, G. J. Jameson, and R. J. Pugh, "Non-ionic surfactant interactions with hydrophobic nanoparticles: Impact on foam stability," *Colloids and Surfaces A: Physicochemical and Engineering Aspects,* vol. 347, no. 1-3, pp. 81-89, 2009.

[82] W. Cao, Y. Hang, M. Zhou, and Y. Yang, "Influence of pore size and distribution on the performance of porous concrete," (in Chinese), *New Building Materials,* vol. 41, no. 3, pp. 75-77, 2014.

[83] D. L. Y. Kong, J. G. Sanjayan, and K. Sagoe-Crentsil, "Comparative performance of geopolymers made with metakaolin and fly ash after exposure to elevated temperatures," *Cement and Concrete Research,* vol. 37, no. 12, pp. 1583-1589, 2007.

[84] V. Ducman and L. Korat, "Characterization of geopolymer fly-ash based foams obtained with the addition of Al powder or H2O2 as foaming agents," *Materials Characterization,* vol. 113, pp. 207-213, 2016.

[85] P. Zhang, K. Wang, Q. Li, J. Wang, and Y. Ling, "Fabrication and engineering properties of concretes based on geopolymers/alkali-activated binders - A review," *Journal of Cleaner Production,* vol. 258, p. 120896, 2020.

[86] P. Zhang, Y. Zheng, K. Wang, and J. Zhang, "A review on properties of fresh and hardened geopolymer mortar," *Composites Part B: Engineering,* vol. 152, pp. 79-95, 2018.

[87] Z. Xu, Y. Jia, A. Kahaer, Z. Hou, and M. Han, "Synthesis of light foam materials based on fly ash-geopolymer and its properties study," (in Chinese), *New building materials*, 2009.

[88] J. Feng, R. Zhang, L. Gong, Y. Li, W. Cao, and X. Cheng, "Development of porous fly ash-based geopolymer with low thermal conductivity," *Materials & Design (1980-2015),* vol. 65, pp. 529-533, 2015.

[89] N. B. Singh and B. Middendorf, "Geopolymers as an alternative to Portland cement: An overview," *Construction and Building Materials,* vol. 237, p. 117455, 2020.

[90] F. N. Okoye, J. Durgaprasad, and N. B. Singh, "Mechanical properties of alkali activated flyash/Kaolin based geopolymer concrete," *Construction and Building Materials,* vol. 98, pp. 685-691, 2015.

[91] J. Yuan *et al.*, "Effect of curing temperature and SiO2/K2O molar ratio on the performance of metakaolin-based geopolymers," *Ceramics International,* vol. 42, no. 14, pp. 16184-16190, 2016.

[92] A. Graytee, J. G. Sanjayan, and A. Nazari, "Development of a high strength fly ash-based geopolymer in short time by using microwave curing," *Ceramics International,* vol. 44, no. 7, pp. 8216-8222, 2018.

[93] M. Dong, W. Feng, M. Elchalakani, G. Li, A. Karrech, and E. F. May, "Development of a High Strength Geopolymer by Novel Solar Curing," *Ceramics International,* vol. 43, no. 14, pp. 11233-11243, 2017.

[94] M. N. S. Hadi, M. Al-Azzawi, and T. Yu, "Effects of fly ash characteristics and alkaline activator components on compressive strength of fly ash-based geopolymer mortar," *Construction and Building Materials,* vol. 175, pp. 41-54, 2018.

[95] A. Hameed, R. Rawdhan, and S. Al-Mishhadani, "Effect of Various Factors on the Manufacturing of Geopolymer Mortar," *Archives of Science,* vol. 1, no. 3, 2017.

[96] H. Wang, J. Lu, Y. Xu, J. Sheng, and X. Ding, "Study of geopolymer-based foamed concrete prepared from construction waste," (in Chinese), *New building materials*, 2016.

[97] S. Liu, K. Zhu, S. Cui, X. Shen, and G. Tan, "A novel building material with low thermal conductivity: Rapid synthesis of foam concrete reinforced silica aerogel and energy performance simulation," *Energy and Buildings,* vol. 177, pp. 385-393, 2018.

[98] Y. Cui, D. Wang, J. Zhao, D. Li, Z. Liu, and S. Ng, "Thermal and Mechanical Properties of SiO2 Aerogel–Incorporated Geopolymer Insulation Materials," *Journal of Materials in Civil Engineering,* vol. 31, no. 7, 2019.

[99] P. Li, H. Wu, Y. Liu, J. Yang, Z. Fang, and B. Lin, "Preparation and optimization of ultra-light and thermal insulative aerogel foam concrete," *Construction and Building Materials,* vol. 205, pp. 529-542, 2019.

[100] P. Chindaprasirt and U. Rattanasak, "Characterization of porous alkali-activated fly ash composite as a solid absorbent," *International Journal of Greenhouse Gas Control,* vol. 85, pp. 30-35, 2019.

[101] Z. Zhang, J. L. Provis, A. Reid, and H. Wang, "Mechanical, thermal insulation, thermal resistance and acoustic absorption properties of geopolymer foam concrete," *Cement and Concrete Composites,* vol. 62, pp. 97-105, 2015.

[102] K.-H. Yang, C.-W. Lo, and J.-S. Huang, "Production and properties of foamed reservoir sludge inorganic polymers," *Cement and Concrete Composites,* vol. 38, pp. 50-56, 2013.

[103] X. Yue, T. Zhang, H. Jia, H. Li, and J. Xiang, "Development Status and Application Prospect of Aerogels," (in Chinese), *Engineering studies*, vol. 9, no. 6, pp. 558-567, 2017.

[104] S. S. Kistler, "Coherent Expanded Aerogels and Jellies," *Nature,* vol. 127, no. 741, 1931.

[105] J. L. Gurav, I.-K. Jung, H.-H. Park, E. S. Kang, and D. Y. Nadargi, "Silica Aerogel: Synthesis and Applications," *Journal of Nanomaterials,* vol. 2010, pp. 1-11, 2010.

[106] G. A. Nicolaon and S. J. Teichner, "New preparation process for silica xerogels and aerogels, and their textural properties," *Bulletin de la Soci´et´e Chimique de France,* vol. 5, pp. 1900-1906, 1968.

[107] A. Soleimani Dorcheh and M. H. Abbasi, "Silica aerogel; synthesis, properties and characterization," *Journal of Materials Processing Technology,* vol. 199, no. 1-3, pp. 10-26, 2008.

[108] IUPAC, *Compendium of Chemical Terminology (Gold Book),* . Oxford: Blackwell Publishing, 2014.

[109] H. Maleki, L. Durães, and A. Portugal, "An overview on silica aerogels synthesis and different mechanical reinforcing strategies," *Journal of Non-Crystalline Solids,* vol. 385, pp. 55-74, 2014.

[110] J. Livage, M. Henry, and C. Sanchez, "Sol-gel chemistry of transition metal oxides," *Progress in solid state chemistry,* vol. 18, no. 4, pp. 259-341, 1988.

[111] J. Zha and H. Roggendorf, "Sol–gel science, the physics and chemistry of sol–gel processing, Ed. by C. J. Brinker and G. W. Scherer, Academic Press, Boston 1990, xiv, 908 pp., bound—ISBN 0-12-134970-5," *Advanced Materials,* vol. 3, no. 10, pp. 522-522, 1991.

[112] H.-P. Boehm, "The Chemistry of Silica. Solubility, Polymerization, Colloid and Surface Properties, and Biochemistry. Von R. K. Iler. John Wiley and Sons,

Chichester 1979. XXIV, 886 S., geb. £ 39.50," *Angewandte Chemie,* vol. 92, no. 4, pp. 328-328, 1980.

[113] M. H. Sun, L. H. Chen, and B. L. Su, in *The Sol-Gel Handbook: Characterization and Properties of Sol- Gel Materials*, vol. 2, D. Levy and M. Zayat, Eds. Weinheim: Wiley-VHC, 2015, pp. 987-1030.

[114] Y. Yu, D. Guo, and J. Fang, "Synthesis of silica aerogel microspheres by a two-step acid–base sol–gel reaction with emulsification technique," *Journal of Porous Materials,* vol. 22, no. 3, pp. 621-628, 2015.

[115] J. Fricke and A. Emmerling, "Aerogels—Preparation, properties, applications," in *Chemistry, Spectroscopy and Applications of Sol-Gel Glasses*, R. Reisfeld and C. K. Jjørgensen, Eds. Berlin, Heidelberg: Springer Berlin Heidelberg, 1992, pp. 37-87.

[116] R. A. Strøm *et al.*, "Strengthening and aging of wet silica gels for up-scaling of aerogel preparation," *Journal of Sol-Gel Science and Technology,* vol. 41, no. 3, pp. 291-298, 2006.

[117] Hüsing N and S. U., "Aerogels-Airy Materials: Chemistry, Structure, and Properties," *Angew Chem Int Ed Engl,* vol. 37, no. 1-2, pp. 22-45, 1998.

[118] F. Kirkbir, H. Murata, D. Meyers, and S. R. Chaudhuri, "Drying of aerogels in different solvents between atmospheric and supercritical pressures," *Non-Crystalline Solids,* vol. 225, pp. 14-18, 1998.

[119] S. Smitha, P. Shajesh, P. R. Aravind, S. R. Kumar, P. K. Pillai, and K. G. K. Warrier, "Effect of aging time and concentration of aging solution on the porosity characteristics of subcritically dried silica aerogels," *Microporous and Mesoporous Materials,* vol. 91, no. 1-3, pp. 286-292, 2006.

[120] R. M. Trifu, G. L. Gould, K. Qassim, and J. L. Clark, "Ultra-Lightweight Aerogel Superinsulation as an MLI Replacement," in *Engineering, Construction, and Operations in Challenging Environments: Earth and Space*, Texas, 2004.

[121] S. He, Z. Li, X. Shi, H. Yang, L. Gong, and X. Cheng, "Rapid synthesis of sodium silicate based hydrophobic silica aerogel granules with large surface area," *Advanced Powder Technology,* vol. 26, no. 2, pp. 537-541, 2015.

[122] S. M. Hassanizadeh and W. G. Gray, "Thermodynamic Basis of Capillary Pressure in Porous Media," *Water resources research,* vol. 29, no. 10, pp. 3389-3405, 1993.

[123] D. M. Smith, G. W. Scherer, and J. M. Anderson, "Shrinkage during drying of silica gel," *Non-Crystalline Solids,* vol. 188, pp. 191-206, 1995.

[124] A. V. Rao, E. Nilsen, and M.-A. Einarsrud, "Effect ot precursors, methylation agents and solvents on the physicochemical properties of silica aerogels prepared by atmospheric pressure drying method," *Non-Crystalline solids,* vol. 296, pp. 165-171, 2001.

[125] A. M. Anderson and M. K. Carroll, "Hydrophobic Silica Aerogels: Review of Synthesis, Properties and Applications," in *Aerogel Handbook*, M. A. Aegerter, N. Leventis, and M. M. Koebel, Eds.: Spinger Science+Business Media, LLC, 2011, pp. 47-77.

[126] A. V. Rao, G. M. Pajonk, U. K. H. Bangi, A. P. Rao, and M. M. Koebe, "Sodium Silicate Based Aerogels via Ambient Pressure Drying," in *Aerogel Handbook*, M. A. Aegerter, N. Leventis, and M. M. Koebel, Eds.: Spinger Science+Business Media, LLC, 2011, pp. 103-124.

[127] W. J. Malfait *et al.*, "Surface Chemistry of Hydrophobic Silica Aerogels," *Chemistry of Materials,* vol. 27, no. 19, pp. 6737-6745, 2015.

[128] S. Zhao, M. S. Manic, F. Ruiz-Gonzalez, and M. M. Koebel, in *The Sol-Gel Handbook, Volume 1: Synthesis and processing*, vol. 1, D. Levy and M. Zayat, Eds. Weinheim: Wiley-VHC, 2015, pp. 519-574.

[129] P. B. Wagh, R. Begag, G. M. Pajonk, A. V. Rao, and D. Haranath, "Comparison of some physical properties of silica aerogel monoliths synthesized by different

precursors," *Materials Chemistry and Physics,* vol. 57, no. 3, pp. 214-218, 1999/01/25/ 1999.

[130] U. Schubert, in *The Sol-Gel Handbook: Part One Sol-Gel Chemistry and Methods*, D. Levy and M. Zayat, Eds. Weinheim: Wiley-VHC, 2015, pp. 3-27.

[131] X. Wu, G. Shao, S. Liu, X. Shen, S. Cui, and X. Chen, "A new rapid and economical one-step method for preparing SiO2 aerogels using supercritical extraction," *Powder Technology,* vol. 312, pp. 1-10, 2017.

[132] P. H. Tewari, A. J. Hunt, and K. D. Lofftus, "Ambient-temperature supercritical drying of transparent silica aerogels," *Materials Letters,* vol. 3, no. 9, pp. 363-367, 1985/07/01/ 1985.

[133] F. Ehrburger-Dolle, J. Dallamano, E. Elaloui, and G. M. Pajonk, "Relations between the texture of silica aerogels and their preparation," *Journal of Non-Crystalline Solids,* vol. 186, pp. 9-17, 1995/06/02/ 1995.

[134] P. Dieudonné, A. H. Alaoui, P. Delord, and J. Phalippou, "Transformation of nanostructure of silica gels during drying," *Journal of Non-Crystalline Solids,* vol. 262, no. 1, pp. 155-161, 2000/02/01/ 2000.

[135] S. V. Kalinin, L. I. Kheifets, A. I. Mamchik, A. G. Knot'ko, and A. A. Vertigel, "Influence of the Drying Technique on the Structure of Silica Gels," *Journal of Sol-Gel Science and Technology,* vol. 15, no. 1, pp. 31-35, 1999/06/01 1999.

[136] G. Markevicius, R. Ladj, P. Niemeyer, T. Budtova, and A. Rigacci, "Ambient-dried thermal superinsulating monolithic silica-based aerogels with short cellulosic fibers," *Journal of Materials Science,* vol. 52, no. 4, pp. 2210-2221, 2016.

[137] J. K. Floess, R. Field, and S. Rouanet, "The use of vinyl functional aerogels for reinforcement of silicone rubbers," *Journal of Non-Crystalline Solids,* vol. 285, no. 1, pp. 101-108, 2001/06/01/ 2001.

[138] K. Kanamori, M. Aizawa, K. Nakanishi, and T. Hanada, "Elastic organic–inorganic hybrid aerogels and xerogels," *Journal of Sol-Gel Science and Technology,* vol. 48, no. 1, pp. 172-181, 2008/11/01 2008.

[139] L. Durães, A. Maia, and A. Portugal, "Effect of additives on the properties of silica based aerogels synthesized from methyltrimethoxysilane (MTMS)," *The Journal of Supercritical Fluids,* vol. 106, pp. 85-92, 2015/11/01/ 2015.

[140] A. Borba, J. P. Vareda, L. Durães, A. Portugal, and P. N. Simões, "Spectroscopic characterization of silica aerogels prepared using several precursors – effect on the formation of molecular clusters," *New Journal of Chemistry,* 10.1039/C7NJ01082F vol. 41, no. 14, pp. 6742-6759, 2017.

[141] S. A. Al-Muhtaseb and J. A. Ritter, "Preparation and properties of RF organnic and carbon gels," *Advanced Materials,* vol. 15, no. 2, pp. 101-114, 2003.

[142] J. Shen, J. Hou, Y. Guo, H. Xue, H. Wu, and B. Zhou, "Microstructure Control of RF and Carbon Aerogels Prepared by Sol-Gel Process," *Sol-Gel Science and Technology,* vol. 36, pp. 131-136, 2005.

[143] C.-J. Yu, H. H. Eifert, J. Banhart, and J. Baumeister, "Metal foaming by a powder metallurgy method: Production, properties and applications," *Materials Research Innovations,* vol. 2, no. 3, pp. 181-188, 1998/11/01 1998.

[144] G. Gorgolis and C. Galiotis, "Graphene aerogels: a review," *2D Materials,* vol. 4, no. 3, p. 032001, 2017.

[145] Y. Zhou, X. Hu, S. Guo, C. Yu, S. Zhong, and X. Liu, "Multi-functional graphene/carbon nanotube aerogels for its applications in supercapacitor and direct methanol fuel cell," *Electrochimica Acta,* vol. 264, pp. 12-19, 2018.

[146] H. Cheng, B. Gu, M. P. Pennefather, T. X. Nguyen, N. Phan-Thien, and H. M. Duong, "Cotton aerogels and cotton-cellulose aerogels from environmental waste for oil spillage cleanup," *Materials & Design,* vol. 130, pp. 452-458, 2017.

[147] P. M. Shewale, A. V. Rao, J. L. Gurav, and A. P. Rao, "Synthesis and characterization of low density and hydrophobic silica aerogels dried at ambient pressure using sodium silicate precursor," *Journal of Porous Materials,* vol. 16, no. 1, pp. 101-108, 2007.

[148] A. P. Rao, A. V. Rao, and U. K. H. Bangi, "Low thermalconductive, transparent and hydrophobic ambient pressure dried silica aerogels with various preparation conditions using sodium silicate solutions," *Journal of Sol-Gel Science and Technology,* vol. 47, no. 1, pp. 85-94, 2008.

[149] A. UK, "Aerogel UK Price List - March 2017," ed, 2018.

[150] C. J. Lee, G. S. Kim, and S. H. Hyun, "Synthesis of silica aerogels from waterglass via new modified ambient drying," *Journal of Materials Science,* vol. 37, no. 11, pp. 2237-2241, 2002/06/01 2002.

[151] S.-W. Hwang, T.-Y. Kim, and S.-H. Hyun, "Optimization of instantaneous solvent exchange/surface modification process for ambient synthesis of monolithic silica aerogels," *Journal of Colloid and Interface Science,* vol. 322, no. 1, pp. 224-230, 2008/06/01/ 2008.

[152] S.-W. Hwang, T.-Y. Kim, and S.-H. Hyun, "Effect of surface modification conditions on the synthesis of mesoporous crack-free silica aerogel monoliths from waterglass via ambient-drying," *Microporous and Mesoporous Materials,* vol. 130, no. 1, pp. 295-302, 2010/05/01/ 2010.

[153] F. Shi, L. Wang, and J. Liu, "Synthesis and characterization of silica aerogels by a novel fast ambient pressure drying process," *Materials Letters,* vol. 60, no. 29, pp. 3718-3722, 2006/12/01/ 2006.

[154] S. D. Bhagat, C.-S. Oh, Y.-H. Kim, Y.-S. Ahn, and J.-G. Yeo, "Methyltrimethoxysilane based monolithic silica aerogels via ambient pressure drying," *Microporous and Mesoporous Materials,* vol. 100, no. 1, pp. 350-355, 2007/03/23/ 2007.

[155] Y. Pan *et al.*, "Low thermal-conductivity and high thermal stable silica aerogel based on MTMS/Water-glass co-precursor prepared by freeze drying," *Materials & Design,* vol. 113, pp. 246-253, 2017/01/05/ 2017.

[156] X. Cheng, C. Li, X. Shi, Z. Li, L. Gong, and H. Zhang, "Rapid synthesis of ambient pressure dried monolithic silica aerogels using water as the only solvent," *Materials Letters,* vol. 204, pp. 157-160, 2017.

[157] Z. Shao, X. He, X. Cheng, and Y. Zhang, "A simple facile preparation of methyltriethoxysilane based flexible silica aerogel monoliths," *Materials Letters,* vol. 204, pp. 93-96, 2017.

[158] S. D. Bhagat, Y.-H. Kim, K.-H. Suh, Y.-S. Ahn, J.-G. Yeo, and J.-H. Han, "Superhydrophobic silica aerogel powders with simultaneous surface modification, solvent exchange and sodium ion removal from hydrogels," *Microporous and Mesoporous Materials,* vol. 112, no. 1, pp. 504-509, 2008/07/01/ 2008.

[159] S. Štandeker, Z. Novak, and Ž. Knez, "Adsorption of toxic organic compounds from water with hydrophobic silica aerogels," *Journal of Colloid and Interface Science,* vol. 310, no. 2, pp. 362-368, 2007/06/15/ 2007.

[160] U. Berardi, "The benefits of using aerogel-enhanced systems in building retrofits," *Energy Procedia,* vol. 134, pp. 626-635, 2017.

[161] Y. Lv, R. Huang, H. Wu, S. Wang, and X. Zhou, "Study on Thermal and Optical Properties and Influence Factors of Aerogel Glazing Units," *Procedia Engineering,* vol. 205, pp. 3228-3234, 2017.

[162] T. Stahl, S. Brunner, M. Zimmermann, and K. Ghazi Wakili, "Thermo-hygric properties of a newly developed aerogel based insulation rendering for both exterior and interior applications," *Energy and Buildings,* vol. 44, pp. 114-117, 2012/01/01/ 2012.

[163] R. Nosrati and U. Berardi, "Long-term performance of aerogel-enhanced materials," *Energy Procedia,* vol. 132, pp. 303-308, 2017/10/01/ 2017.

[164] C. Buratti, E. Moretti, and E. Belloni, "Aerogel Plasters for Building Energy Efficiency," in *Nano and Biotech Based Materials for Energy Building Efficiency*, F. Pacheco Torgal, C. Buratti, S. Kalaiselvam, C.-G. Granqvist, and V. Ivanov, Eds. Cham: Springer International Publishing, 2016, pp. 17-40.

[165] Y.-L. Han, "Aerogel Materials for Aerospace," in *Aerospace Materials Handbook*, S. Zhang and D. Zhao, Eds. 1 ed. Boca Raton: CRC Press, 2013, pp. 699-743.

[166] H. Lu, H. Luo, and N. Leventis, "Mechanical Characterization of Aerogels," in *Aerogel Handbook*, M. A. Aegerter, N. Leventis, and M. M. Koebel, Eds.: Spinger Science+Business Media, LLC, 2011, pp. 499-581.

[167] K. E. Parmenter and F. Milstein, "Mechanical properties of silica aerogels," *Journal of Non-Crystalline Solids*, vol. 223, no. 3, pp. 179-189, 1998/01/01/ 1998.

[168] L. Forest, V. Gibiat, and T. Woignier, "Biot's theory of acoustic propagation in porous media applied to aerogels and alcogels," *Journal of Non-Crystalline Solids,* vol. 225, no. Complete, pp. 287-292, 1998.

[169] H. Maleki, "Recent advances in aerogels for environmental remediation applications: A review," *Chemical Engineering Journal*, vol. 300, pp. 98-118, 2016.

[170] A. Kabalnov, "Ostwald Ripening and Related Phenomena," *Journal of Dispersion Science and Technology,* vol. 22, no. 1, pp. 1-12, 2001/02/04 2001.

[171] C. A. M. Mulder, J. G. van Lierop, and G. Frens, "Densification of SiO2-xerogels to glass by ostwald ripening," *Journal of Non-Crystalline Solids,* vol. 82, no. 1, pp. 92-96, 1986/06/01/ 1986.

[172] S. Hæreid, E. Nilsen, and M.-A. Einarsrud, "Properties of silica gels aged in TEOS," *Journal of Non-Crystalline Solids,* vol. 204, no. 3, pp. 228-234, 1996/10/01/ 1996.

[173] M.-A. Einarsrud and E. Nilsen, "Thermal and Temporal Aging of Silica Gels in Monomer Solutions," *Journal of Sol-Gel Science and Technology,* vol. 13, no. 1, pp. 317-322, 1998/01/01 1998.

[174] S. Hæreid, J. Anderson, M. A. Einarsrud, D. W. Hua, and D. M. Smith, "Thermal and temporal aging of TMOS-based aerogel precursors in water," *Journal of Non-Crystalline Solids,* vol. 185, no. 3, pp. 221-226, 1995/06/01/ 1995.

[175] X. Wang, J. Yu, G. Sun, and B. Ding, "Electrospun nanofibrous materials: a versatile medium for effective oil/water separation," *Materials Today,* vol. 19, no. 7, pp. 403-414, 2016/09/01/ 2016.

[176] L. Li, B. Yalcin, B. N. Nguyen, M. A. B. Meador, and M. Cakmak, "Flexible Nanofiber-Reinforced Aerogel (Xerogel) Synthesis, Manufacture, and Characterization," *ACS Applied Materials & Interfaces,* vol. 1, no. 11, pp. 2491-2501, 2009/11/25 2009.

[177] S. Batra, W. Zhao, B. Yalcin, and M. Cakma, "Novel Hybrid Composite Films by Roll-to-Roll Processing " in *Roll-to-Roll Manufacturing: Process Elements and Recent Advances*, J. Greener, G. Pearson, and M. Cakmak, Eds. Hoboken: John Wiley & Sons, Inc.,, 2018, pp. 261-284.

[178] J.-J. Zhao, Y.-Y. Duan, X.-D. Wang, and B.-X. Wang, "Radiative properties and heat transfer characteristics of fiber-loaded silica aerogel composites for thermal insulation," *International Journal of Heat and Mass Transfer,* vol. 55, no. 19, pp. 5196-5204, 2012/09/01/ 2012.

[179] C. Siligardi, P. Miselli, E. Francia, and M. Lassinantti Gualtieri, "Temperature-induced microstructural changes of fiber-reinforced silica aerogel (FRAB) and rock wool thermal insulation materials: A comparative study," *Energy and Buildings,* vol. 138, pp. 80-87, 2017/03/01/ 2017.

[180] H. Wu, Y. Chen, Q. Chen, Y. Ding, X. Zhou, and H. Gao, "Synthesis of Flexible Aerogel Composites Reinforced with Electrospun Nanofibers and Microparticles for Thermal Insulation," *Journal of Nanomaterials,* vol. 2013, pp. 1-8, 2013.

[181] Z. Zhang *et al.*, "Hydrophobic silica aerogels strengthened with nonwoven fibers," *Macromolecular Science, Part A: Pure and Applied Chemistry,* vol. 43, no. 11, pp. 1663-1670, 2007.

[182] K. W. Oh, D. K. Kim, and S. H. Kim, "Ultra-porous flexible PET/Aerogel blanket for sound absorption and thermal insulation," *Fibers and Polymers,* vol. 10, no. 5, pp. 731-737, 2009.

[183] R. Garay Martinez, E. Goiti, G. Reichenauer, S. Zhao, M. Koebel, and A. Barrio, "Thermal assessment of ambient pressure dried silica aerogel composite boards at laboratory and field scale," *Energy and Buildings,* vol. 128, pp. 111-118, 2016.

[184] S. Motahari, H. Javadi, and A. Motahari, "Silica-Aerogel Cotton Composites as Sound Absorber," *Materials in civil engineering,* vol. 27, no. 9, 2014.

[185] J. Feng, D. Le, S. T. Nguyen, V. Tan Chin Nien, D. Jewell, and H. M. Duong, "Silica-cellulose hybrid aerogels for thermal and acoustic insulation applications," *Colloids and Surfaces A: Physicochemical and Engineering Aspects,* vol. 506, pp. 298-305, 2016.

[186] A. R. Horrocks, H. Eichhorn, H. Schwaenke, N. Saville, and C. Thomas, "9 - Thermally resistant fibres," in *High-Performance Fibres*, J. W. S. Hearle, Ed.: Woodhead Publishing, 2001, pp. 281-324.

[187] S. Rebouillat, "2 - Aramids," in *High-Performance Fibres*, J. W. S. Hearle, Ed.: Woodhead Publishing, 2001, pp. 23-61.

[188] K. K. Chawla, *Composite Materials, Science and Engineering,* 3 ed. New York: Springer Science+Business Media, 2012.

[189] M. Li, H. Jiang, D. Xu, and Y. Yang, "A facile method to prepare cellulose whiskers–silica aerogel composites," *Journal of Sol-Gel Science and Technology,* vol. 83, no. 1, pp. 72-80, 2017.

[190] Y. Huang *et al.*, "Fast preparation of glass fiber/silica aerogel blanket in ethanol & water solvent system," *Journal of Non-Crystalline Solids,* vol. 505, pp. 286-291, 2019.

[191] S. Shafi, R. Navik, X. Ding, and Y. Zhao, "Improved heat insulation and mechanical properties of silica aerogel/glass fiber composite by impregnating silica gel," *Journal of Non-Crystalline Solids,* vol. 503-504, pp. 78-83, 2019.

[192] C. Li, X. Cheng, Z. Li, Y. Pan, Y. Huang, and L. Gong, "Mechanical, thermal and flammability properties of glass fiber film/silica aerogel composites," *Journal of Non-Crystalline Solids,* vol. 457, pp. 52-59, 2017.

[193] S. Motahari and A. Abolghasemi, "Silica Aerogel–Glass Fiber Composites As Fire Shield for Steel Frame Structures," *Journal of Materials in Civil Engineering,* vol. 27, no. 10, p. 04015008, 2015.

[194] B. Yuan, S. Ding, D. Wang, G. Wang, and H. Li, "Heat insulation properties of silica aerogel/glass fiber composites fabricated by press forming," *Materials Letters,* vol. 75, pp. 204-206, 2012.

[195] S. Lyu, X. Yang, D. Shi, H. Qi, X. Jing, and S. Li, "Effect of high temperature on compression property and deformation recovery of ceramic fiber reinforced silica aerogel composites," *Science China Technological Sciences,* vol. 60, no. 11, pp. 1681-1691, 2017.

[196] J. Yang, S. Li, Y. Luo, L. Yan, and F. Wang, "Compressive properties and fracture behavior of ceramic fiber-reinforced carbon aerogel under quasi-static and dynamic loading," *Carbon,* vol. 49, no. 5, pp. 1542-1549, 2011/04/01/ 2011.

[197] L. Daelemans *et al.*, "Electrospun nanofibrous interleaves for improved low velocity impact resistance of glass fibre reinforced composite laminates," *Materials & Design,* vol. 141, pp. 170-184, 2018/03/05/ 2018.

[198] S. M. Burkinshaw, "Cellulosic Fibres," in *Physico-chemical Aspects of Textile Coloration*: John Wiley & Sons, Inc., 2016, pp. 249-357.

[199] D. S. Cousins, Y. Suzuki, R. E. Murray, J. R. Samaniuk, and A. P. Stebner, "Recycling glass fiber thermoplastic composites from wind turbine blades," *Journal of Cleaner Production*, vol. 209, pp. 1252-1263, 2019.

[200] S. Mazumdar, D. Karthikeyan, D. Pichler, M. Benevento, and R. Frassine. (2017) State of the Composites Industry Report for 2017. *Composites Manufacturing*. Available: http://compositesmanufacturingmagazine.com/2017/01/composites-industry-report-2017/

[201] J. Feng, S. T. Nguyen, Z. Fan, and H. M. Duong, "Advanced fabrication and oil absorption properties of super-hydrophobic recycled cellulose aerogels," *Chemical Engineering Journal*, vol. 270, pp. 168-175, 2015.

[202] I. Smirnova and P. Gurikov, "Aerogel production: Current status, research directions, and future opportunities," *The Journal of Supercritical Fluids*, vol. 134, pp. 228-233, 2018.

[203] Y. Jiang, J. Feng, J. Feng, and C. Shi, "High-Temperature Mechanical Properties of Silica Aerogel Composites Reinforced by Mullite Fibers," in *Advances in High Temperature Ceramic Matrix Compo sites and Materials for Sustainable Development; Ceramic Transactions, Volume CCLXIII*: John Wiley & Sons, Inc., 2017, pp. 333-339.

[204] J. Li *et al.*, "Improved mechanical and thermal insulation properties of monolithic attapulgite nanofiber/silica aerogel composites dried at ambient pressure," *Journal of Sol-Gel Science and Technology*, vol. 82, no. 3, pp. 702-711, 2017.

[205] Y. Jiang, J. Feng, and J. Feng, "Synthesis and characterization of ambient-dried microglass fibers/silica aerogel nanocomposites with low thermal conductivity," *Journal of Sol-Gel Science and Technology*, vol. 83, no. 1, pp. 64-71, 2017.

[206] J. Jaxel, G. Markevicius, A. Rigacci, and T. Budtova, "Thermal superinsulating silica aerogels reinforced with short man-made cellulose fibers," *Composites Part A: Applied Science and Manufacturing*, vol. 103, pp. 113-121, 2017.

[207] Y. Liao, H. Wu, Y. Ding, S. Yin, M. Wang, and A. Cao, "Engineering thermal and mechanical properties of flexible fiber-reinforced aerogel composites," *Journal of Sol-Gel Science and Technology*, vol. 63, no. 3, pp. 445-456, 2012.

[208] X. Hou, R. Zhang, and D. Fang, "An ultralight silica-modified ZrO 2 –SiO 2 aerogel composite with ultra-low thermal conductivity and enhanced mechanical strength," *Scripta Materialia*, vol. 143, pp. 113-116, 2018.

[209] X. Li, Q. Wang, H. Li, H. Ji, X. Sun, and J. He, "Effect of sepiolite fiber on the structure and properties of the sepiolite/silica aerogel composite," *Journal of Sol-Gel Science and Technology*, vol. 67, no. 3, pp. 646-653, 2013.

[210] J.-J. Zhao, Y.-Y. Duan, X.-D. Wang, and B.-X. Wang, "An analytical model for combined radiative and conductive heat transfer in fiber-loaded silica aerogels," *Journal of Non-Crystalline Solids*, vol. 358, no. 10, pp. 1303-1312, 2012.

[211] S.-C. Lee and G. R. Cunnington, "Conduction and Radiation Heat Transfer in High-Porosity Fiber Thermal Insulation," *Journal of Thermophysics and Heat Transfer*, vol. 14, no. 2, pp. 121-136, 2000.

[212] S.-C. Lee and G. Cunnington, "Fiber orientation effect on radiative heat transfer through fiber composites," in *7th AIAA/ASME Joint Thermophysics and Heat Transfer Conference*, 1998.

[213] G. H. Tang, Y. Zhao, and J. F. Guo, "Multi-layer graded doping in silica aerogel insulation with temperature gradient," *International Journal of Heat and Mass Transfer*, vol. 99, pp. 192-200, 2016.

[214] F. P. Soorbaghi, M. Kokabi, and A. R. Bahramian, "Predicting the effective thermal conductivity of silica/clay mineral nanocomposite aerogels," *International Journal of Heat and Mass Transfer*, vol. 136, pp. 899-910, 2019.

[215] A. Webley, L. Yang, and D. Nash, "Simulation of the heat transfer through fibrous insulation," in *ECCM17 - 17th European Conference on Composite Materials*, Munich, Germany, 2016.

[216] Z. Lu, Z. Yuan, Q. Liu, Z. Hu, F. Xie, and M. Zhu, "Multi-scale simulation of the tensile properties of fiber-reinforced silica aerogel composites," *Materials Science and Engineering: A*, vol. 625, pp. 278-287, 2015.

[217] C. Li, Z. Chen, B. Yao, and L. Wang, "Research progress of silica aerogel thermal insulation composites," (in Chinese), *Functional materials*, vol. 50, no. 4, 2019.

[218] "Wood Framing Insulated With Aerogel Improves Energy Efficiency by 15%," in *Aspen Aerogels*, ed, 2011.

[219] "Aerogel Interior Wall Insulation Reduces U-Values by 44% and Lowers Energy Use and Carbon Emissions," in *Aspen Aerogels*, ed, 2011.

[220] M. Shatat, T. Elmer, D. Tetlow, and S. Riffat, "The state of the art Superinsulation construction materials under the UK's domestic energy building," in *14th International Conference on Sustainable Energy Technologies*, Nottingham, UK, 2015.

[221] J. He, X. Li, D. Su, H. Ji, and X. Wang, "Ultra-low thermal conductivity and high strength of aerogels/fibrous ceramic composites," *Journal of the European Ceramic Society*, vol. 36, no. 6, pp. 1487-1493, 2016.

[222] Z. Talebi, P. Soltani, N. Habibi, and F. Latifi, "Silica aerogel/polyester blankets for efficient sound absorption in buildings," *Construction and Building Materials*, vol. 220, pp. 76-89, 2019.

[223] J.-O. Yeon, K.-W. Kim, K.-S. Yang, J.-M. Kim, and M.-J. Kim, "Physical properties of cellulose sound absorbers produced using recycled paper," *Construction and Building Materials*, vol. 70, pp. 494-500, 2014/11/15/ 2014.

[224] S. Malakooti *et al.*, "Sound insulation properties in low-density, mechanically strong and ductile nanoporous polyurea aerogels," *Journal of Non-Crystalline Solids*, vol. 476, pp. 36-45, 2017/11/15/ 2017.

[225] S. Amares, E. Sujatmika, T. W. Hong, R. Durairaj, and H. S. H. B. Hamid, "A Review: Characteristics of Noise Absorption Material," *Journal of Physics: Conference Series*, vol. 908, p. 012005, 2017.

[226] Y. Ananthan, K. K. Sanghamitra, and N. Hebalkar, "Silica Aerogels for Energy Conservation and Saving," in *Nanotechnology for Energy Sustainability*, B. Rag, M. V. d. Voorde, and Y. Mahajan, Eds.: Wiley-VCH Verlag GmbH & Co. KGaA, 2017, pp. 937-966.

[227] J. Groß and J. Fricke, "Scaling of elastic properties in highly porous nanostructured aerogels," *Nanostructured materials*, vol. 6, pp. 905-908, 1995.

[228] B. H. John F. T. Conroy, "Microscale Thermal Relaxation during Acoustic Propagation in Aerogel and Other Porous Media," *Microscale Thermophysical Engineering*, vol. 3, no. 3, pp. 199-215, 1999.

[229] J. Martin, B. Hosticka, C. Lattimer, and P. M. Norris, "Mechanical and acoustic properties as a function of PEG concentration in silica gel," *Non-Crystalline solids*, vol. 285, pp. 222-229, 2001.

[230] J. Feng, D. Le, S. T. Nguyen, V. Tan Chin Nien, D. Jewell, and H. M. Duong, "Silica cellulose hybrid aerogels for thermal and acoustic insulation applications," *Colloids and Surfaces A: Physicochemical and Engineering Aspects*, vol. 506, pp. 298-305, 2016.

[231] E. Moretti, F. Merli, E. Cuce, and C. Buratti, "Thermal and Acoustic Properties of Aerogels: Preliminary Investigation of the Influence of Granule Size," *Energy Procedia*, vol. 111, pp. 472-480, 2017/03/01/ 2017.

[232] M. Shi *et al.*, "Superhydrophobic silica aerogels reinforced with polyacrylonitrile fibers for adsorbing oil from water and oil mixtures," *RSC Advances,* vol. 7, no. 7, pp. 4039-4045, 2017.

[233] W. Wei, C. W. Li, J. M. Xie, J. J. Zhu, X. M. Lü, and C. H. Yan, "Application of Hydrophobic Silica/Fiber Composite Aerogels in Organic Absorption," *Materials Science Forum,* vol. 675-677, pp. 1035-1039, 2011.

[234] H. Wu, D. Li, F. Huang, and C. Guo, "Experimental Study on Ballistic Characteristics of Fiber Reinforced Aerogel Composite Structures," in *8th International Symposium on Ballistics*, atlanta, georgia, USA, 2014.

[235] D. J. Boday, B. Muriithi, R. J. Stover, and D. A. Loy, "Polyaniline nanofiber–silica composite aerogels," *Journal of Non-Crystalline Solids,* vol. 358, no. 12-13, pp. 1575-1580, 2012.

[236] S. Chakraborty, A. A. Pisal, V. K. Kothari, and A. Venkateswara Rao, "Synthesis and Characterization of Fibre Reinforced Silica Aerogel Blankets for Thermal Protection," *Advances in Materials Science and Engineering,* vol. 2016, pp. 1-8, 2016.

[237] M. Venkataraman, R. Mishra, T. M. Kotresh, J. Militky, and H. Jamshaid, "Aerogels for thermal insulation in high-performance textiles," *Textile Progress,* vol. 48, no. 2, pp. 55-118, 2016/04/02 2016.

[238] H. Maleki, L. Durães, C. A. García-González, P. del Gaudio, A. Portugal, and M. Mahmoudi, "Synthesis and biomedical applications of aerogels: Possibilities and challenges," *Advances in Colloid and Interface Science,* vol. 236, pp. 1-27, 2016/10/01/ 2016.

[239] M. A. B. Meador, "Improving Elastic Properties of Polymer-Reinforced Aerogels," in *Aerogel Handbook*, M. A. Aegerter, N. Leventis, and M. M. Koebel, Eds.: Spinger Science+Business Media, LLC, 2011, pp. 315-334.

[240] I. Smirnova and P. Gurikov, "Aerogels in Chemical Engineering: Strategies Toward Tailor-Made Aerogels," *Annu Rev Chem Biomol Eng,* vol. 8, pp. 307-334, Jun 7 2017.

[241] Y. Liang, H. Wu, G. Huang, J. Yang, and H. Wang, "Thermal performance and service life of vacuum insulation panels with aerogel composite cores," *Energy and Buildings,* vol. 154, pp. 606-617, 2017.

[242] AVK and CCeV, "Composites market report 2015. Market developments, tredns, outlook and challenges," 2015.

[243] J. P. Jensen and K. Skelton, "Wind turbine blade recycling: Experiences, challenges and possibilities in a circular economy," *Renewable and Sustainable Energy Reviews,* vol. 97, pp. 165-176, 2018.

[244] K. Pender and L. Yang, "Investigation of catalyzed thermal recycling for glass fiber-reinforced epoxy using fluidized bed process," *Polymer Composites,* vol. 40, no. 9, pp. 3510-3519, 2019.

[245] K. Pender and L. Yang, "Regenerating performance of glass fibre recycled from wind turbine blade," *Composites Part B: Engineering,* vol. 198, p. 108230, 2020.

[246] S. T. Bashir, L. Yang, J. J. Liggat, and J. L. Thomason, "Kinetics of dissolution of glass fibre in hot alkaline solution," *Journal of Materials Science,* vol. 53, no. 3, pp. 1710-1722, 2017.

[247] L. Yang, E. R. Sáez, U. Nagel, and J. L. Thomason, "Can thermally degraded glass fibre be regenerated for closed-loop recycling of thermosetting composites?," *Composites Part A: Applied Science and Manufacturing,* vol. 72, pp. 167-174, 2015/05/01/ 2015.

[248] J. L. Thomason, U. Nagel, L. Yang, and E. Sáez, "Regenerating the strength of thermally recycled glass fibres using hot sodium hydroxide," *Composites Part A: Applied Science and Manufacturing,* vol. 87, pp. 220-227, 2016/08/01/ 2016.

[249] S. S. Kouassi, J. Andji, J.-P. Bonnet, and S. Rossignol, "Dissolution of waste glasses in high alkaline solutions," *Ceramics - Silikáty,* vol. 54, no. 3, pp. 235-240, 2010.

[250] H. Maraghechi, F. Rajabipour, C. G. Pantano, and W. D. Burgos, "Effect of calcium on dissolution and precipitation reactions of amorphous silica at high alkalinity," *Cement and Concrete Research,* vol. 87, pp. 1-13, 2016.

[251] M. Torres-Carrasco, J. G. Palomo, and F. Puertas, "Sodium silicate solutions from dissolution of glasswastes. Statistical analysis," *Materiales de Construcción,* vol. 64, no. 314, 2014.

[252] R. M. Novais, J. Carvalheiras, M. P. Seabra, R. C. Pullar, and J. A. Labrincha, "Effective mechanical reinforcement of inorganic polymers using glass fibre waste," *Journal of Cleaner Production,* vol. 166, pp. 343-349, 2017.

[253] R. M. Novais, J. Carvalheiras, M. N. Capela, M. P. Seabra, R. C. Pullar, and J. A. Labrincha, "Incorporation of glass fibre fabrics waste into geopolymer matrices: An eco-friendly solution for off-cuts coming from wind turbine blade production," *Construction and Building Materials,* vol. 187, pp. 876-883, 2018.

[254] M. Torres-Carrasco and F. Puertas, "Waste glass in the geopolymer preparation. Mechanical and microstructural characterisation," *Journal of Cleaner Production,* vol. 90, pp. 397-408, 2015.

[255] N. Toniolo, A. Rincón, J. A. Roether, P. Ercole, E. Bernardo, and A. R. Boccaccini, "Extensive reuse of soda-lime waste glass in fly ash-based geopolymers," *Construction and Building Materials,* vol. 188, pp. 1077-1084, 2018.

[256] Plastena. (18/12/2020). *Construction glass-fibre fabrics and non-woven materials*. Available: https://plastena.lt/en/construction-glass-fibre-fabrics-and-non-woven-materials

[257] Edana. (18/12/2020). *How are nonwovens made?* Available: https://www.edana.org/nw-related-industry/how-are-nonwovens-made

[258] K. Pender, "Recycling regenerating and reusing reinforcement glass fibres," PhD, Mechanical and Aerospace Engineering, University of Strathclyde, 2018.

[259] J. L. Thomason, "Glass fibre sizing: A review," *Composites Part A: Applied Science and Manufacturing,* vol. 127, p. 105619, 2019.

[260] Michelman. (20/12/2020). *Reinforced plastic composites - Fiber Sizing*. Available: https://www.michelman.com/markets/reinforced-plastic-composites/fiber-sizing/

[261] X. M. Liu, J. L. Thomason, and F. R. Jones, "XPS and AFM Study of Interaction of Organosilane and Sizing with E-glass Fibre Surface," *Journal of Adhesion,* vol. 84, no. 4, pp. 322-338, 2008.

[262] S. Van Boxstael *et al.*, "Food safety issues in fresh produce: bacterial pathogens, viruses and pesticide residues indicated as major concerns by stakeholders in the fresh produce chain," *Food Control,* vol. 32, no. 1, pp. 190-197, 2013.

[263] S. James and C. James, "The food cold-chain and climate change," *Food Research International,* vol. 43, no. 7, pp. 1944-1956, 2010.

[264] U. I. T. Comitee, *Agreement on the international carriage of perishable foodstuffs and on the special equipment to be used for such carriage*. Geneva: United Nation Publications, 2011, p. 85.

[265] M. D. Pierson, *HACCP: principles and applications*. Springer Science & Business Media, 2012.

[266] D. Restuccia *et al.*, "New EU regulation aspects and global market of active and intelligent packaging for food industry applications," *Food Control,* vol. 21, no. 11, pp. 1425-1435, 2010.

[267] C. TSNI, "Managing the cold chain for quality and safety," Oregon State University2013.

[268] S. P. Singh, G. Burgess, and J. Singh, "Performance Comparison of Thermal Insulated Packaging Boxes, Bags and Refrigerants for Single-parcel Shipments," *Packaging Technology and Science,* vol. 21, pp. 25-35, 2008.

[269] M. Gonçalves, N. Simões, C. Serra, and I. Flores-Colen, "A review of the challenges posed by the use of vacuum panels in external insulation finishing systems," *Applied Energy,* vol. 257, 2020.

[270] D. N. Pei. (2020, 19/07/2021). *What's Inside an Ice Pack?* Available: https://www.poison.org/articles/whats-inside-ice-packs-201

[271] A. Alleva. (2016, 10/03/2020). *Why You Should Use Gel Packs Instead of Frozen Water*. Available: https://blog.cryopak.com/blog/2017/04/use-gel-packs-instead-frozen-water

[272] "Heat, air and moisture control in building assemblies – material properties," in *ASHRAE Handbook of Fundamentals, American Society of Heating, Refrigerating and Air Conditioning Engineers*Atlanta, 2009.

[273] F. Domínguez-Muñoz, B. Anderson, J. M. Cejudo-López, and A. Carrillo-Andrés, "Uncertainty in the thermal conductivity of insulation materials," *Energy and Buildings,* vol. 42, no. 11, pp. 2159-2168, 2010.

[274] M. Kolich, P. Hoke, D. Dooge, M. Doroudian, E. Litovsky, and J. Kleiman, "Influence of temperature and mechanical compression on thermophysical properties of car interior foam plastics insulation," *Journal of Elastomers & Plastics,* vol. 46, no. 2, pp. 132-143, 2012.

[275] M. Sletnes, B. P. Jelle, and B. Risholt, "Feasibility study of novel integrated aerogel solutions," *Energy Procedia,* vol. 132, pp. 327-332, 2017.

[276] V. Kočí *et al.*, "Effect of Moisture Content on Thermal Properties of Porous Building Materials," *International Journal of Thermophysics,* vol. 38, no. 2, p. 28, 2016/12/14 2016.

[277] N. C. Balaji, M. Mani, and B. V. V. Reddy, "Discerning Heat Transfer in Building Materials," *Energy Procedia,* vol. 54, pp. 654-668, 2014.

[278] J. B. Alvey, J. Patel, and L. D. Stephenson, "Experimental study on the effects of humidity and temperature on aerogel composite and foam insulations," *Energy and Buildings,* vol. 144, pp. 358-371, 2017/06/01/ 2017.

[279] D. Belanger and U. Berardi, "The Impact of Aging on the Effective Thermal Conductivity of Foam Insulation: A Simulation Investigation Using Laboratory Characterization Data," in *eSim 2018, the 10th conference of IBPSA-Canada,* Canada, 2018, pp. 433-442.

[280] D. Shi *et al.*, "Experimental investigation on high temperature anisotropic compression properties of ceramic-fiber-reinforced SiO2 aerogel," *Materials Science and Engineering: A,* vol. 585, pp. 25-31, 2013.

[281] G. Changfeng, C. Yujie, and L. Bo, "Numerical simulation and experimental study of the heat transition in a foam container," *Journal of Cellular Plastics,* vol. 50, no. 1, pp. 15-36, 2013.

[282] G. Burgess, "Practical Thermal Resistance and Ice Requirement Calculations for Insulating packages," *Packaging Technology and Science,* vol. 12, pp. 75-80, 1999.

[283] S. Jay, J. Sanjiv, and S. Koushik, "The Effect of Distribution on Product Temperature Profile in Thermally Insulated Containers for Express Shipments," *Packaging Technology and Science,* vol. 26, pp. 327-338, 2012.

[284] D. M. Stubbs, S. H. Pulko, and A. J. Wilkinson, "Wrapping strategies for temperature control of chilled foodstuffs during transport," *Transactions of the Institute of Measurement and Control,* vol. 26, no. 1, pp. 69-80, 2004.

[285] B. Margeirsson *et al.*, "Temperature fluctuations and quality deterioration of chilled cod (Gadus morhua) fillets packaged in different boxes stored on pallets under dynamic temperature conditions," *International Journal of Refrigeration,* vol. 35, no. 1, pp. 187-201, 2012.

[286] K. L. Valtysdottir, B. Margeirsson, S. Arason, H. Palsson, R. Gospavic, and V. Popov, "Heat Transfer Modelling for Improving Thermal Protection of Fish Packaging," presented at the CIGR Section VI International Symposium, 2011.

[287] C. Ng, U. J. Alengaram, L. S. Wong, K. H. Mo, M. Z. Jumaat, and S. Ramesh, "A review on microstructural study and compressive strength of geopolymer mortar, paste and concrete," *Construction and Building Materials,* vol. 186, pp. 550-576, 2018.

[288] A. Sugawara and Y. Yoshizawa, "An investigation on the thermal conductivity of porous materials and its application in porous rocks," *Australian Journal of Physics,* vol. 14, no. 4, pp. 469-480, 1961.

[289] P. Pędziwiatr, F. Mikołajczyk, D. Zawadzki, K. Mikołajczyk, and A. Bedka, "Decomposition of hydrogen peroxide - kinetics and review of chosen catalysts," *Acta Innovations*, no. 26, pp. 45-52, 2018.

[290] X. Hu *et al.*, "Structure-behavior-property relationship study of surfactants as foam stabilizers explored by experimental and molecular simulation approaches," *J Phys Chem B,* vol. 116, no. 1, pp. 160-7, Jan 12 2012.

[291] V. B. K. M. C. Thaumaturgo, "Synthesis and characterisation of materials based on inorganic polymers of alumina and silica," *International Journal of Inorganic Materials,* vol. 2, pp. 309-317, 2000.

[292] H.-U. G. Helmut Günzler, *IR Spectroscopy: An Introduction*. Germany: Wiley-VCH Verlag GmbH, 2002.

[293] P. Chindaprasirt, C. Jaturapitakkul, W. Chalee, and U. Rattanasak, "Comparative study on the characteristics of fly ash and bottom ash geopolymers," *Waste Manag,* vol. 29, no. 2, pp. 539-43, Feb 2009.

[294] Z. Liu, N.-n. Shao, J.-f. Qin, F.-l. Kong, C.-x. Wang, and D.-m. Wang, "Strength and thermal behavior of low weight foam geopolymer using circulating fluidized bed combustion fly ash," *Journal of Central South University,* vol. 22, no. 9, pp. 3633-3640, 2015.

[295] C. Rees, J. Provis, G. Luckey, and J. Deventer, "Attenuated Total Reflectance Fourier Transform Infrared Analysis of Fly Ash Geopolymer Gel Aging," *Langmuir,* no. 23, pp. 8170-8179, 2007.

[296] A. Fernández-Jiménez and A. Palomo, "Mid-infrared spectroscopic studies of alkali-activated fly ash structure," *Microporous and Mesoporous Materials,* vol. 86, no. 1-3, pp. 207-214, 2005.

[297] F. Skvara, L. Kopecky, V. Smilauer, and Z. Bittnar, "Material and structural characterization of alkali activated low-calcium brown coal fly ash," *J Hazard Mater,* vol. 168, no. 2-3, pp. 711-20, Sep 15 2009.

[298] A. Venkateswara Rao, H. M. Sakhare, A. K. Tamhankar, M. L. Shinde, D. B. Gadave, and P. B. Wagh, "Influence of N,N-dimethylformamide additive on the physical properties of citric acid catalyzed TEOS silica aerogels," *Materials Chemistry and Physics,* vol. 60, no. 3, pp. 268-273, 1999/09/15/ 1999.

[299] H. Omranpour and S. Motahari, "Effects of processing conditions on silica aerogel during aging: Role of solvent, time and temperature," *Journal of Non-Crystalline Solids,* vol. 379, pp. 7-11, 2013.

[300] M. Thommes *et al.*, "Physisorption of gases, with special reference to the evaluation of surface area and pore size distribution (IUPAC Technical Report)," *Pure and Applied Chemistry,* vol. 87, no. 9-10, pp. 1051-1069, 2015.

[301] H.-P. Ebert, "Thermal properties of aerogels," in *Aerogel Handbook*, M. A. Aegerter, N. Leventis, and M. M. Koebel, Eds.: Spinger Science+Business Media, LLC, 2011, pp. 537-564.

[302] Y. Huang, S. He, M. Feng, H. Dai, Y. Pan, and X. Cheng, "Organic solvent-saving preparation of water glass based aerogel granules under ambient pressure drying," *Journal of Non-Crystalline Solids,* vol. 521, 2019.

[303] Y. Lv, H. Wu, S. Wang, P. Fu, and X. Zhou, "Influencing factors of aerogel architectural glazing thermal and light properties," (in Chinese), *Journal of Civic, Architectural and Environmental Engineering,* vol. 40, no. 1, pp. 134-140, 2018.

[304] M. Li and Y. Chen, "Relation of density and thermal conductivity of micro-porous calcium silicate insulation material," (in Chinese), *JOURNAL OF THE CHINESE CERAMIC SOCIETY,* vol. 33, no. 11, pp. 1414-1417, 2005.

[305] M.-T. AG, "Operating instructions of density kit," ed.

[306] V. Moreno-Maldonado, L. S. Acosta-Torres, F. H. Barceló-Santana, R. D. Vanegas-Lancón, M. E. Plata-Rodríguez, and V. M. Castaño, "Fiber-reinforced nanopigmented poly(methyl methacrylate) as improved denture base," *Journal of Applied Polymer Science,* vol. 132, no. 2, 2015.

[307] A. P. d. S. Pereira, M. H. P. d. Silva, É. P. Lima Júnior, A. d. S. Paula, and F. J. Tommasini, "Processing and Characterization of PET Composites Reinforced With Geopolymer Concrete Waste," *Materials Research,* vol. 20, no. suppl 2, pp. 411-420, 2017.

[308] H. Simmler *et al.*, "Vacuum Insulation Panels - Study on VIP-components and panels for service life prediction of VIP in building applications (Subtask A)," Switzerland2005.

[309] A. Hoseini, C. McCague, M. Andisheh-Tadbir, and M. Bahrami, "Aerogel blankets: From mathematical modeling to material characterization and experimental analysis," *International Journal of Heat and Mass Transfer,* vol. 93, pp. 1124-1131, 2016.

[310] G. Wei, Y. Liu, X. Zhang, F. Yu, and X. Du, "Thermal conductivities study on silica aerogel and its composite insulation materials," *International Journal of Heat and Mass Transfer,* vol. 54, no. 11-12, pp. 2355-2366, 2011.

[311] A. Hoseini, A. Malekian, and M. Bahrami, "Deformation and thermal resistance study of aerogel blanket insulation material under uniaxial compression," *Energy and Buildings,* vol. 130, pp. 228-237, 2016.

[312] P. JOHANSSON, "Building Retrofit using Vacuum Insulation Panels," Doctoral, Department of Civil and Environmental Engineering, CHALMERS UNIVERSITY OF TECHNOLOGY, Sweden, 2014.

[313] T. Zhou, X. Cheng, Y. Pan, C. Li, L. Gong, and H. Zhang, "Mechanical performance and thermal stability of glass fiber reinforced silica aerogel composites based on co-precursor method by freeze drying," *Applied Surface Science,* vol. 437, pp. 321-328, 2018.

[314] B. Li *et al.*, "Calcined sodium silicate as an efficient and benign heterogeneous catalyst for the transesterification of natural lecithin to L-α-glycerophosphocholine," *Green Processing and Synthesis,* vol. 8, no. 1, pp. 78-84, 2019.

[315] R. Vinai and M. Soutsos, "Production of sodium silicate powder from waste glass cullet for alkali activation of alternative binders," *Cement and Concrete Research,* vol. 116, pp. 45-56, 2019.

[316] S. T. Bashir, "A chemical approach to regenerating the performance of thermally damaged glass fibres," Doctor of Philosophy, Mechanical and Aerospace Engineering, University of Strathclyde, 2019.

[317] M. O. Daramola, D. Nkazi, and K. Mtshali, "Synthesis and Evaluation of Catalytic Activity of Calcined Sodium Silicate for Transesterification of Waste Cooking Oil to Biodiesel," *Renewable Energy Research,* vol. 5, no. 2, pp. 517-523, 2015.

[318] M. Kucharek, L. Yang, and K. Wang, "Assessment of insulating package performance by mathematical modelling," *Packaging Technology and Science,* vol. 33, no. 2, pp. 65-73, 2020.

[319] M. A. Echols, "Food safety regulation in the European Union and the United States: different cultures, different laws," *Colum. J. Eur. L.,* vol. 4, p. 525, 1998.

[320] L. electronics. (28/09/2018). *Easylog EL-21CFR-TP-LCD* Available: https://www.lascarelectronics.com/easylog-el-21cfr-tp-lcd

[321] L. electronics. (18/07/2018). *Easylog EL-SGD 43-ATP*. Available: https://www.lascarelectronics.com/easylog-el-sgd-43-atp

[322] X. Luo and J. Sun, "Method for measuring object surface emissivity," (in Chinese), *Automatic Measurement and Control,* vol. 26, no. 8, 2007.

[323] J. Coulson and J. F. Richardson, "Chapter 1 - Heat Transfer," in *Coulson and Richardson's Chemical Engineering (Seventh Edition): Volume 1B: Heat and Mass Transfer: Fundamentals and Applications*, R. Chhabra and V. Shankar, Eds.: Butterworth-Heinemann, 2018, pp. 3-264.

[324] J. B. Heaney, "Efficiency of aluminized mylar insulation at cryogenic temperatures," presented at the Cryogenic Optical Systems and Instruments VIII, 1998.

[325] K. I. Ltd, "Kingspan Thermal Structiral Applications - Kingspan Thermafloor TF70," ed, 2017.

[326] E. Ltd, "Electronic Temperature Instruments Emissivity table," ed.

[327] A. Stojanovic, S. Zhao, E. Angelica, W. J. Malfait, and M. M. Koebel, "Three routes to superinsulating silica aerogel powder," *Journal of Sol-Gel Science and Technology,* vol. 90, no. 1, pp. 57-66, 2019.

Appendix-A The UK insulated packaging market 2018

Appendix-A summarises the insulation material used, coolant types (if any), estimated transportation time, and cost per package for major UK package manufacturers. All data were obtained by visiting the official websites of the companies.

The UK insulated packaging market 2018						
Company	**Material**	**Performance (Hr)**	**Coolant**	**Description**	**Dimension (mm)***	**Price (£)****
C.R. Distribution	polystyrene	N/A	N/A	N/A		
Camilla and Roly	Natural Wool	24	None	N/A		
Chilled Packaging	AI bubble wrap	72	with Gel packs	ice cube box	273x273x143 - 413x273x273	2.57-3.9
EPS Group	polystyrene	24	with ice	N/A		
Excel	polystyrene	N/A	with gel packs			
Hydropac	polystyrene	24+	N/A	postal pocket	200x250 - 600x250	1.2-2.65
Hydropac	polymer based wrap	24+	N/A	air bag	400x270x160 - 590x320x225	2.14-3.93
Hydropac	polymer based wrap	24+	N/A	cool bag	240x260x100 - 480x480x140	0.5-1.12
Hydropac	polystyrene	24+	N/A	freshpac box set	325x205x190 - 498x287x178	2.63-8.68
Icertech	polystyrene	48	with Gel packs	foil-box	245x245x240 - 405x405x300	1.5-3.3
Icertech	polystyrene	72	with Gel packs	Tile-box	190x190x190 - 490x490x290	1.75-3.6
JBP	polystyrene	N/A	with ice	deluxe box	305x220x60 - 730x335x195	15.45-45.78
JBP	polystyrene	N/A	with ice	box	310x225x60 - 740x340x200	1.37-6.7

K.B. Packaging & insulation	polystyrene	24	N/A	N/A		
Kevothermal	VIP	N/A	with Gel packs	N/A		
Laminarmedica	polystyrene	72	wirh ice packs	N/A		
Phoenix specialists	polystyrene	N/A	N/A	N/A		
Puffin Packaging	Natural Wool	48	with ice packs	box with two liners	28x21x27 - 47x32x32	3.08-6.35
Puffin Packaging	Natural Wool	48	with ice packs	box liners only	27x66 - 32x123	0.99-1.95
Puffin Packaging	Natural Wool	48	with ice packs	box with pouch	21x21x20 - 48x33x36	3.25-6.7
Puffin Packaging	Natural Wool	48	with ice packs	pouch	37x38 - 77x70	1.44-4.38
simplipac	polystyrene	N/A	with ice	N/A		
sofrigam	VIP	240	with Gel packs	N/A		
Soft Box system	polystyrene	96	with Gel packs	N/A		
sonoco thermosafe	biodegradable fiber	48	with ice	panel	203x203x203 - 356x356x356	2.12-4.92
sonoco thermosafe	biodegradable fiber	48	with ice	envelope	279x229 - 457x356	2.18-3.47
sorba freeze	polystyrene	48	sorba-freeze blocks	box	240x240x240 - 560x330x220	2.15-4.97
sorba freeze	polystyrene	48	sorba-freeze blocks	wrap	268x190 - 268x370	0.1-0.3
sorba freeze	polystyrene	48	sorba-freeze blocks	envelopes	250x300 - 250x600	1.1-2.55
St Vincents Insulation Limited	polystyrene	N/A	N/A	N/A		
Starlight Packaging	polystyrene	N/A	with ice	Heavy duty black	305x220x60 - 730x335x195	11.98-50.73
Starlight Packaging	polystyrene	N/A	with ice	Polysterene box	300x165x100- 665x440x180	1.71-14.8
Sundolitt	polystyrene	N/A	with ice	N/A		
Temperature Controlled Packaging	polystyrene foam	24	with ice packs	N/A		
The wild meat company	Natural Wool	36	with ice packs	N/A		

Thermal Packaging Solution	AI bubble wrap	N/A	with ice packs	Courier packs	200x120x290 - 300x120x400	1.99-2.99
Thermal Packaging Solution	AI bubble wrap	N/A	with ice packs	Pallet cover	1200x800x1200 - 1200x1200x1800	35.8-92.8
Thermal Packaging Solution	AI bubble wrap	N/A	with ice packs	Shipping container	2620x2440x6000 - 12000x2440x6000	259-808
Thermal Packaging Solution	AI bubble wrap	N/A	with ice packs	Envelopes	200x255 - 460x560	0.78-2.12
Woolcool	Natural Wool	62	with ice packs	Fleece Liners	180x525x25 - 580x980x25	0.89-2.71
Woolcool	Natural Wool	62	with ice packs	Box sets	180x180x180 - 580x380x200	2.63-7.32
Woolcool	Natural Wool	62	with ice packs	Envelopes	360x300 - 730x280	1.43-2.22
Woolcool	Natural Wool	62	with ice packs	Carrier bag	330x190x130 - 430x430x130	1.83-2.93

* : Dimension varies

**: Price varies for different size and performance

Appendix-B Development of Graphical User Interface (GUI) application

The mathematical model was implemented in a MATLAB environment. It takes time for the user to understand all logic behind the framework and to change design parameters to meet the user's needs. Besides, MATLAB is not commonly accessible software that limits the use of the model.

A graphical user interface (GUI) application was then developed based on Microsoft Visual Studio to enter the desired parameters and display results easily. The results are shown in the form of graphs and values. A functional simulation model in the form of a software application results from implementation [37]. Figure B-1 displays the opening window when the application is initiated. The parameters are categorised into the following groups: parameter of products, the parameter of coolants, the parameter of the external environment, the parameter of the insulation layer, and the parameter of packaging, including external dimensions as well as material emissivity. It is worth mentioning that the thermal conductivity and emissivity value are pre-set in the program when the material is selected. The corresponding value will be activated to involve in the simulation.

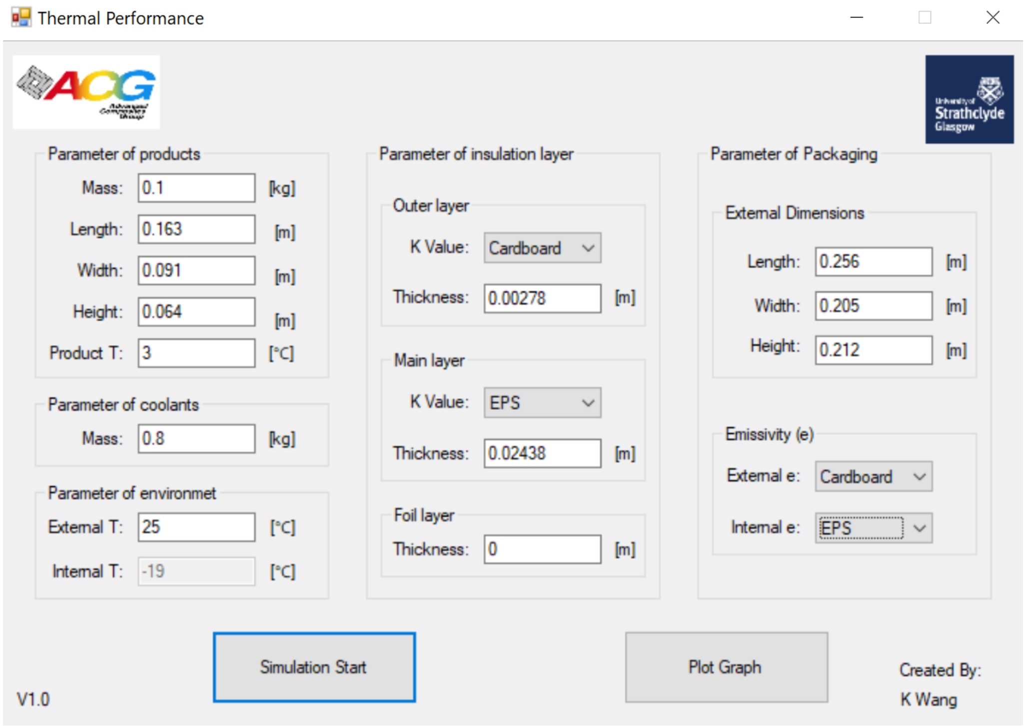

Mass: 0.1 [kg]
Length: 0.163 [m]
Width: 0.091 [m]
Height: 0.064 [m]
Product T: 3 [°C]
Mass: 0.8 [kg]
External T: 25 [°C]
Internal T: -19 [°C]
K Value: Cardboard
Thickness: 0.00278 [m]
K Value: EPS
Thickness: 0.02438 [m]
Thickness: 0 [m]
Length: 0.256 [m]
Width: 0.205 [m]
Height: 0.212 [m]
External e: Cardboard
Internal e: EPS

Figure B-1 Application window of GUI

When all parameters were entered, the simulation could then be started. Both values and graph could be displayed, as shown in Figure B-2. This application is user convenient and time-saving, which can be utilised as a cost-effective tool for packaging design concerning passive temperature control.

Parameter of products
Mass: 0.1 [kg]
Length: 0.163 [m]
Width: 0.091 [m]
Height: 0.064 [m]
Product T: 3 [°C]

Parameter of coolants
Mass: 0.8 [kg]

Parameter of environmet
External T: 25 [°C]
Internal T: -19 [°C]

Parameter of insulation layer
Outer layer
K Value: Cardboard
Thickness: 0.00278 [m]
Foil layer
Thickness: 0 [m]

Parameter of Packaging
External Dimensions
Length: 0.256 [m]
Width: 0.205 [m]
Height: 0.212 [m]
Emissivity (e)
External e: Cardboard
Internal e: EPS

The time required to reach 5 °C is 21.14 hours.

V1.0

Created By:
K Wang

Figure B-2 Result output of GUI